รายงานวิจัยฉบับสมบูรณ์

โครงการ: นาโนเทคโนโลยีในอุตสาหกรรมปิโตรเคมี: การออกแบบสังเคราะห์และวิเคราะห์ วัสดุนาโนที่มีรูพรุน

โดย

นาย จำรัส ลิ้มตระกูล

15 กันยายน พ.ศ. 2551 ถึง 14 กันยายน พ.ศ. 2554

สัญญาเลขที่ DBG5180027

รายงานวิจัยฉบับสมบูรณ์

โครงการ: นาโนเทคโนโลยีในอุตสาหกรรมปิโตรเคมี: การออกแบบสังเคราะห์และวิเคราะห์ วัสดุนาโนที่มีรูพรุน

คณะผู้วิจัย

นายจำรัส ลิ้มตระกูล

สังกัด

ภาควิชาเคมี คณะวิทยาศาสตร์

มหาวิทยาลัยเกษตรศาสตร์

สนับสนุนโดยสำนักงานกองทุนสนับสนุนการวิจัย

(ความเห็นในรายงานนี้เป็นของผู้วิจัย สกว. ไม่จำเป็นต้องเห็นด้วยเสมอไป)

สารบัญ

บทคัดย่อ

การออกแบบตัวเร่งปฏิกิริยาและการศึกษากระบวนการเร่งปฏิกิริยาเคมีระดับโมเลกุล เป็นงานวิจัยด้านหนึ่งที่มีบทบาทและเป็นประโยชน์อย่างมาก ต่อการพัฒนาอุตสาหกรรมเคมีและปิโตรเคมี ซึ่งจากการศึกษาโดยอาศัยความรู้ด้านนาโนเทคโนโลยีของวัสดุนาโนที่มีรูพรุน พบว่า ตัวเร่งปฏิกิริยาที่มีโครงสร้างในระดับนาโนเมตรแสดงสมบัติพิเศษแตกต่างไป เช่น มีความว่องไวสูงและมีคุณสมบัติที่ดีในการเลือกเกิดปฏิกิริยาที่จำเพาะกับขนาดและรูปร่างของโมเลกุล ดังนั้นการออกแบบตัวเร่งปฏิกิริยาเพื่อให้ได้คุณสมบัติตามต้องการและมีประสิทธิภาพสูงสุดนั้น จำเป็นอย่างยิ่งที่จะต้องเข้าใจโครงสร้างระดับนาโนเมตร อิทธิพลของโครงสร้างต่อสมบัติทางเคมีและสมบัติทางกายภาพและกลไลการเกิดปฏิกิริยาเคมีในระดับโมเลกุล

คณะวิจัยได้ดำเนินงานวิจัยอย่างต่อเนื่องเพื่อพัฒนางานวิจัยด้านการออกแบบ สังเคราะห์และวิเคราะห์วัสดุที่มีโครงสร้างระดับนาโนเมตร โดยเฉพาะอย่างยิ่งวัสดุนาโนที่มีรูพรุนในกลุ่มซีโอไลต์ เพราะเป็นตัวเร่งปฏิกิริยาที่มีประสิทธิภาพสูงในหลากหลายปฏิกิริยาที่มีความสำคัญในอุตสาหกรรมเคมีและปิโตรเคมี โดยได้ทำการปรับปรุงโครงสร้างของซีโอไลต์ทั้งขนาดผลึกและขนาดของรูพรุน เพื่อแก้ปัญหาเกี่ยวการแพร่ของสารตั้งต้นหรือสารผลิตภัณฑ์ที่มีขนาดใหญ่ เช่น โมเลกุลไฮโดรคาร์บอนในน้ำมันดิบจากแหล่งปิโตรเลียมธรรมชาติ ซึ่งมีผลให้ซีโอไลต์มีประสิทธิภาพในการเร่งปฏิกิริยาดีขึ้น นอกเหนือจากการสังเคราะห์และทดสอบประสิทธิภาพของตัวเร่งปฏิกิริยาในห้องปฏิบัติการจริงแล้ว คณะวิจัยยังได้ศึกษาทางทฤษฎีด้วยการคำนวนทางเคมีคอมพิวเตอร์ควบคู่กัน โดยการจำลองแบบโครงสร้างซีโอไลต์ที่ถูกดัดแปลงซึ่งมีผลต่อประสิทธิภาพในการเร่งปฏิกิริยาที่ศึกษา เสนอและอธิบายกลไกการเกิดปฏิกิริยา คำนวณค่าคงที่ทางจลนพลศาสตร์และอุณหพลศาสตร์ ในแต่ละขั้นตอนของปฏิกิริยาพื้นฐานเพื่อทำนายผลการทดลอง ซึ่งการวิเคราะห์ข้อมูลต่างๆเหล่านี้นำไปสู่การพัฒนาตัวเร่งปฏิกิริยาซีโอไลต์ได้อย่างมีประสิทธิผลมากขึ้น นอกจากนี้คณะวิจัยยังได้ศึกษาวัสดุนาโนที่มีรูพรุนอื่นๆ เช่น Nanoporous carbons, Metal-organic frameworks และ Nanoporous alkali halide polymophs เพื่อให้ได้ข้อมูลอันเป็นแนวทางในการประยุกต์ใช้งานด้านต่างๆ อาทิเช่น ด้านอิเลคทรอนิกส์ พลังงาน และการแพทย์

ตลอดระยะเวลา 3 ปีของการดำเนินโครงการ คณะวิจัยสามารถตีพิมพ์ผลงานในวารสารวิชาการนานาชาติชั้นนำจำนวนทั้งสิ้น 29 ผลงาน โดยเป็นงานวิจัยที่เกี่ยวข้องกับการออกแบบโครงสร้างเพื่อพัฒนาคุณสมบัติของตัวเร่งปฏิกิริยาซีโอไลต์มากถึง 13 ผลงาน และงานวิจัยด้านวัสดุนาโนรูพรุนชนิดอื่นๆ อีก 16 ผลงาน ซึ่งผลผลิตจากคณะวิจัยโครงการฯนี้ ถือเป็นองค์ความรู้ที่สำคัญและเป็นประโยชน์อย่างยิ่งต่อภาคการผลิตในอุตสาหกรรมเคมีและปิโตรเคมี ซึ่งจะนำไปสู่ความร่วมมือด้านงานวิจัยของประเทศต่อไปในอนาคต

Abstract

Our research project has been carefully developed to focus on molecular design, fabrication and characterization of nanostrcutured and nanoporous materials, in particular, on design, synthesis and reaction mechanism of the industrially important zeolite catalysts. Our newly developed synthetic methods are able to effectively control their crystals and pore sizes for facilitating the diffusion of the large chemical molecules such as the long chain hydrocarbon compounds. These excellent properties are very important and one of the essential key factors for cracking reactions frequently undertaken in Thai chemical industries. In addition to this, fine experiments, either state-of-the-art syntheses or the high performance of catalysts, the Nanoscale ab initio electronic structure theory and cutting-edge simulations are also employed as effective tools to design the molecular structure and reaction mechanisms and, more importantly, to derive kinetic and thermodynamic parameters which are employed to predict the feasibility of reaction. Thus, the combined state-of-the-art methods lead to the fabrication of novel and high efficiency nanoporous and nanostructured materials. Moreover, other porous materials including nanoporous carbons, metal-organic frameworks and nanoporous alkali halide polymophs are investigated. Such systematic and accurate findings provide not only reliable data for experimental and theoretical researchers for further development, but real-time beneficial information for utilizing them as nano-materials for many important areas such as, chemical, electronic, energy and medical applications.

Our small project of 3 MB could generate 29 articles published in prestige international journals, each with a very high impact factor, including the American Chemical Society Journals and Royal Society of Chemistry, England. These scientific outputs are crucial and indeed beneficial information for creating nano-materials used in chemical and petrochemical industries and do lead to collaboration between academic and industrial sections to propel the development of the potential researches in Thailand.

หน้าสรุปโครงการ (Executive Summary)
ทุนวิจัยพื้นฐานแบบกำหนดทิศทาง
"นาโนศาสตร์และนาโนเทคโนโลยี"

---

1. ชื่อโครงการ: (ภาษาไทย) โครงการ: นาโนเทคโนโลยีในอุตสาหกรรมปิโตรเคมี: การออกแบบ สังเคราะห์และวิเคราะห์ วัสดุนาโนที่มีรูพรุน

(ภาษาอังกฤษ) Applications of Nanotechnology to Petrochemical Industries: Molecular Design, Fabrication and Characterization of Nanostrcutured and Nanoporous Materials

2. ชื่อหัวหน้าโครงการ: ศ.ดร. จำรัส ลิ้มตระกูล

ที่อยู่: ภาควิชาเคมี คณะวิทยาศาสตร์ มหาวิทยาลัยเกษตรศาสตร์
50 ถนนงามวงศ์วาน แขวงลาดยาว เขตจตุจักร กรุงเทพฯ 10900
โทรศัพท์: 02-562-5555 ต่อ 2169, โทรสาร: 02-562-5555 ต่อ 2176
e-mail: fscijrl@ku.ac.th

3. สาขาที่ทำการวิจัย: สาขาเคมีเชิงฟิสิกส์

4. ปัญหาที่ทำการวิจัย และความสำคัญของปัญหา:

วัสดุนาโนที่มีรูพรุนโดยเฉพาะอย่างยิ่งวัสดุประเภทซีโอไลต์ มีความสำคัญอย่างมากต่ออุตสาหกรรมปิโตรเคมี โดยมีการใช้งานกันอย่างกว้างขวางทั้งเป็นตัวเร่งปฏิกิริยา เป็นตัวดูดซับ และใช้ในการแลกเปลี่ยนไอออน ซีโอไลต์ Y (FAU) เป็นชนิดที่มีการใช้งานมากที่สุดในกระบวนการ Fluid Catalytic Cracking (FCC) เพื่อแตกโมเลกุลไฮโดรคาร์บอนขนาดใหญ่ในน้ำมันดิบจากแหล่งปิโตรเลียมธรรมชาติ ให้ได้เป็นเชื้อเพลิงและผลิตภัณฑ์ที่เป็นประโยชน์อื่นๆ สำหรับซีโอไลต์ชนิด ZSM-5 (MFI) ซึ่งมีความเป็นกรดที่แรงกว่าและมีขนาดรูพรุนที่เล็กกว่า จะช่วยในการแตกโมเลกุลน้ำมันดิบให้ได้ผลิตภัณฑ์เป็นโอลิฟินขนาดเล็ก เช่น ethylene, propylene ซึ่งเป็นสารตั้งต้นที่สำคัญในอุตสาหกรรมพอลิเมอร์ ปัจจัยสำคัญที่มีผลต่อการใช้งานตัวเร่งปฏิกิริยาซีโอไลต์ได้แก่ลักษณะจำเพาะทางโครงสร้าง ขนาดและรูปร่างของรูพรุน สมบัติความเป็นกรด และความจำเพาะในการเลือกเกิดปฏิกิริยาตามขนาดโมเลกุล (Shape Selectivity) ซึ่งเป็นสมบัติที่เกิดจากขนาดรูพรุนซีโอไลต์ที่เล็กใกล้เคียงกับขนาดของโมเลกุลที่เข้าทำปฏิกิริยา แต่ในขณะเดียวกันขนาดของรูพรุนที่เล็กมากๆ ก็เป็นข้อจำกัดของการใช้งานซีโอไลต์ สารโมเลกุลใหญ่ไม่สามารถเข้าทำปฏิกิริยาได้และเกิดปัญหาเกี่ยวการแพร่ของสารเข้า-ออกจากรูพรุนของซีโอไลต์ ทำให้ในบางกรณี

อัตราการเกิดปฏิกิริยาถูกจำกัดด้วยอัตราการแพร่ที่ช้า และในบางกรณีการแพร่ของสารที่ช้าทำให้โมเลกุลที่เข้าทำปฏิกิริยาอยู่ในรูพรุนของซีโอไลต์นานเกินไป จนเกิดปฏิกิริยาต่อเนื่องเป็นสารอื่นที่ไม่ต้องการหรือกลายเป็น Coke อุดตันรูพรุนทำให้ซีโอไลต์เสื่อมสภาพ มีการศึกษาพบว่าถ้าสามารถลดระยะทางในการแพร่เข้า-ออกจากผลึกของซีโอไลต์ได้ จะทำให้ซีโอไลต์มีประสิทธิภาพดีขึ้น มีอัตราการเร่งปฏิกิริยาดีขึ้น มีความจำเพาะในการเลือกเกิดผลิตภัณฑ์ที่ต้องการสูงขึ้น และลดการเกิดปฏิกิริยาต่อเนื่องไปเป็นสารที่ไม่ต้องการ

โครงการวิจัยนี้เสนอการศึกษาการพัฒนาซีโอไลต์โดยเน้นที่ประเภท FAU, LTA และ MFI เพื่อลดปัญหาในการแพร่ของสารเคมีที่เข้าทำปฏิกิริยา โดยการสังเคราะห์เป็นผลึกขนาดนาโนเมตร และ/หรือ เติมรูพรุนขนาดมีโซพอร์ (Mesopore 2-50 nm) ในโครงการวิจัยนี้จะใช้ความก้าวหน้าทางเทคโนโลยีคอมพิวเตอร์ช่วยในการศึกษาร่วมกับการปฏิบัติทดลอง เพื่อสร้างความเข้าใจในปฏิกิริยาที่เกิดขึ้น และเข้าใจปัจจัยที่มีผลต่ออัตราการเกิดปฏิกิริยาและชนิดของผลิตภัณฑ์ที่ได้ สร้างเป็นฐานความรู้ในการพัฒนาปรับปรุงตัวเร่งปฏิกิริยา และกระบวนการทำปฏิกิริยาให้มีประสิทธิภาพดียิ่งขึ้น รวมถึงศึกษาผลของการปรับปรุงโครงสร้างของซีโอไลต์ดังกล่าวต่อกระบวนการดูดซับ การแลกเปลี่ยนไอออนและการเร่งปฏิกิริยา โดยเน้นที่ปฏิกิริยาพื้นฐานได้แก่ Isomerization และ Cracking ของ Butene ซึ่งเป็นปฏิกิริยาที่เหมาะสมในการศึกษาผลกระทบจากการดัดแปลงโครงสร้างผลึกซีโอไลต์ ความเป็นกรดของซีโอไลต์ต่อความจำเพาะในการเลือกเกิดปฏิกิริยา และยังเป็นปฏิกิริยาพื้นฐานในกระบวนการ Catalytic cracking ซึ่งมีความสำคัญในอุตสาหกรรม สร้างฐานความรู้ที่สำคัญเกี่ยวกับ การแพร่ การดูดซับ กลไกการเกิดปฏิกิริยา และจลนพลศาสตร์ของปฏิกิริยาของสารประกอบไฮโดรคาร์บอนในซีโอไลต์ โดยใช้เคมีคอมพิวเตอร์เพื่อศึกษากลไกปฏิกิริยา คำนวณค่าคงที่ทางจลนพลศาสตร์และอุณหพลศาสตร์ควบคู่ไปกับการศึกษาวิจัยในห้องปฏิบัติการ ดังนั้นผลของโครงการวิจัยนี้จะเป็นการสร้างองค์ความรู้ในด้านการพัฒนาซีโอไลต์ในอุตสาหกรรม เป็นประโยชน์ในการพัฒนาการผลิตซีโอไลต์เพื่อเป็นตัวดูดซับ ตัวแลกเปลี่ยนไอออน และใช้ในกระบวนการเร่งปฏิกิริยา อีกทั้งเป็นการสร้างความร่วมมือในด้านงานวิจัยและให้คำปรึกษาแก่ภาคอุตสาหกรรมในการใช้เคมีคอมพิวเตอร์ในการพัฒนาตัวเร่งปฏิกิริยา และปรับปรุงกระบวนทำปฏิกิริยาให้มีประสิทธิภาพสูงสุด

5. วัตถุประสงค์

5.1 สร้างความเชื่อมโยงอย่างเป็นรูปธรรมระหว่างสถาบันการศึกษากับภาคอุตสาหกรรม เพื่อผลักดันให้เกิดงานวิจัยที่เป็นประโยชน์ต่อภาคอุตสาหกรรมโดยตรง

5.2 พัฒนาการสังเคราะห์ซีโอไลต์ขนาดนาโนเมตร โดยเน้นที่ซีโอไลต์ประเภท FAU, LTA และ MFI

5.3 สร้างฐานความรู้เกี่ยวกับ การแพร่และการดูดซับ และกลไกปฏิกิริยา และคำนวณค่าคงที่ทางจลนพลศาสตร์และอุณหพลศาสตร์ ของปฏิกิริยาระหว่างไฮโดรคาร์บอนในซีโอไลต์ เพื่อประโยชน์ในการพัฒนาซีโอไลต์สำหรับกระบวนการดูดซับ การแลกเปลี่ยนไอออน และการเร่งปฏิกิริยา

5.4 ให้คำปรึกษาและพัฒนาศักยภาพของนักวิจัยจากภาคอุตสาหกรรม ในการประยุกต์ใช้เทคโนโลยีคอมพิวเตอร์เพื่อการพัฒนาในอุตสาหกรรมปิโตรเคมี

5.5 ผลิตบุคลากรที่มีความรู้และความเชี่ยวชาญตรงกับความต้องการของภาคอุตสาหกรรม

6. สรุปผลการดำเนินการของโครงการ

จากการดำเนินงานโครงการฯ ในระยะเวลา 3 ปี ภายใต้การสนับสนุนจากทุนวิจัยพื้นฐานแบบกำหนดทิศทาง “นาโนศาสตร์และนาโนเทคโนโลยี” นั้น คณะวิจัยโครงการฯ ได้มุ่งเน้นศึกษาการออกแบบ การสังเคราะห์และการวิเคราะห์ วัสดุนาโนที่มีรูพรุน โดยเฉพาะอย่างยิ่งวัสดุในกลุ่มซีโอไลต์ รวมไปถึงโครงสร้างที่มีรูพรุนชนิดอื่นๆ เช่น Nanoporous carbons, Metal organic frameworks และ Nanoporous alkali halide polymophs โดยอาศัยการทดลองขั้นสูงในห้องปฏิบัติการจริงพัฒนากระบวนการสังเคราะห์แบบใหม่ เพื่อดัดแปลงขนาดของผลึกให้เล็กลงอยู่ในระดับนาโนเมตรและเพิ่มขนาดรูพรุนของซีโอไลต์ให้เป็นแบบมีโซพอร์ ซึ่งลักษณะของผลึกซีโอไลต์ดังกล่าว มีความเหมาะสมต่อปฏิกิริยาการแตกโมเลกุลไฮโดรคาร์บอนขนาดใหญ่ที่มีอยู่ในน้ำมันดิบให้ได้เป็นผลิตภัณฑ์ที่เป็นประโยชน์ต่ออุตสาหกรรมเคมีและปิโตรเคมี เนื่องจากช่วยปรับปรุงอัตราการแพร่ของสารตั้งต้นและสารผลิตภัณฑ์ ซึ่งเป็นการช่วยลดการเกิดสารอื่นๆที่ไม่ต้องการอีกด้วย นอกจากนี้ยังมีการศึกษาทางทฤษฎีโดยใช้ระเบียบวิธีทางเคมีคอมพิวเตอร์ควบคู่กัน ทำการจำลองแบบโครงสร้างและวิเคราะห์ปัจจัยต่างๆ เช่น ขนาดของรูพรุน ลักษณะของรูพรุน และองค์ประกอบทางเคมีของตัวเร่งปฏิกิริยาซีโอไลต์ ต่อการดูดซับ กลไกการเกิดปฏิกิริยาเคมี จลนพลศาสตร์และอุณหพลศาสตร์ของปฏิกิริยาเคมี เพื่อให้เกิดความเข้าใจถึงอิทธิพลของปัจจัยต่างๆเหล่านั้นต่อการเกิดปฏิกิริยาอย่างละเอียดลึกซึ้ง ซึ่งนำไปสู่การดัดแปลงโครงสร้างของตัวเร่งปฏิกิริยาซีโอไลต์ให้มีประสิทธิภาพสูงสุด สำหรับวัสดุนาโนที่มีรูพรุนชนิดอื่นๆนั้น ได้มีการออกแบบโครงสร้างใหม่ๆ เพื่อปรับปรุงคุณสมบัติการใช้งานในด้านต่างๆ อาทิเช่น ด้านอิเลคทรอนิกส์ พลังงาน และการแพทย์ เป็นต้น ซึ่งงานทั้งหมดดังกล่าวจะเป็นแนวทางนำไปสู่ในการพัฒนางานวิจัยและความร่วมมือในภาคการศึกษาและภาคอุตสาหกรรมที่เกี่ยวข้องต่อไป

ผลลัพธ์ของโครงการฯ ทำให้เกิดงานวิจัยที่สามารถถูกตีพิมพ์ในวารสารวิชาการนานาชาติ
ทั้งสิ้นจำนวน 29 เรื่อง

เนื้อหางานวิจัย

คณะวิจัยโครงการฯ ได้มุ่งเน้นศึกษาการสังเคราะห์วัสดุนาโนที่มีรูพรุนอย่างซีโอไลต์ ซึ่งถูกใช้เป็นตัวเร่งปฏิกิริยาที่มีความสำคัญในอุตสาหกรรมเคมีและปิโตรเคมี เช่น การแตกโมเลกุลน้ำมันดิบให้ได้ผลิตภัณฑ์เป็นโอลิฟินขนาดเล็ก เช่น Ethylene และ Propylene ซึ่งเป็นสารตั้งต้นที่สำคัญในอุตสาหกรรมพอลิเมอร์ คณะวิจัยได้ทำการสังเคราะห์ซีโอไลต์ชนิด ZSM-5 ด้วยกระบวนการสังเคราะห์แบบใหม่เพื่อลดปัญหาการแพร่ของสารเคมีที่เข้าทำปฏิกิริยา โดยทำให้เป็นผลึกขนาดนาโนเมตรและเติมรูพรุนมีโซพอร์ (Mesopore 2-50 nm) ปัจจัยที่สำคัญในการสังเคราะห์ผลึกขนาดนาโนเมตรคือ ต้องเพิ่มอัตราการเกิด nuclei (nucleation rate) และลดอัตราการเติบโตของผลึก (Crystal growth) ซึ่งสามารถทำได้โดยการใช้สารละลายความเข้มข้นสูงเพื่อให้เกิด Nuclei จำนวนมาก สำหรับการดัดแปลงโครงสร้างผลึกโดยเติมรูพรุนขนาดมีโซพอร์นั้น ได้สังเคราะห์ซีโอไลต์จากสารตั้งต้นที่เป็นสารผสมของซิลิกาและคาร์บอน (Si/C) ซึ่งมีคุณสมบัติพิเศษคือนอกจากเป็นแหล่งให้ซิลิกา (Silica source) ที่เป็นองค์ประกอบหลักในโครงสร้างแล้ว อนุภาคคาร์บอนในสารผสมดังกล่าวยังทำหน้าที่เป็นแม่แบบเพื่อให้เกิดรูพรุนขนาดมีโซพอร์ (Mesoporous template) อีกด้วย โดยอนุภาคคาร์บอนนี้จะถูกเผาทิ้งภายหลังการสังเคราะห์ผลึกจากกระบวนการ Hydrothermal ซึ่งจะทำให้เกิดเป็นรูพรุนขนาดมีโซพอร์อยู่ภายใน ซึ่งการวิจัยนี้ได้ควบคุมปัจจัยต่างๆ ให้เหมาะสมที่สามารถทำให้เกิดช่องว่างรูพรุนขนาด 2-50 นาโนเมตร (Mesopore) ได้แก่ ชนิดของก๊าซที่เป็นแหล่งกำเนิดคาร์บอน, อัตราส่วนของ Si:C ซึ่งแปรผันกับระยะเวลาในการเผาไหม้และความเข้มข้นของก๊าซขณะเผาไหม้

นอกเหนือจากการสังเคราะห์และวิเคราะห์ตัวเร่งปฏิกิริยาในห้องปฏิบัติการจริงแล้ว คณะผู้วิจัยยังได้ศึกษาทางทฤษฎีด้วยระเบียบวิธีทางเคมีคอมพิวเตอร์ควบคู่กัน ในการออกแบบโครงสร้างของวัสดุและตัวเร่งปฏิกิริยาที่มีขนาดระดับนาโนเมตรเพื่อปรับปรุงคุณสมบัติที่ต้องการให้ดียิ่งขึ้น โดยทำการศึกษาการดูดซับของสารตั้งต้นในปฏิกิริยาที่สำคัญต่างๆบนตัวเร่งปฏิกิริยาซีโอไลต์ ซึ่งถือว่าเป็นขั้นแรกของกระบวนการเร่งปฏิกิริยาและศึกษากลไกการเกิดปฏิกิริยาในระดับโมเลกุล รวมถึงวิเคราะห์ปัจจัยต่างๆที่มีผลต่อการเกิดปฏิกิริยาซึ่งมีรายละเอียดดังนี้

- ศึกษาผลของความเป็นกรดของตัวเร่งปฏิกิริยาซีโอไลต์ชนิด ZSM-5 ต่อการเกิดปฏิกิริยา Beckmann Rearrangement ของสารประกอบ Cyclohexanone Oxime ไปเป็นสารประกอบ ε-caprolactam ซึ่งเป็นสารตั้งต้นที่สำคัญในการผลิต Nylon-6 polymer ที่ใช้ในอุตสาหกรรมเคมีสิ่งทอ
- ศึกษากลไกของปฏิกิริยาการเติมหมู่ Methyl ไปยังโมเลกุลของ Ethylene ด้วย Methanol และ Dimethyl Ether โดยใช้ซีโอไลต์ชนิด H-ZSM-5 เป็นตัวเร่งปฏิกิริยา และศึกษากลไกปฏิกิริยาการเติมหมู่ Methyl ด้วย Methanol ไปยังโมเลกุลของ 2-methylnaphthalene โดยใช้

ซีโอไลต์ชนิด H-BEA เป็นตัวเร่งปฏิกิริยา ซึ่งทั้งสองปฏิกิริยาดังกล่าวเป็นกระบวนการเปลี่ยน Methanol ที่เป็นสารพลอยได้จากกระบวนการเปลี่ยนก๊าซธรรมชาติหรือถ่านหินไปเป็นน้ำมันเชื้อเพลิงในอุตสาหกรรมปิโตรเลียม ให้กลายเป็นสารประกอบไฮโดรคาร์บอนที่สำคัญในอุตสาหกรรมปิโตรเคมี

- ศึกษากลไกปฏิกิริยาการ Isomerization บนตัวเร่งปฏิกิริยา β-ซีโอไลต์ ของ 1,5-Dimethylnaphthalene ไปเป็น 2,6-Dimethylnaphthalene ซึ่งเป็นโมโนเมอร์สำคัญในการผลิตพอลิเมอร์ชนิด Polyethylene naphthalate (PEN) ที่มีคุณสมบัติพิเศษและนิยมใช้ในการผลิตไฟเบอร์ ฟิล์ม และบรรจุภัณฑ์
- ศึกษาผลของโครงสร้างซีโอไลต์ ZSM-5 ต่อการดูดซับสารประกอบ Unsaturated Aliphatic, Aromatic, และ Heterocyclic ซึ่งทั้งหมดเป็นสารประกอบสำคัญที่ถูกใช้ในอุตสาหกรรมเคมี รวมถึงศึกษาปฏิกิริยาการแลกเปลี่ยนอะตอมไฮโดรเจนบนสารประกอบ Aromatic ซึ่งเป็นปฏิกิริยาพื้นฐานในการต่อยอดงานวิจัยที่เกี่ยวข้องต่อไป
- ศึกษาอิทธิพลของความเป็นกรดในซีโอไลต์ชนิด H-FER, H-ZSM-5 และ H-MCM-22 ต่อประสิทธิภาพการดูดซับและการเกิดปฏิกิริยา Tautomerization ของ Acetone ไปเป็นสารประกอบในรูป Enol ซึ่งเป็นขั้นตอนแรกของการเกิดปฏิกิริยา Aldol condensation ในการสังเคราะห์สารอินทรีย์ที่สำคัญหลายชนิด
- ศึกษาอิทธิพลทางโครงสร้างของตัวเร่งปฏิกิริยาซีโอไลต์ชนิด H-FAU and H-ZSM-5 ต่อปฏิกิริยาการแตกพันธะของ Hexane ซึ่งปฏิกิริยาการแตกพันธะคาร์บอนในลักษณะนี้เป็นปฏิกิริยาสำคัญในอุตสาหกรรมปิโตรเคมี ที่ใช้สำหรับเปลี่ยนไฮโดรคาร์บอนสายโซ่ยาวให้เป็นไฮโดรคาร์บอนสายสั้นลงเพื่อนำไปผลิตเชื้อเพลิง
- ศึกษากลไกการเกิดปฏิกิริยา Oxidative Dehydrogenation บนตัวเร่งปฏิกิริยาซีโอไลต์ชนิด MCM22 ของ Propane ไปเป็น Propene ซึ่งเป็นสารตั้งต้นสำคัญในอุตสาหกรรมพอลิเมอร์
- ศึกษากลไกการเกิดปฏิกิริยา Dehydration บนตัวเร่งปฏิกิริยาซีโอไลต์ H-ZSM-5 ของ Glycerol ไปเป็นสารประกอบ Acrolein ที่เป็นสารตั้งต้นสำคัญและนิยมใช้ในอุตสาหกรรมผลิตสารเคมีหลายชนิด เช่น DL-Methionine, Acrylic acid, Super absorber polymers, และ Detergents
- ศึกษาอิทธิพลของโลหะทรานซิชั่น Cu, Ag และ Au ในโครงสร้างของซีโอไลต์ชนิด FAU ต่อการเกิดปฏิกิริยา Carbonyl-ene ของสารประกอบ Formaldehyde

พบว่าปัจจัยด้านโครงสร้าง อาทิเช่น ขนาดของรูพรุน ลักษณะของรูพรุน ตำแหน่งและลักษณะของ Active site รวมถึงองค์ประกอบทางเคมีของซีโอไลต์ ส่งผลอย่างมากต่อค่าพลังงานดูดซับ พลังงานกระตุ้นและพลังงานของปฏิกิริยา ดังนั้นการที่จะเลือกตัวเร่งปฏิกิริยามาใช้ประโยชน์จำเป็น

ที่จะต้องศึกษาให้เข้าใจกลไกการเกิดปฏิกิริยา และปัจจัยต่างๆที่มีผลต่อการเกิดปฏิกิริยาอย่างละเอียด เพราะจะทำให้ได้ข้อมูลที่จะนำไปสู่การออกแบบดัดแปลงโครงสร้าง รวมถึงการพัฒนากระบวนการเคมีให้มีประสิทธิภาพสูงสุด นอกจากนี้การเลือกระเบียบวิธีการคำนวณให้เหมาะสมกับระบบที่ศึกษาถือเป็นอีกปัจจัยหนึ่งที่มีผลต่อความน่าเชื่อถือของข้อมูลที่ได้รับ โดยกรณีที่ระบบที่ต้องการศึกษาประกอบด้วยโมเลกุลที่ถูกดูดซับซึ่งมีขนาดใกล้เคียงกับรูพรุนของซีโอไลต์ และเป็นโมเลกุลไม่มีขั้ว พลังงานการดูดซับที่ได้นั้นจะเกิดจากแรงดึงดูดแบบ van der Waals ระหว่างโมเลกุลกับผนังรูพรุนของซีโอไลต์เป็นส่วนใหญ่ อย่างไรก็ตามเมื่อโมเลกุลที่ถูกดูดซับเป็นโมเลกุลมีขั้วแรงดึงดูดแบบ van der Waals จะมีผลต่อพลังงานการดูดซับน้อยลง แต่ผลของแรงดึงดูดแบบ Electrostatic จากโครงผลึกของซีโอไลต์จะเพิ่มขึ้น ดังนั้นเมื่อต้องการศึกษาการดูดซับของสารประกอบอะโรมาติกส์บนตัวเร่งปฏิกิริยาซีโอไลต์ จึงควรเลือกใช้ระเบียบวิธีที่รวมอิทธิพลของแรงดึงดูดแบบ van der Waals ไว้ด้วย ซึ่งวิธีหนึ่งที่ประหยัดเวลาและให้ผลที่เชื่อถือได้คือ DFT:UFF Hybrid method ในขณะที่ระบบมีสารดูดซับเป็นโมเลกุลมีขั้ว เช่น น้ำหรือเมทานอล ควรเลือกใช้ระเบียบวิธีที่รวมผลของแรงดึงดูดแบบ electrostatic ไว้ด้วย เช่น SCREEP method อย่างไรก็ดี ถึงแม้ DFT:UFF และ SCREEP Hybrid methods จะสามารถใช้ศึกษาการดูดซับของโมเลกุลบนตัวเร่งซีโอไลต์ได้ดี แต่ทั้งสองวิธีนี้ยังมีข้อจำกัด โดยเฉพาะอย่างยิ่งเมื่อต้องการศึกษากลไกการเร่งปฏิกิริยาของซีโอไลต์ที่เกี่ยวข้องกับ Transition states หรือ Intermediates ที่มีโครงสร้างเกะกะและมีประจุ การใช้แบบจำลองที่มีเพียงแรงดึงดูดแบบ van der Waals หรือ Electrostatic อย่างใดอย่างหนึ่งจึงไม่เพียงพอที่จะอธิบายโครงสร้างที่ไม่เสถียรเหล่านี้ได้ คณะผู้วิจัยจึงได้พัฒนาระเบียบวิธีใหม่บนพื้นฐานของระเบียบวิธีเดิมคือ การรวมอิทธิพลของแรงดึงดูดแบบ van der Waals และ Electrostatic ไว้ในแบบจำลองเดียวกัน เพื่อเปรียบเทียบการดูดซับและการเร่งปฏิกิริยาของซีโอไลต์ที่มีโครงสร้างผลึกต่างกันและเรียกแบบจำลองนี้ว่า Embedded ONIOM method รวมถึงการใช้ระเบียบวิธีการคำนวณที่มีความถูกต้องสูง และมีการพัฒนาอย่างต่อเนื่องให้เหมาะสมกับการศึกษาปฏิกิริยาเคมีในโครงสร้างของซีโอไลต์อย่าง M06-L อีกด้วย

นอกเหนือจากตัวเร่งปฏิกิริยาซีโอไลต์แล้ว คณะผู้วิจัยยังได้ศึกษาวัสดุที่มีรูพรุนอย่างโครงสร้างของ Metal-organic frameworks ในการดูดซับสารตั้งต้นที่สำคัญในอุตสาหกรรมเคมีอย่าง Formaldehyde ซึ่งทำให้ได้ข้อมูลที่เป็นประโยชน์ในการปรับปรุงโครงสร้างเพื่อนำไปใช้เป็นตัวเร่งปฏิกิริยาที่เกี่ยวข้องต่อไป นอกจากนี้ยังได้ศึกษาวัสดุที่มีโครงสร้างระดับนาโนเมตรอย่างคาร์บอนนาโนทิวบ์ โดยการดัดแปลงโครงสร้างด้วยการเติมหมู่ฟังก์ชั่นหรือโลหะเพื่อปรับปรุงคุณสมบัติของคาร์บอนนาโนทิวบ์ให้เหมาะสมกับการนำไปประยุกต์ใช้งานด้านต่างๆ อาทิเช่น ตัวเร่งปฏิกิริยาและตัวตรวจจับสารเคมี (Sensor) โดยพบว่าคาร์บอนนาโนทิวบ์เป็นตัวกลางที่ดีในการถ่ายเทอิเล็กตรอน เช่น อิเล็กตรอนจากปฏิกิริยา Oxidation ของ Anthraquinonyl สามารถถ่ายเทผ่านคาร์บอนนาโนทิวบ์ไปเกิดปฏิกิริยา Reduction ของ 4-arylhydroxyl amine ได้ สำหรับคาร์บอนนา

โนทิวบ์ที่ถูกปรับปรุงโครงสร้างด้วยโลหะทรานซิชั่นไปบนผนังท่อ ยังสามารถแสดงการเปลี่ยนแปลงสมบัติทางไฟฟ้าได้อย่างเด่นชัด ในกระบวนการตรวจจับสารพิษและสารก่อมลพิษอย่าง Ammonia และ Nitrogen dioxide และเนื่องด้วยโครงสร้างที่มีลักษณะเป็นท่อ คณะวิจัยจึงได้ทำการศึกษาการเคลื่อนที่ของโมเลกุลขนาดเล็กอย่างน้ำภายในท่อคาร์บอนนาโนทิวบ์ ซึ่งได้ข้อมูลเชิงลึกและเป็นประโยชน์ ในการประยุกต์ใช้คาร์บอนนาโนทิวบ์ทำหน้าที่กักเก็บและถ่ายเทสารบางชนิดได้ สำหรับวัสดุนาโนที่มีรูพรุนอีกชนิดที่ได้ทำการศึกษาคือ สารประกอบ Alkali halide โดยได้พยายามออกแบบและวิเคราะห์สารประกอบ alkali halide หลายชนิด เช่น LiF, NaBr, KCl และ RbI เป็นต้น เพื่อให้ได้รูปแบบโครงสร้างที่เสถียรในการนำไปสังเคราะห์และใช้ประโยชน์ต่อไป

ผลลัพธ์ที่ได้จากโครงการ

1. สรุปผลงานที่ได้รับการตีพิมพ์ในวารสารวิชาการนานาชาติในตลอดระยะเวลา 3 ปี ของการดำเนินโครงการ อันได้แก่

   1.1 บทความทางวิชาการที่เกี่ยวข้องกับตัวเร่งปฏิกิริยาซีโอไลต์ จำนวน 13 ผลงาน

   1.1.1 Jakkapan Sirijaraensrea, Jumras Limtrakul, **Effect of the acidic strength on the vapor phase Beckmann rearrangement of cyclohexanone oxime over the MFI zeolite: An embedded ONIOM study**. *Physical Chemistry Chemical Physics,* **2009**, *11*, 578–585.

   1.1.2 Thana Maihom, Bundet Boekfa, Jakkapan Sirijaraensre, Tanin Nanok, Micael Probst, Jumras Limtrakul, **Reaction mechanisms of the methylation of ethene with methanol and dimethyl Ether over H-ZSM-5: An ONIOM study**. *The Journal of Phyicals. Chemistry C,* **2009**, *113*, 6654–6662.

   1.1.3 Chawanwit Kumsapaya, Karan Bobuatong, Pipat Khongpracha, Yuthana Tantirungrotechai, Jumras Limtrakul, **Mechanistic investigation on 1,5- to 2,6-Dimethylnaphthalene isomerization catalyzed by acidic β zeolite: ONIOM study with an M06-L functional**. *The Journal of Phyical Cheistrry C,* **2009**, *113,* 16128–16137.

   1.1.4 Bundet Boekfa, Saowapak Choomwattana, Pipat Khongpracha, Jumras Limtrakul, **Effects of the zeolite framework on the adsorptions and hydrogen-exchange reactions of unsaturated aliphatic, aromatic, and heterocyclic compounds in ZSM-5 zeolite: A combination of perturbation**

theory (MP2) and a newly developed density functional theory (M06-2X) in ONIOM scheme. *Langmuir*, **2009**, *25*, 12990–12999.

1.1.5 Bundet Boekfa, Piboon Pantu, Michael Probst, Jumras Limtrakul, **Adsorption and tautomerization reaction of acetone on acidic zeolites: the confinement effect in different types of zeolites**. *Journal of Physical Chemistry C,* **2010**, *114*, 15061–15067.

1.1.6 Thana Maihom, Piboon. Pantu, Chaiwat Tachakritikul, Michael Probst, Jumras Limtrakul, **Effect of the zeolite nanocavity on the reaction mechanism of n-Hexane cracking: A density functional theory study**. *Journal of Physical Chemistry C,* **2010**, *114*, 7850–7856.

1.1.7 Sippakorn Wannakao, Bundet Boekfa, Pipat Khongpracha, Michael Probst, Jumras Limtrakul, **Oxidative dehydrogenation of propane over a VO_2-exchanged MCM-22 zeolite: A DFT Study**. *ChemPhysChem*, **2010,** *11*, 3432-3438.

1.1.8 Karan Bobuatong, Michael Probst, Jumras Limtrakul, **Structures and energetics of the methylation of 2-methylnaphthalene with methanol over H-BEA Zeolite**. *Journal of Physical Chemistry C*, **2010,** *114*, 21611-21617.

1.1.9 Kanokwan Kongpatpanich, Tanin Nanok, Bundet Boekfa, Michael Probst, Jumras Limtrakul, **Structures and reaction mechanisms of glycerol dehydration over H-ZSM-5 zeolite: A density functional theory study.** *Physical Chemistry Chemical Physics*, **2011,** *13*, 6462-6470.

1.1.10 Siriporn Jungsuttiwong, Jarun Lomratsiri, Jumras Limtrakul, **Characterization of acidity in [B], [Al], and [Ga] isomorphously substituted ZSM-5: Embedded DFT/UFF approach**. *International Journal of Quantum Chemistry*, **2011**, *111*, 2275-2282.

1.1.11 Oranit Phuakkong, Karan Bobuatong, Piboon Pantu, Bundet Boekfa, Michael Probst, Jumras Limtrakul, **Glycine peptide bond formation catalyzed by Faujasite**. *ChemPhysChem*, **2011**, *12*, 2160-2168.

1.1.12 Sippakorn Wannakao, Pipat Khongpracha, Jumras Limtrakul, **Density functional theory study of the carbonyl-ene reaction of encapsulated**

formaldehyde in Cu(I), Ag(I), and Au(I) exchanged FAU zeolites. *Journal of Physical Chemistry A,* **2011**, *115*, 12486-12492.

1.1.13 Chularat Wattanakit, Chompunuch Warakulwit, Piboon Pantu, Boonruen Sunpetch, Metta Charoenpanich, Jumras Limtrakul, **The versatile synthesis method for hierarchical micro- and mesoporous zeolite: an embedded nanocarbon cluster approach**. *The Canadian Journal of Chemical Engineering,* **Inpress**.

1.2 บทความทางวิชาการที่เกี่ยวข้องกับวัสดุที่มีรูพรุนชนิดอื่นๆ จำนวน 16 ผลงาน

1.2.1 Panvika Pannopard, Pipat Khongpracha, Michael Probst, Jumras Limtrakul, **Gas sensing properties of platinum derivatives of single-walled carbon nanotubes: A DFT analysis**. *Journal of Molecular Graphics and Modelling,* **2009**, *28*, 62–69.

1.2.2 Tanin Nanok, Nongnuch Artrith, Piboon Pantu, Philippe A. Bopp, Jumras Limtrakul, **Structure and dynamics of water confined in single-wall nanotubes**. *The Journal of Phyical Cheistrry A,* **2009**, *113,* 2103–2108.

1.2.3 Winyoo Sangthong, Jumras Limtrakul, Francesc Illasa, Stefan Thomas Bromley, **Stable nanoporous alkali halide polymorphs: a first principles bottom-up study**. *Journal of Materials Chemistry,* **2008***, 18,* 5871–5879.

1.2.4 Winyoo Sangthong, Jumras Limtrakul, Francesc Illas, Stefan T. Bromley, **Predicting transition pressures for obtaining nanoporous semiconductor polymorphs: oxides and chalcogenides of Zn, Cd and Mg**. *Physical Chemistry Chemical Physics,* **2010**, *12,* 8513-8520.

1.2.5 G. Loget, G. Larcade, V. Lapeyre, P. Garrigue, C. Warakulwit, J. Limtrakul, M.-H. Delville, V. Ravaine, A. Kuhn, **Single point electrodeposition of nickel for the dissymmetric decoration of carbon tubes**. *Electrochimica Acta*, **2011**, *55*, 8116-8120.

1.2.6 Winyoo Sangthong, Jumras Limtrakul, Francesc Illas, Stefan T. Bromley, **Persistence of magic cluster stability in ultra-thin semiconductor nanorods**. *Nanoscale,* **2010**, *2*, 72–77.

1.2.7 Teeranan Nongnual, Somkiat Nokbin, Pipat Khongpracha, Philippe Anthony Bopp, Jumras Limtrakul, **Density functional theory evidence for an electron hopping process in single-walled carbon nanotube-mediated redox reactions**. *Carbon*, **2010**, *48*, 1524 –1530.

1.2.8 Amporn Sane, Jumras Limtrakul, **Formation of retinyl palmitate-loaded poly(l-lactide) nanoparticles using rapid expansion of supercritical solutions into liquid solvents (RESOLV)**. *Journal of Supercritical Fluids,* **2009**, *51*, 230–237.

1.2.9 Natcha Injan, Tuende Megyes, Tamas Radnai, Imre Bako, Szabolcz Balint, Jumras Limtrakul, Daniel Spangberg, Michael Probst, **Potential energy surface and molecular dynamics simulation of gold(I) in liquid nitromethane**. *Journal of Molecular Liquids*, **2009**, *147*, 64-70.

1.2.10 Chan Inntam, Jumras Limtrakul, **Adsorption of M species and M2 dimers (M = Cu, Ag, and Au) on the pristine and defective single-walled carbon nanotubes: A density functional theory study**. *Journal of Physical Chemistry C*, **2010**, *114*, 21327-21337.

1.2.11 Teeranan Nongnual, Jumras Limtrakul, **Healing of a vacancy defect in a single-walled carbon nanotube by carbon monoxide disproportionation**. *Journal of Physical Chemistry C*, **2011,** *115*, 4649-4655.

1.2.12 Fattah Z., Loget G., Lapeyre V., Garrigue P., Chompunuch Warakulwit, Jumras Limtrakul, Bouffier L., Kuhn A., **Straightforward single-step generation of microswimmers by bipolar electrochemistry**. *Electrochimica Acta*, **2011**, 56, 10562-10566.

1.2.13 Natcha Injan, Tuende Megyes, Tamas Radnai, Imre Bako, Szabolcz Balint, Jumras Limtrakul, Michael Probst, **$Au(CN)_2(CH_3NO_2)_n$ cluster anions: Energetics and geometrical features**. *Journal of Molecular Liquids*, **2011,** *159*, 38-41.

1.2.14 Gabriel Loget, Veronique Lapeyre, Patrick Garrigue, Chompunuch Warakulwit, Jumras Limtrakul, Marie-Helene Delville, Alexander Kuhn**, Versatile Procedure for Synthesis of Janus-Type**. *Chemistry of Materials*, **2011**, *23*, 2595-2599.

1.2.15 Norawit Krainara, Jumras Limtrakul, Francesc Illas, Stefan T. Bromley, **Structural and electronic bistability in ZnS single sheets and single-walled nanotubes**. *Physical Review B: Condensed Matter and Materials Physics*, **2011**, *83*, 233305/1-233305/4.

1.2.16 Thana Maihom, Saowapak Choomwattana, Pipat Khongpracha, Michael Probst, Jumras Limtrakul, **Formaldehyde Encapsulated in Lithium-Decorated Metal-Organic Frameworks: A Density Functional Theory Study**. *ChemPhysChem*, **Inpress**.

2. สรุปผลงานในการประชุมนานาชาติตลอดระยะเวลา 3 ปี ของการดำเนินโครงการ อันได้แก่

2.1 งานวิจัยที่นำเสนอในการประชุมวิชาการนานาชาติ “Nanotech Conference 2009” ณ เมือง Houston ประเทศสหรัฐอเมริกา ระหว่างวันที่ 3-7 พฤษภาคม 2552 จำนวน 8 เรื่อง

2.1.1 Bundet Boekfa, Saowapak Choomwattana, Phornpimon Maitarad, Jumras Limtrakul, **The quantum confinement effect on the adsorption and reaction of aliphatic and aromatic hydrocarbons on ‘nano reactor’ ZSM-5 zeolite: A newly developed density functional theory (DFT) investigation**.

2.1.2 Chawanwit Kumsapaya, Karan Bobuatong ,Saowapak Choomwattana, Pipat Khongpracha,Yuthana Tantirungrotechai, Jumras Limtrakul, **A mechanistic investigation on 1,5- to 2,6-Dimethylnaphthalene isomerization catalyzed by acidic Beta zeolite: An ONIOM study with a newly developed density functional theory**.

2.1.3 Jittima Meeprasert, Saowapak Choomwattana, Piboon Pantu, Jumras Limtrakul, **Dehydration of ethanol into ethylene over H-MOR: A quantum chemical investigation of possible reaction mechanisms in the presence of water**.

2.1.4 Karan Bobuatong, Jakkapan Sirijaraensre, Pipat Khongpracha, Piboon Pantu, Jumras Limtrakul, **The Theoretical Investigation of Oxidative dehydrogenation of ethane to ethene over Fe-ZSM-5: A QM/MM study**.

2.1.5 Sudarat Yadnum, Saowapak Choomwattana, Pipat Khongpracha, Jumras Limtrakul, **structures and mechanism of MOF-505 and Cu-ZSM-5 promoted Mukaiyama aldol reaction: An ONIOM study**.

2.1.6 Chompunuch Warakulwit, M.-H. Delville, V. Ravaine, Jumras Limtrakul, Alexander Kuhn, **Dissymetric metal deposition on carbon nanotubes**.

2.1.7 Teeranan Nongnual, Saowapak Choomwattana, Somkiat Nokbin, Pipat Khongpracha, Jumras Limtrakul, **Electron hopping process in SWCNT-mediated redox reaction: An evidence observed by DFT theory**.

2.1.8 Winyoo Sangthong, Jumras Limtrakul, Francesc Illasa, Stefan Thomas Bromley, **Comparing the stabilities of nanoclusters and cluster-based materials: alkali halides and the first row element compounds**.

2.2 งานวิจัยที่นำเสนอในการประชุมวิชาการนานาชาติ “ 239th American Chemical Society National meeting & Exposition” ณ เมือง San Francisco ประเทศสหรัฐอเมริกา ระหว่างวันที่ 21-25 มีนาคม 2553 จำนวน 11 เรื่อง

2.2.1 Sarawoot Impeng, Thana Maihom, Pipat Kongpracha, Somkiat Nokbin, Jumras Limtrakul, **Propane cracking reaction over different types of nanostructured zeolites: A newly developed DFT approach**.

2.2.2 Supalak Khueanphet, Bundet Boekfa, Tanin Nanok, Jumras Limtrakul, **Adsorption of a basic probe molecule over nanostructured zeolitic catalysts (H-FAU, H-MOR, and H-MCM-22): A newly developed density functional M06-2X study**.

2.2.3 Chularat Wattanakit, Butdet Boekfa, Somkiat Nokbin, Piboon Pantu, Jumras Limtrakul, **Skeletal isomerization of 1-Butene over ferrierite zeolite: A quantum chemical analysis of structures and reaction mechanisms**.

2.2.4 Kanokwan Kongpatpanich, Tanin Nanok, Bundet Boekfa, Jumras Limtrakul**, Structures and reaction mechanisms of glycerol dehydration over H-ZSM-5 zeolites**.

2.2.5 Bundet Boekfa, Piboon Pantu, Pailin Limtrakul, Michael Probst, Jumras Limtrakul, **Application of newly developed M06-2X functional for identifying A suitable industrially important petrochemical zeolite catalyst for a particular reaction**.

2.2.6 Pemikar Srifa, Somkiat Nokbin, Bundet Boekfa, Jumras Limtrakul, **Quantum-chemical analysis of reactions between Pyridine and the industrially important petrochemical zeolite catalyst**.

2.2.7 Sippakorn Wannakao, Bundet Boekfa, Pipat Kongpracha, Jumras Limtrakul, **Oxidative dehydrogenation of propane over a VO_2-exchanged MCM-22: A newly developed DFT study**.

2.2.8 Thana Maihom, Piboon Pantu, Chaiwat Tachakrittikul, Jumras Limtrakul, **Adsorption and cracking reaction of n-Hexane over H-ZSM-5: A M06-2X study**.

2.2.9 Sudarat Yadnum, Soawapak Choomwattana, Pipat Kongpracha, Jumras Limtrakul, **Density functional study of epoxide ring-opening reaction with methanol promoted by dicopper carboxylate in metal-organic framework.**

2.2.10 Chardchalerm Raksakoon, Saowapak Choomwattana, Jumras Limtrakul, **Molecular dynamics simulation of otho-, para- and meta-xylenes diffusion in MOF-5 with a model potential of Zn-O bonds for MOF materials**.

2.2.11 Panvika Pannopard, Pipat Kongpracha, Chompunuch Warakulwit, Jumras Limtrakul**, Decomposition of nitrous oxide on transition metal-doped carbon nano-tubes**.

2.3 งานวิจัยที่นำเสนอในการประชุมวิชาการนานาชาติ "240th American Chemical Society National meeting & Exposition" ณ เมือง Boston ประเทศสหรัฐอเมริกา ระหว่างวันที่ 22-26 สิงหาคม 2553 จำนวน 6 เรื่อง

2.3.1 Bundet Boekfa, Thana Maihom, Sippakorn Wannakao, Karan Bobuatong, Jumras Limtrakul, **Structures and reaction mechanisms of propene oxide isomerization to propanal on H-FER zeolite: A theoretical study using the newly developed density functional theory**.

2.3.2 Bundet Boekfa, Thana Maihom, Sippakorn Wannakao, Pailin Limtrakul, Jumras Limtrakul, **Catalytic dehydrogenation of ethylbenzene to styrene over Fe-ZSM-5 zeolite: A newly developed density functional theory (M06-L) in ONIOM scheme**.

2.3.3 Karan Bobuatong, Bundet Boekfa, Sippakorn Wannakao, Jumras Limtrakul, **Structures and Reaction pathways of Methylation of 2-methylnaphthalene with Methanol over HBEA zeolite**.

2.3.4 Sippakorn Wannakao, Thana Maihom, Winyoo Sangthong, Bundet Boekfa, Pipat Khongpracha, Jumras Limtrakul, **DFT study of oxidative dehydrogenation of propane over a VO2-exchanged MCM-22 and ZSM-5 zeolites**.

2.3.5 Thana Maihom, Bundet Boekfa, Sippakorn Wannakao, Jumras Limtrakul, **Reaction mechanisms of ethene formation via ethanol dehydration catalyzed by Fe-ZSM-5 zeolite: An ONIOM study with an M06-L functional**.

2.3.6 Winyoo Sangthong, Sippakorn Wannakao, Saowapak Choomwattana, Thana Maihom, , Bundet Boekfa, Jumras Limtrakul, **Quantum chemical calculation of the hydrogenation reaction of encapsulated formaldehyde in Na-FAU zeolite**.

2.4 งานวิจัยที่นำเสนอในการประชุมวิชาการนานาชาติ “Nanothailand 2010: Nanotechnology for a Sustainable World” ณ โรงแรมรามา การ์เด้นส์ กรุงเทพฯ ประเทศไทย ระหว่างวันที่ 18-20 พฤศจิกายน 2553 จำนวน 15 เรื่อง

2.4.1 Teeranan Nongnual, Jmras Limtrakul, **Healing of a vacancy defect in a Single-Walled Carbon Nanotube by carbon monoxide disproportionation**.

2.4.2 Sippakorn Wannakao, Pipat Khongpracha, Jumras Limtrakul, **Carbonyl-ene reaction of encapsulated formaldehyde in Cu(I), Ag(I) and Au(I) exchanged FAU zeolites**.

2.4.3 Thana Maihom, Jumras Limtrakul, **Theoretical investigation of the effect of the zeolite acidic strength on the reaction mechanism of n-Hexane cracking**.

2.4.4 Anawat Thivasasith, Panvika Pannopard, Pipat Khongpracha, Chompunuch Warakulwit, Jumras Limtrakul, **H-Bond formation assisted by a single Au atom and an Au_{13} cluster: A DFT study**.

2.4.5 Boonruen Sunpetch, Bundet Boekfa, Piboon Pantu, Jumras Limtrakul, **Theoretical studies of nitrous oxide decomposition reaction in transition metals (TM) ion exchanged ZSM-5 zeolite**.

2.4.6 Winyoo Sangthong, Jumras Limtrakul, **Corporative effect of zeolite framework and cation on dehydrogenation of methanol over Na-exchanged faujasite zeolite: A newly developed density functional (M06-2X)**.

2.4.7 Bundet Boekfa, Jumras Limtrakul, **The confinement effect of the zeolite framework on the isomerization reaction of propene oxide over nanostructured H-FER zeolite catalyst using a newly developed "Embedded MP2:M06" method**.

2.4.8 Chularat Wattanakit, Somkiat Nokbin, Bundet Boekfa, Piboon Pantu, Jumras Limtrakul, **Structures and reaction mechanisms of skeletal isomerization of 1-Butene over ferrierite zeolite: An embeded nanocluster approach**.

2.4.9 Sudarat Yadnum, Saowapak Choomwattana, Pipat Khongpracha, Chompunuch Warakulwit, Jumras Limtrakul, **DFT analysis of the MOF catalyzed ring-opening reaction of epoxides: An important process in alkoxy alcohol synthesis.**

2.4.10 Chadchalerm Raksakoon, Saowapak Choomwattana, Jumras Limtrakul, **First-principle-derived potential energy function for Zn_4O tetrahedron-based metal-organic frameworks**.

2.4.11 Pemikar Srifa, Somkiat Nokbin, Bundet Boekfa, Jumras Limtrakul, **Density functional analysis of the confinement effect in nanoporous MCM-22 petrochemical catalyst: nanocluster model approach**.

2.4.12 Panida Singra, Pipat Khongpracha, Jumras Limtrakul, **Reaction mechanisms for ETBE production catalyzed by H-BEA as nanoporous zeolite**.

2.4.13 Supalak Khueanphet, Bundet Boekfa, Tanin Nanok, Jumras Limtrakul, **Adsorption of a basic probe molecule over nanoporous catalysts (H-FAU and H-MOR): An embedded nanocluster approach**.

2.4.14 Patanachai Janthon, Teeranan Nongnual, Piboon Pantu, Jumras Limtrakul, **Catalytic dehydrogenation of ethylbenzene to styrene over a tetrahedral platinum nanocluster: A DFT study**.

2.4.15 Saowapak Choomwattana, Jakkapan Sirijaraensre, Jumras Limtrakul, **DFT study on the effect of phosphate ionic core on basicity of $PW_{12}O_{40}^{3-}$ Polyoxometalate.**

2.5 งานวิจัยที่นำเสนอในการประชุมวิชาการนานาชาติ "241th American Chemical Society National meeting & Exposition" ณ เมือง Anaheim ประเทศสหรัฐอเมริกา ระหว่างวันที่ 27-31 มีนาคม 2554 จำนวน 12 เรื่อง

2.5.1 Bundet Boekfa, Kanokwan Kongpatpanich, Pailin Limtrakul, Jumras Limtrakul, **Skeletal isomerization of 1-butene to isobutene on H-ZSM-5 zeolite: A newly developed density functional theory study**.

2.5.2 Jitwadee Wiangngean, Kanokwan Kongpatpanich, Sippakorn Wannakao, Bundet Boekfa, Jumras Limtrakul, **Structures and reaction mechanisms of n-butyl alcohol conversion to isobutylene over theta-1 zeolite: A DFT study**.

2.5.3 Kulwadee Theanngern, Bundet Boekfa, Pipat Khongpracha, Jumras Limtrakul**, Quantum effect on the reaction mechanism of propene oxide isomerization in H-ITQ-22: A DFT investigation**.

2.5.4 Thittaya Yutthalekha, Kanokwan Kongpatpanich, Thana Maihom, Bundet Boekfa, Jumras Limtrakul, **Structures and reaction mechanisms of butadiene cycloaddition over metal-exchanged faujasite**.

2.5.5 Patanachai Janthon, Teeranan Nongnual, Piboon Pantu, Jumras Limtrakul, **Catalytic dehydrogenation of ethylbenzene to styrene over a tetrahedral platinum nanocluster: A DFT study.**

2.5.6 Panida Singra, Kanokwan Kongpatpanich, Pipat Khongpracha, Jumras Limtrakul, **Density functional theory study of possible mechanisms of isooctene formation via isobutene dimerization over acidic beta zeolite.**

2.5.7 Bundet Boekfa, Jumras Limtrakul, **The acid location of the Bronsted acid site in ITQ-22 zeolite: A newly developed density functional theory study**.

2.5.8 Bundet Boekfa, Jumras Limtrakul, **Strength and Bronsted acid sites of ITQ-34/pyridine complexes: A newly developed density functional theory study**.

2.5.9 Sippakorn Wannakao, Kanokwan Kongpatpanich, Pipat Khongpracha, Jumras Limtrakul, **Activities of Au and Au2 cation-exchanged zeolite for methane C-H bond activation: A DFT study**.

2.5.10 Phornphimon Maitarad, Pimpa Hormnirun, Pipat Khongpracha, Jumras Limtrakul, **Structure activity relationship and the electronic property of bis(phenoxyimine) ligated zirconium catalysts for ethylene polymerization: A combined CoMFA and DFT study**.

2.5.11 Thana Maihom, Jumras Limtrakul, **Formaldehyde encapsulated in lithium-decorated metal-organic frameworks: A DFT study**.

2.5.12 Supawadee Namuangruk, Pipat Khongpracha, Jumras Limtrakul, **Theoretical study of the oxidative dehydrogenation of ethylbenzene to styrene over Fe-ZSM-5**.

2.6 งานวิจัยที่นำเสนอในการประชุมวิชาการนานาชาติ "242th American Chemical Society National meeting & Exposition" ณ เมือง Denver ประเทศสหรัฐอเมริกา ระหว่างวันที่ 28 สิงหาคม -1 กันยายน 2554 จำนวน 10 เรื่อง

2.6.1 Bundet Boekfa, Piti Treesukol, Jumras Limtrakul, **Reaction mechanism of isomerization of 1-butene to isobutene over multipore H-ITQ-22 zeolite: a DFT study**.

2.6.2 Anawat Thivasasith, Pipat Khongpracha, Chompunuch Warakulwit, Jumras Limtrakul, **Decomposition of nitrous oxide on Au-embedded graphene**.

2.6.3 Saowapak Choomwattana, Thana Maihom, Jumras Limtrakul, **Density functional theory study on catalytic cracking of n-hexane on heteropoly acid comparison with FAU zeolite.**

2.6.4 Sarawoot Impeng, Amporn Sane, Chompunuch Warakulwit1, Panvika Pannopard, Boonruen Sunpetch, Pipat Khongpracha, Jumras Limtrakul, **Synthesis of precisely size-controlled gold nanoparticles and their infusion into mesoporous silica SBA-15 by compressed carbon dioxide solution technique.**

2.6.5 Sippakorn Wannakao, Thana Maihom, Pipat Khongpracha, Bundet Boekfa, Jumras Limtrakul, **Oxidation of carbon monoxide by nitrous oxide decomposition on Fe-embedded graphene.**

2.6.6 Sudarat Yadnum, Pipat Khongpracha, Chompunuch Warakulwit, Jumras Limtrakul, **Precisely size-controlled metal nanoparticles (Au, Pd and Pt) inserted into metal-organic frameworks (MOFs): synthesis and catalytic properties**.

2.6.7 Supakit Tiewcharoen, Bundet Boekfa, Piti Treesukol, Thana Maihom, Jumras Limtrakul, **Shape-selective hydrocarbon cracking of n-hexane on MCM-22 zeolite**.

2.6.8 Thana Maihom, Pipat Khongpracha, Jumras Limtrakul, **Activity of gold-supported MFI zeolites for nitrous oxide decomposition: a density functional study**.

2.6.9 Thittaya Yutthalekha, Bundet Boekfa, Jumras Limtrakul**, Structures and reaction mechanisms of butadiene cycloaddition over metal-exchanged faujasite**.

2.6.10 Winyoo Sangthong, Jumras Limtrakul, **Catalytic dehydrogenation of propane over Au(I) exchanged ZSM-5: density functional theory calculations**.

ภาคผนวก

บทความที่ตีพิมพ์
ในวารสารวิชาการต่างประเทศ
จำนวน 29 ผลงาน

บทความทางวิชาการที่เกี่ยวข้องกับ
ตัวเร่งปฏิกิริยาซีโอไลต์
จำนวน 13 ผลงาน

Effect of the acidic strength on the vapor phase Beckmann rearrangement of cyclohexanone oxime over the MFI zeolite: an embedded ONIOM study†

Jakkapan Sirijaraensre[ab] and Jumras Limtrakul*[ab]

Received 22nd May 2008, Accepted 7th October 2008
First published as an Advance Article on the web 5th November 2008
DOI: 10.1039/b808662a

The mechanism and energetic profile of the Beckmann rearrangement reaction of cyclohexanone oxime to ε-caprolactam catalyzed by the H-[Al]-MFI and H-[B]-MFI zeolites were investigated by both the bare cluster and the ONIOM models at the B3LYP/6-31G(d,p) and the B3LYP/6-31G(d,p) : MNDO levels of theory, respectively. In order to improve the energetic properties and take into account the whole zeolite framework effect, single point calculations are undertaken at the embedded ONIOM2 schemes; MP2/6-311G(d,p) : HF/6-31G(d) with an additional long-range electrostatic potential from the extended zeolite framework. The reaction mechanism of the Beckmann rearrangement over the acid site of zeolites consists of three steps: the 1,2 H shift, the rearrangement and the tautomerization. The activation energies for the Beckmann rearrangement of cyclohexanone oxime on the H-[Al]-MFI zeolite are calculated to be 31.46, 16.15 and 18.95 kcal mol^{-1}, for the first, second and third steps, respectively, whereas in the H-[B]-MFI zeolite, the energy barriers for each step of the reaction are 24.33, 7.46 and 20.43 kcal mol^{-1}, respectively. The rate-determining step of the reaction is the first step, which is the transformation from the N-ended cyclohexanone oxime adsorption complex and the O-ended one. These results signify the important role that the acid strength of zeolites plays in altering the energy profile of the reaction. The results further indicate that the weak Brønsted acid sites in the [B]-MFI zeolite could better catalyze the Beckmann rearrangement of cyclohexanone oxime than the strong acid sites in the [Al]-MFI zeolite, as compared with the quantitatively low activation energy of most steps. However, the turnover reaction of the H-[B]-MFI zeolite might be delayed by the quantitatively high desorption energy of the product as compared to the adsorption energy of the reactant.

Introduction

The Beckmann rearrangement[1–6] is one of the most important industrial reactions for producing the ε-caprolactam, an important intermediate for the production of the Nylon-6 polymer. In the conventional method, this process uses acid solution, ammonia and cyclohexane as the principal raw materials. However, it is both environmentally unfavorable; due mainly to the use of corrosive sulfuric acid, instrument corrosion occurs and wastes the resources; and ammonium sulfate, a by-product formed during the neutralization process, is produced at approximately 1–5 times that of ε-caprolactam. Hence, a range of heterogeneous catalysts are used in this reaction with the objective of overcoming these problems. Zeolites have been widely investigated on this reaction, for example MFI,[7–16] FAU,[15–20] Beta,[20–25] and MOR[15,16,20] zeolites. From previous studies, it is of interest to note that porous catalysts like zeolites show both high activity and provide a highly selective product. As a result of these investigations, Sumitomo Chemical Co., Ltd., have industrialized the production of ε-caprolactam, using high-silica MFI zeolite as the catalyst for the vapor phase Beckmann rearrangement. This process does not produce any ammonium sulfate, a by-product through the Beckmann rearrangement without a catalyst.

The Beckmann rearrangement catalyzed by solid catalysts (usually called the vapor-phase Beckmann rearrangement) has been the subject of many researchers who have developed suitable experimental and computational techniques for finding an efficient catalyst which can enhance the process of manufacturing the desired product. In earlier studies,[18,19,23,26,31] strong Brønsted acid sites in zeolites were suggested as playing a crucial role in catalyzing this reaction by protonating the oxime molecule, whereas external silanols appear to be nonreactive, while in some previous works,[8,11,12,21,32,33] they have reported that the weak acidic groups in zeolites such as high-silica MFI, [B]-MFI and [B]-Beta are also active catalysts for the rearrangement reaction with high activity and selectivity toward ε-caprolactam.

[a] *Laboratory for Computational and Applied Chemistry, Chemistry Department, Faculty of Science, Kasetsart University, 10900 Bangkok, Thailand. E-mail: fscijrl@ku.ac.th*
[b] *Center of Nanotechnology, Kasetsart University Research and Development Institute, Kasetsart University, 10900 Bangkok, Thailand. E-mail: fscijrl@ku.ac.th*

† Electronic supplementary information (ESI) available: Additional experimental details. See DOI: 10.1039/b808662a

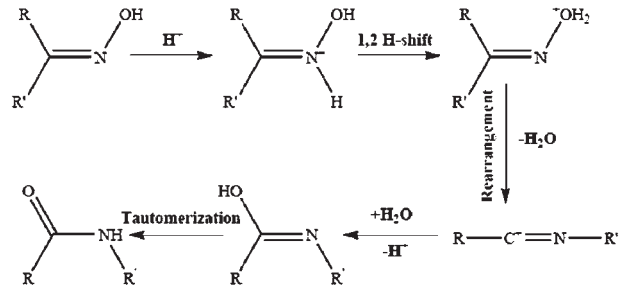

Scheme 1 The reaction mechanism for the Beckmann rearrangement.

Therefore, the role of the acid site strength in the Beckmann rearrangement is a matter of debate.

The reaction mechanism over the Brønsted acid site of zeolite catalysts is intensively investigated both experimentally[22,23,34–36] and theoretically.[26–28,36,37] The reaction mechanism, commonly suggested for the Beckmann rearrangement, is described in Scheme 1 as follows:

The reaction initially involves the protonation of the oxime molecule at the nitrogen atom of the oxime molecule (designated by N-Bound). Then, in the first TS step, named the 1,2 H-shift step, the hydrogen is transferred from the nitrogen-end to the oxygen atom of the oxime molecule (designated as O-Bound) and followed by migration of an R group (R = alkyl, aryl or hydrogen), which is *anti* to both the hydroxyl group and to the nitrogen atom, and a water molecule is displaced. This second step is called the rearrangement step. Subsequently, the displaced water molecule binds to the carbon atom, simultaneously transferring a proton to the acid catalyst. The last transforming step is the tautomerization from the enol–amide complex to the amide complex and desorption of the amide molecule in the final step. Recently, theoretical investigations reveal that the transfer of proton from the nitrogen-end to the oxygen-end of oxime molecules is the rate-determining step of the reaction when it occurs over zeolite catalysts. Nevertheless, the theoretical investigation of the Beckmann rearrangement on zeolite systems is not yet well-founded.

The aim of this work is to investigate the effect of the Brønsted acid site strength in isomorphously substituted MFI zeolites: H-[Al]-MFI and H-[B]-MFI zeolites, on the reaction mechanism and the energetic profile of the Beckmann rearrangement of cyclohexanone oxime. To the best of our knowledge, no theoretical study has investigated the Beckmann rearrangement mechanism of cyclohexanone oxime catalyzed by as large a unit cell zeolite as MFI zeolite. This finding can provide more insight into the role of the acidic strength of zeolite on the Beckmann rearrangement reaction. The interaction of the MFI zeolite and the oxime molecule has been investigated by using the bare cluster and embedded ONIOM approaches.

Computational details

To determine the adsorbed structure of cyclohexanone oxime molecules in H-[Al]-MFI and H-[B]-MFI zeolites, the ONIOM models were used. The T12 site, which has been widely used to model the active site of MFI in many theoretical studies, is substituted with two different types of trivalent atoms; Al^{3+} and B^{3+}. Either B substitution or Al substitution introduces a net negative charge in the zeolite framework which is compensated by a proton acting as a Brønsted acid site to preserve neutrality. Due mainly to the large unit cell of the MFI zeolite, the use of periodic calculation is computationally too expensive and even impractical. Recently, hybrid methods such as the embedded cluster,[26,27,38–46] QM-Pot[47–49] as well as the ONIOM methods[50–59] have been used for including the framework effects of zeolite with the benefit of the computational cost becoming economically feasible. In the ONIOM2 scheme, the MFI zeolite is represented by the 128T model which covers the nanometer-sized cavity that is the intersection of the main and sinusoidal channels and the location of the active site of MFI zeolite. The 128T ONIOM model (see Fig. 1) is divided into two layers: only the small active region (12T) located at the intersection of the main and sinusoidal channel is accessible to the adsorbates (see Fig. 1a–b), the active site of the H-MFI zeolite was treated accurately with the density functional theory (B3LYP) with the 6-31G(d,p) basis set, while the contribution of influences from the rest of the model was approximated by a less expensive method (MNDO). This combination was previously used to investigate the adsorption of NH_3 and H_2O in H-CHA zeolite.[59] These results showed that the adsorbed structures obtained from the ONIOM2(B3LYP : MNDO) scheme are in agreement with those obtained from periodic calculations. In order to obtain more accurate adsorption energies, single point calculations were carried out at the ONIOM2(MP2/6-311G(d,p) : HF/6-31G(d)) level of theory. Attempts have been made to demonstrate that the geometry constraints imposed in this work do not influence the results. Some test calculations on cyclohexanone oxime over the H-[Al]-MFI and H-[B]-MFI zeolite have been performed using two different sizes of QM region: 12T and 30T atoms with a different degree of relaxation in QM regions (see ESI, Fig. S1 and Table S1).† It was found that no significant structural differences were obtained when using 5T, 8T and 24T clusters during optimization. Furthermore, the combination of B3LYP and UFF, which has shown good results in predicting the structural parameters and reaction energies in previous works, is preformed to compare the results with the MNDO environment. The B3LYP : UFF combination[60–65] has been found to provide a good description of the short range van der Waals

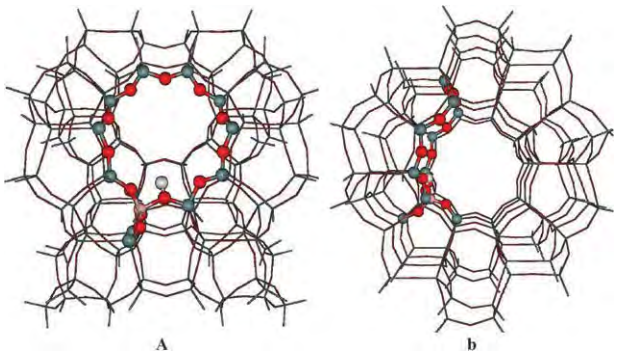

Fig. 1 Presentation of the 128T ONIOM2 model of H-MFI zeolite. The atoms belonging to the high-level region are presented as bonds and sticks, while the rest of the atoms belong to the low-level region.

interactions. The ONIOM calculation using B3LYP : MNDO with the 12T : 128T cluster leads to geometry similar to that obtained from the B3LYP : UFF calculations. The adsorption energy computed from MP2/6-311G(d,p) : HF/6-31G(d) single point calculations at the B3LYP/6-31G(d,p) : MNDO optimized structures, is also in agreement with the B3LYP : UFF value. Consequently, the use of the MP2/6-311G(d,p) : HF/6-31G(d)//B3LYP/6-31G(d,p) : MNDO approach seems to be a good strategy to model this system (see ESI, Table S2).† All optimizations have been preformed on the 12T/5T cluster embedded in the 116T cluster treated by the MNDO method. However, the 128T ONIOM model neglects the long-range effects from the remaining infinite lattice of zeolite (excluding the 128T ONIOM model). Hence, in order to fulfil the entire behavior of the adsorption properties of the probe molecule in the zeolite pore, the ONIOM model is embedded in the zeolitic Madelung potential field which is represented by two sets of point charges generated by the SCREEP method.[26,27,40–46] The detailed description of the SCREEP method which reproduces the correct Madelung potential calculated from the Ewald-sum method was previously reported elsewhere.[38,40] This new model can take into consideration the long-range effects extended from the general ONIOM model. The combination of the SCREEP and ONIOM approach is called the embedded-ONIOM approach (e-ONIOM) which is a sufficiently accurate and practical model for studying reaction mechanisms on zeolite systems.[64,66,67] Verification that the optimized transition state connects the intended reactant and product, was made by normal mode analysis. All calculations were carried out using the Gaussian 03 program.[68]

Results and discussion

The local structure of the isomorphously substituted MFI structure

Selected parameters of the active sites of both zeolites are listed in Table 1 and illustrated in Fig. 2a–b. It is obvious that the type of trivalent atom substituted into the zeolite framework has a significant effect on the structure of the zeolite framework and the length of the O–H bond of the Brønsted acid site. For the acid site structure, the O–H bond distance of the H-[B]-MFI zeolite is slightly shorter than that of the H-[Al]-MFI zeolite by 0.003 Å. The negligible difference of the O1–H1 bond distance has an effect on the charge-population changes for the H1 atom (0.5419 *vs.* 0.5755), suggesting that the acid site of the H-[Al]-MFI zeolite is more acidic than that of the H-[B]-MFI zeolite. Some significant differences are found in the bond distances and bond angles of the zeolite framework. The distances between the silicon atom and the bridging oxygen atom (Si–O bond distance) of the H-[B]-MFI zeolite are slightly longer than those of the H-[Al]-MFI zeolite and the angles between the substituted site and neighboring silicon atoms (M^{3+}–O–Si) in the H-[B]-MFI zeolite are larger than those in the [Al]-MFI by around 10–13°. The distances between the substituted site and the bridging oxygen atoms (M^{3+}–O) in the H-[B]-MFI are significantly shorter than those in the [Al]-MFI zeolite by 0.02 and 0.26 Å for the M^{3+}–O1 and M^{3+}–O2 bond distances, respectively. Because of the small size of the B^{3+} cation, the length of the B–O1 bond distance no bonding occurs between the B and the bridging hydroxyl group, and the structure is in the form of a trigonal BO_3 and a terminal silanol group is formed in the H-[B]-MFI zeolite. These observations are consistent with previous experimental and theoretical studies.[69–74]

Table 1 Optimized geometries and proton affinity (PA) of H-[B]-MFI and H-[Al]-MFI at the ONIOM2(B3LYP : 6-31G(d,p) : MNDO) scheme

Parameters	H-[B]-MFI	H-[Al]-MFI
O1–H1	0.970	0.973
Si1–O1	1.656	1.653
M^{3+}–O1	1.782	1.802
Si–O2	1.607	1.582
M^{3+}–O2	1.402	1.663
M–H	2.195	2.301
∠Si1–O1–M	137.6	127.8
∠Si2–O2–M	149.2	133.8
q(H1)[a]	0.5419	0.5755

[a] The atomic charges from the Mulliken population analysis were carried out by single point calculations with the full quantum calculation, HF/6-31G(d) level of theory.

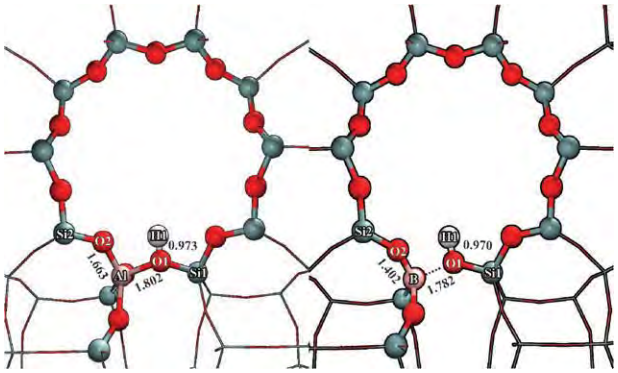

Fig. 2 Optimized geometric parameters of the 128T ONIOM model of zeolites at the B3LYP/6-31G(d,p) : MNDO scheme: (a) H-[Al]-MFI zeolite and (b) H-[B]-MFI zeolite.

The Beckmann rearrangement on an isomorphously substituted MFI structure

The 1,2 H-shift step. The geometrical parameters of the N-bound complex, the H-shift transition state and the O-bound complexes calculated by the ONIOM2 scheme are illustrated in Fig. 3a–c for the H-[Al]-MFI zeolite and Fig. 3d–f for the H-[B]-MFI zeolite. At the initial step, the cyclohexanone oxime molecule interacts with the acidic site of the zeolite *via* its nitrogen atom. The reaction subsequently proceeds in three consecutive steps. The first step is called 1,2 H-shift step. The initial adsorption complex; N-bound complex on both zeolites: H-[Al]-MFI and H-[B]-MFI zeolites, is in the form of a protonated complex, which is consistent with previous experimental studies[23,34] that observed the protonated form of cyclohexanone oxime over the Brønsted acid site. In both zeolitic systems, the O1–H1 bond in the N–bond complex is lengthened to 1.775 and 1.764 Å to form the N–H1 single bond. The N–H1 bond distance is predicted to be 1.035 and 1.043 Å for the H-[Al]-MFI and the H-[B]-MFI systems,

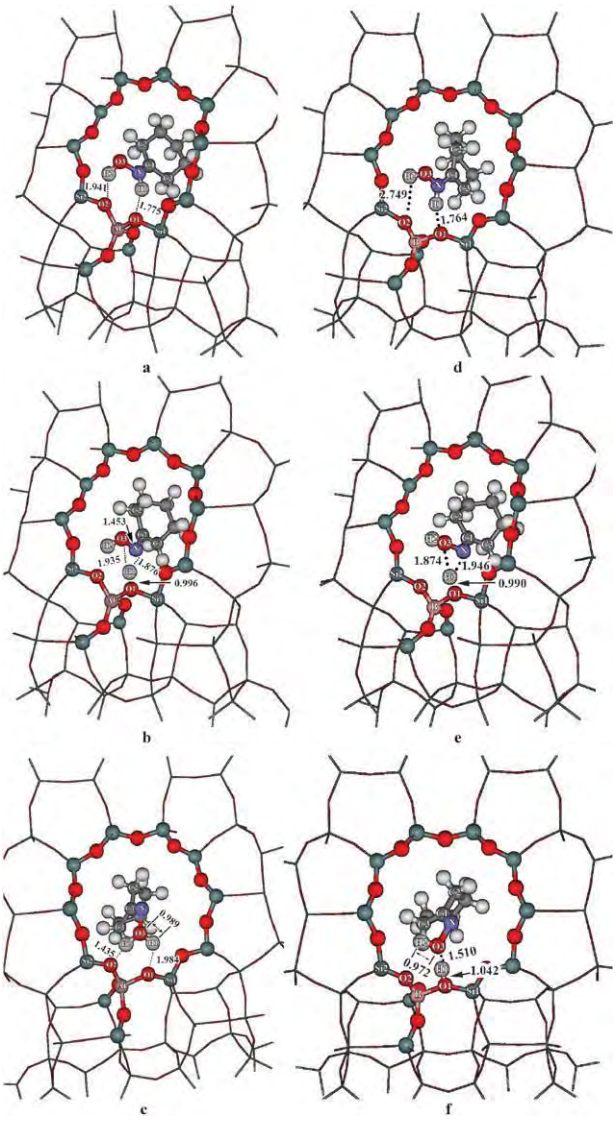

Fig. 3 Optimized geometrical parameters of the stationary points corresponding to 1,2 H-shift step of cyclohexanone oxime: (a) N-bound complex, (b) 1,2 H-shift transition state complex and (c) O-bound complex, respectively. They are catalyzed by the H-[Al]-MFI zeolite. Sections (d)–(f) present the corresponding complexes on the H-[B]-MFI zeolite.

respectively. This complex consists of the two strong hydrogen bond interactions between O5–H2–O2 and N–H1–O1 and corresponds to the previous theoretical studies on the MFI[26] and FAU[27] zeolites. The adsorption energy of this complex is calculated to be −50.67 and −39.91 kcal mol^{-1} for the H-[Al]-MFI and H-[B]-MFI systems, respectively. The difference of the adsorption energy of this complex is due mainly to the acidic strength of the Brønsted acid sites of both zeolites. Due to the H-[Al]-MFI zeolite being more acidic than the H-[B]-MFI zeolite, the adsorption energy of cyclohexanone oxime on the H-[Al]-MFI zeolite is more exothermic. The transition state (*cf*. Fig. 3b and e) of the first step is the transfer of the active proton (H1) from the nitrogen-ended site to the oxygen-ended site of the cyclohexanone oxime. The structural changing from the N-bound complex to the other one in this transition state can be observed from the N–H1, O3–H1 and N–O3 bond distances. At the TS, the N–O3 bond distance is elongated by about 0.08 and 0.06 Å for the H-[Al]-MFI and H-[B]-MFI systems, respectively. For the active H1 atom, the bond distance between it and the nitrogen atom is broken and located in the midway point between the N and O atoms, with the N–H1 and O3–H1 active distances being 1.876 and 1.935 Å for the H-[Al]-MFI system, and 1.946 and 1.874 Å for the H-[B]-MFI system. These distances correspond to a previous observation in the zeolitic systems: MOR[28] (1.90 Å), MFI[26] (1.95 Å) and FAU[27] (1.85 Å). With assistance from the zeolite framework in shuttling the proton, the barrier height of this step is 31.5 and 24.3 kcal mol^{-1} for the H-[Al]-MFI and H-[B]-MFI zeolites, respectively. They are quantitatively similar to the activation energies of the oximes in the zeolite systems in previous studies[26–28] by 21–31 kcal mol^{-1}. The reduction of the activation energy for this step in the H-[B]-MFI zeolite, as compared to that in the H-[Al]-MFI zeolite, is due mainly to the decrease of the acidity of Brønsted site of the zeolite that leads to a significantly weak interaction in the initial-state adsorption of reaction, N-bound complex. This observation is consistent with previous works,[26,27] concluding that the barrier height of this step corresponds to the strength of the adsorption in the N-bound complex. Subsequently, after the 1,2 H-shift process, the O-bound complex, which is an interaction between the oxygen atom of cyclohexanone oxime and the Brønsted acid site of zeolite, is formed with the adsorption energy of −31.51 and −18.91 kcal mol^{-1}. Contrary to the N-bound complex, it can be seen clearly from Fig. 3c and f that only the H-[Al]-MFI zeolite promotes the protonation of the O-bound complex, whereas the corresponding complex on the H-[B]-MFI system is in a molecularly adsorbed state. In the [Al]-MFI system, the protonated-oxygen cyclohexanone oxime interacts with the bridging oxygens of zeolite *via* two strong hydrogen bonds: O1···H1–O3 and O2···H2–O3 (1.984 and 1.435 Å), while for the [B]-MFI system, the physisorbed oxime molecule is stabilized by one strong O3···H1–O1 hydrogen bond (1.510 Å) and one weaker O2···H2–O3 hydrogen bond (2.414 Å). The difference between the geometrical O-bound complex and the calculated heat of adsorption values corresponds to the acidic strength of the Brønsted acid site of the zeolites.

The rearrangement step. The key parameters of the rearrangement transition state and the corresponding intermediate product are illustrated in Fig. 4a–b for the H-[Al]-MFI zeolite and Fig. 4c–d for the H-[B]-MFI, respectively. In the transition state of the [Al]-MFI zeolite, the C1–C2 bond is broken and the C2 is shifted toward the N atom and located above the C1–N bond, causing a shortening of the N–C1 bond distance from 1.280 to 1.187 Å. The bond distances of the C1–C2 and N–C2 bonds are predicted to be 1.864 and 1.995 Å, respectively. Concurrently with the breaking of the C1–C2 bond, the N–O3 bond is broken and a water molecule is separated from the rest of the molecules. The intermolecular N–O bond distance is significantly elongated to 2.545 Å. The O3–H1 and O3–H2 bond distances are shortened to 0.966 and 0.976, respectively, and the bond angle of H1–O2–H2 is slightly spread from 103.0 to 103.7°, while in the rearrangement TS step over the H-[B]-MFI zeolite, the

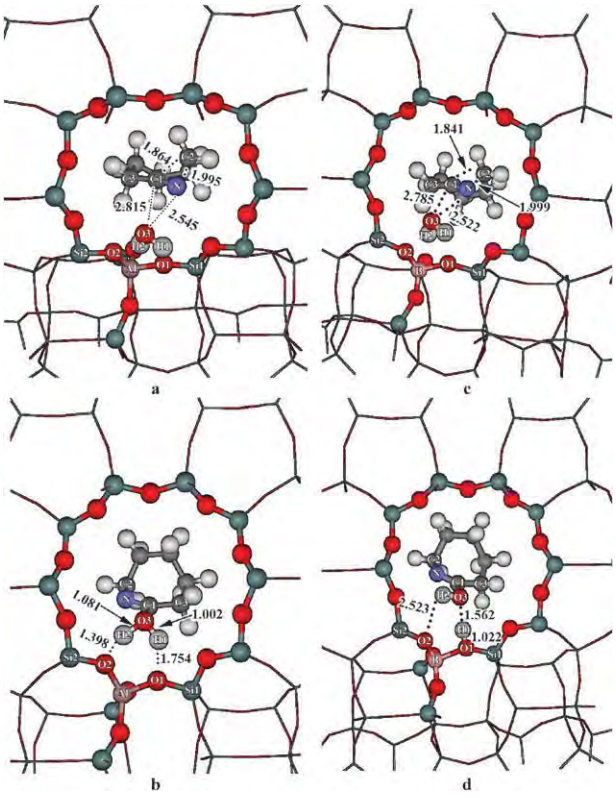

Fig. 4 Optimized geometrical parameters of the stationary points corresponding to the rearrangement step of cyclohexanone oxime: (a) the rearrangement transition state complex and (b) the enol–amide adsorption complex, respectively. Those are catalyzed by the H-[Al]-MFI zeolite. Sections (c) and (d) present the corresponding complexes on the H-[B]-MFI zeolite.

elimination of the C1–C2 bond and the transfer of the C2 to the N atom take place with low activation energy. The C2 atom is located in between the C1 atom and N atom with bond distances of 1.841 and 1.999 Å for the C1–C2 and N–C2 bond lengths, respectively. Furthermore, comparing the rearrangement transition state between both zeolitic systems, we found that the protonation occurred during the rearrangement in the H-[B]-MFI zeolite. The activation energy for this step is calculated to be 16.15 and 7.46 kcal mol^{-1} for the H-[Al]-MFI and the H-[B]-MFI zeolites, respectively. The reduction of the energy barrier for this step is due mainly to the adsorption strength of the O-bound complex. In the H-[B]-MFI zeolite, this complex is in the neutral form complex, whereas in the other zeolite, it is in the protonated complex. Therefore, the effects from the zeolite framework have a much larger degree of stabilization of the O-bound complex in the H-[Al]-MFI zeolite than that in the H-[B]-MFI zeolite. Our results compare well to the periodic calculation[28] that predicted the activation energies to be 21.05 and 15.31 kcal mol^{-1} for the 1,2 H-shift and rearrangement steps on the Brønsted acid site of MOR zeolite. After the rearrangement process, the enol–amide complex is formed. The distances of the forming bonds, N–C2 and C1–O3, are 1.465 and 1.469 Å, respectively, resulting in slight shortening of the N–C1 bond. The adsorbed complex is in a protonated form, forming two slightly stronger hydrogen bonds to the bridging oxygen atoms of zeolite with the $–OH_2$ group. The intermolecular O1–H1 and O2–H2 bond distances are 1.754 and 1.398 Å, respectively. In the H-[B]-MFI zeolite, the enol–amide complex is in the neutral complex consisting of only a strong hydrogen bond between the O3 atom and the Brønsted acid site of [B]-MFI zeolite. The distances of the newly formed N–C2, C1–O3 and O3–H1 bonds are 1.460, 1.402 and 1.562 Å, respectively. The adsorption energies are predicted to be −59.86 and −52.19 kcal mol^{-1} for H-[Al]-MFI and H-[B]-MFI zeolites, respectively. The difference in the adsorption energies of these complexes is in agreement with their structural adsorption complexes, as shown in Fig. 4b and d.

Tautomerization step. The optimized structures of this state are illustrated in Fig. 5a–b for H-[Al]-MFI zeolite and Fig. 5c–d for H-[B]-MFI, respectively. The transition state of this step (*cf*. Fig. 5a and c) is the migration of the H atom from the –OH group to the N atom to form the ε-caprolactam. In the H-[Al]-MFI system, the migrating proton (H2) is close to the midway point between the O3 and N atoms (the distances of O3–H2 and N–H2 bonds are 1.218 and 1.414 Å) where it is nearly in the same plane with the O3 and N atoms of the enol–amide complex (the N–C1–O3–H2 dihedral angle is 3.0°; see Fig. 5a and c). These take place simultaneously with shortening of the C–O bond (by about 0.05 Å) and the slight elongation of the N–C1 bond (by about 0.02 Å) for transferring to the amide compound, the keto–amide complex. Whilst in the H-[B]-MFI zeolite, the migration proton is located in a

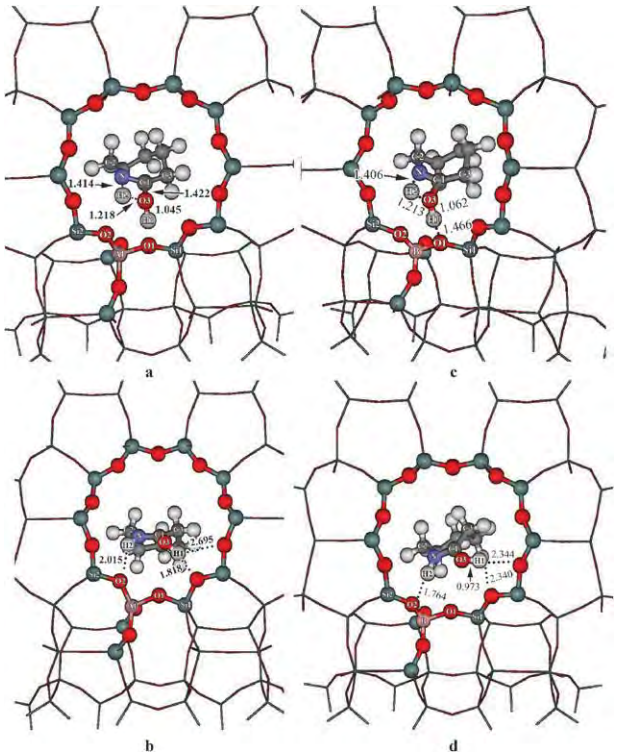

Fig. 5 Optimized geometric parameters of the complexes corresponding to the tautomerization step of cyclohexanone oxime: (a) the tautomerization transition state complex and (b) the keto–amide adsorption complex, respectively. Those are catalyzed by the H-[Al]-MFI zeolite. Sections (c) and (d) present the corresponding complexes on the H-[B]-MFI zeolite.

similar geometry as that found in the H-[Al]-MFI zeolite. The N–H2 and O3–H2 bond distances are 1.406 and 1.213 Å, respectively. These are quantitatively similar to the corresponding bonds in the H-[Al]-MFI zeolite. Concurrently with the migration of the H2 atom, the proton of the Brønsted acid site is transferred to protonate the O2 atom of the enol–amide complex during the transition state. The activation energy for this step, using the embedded-ONIOM2 model, is evaluated to be 18.95 and 20.43 kcal mol^{-1} for the H-[Al]-MFI and H-[B]-MFI zeolites, respectively. The barrier for this step in the H-[Al]-MFI zeolite is slightly lower than that in the H-[B]-MFI zeolite because of the enhancement of the acidity of the H2 atom caused by the protonation at the oxygen atom of the enol–amide product. After the tautomerization process, the keto–amide product or ε-caprolactam is formed (*cf*. Fig. 5b and d). The interaction between the keto–amide complex and the Brønsted acid site of both zeolites is in the form of a protonated complex which agrees well with the experiment observation[34,37] that the O-protonated ε-caprolactam is formed over the Brønsted acid sites of zeolite. The desorption energy of the ε-caprolactam molecule is calculated to be −44.96 and −39.11 kcal mol^{-1} for the H-[Al]-MFI and H-[B]-MFI zeolites, respectively. The high value of the desorption energy indicates that the desorbing process of the reaction product from the zeolites possibly obstructs the adsorption of the oxime molecule in the first step of the reaction. These results agree well with previous experimental studies,[14,15] concluding that the reaction on the strong Brønsted acid of MFI is very active in the rearrangement of the cyclohexanone oxime to the ε-caprolactam, but a problem will be encountered due to a difficulty in the desorption step, which also leads to the catalyst deactivation because of coke deposition in the zeolite pores. Because the produced ε-caprolactam remains on the acid sites, it is converted to an oligomer, which could be a precursor of coke.

A comparison of the results of the embedded ONIOM model and the bare cluster model (see ESI),† reveals that the effects from the zeolite framework play an important role in lowering the activation energies in each step of the reaction, excepting the 1,2 H-shift step. It is because of the zeolite framework effect having a much larger degree of stabilization of the adsorption complex, N-bound complex, than at the TS complex. Consequently, this step is the rate-determining step of the reaction in both zeolites which have activation energies of 31.46 and 24.33 kcal mol^{-1} for the H-[Al]-MFI and H-[B]-MFI zeolites, respectively (*cf*. Fig.6). The largest effect is at the rearrangement step, which is the connection between the O-bound complex and the enol–amide complex. The zeolite framework effects lower the energy barrier by about 10 and 25 kcal mol^{-1} for the H-[Al]-MFI and H-[B]-MFI zeolites, respectively.

Conclusions

In this work, we have examined both the role of acid strength and the zeolite framework effects on the Beckmann rearrangement of cyclohexanone oxime catalyzed by the isomorphously substituted MFI zeolites: the H-[Al]-MFI and the H-[B]-MFI zeolites. All of these systems have been investigated by both the bare cluster and the ONIOM2 scheme. By use of the ONIOM2 scheme in combination with the electrostatic potential

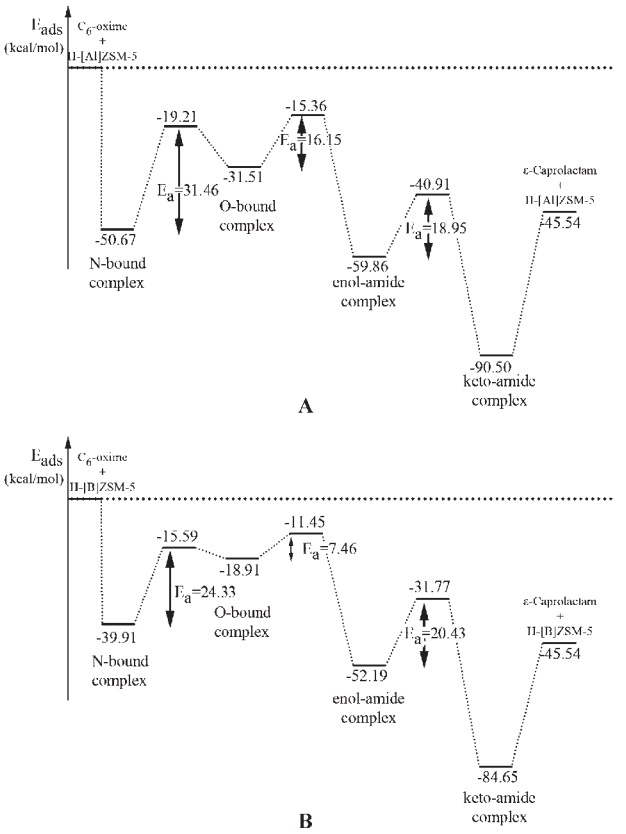

Fig. 6 The energetic profile along the pathway of the Beckmann rearrangement of the cyclohexanone oxime molecule on zeolites at the embedded ONIOM2 scheme (MP2/6-311G(d,p):HF/6-31G(d)//B3LYP/6-31G(d,p):MNDO) level of theory: (a) H-[Al]-MFI zeolite, (b) H-[B]-MFI zeolite. The energetic changes for complexes are in kcal mol^{-1}.

obtained from the SCREEP method, it demonstrates that the electrostatic potential from the extended zeolite framework plays a dominant function in the reduction of the energy barrier. The reaction is initiated by the strong interaction of the N-ended cyclohexanone oxime on the acid sites of the zeolite. The N-ended adsorption complex is transformed to the O-ended adsorption complex *via* the 1,2 H-shift step. Subsequently, the ε-caprolactam is yielded rapidly *via* the rearrangement step and the tautomerization step, respectively. From the embedded ONIOM2 scheme, the rate determining step of the reaction is the 1,2 H-shift step which has an energy barrier of 31.46 and 24.33 kcal mol^{-1} for the H-[Al]-MFI and the H-[B]-MFI zeolites, respectively (*cf*. Fig.6). Furthermore, we found that the protonation of the reaction product ε-caprolactam occurs in both zeolites H-[Al]-MFI and H-[B]-MFI. This leads to a strong adsorption on the catalyst surface. It should be noted that the catalyst deactivation might take place due to the irreversibly adsorbed ε-caprolactam molecule. One may expect that the addition of diluting solvents may play a crucial role in the desorption of the products from the zeolite micorpores, and, consequently, decrease the deactivation of the catalyst.

Acknowledgements

This work was supported in part by grants from the Thailand Research Fund (to J.S. and J.L.) and the Science Research

Fund (ScRF) from the Faculty of Science, Kasetsart University (to J.S.) as well as the Commission of Higher Education, Ministry of Education under Postgraduate Education and Research Programs in Petroleum and Petrochemicals, and Advanced Materials. Support from the National Nanotechnology Center (NANOTEC Center of excellence and CNC) under the National Science and Technology Development Agency is also acknowledged.

References

1 E. Beckmann, *Chem. Ber*., 1886, **19**, 988–993.
2 A. H. Blatt, *Chem. Rev*., 1933, **12**, 215–260.
3 B. Jones, *Chem. Rev*., 1944, **35**, 335–350.
4 H. E. Ungnade and D. A. McLaren, *J. Org. Chem*., 1945, **10**, 29–33.
5 D. E. Pearson and J. D. Bruton, *J. Org. Chem*., 1954, **19**, 957–963.
6 W. Z. Heldt, *J. Org. Chem*., 1961, **26**, 1695–1702.
7 H. Ichihashi and H. Sato, *Appl. Catal., A*, 2001, **221**, 359–366.
8 Y. Izumi, H. Ichihashi, Y. Shimazu, M. Kitamura and H. Sato, *Bull. Chem. Soc. Jpn*., 2007, **80**, 1280–1287.
9 H. Ichihashi, M. Ishida, A. Shiga, M. Kitamura, T. Suzuki, K. Suenobu and K. Sugita, *Catal. Surveys Asia*, 2003, **7**, 261–270.
10 C. Flego and L. Dalloro, *Microporous Mesoporous Mater*., 2003, **60**, 263–271.
11 G. P. Heitmann, G. Dahlhoff and W. F. Holderich, *J. Catal*., 1999, **186**, 12–19.
12 G. P. Heitmann, G. Dahlhoff, J. P. M. Niederer and W. F. Holderich, *J. Catal*., 2000, **194**, 122–129.
13 H. Ichihashi and M. Kitamura, *Catal. Today*, 2002, **73**, 23–28.
14 T. Takahashi, T. Kai and E. Nakao, *Appl. Catal., A*, 2004, **262**, 137–142.
15 P. O'Sullivan, L. Forni and B. K. Hodnett, *Ind. Eng. Chem. Res*., 2001, **40**, 1471–1475.
16 T. Takahashi, M. N. A. Nasution and T. Kai, *Appl. Catal., A*, 2001, **210**, 339–344.
17 L. Dai, K. Koyama, M. Miyamoto and T. Tatsumi, *Appl. Catal., A*, 1999, **189**, 237–242.
18 C. Ngamcharussrivichai, P. Wu and T. Tatsumi, *Chem. Lett*., 2004, **33**, 1288–1289.
19 C. Ngamcharussrivichai, P. Wu and T. Tatsumi, *Appl. Catal., A*, 2005, **288**, 158–168.
20 L.-X. Dai, Y. Iwaki, K. Koyama and T. Tatsumi, *Appl. Surf. Sci*., 1997, **121/122**, 335–338.
21 G. P. Heitmann, G. Dahlhoff and W. F. Holderich, *Appl. Catal., A*, 1999, **185**, 99–108.
22 Y.-M. Chung and H.-K. Rhee, *J. Mol. Catal. A: Chem*., 2000, **159**, 389–396.
23 Y. M. Chung and H. K. Rhee, *J. Mol. Catal. A: Chem*., 2001, **175**, 249–257.
24 Y. Zhang, Y. Wang and Y. Bu, *Microporous Mesoporous Mater*., 2008, **107**, 247–251.
25 P. Botella, A. Corma, S. Iborra, R. Monton, I. Rodriguez and V. Costa, *J. Catal*., 2007, **250**, 161–170.
26 J. Sirijaraensre, T. N. Truong and J. Limtrakul, *J. Phys. Chem. B*, 2005, **109**, 12099–12106.
27 J. Sirijaraensre and J. Limtrakul, *ChemPhysChem*, 2006, **7**, 2424–2432.
28 T. Bucko, J. Hafner and L. Benco, *J. Phys. Chem. A*, 2004, **108**, 11388–11397.
29 C. Ngamcharussrivichai, P. Wu and T. Tatsumi, *J. Catal*., 2005, **235**, 139–149.
30 A. Fernandez, A. Marinas, T. Blasco, V. Fornes and A. Corma, *J. Catal*., 2006, **243**, 270–277.
31 M. A. Camblor, A. Corma, H. Garcia, V. Semmer-Herledan and S. Valencia, *J. Catal*., 1998, **177**, 267–272.
32 B. Bonelli, L. Forni, A. Aloise, J. B. Nagy, G. Fornasari, E. Garrone, A. Gedeon, G. Giordano and F. Trifiro, *Microporous Mesoporous Mater*., 2007, **101**, 153–160.
33 L. Forni, E. Patriarchi, G. Fornasari, F. Trifiro, A. Katovic, G. Giordano and B. Nagy, *Stud. Surf. Sci. Catal*., 2005, **155**, 281–290.
34 V. R. R. Marthala, Y. Jiang, J. Huang, W. Wang, R. Glaeser and M. Hunger, *J. Am. Chem. Soc*., 2006, **128**, 14812–14813.
35 G. A. Fois, G. Ricchiardi, S. Bordiga, C. Busco, L. Dalloro, G. Spano and A. Zecchina, *Stud. Surf. Sci. Catal*., 2001, **135**, 2477–2484.
36 A. B. Fernandez, M. Boronat, T. Blasco and A. Corma, *Angew. Chem., Int. Ed*., 2005, **44**, 2370–2373.
37 A. B. Fernandez, I. Lezcano-Gonzalez, M. Boronat, T. Blasco and A. Corma, *J. Catal*., 2007, **249**, 116–119.
38 J. M. Vollmer, E. V. Stefanovich and T. N. Truong, *J. Phys. Chem. B*, 1999, **103**, 9415–9422.
39 I. H. Hillier, *THEOCHEM*, 1999, **463**, 45–52.
40 E. V. Stefanovich and T. N. Truong, *J. Phys. Chem. B*, 1998, **102**, 3018–3022.
41 J. Limtrakul, S. Jungsuttiwong and P. Khongpracha, *J. Mol. Struct*., 2000, **525**, 153–162.
42 J. Limtrakul, P. Khongpracha, S. Jungsuttiwong and T. N. Truong, *J. Mol. Catal. A: Chem*., 2000, **153**, 155–163.
43 J. Limtrakul, T. Nanok, S. Jungsuttiwong, P. Khongpracha and T. N. Truong, *Chem. Phys. Lett*., 2001, **349**, 161–166.
44 J. Limtrakul, S. Nokbin, P. Chuichay, P. Khongpracha, S. Jungsuttiwong and T. N. Truong, *Stud. Surf. Sci. Catal*., 2001, **135**, 2469–2476.
45 P. Treesukol, K. Srisuk, J. Limtrakul and T. N. Truong, *J. Phys. Chem. B*, 2005, **109**, 11940–11945.
46 S. Jungsuttiwong, J. Limtrakul and T. N. Truong, *J. Phys. Chem. B*, 2005, **109**, 13342–13351.
47 M. Sierka and J. Sauer, *J. Phys. Chem. B*, 2001, **105**, 1603–1613.
48 M. E. Franke, M. Sierka, U. Simon and J. Sauer, *Phys. Chem. Chem. Phys*., 2002, **4**, 5207–5216.
49 O. Bludsky, M. Silhan, P. Nachtigall, T. Bucko, L. Benco and J. Hafner, *J. Phys. Chem. B*, 2005, **109**, 9631–9638.
50 K. Bobuatong and J. Limtrakul, *Appl.Catal., A*, 2003, **253**, 49–64.
51 S. Kasuriya, S. Namuangruk, P. Treesukol, M. Tirtowidjojo and J. Limtrakul, *J. Catal*., 2003, **219**, 320–328.
52 S. Namuangruk, P. Pantu and J. Limtrakul, *J. Catal*., 2004, **225**, 523–530.
53 S. Pabchanda, P. Pantu and J. Limtrakul, *J. Mol. Catal. A: Chem*., 2005, **239**, 103–110.
54 W. Panjan and J. Limtrakul, *J. Mol. Struct*., 2003, **654**, 35–45.
55 P. Pantu, S. Pabchanda and J. Limtrakul, *ChemPhysChem*, 2004, **5**, 1901–1906.
56 C. Raksakoon and J. Limtrakul, *THEOCHEM*, 2003, **631**, 147–156.
57 R. Rungsirisakun, B. Jansang, P. Pantu and J. Limtrakul, *J. Mol. Struct*., 2004, **733**, 239–246.
58 W. Sangthong, M. Probst and J. Limtrakul, *J. Mol. Struct*., 2005, **748**, 119–127.
59 X. Solans-Monfort, M. Sodupe, V. Branchadell, J. Sauer, R. Orlando and P. Ugliengo, *J. Phys. Chem. B*, 2005, **109**, 3539–3545.
60 P. Pantu, B. Boekfa, B. Sunpetch and J. Limtrakul, *Chem. Eng. Commun*., 2008, **195**, 1477–1485.
61 B. Jansang, T. Nanok and J. Limtrakul, *J. Phys. Chem. C*, 2008, **112**, 540–547.
62 W. Panyaburapa, T. Nanok and J. Limtrakul, *J. Phys. Chem. C*, 2007, **111**, 3433–3441.
63 P. Pantu, B. Boekfa and J. Limtrakul, *J. Mol. Catal. A: Chem*., 2007, **277**, 171–179.
64 J. Lomratsiri, M. Probst and J. Limtrakul, *J. Mol. Graphics Modell*., 2006, **25**, 219–225.
65 B. Jansang, T. Nanok and J. Limtrakul, *J. Mol. Catal. A: Chem*., 2007, **264**, 33–39.
66 N. Injan, N. Pannorad, M. Probst and J. Limtrakul, *Int. J. Quantum Chem*., 2005, **105**, 898–905.
67 B. Jansang, T. Nanok and J. Limtrakul, *J. Phys. Chem. B*, 2006, **110**, 12626–12631.
68 M. J. Frisch, G. W. Trucks, H. B. Schlegel, G. E. Scuseria, M. A. Robb, J. R. Cheeseman, J. J. A. Montgomery, T. Vreven, K. N. Kudin, J. C. Burant, J. M. Millam, S. S. Iyengar, J. Tomasi, V. Barone, B. Mennucci, M. Cossi, G. Scalmani, N. Rega, G. A. Petersson, H. Nakatsuji, M. Hada, M. Ehara, K. Toyota, R. Fukuda, J. Hasegawa, M. Ishida, T. Nakajima, Y. Honda, O. Kitao, H. Nakai, M. Klene, X. Li, J. E. Knox, H. P. Hratchian,

J. B. Cross, V. Bakken, C. Adamo, J. Jaramillo, R. Gomperts, R. E. Stratmann, O. Yazyev, A. J. Austin, R. Cammi, C. Pomelli, J. W. Ochterski, P. Y. Ayala, K. Morokuma, G. A. Voth, P. Salvador, J. J. Dannenberg, V. G. Zakrzewski, S. Dapprich, A. D. Daniels, M. C. Strain, O. Farkas, D. K. Malick, A. D. Rabuck, K. Raghavachari, J. B. Foresman, J. V. Ortiz, Q. Cui, A. G. Baboul, S. Clifford, J. Cioslowski, B. B. Stefanov, G. Liu, A. Liashenko, P. Piskorz, I. Komaromi, R. L. Martin, D. J. Fox, T. Keith, M. A. Al-Laham, C. Y. Peng, A. Nanayakkara, M. Challacombe, P. M. W. Gill, B. Johnson, W. Chen, M. W. Wong, C. Gonzalez and J. A. Pople, *GAUSSIAN 03*, Gaussian, Inc., Wallingford CT, 2004.

69 L. Regli, S. Bordiga, C. Lamberti, K. P. Lillerud, S. I. Zones and A. Zecchina, *J. Phys. Chem. C*, 2007, **111**, 2992–2999.

70 Y. Wang, D. Zhou, G. Yang, S. Miao, X. Liu and X. Bao, *J. Phys. Chem. A*, 2004, **108**, 6730–6734.

71 S. P. Yuan, J. G. Wang, Y. W. Li and H. Jiao, *THEOCHEM*, 2004, **674**, 267–274.

72 S. P. Yuan, J. G. Wang, Y. W. Li and H. Jiao, *J. Phys. Chem. A*, 2002, **106**, 8167–8172.

73 R. C. Deka, N. Tajima and K. Hirao, *THEOCHEM*, 2001, **535**, 31–38.

74 H. Berndt, A. Martin, H. Kosslick and B. Luecke, *Microporous Mater.*, 1994, **2**, 197–204.

Reaction Mechanisms of the Methylation of Ethene with Methanol and Dimethyl Ether over H-ZSM-5: An ONIOM Study

T. Maihom,[†,‡] B. Boekfa,[†,‡] J. Sirijaraensre,[†,‡] T. Nanok,[†,‡] M. Probst,[§] and J. Limtrakul*[,†,‡]

Laboratory for Computational and Applied Chemistry, Department of Chemistry, Faculty of Science and Center of Nanotechnology, Kasetsart University Research and Development Institute, and NANOTEC Center of Excellence, National Nanotechnology Center, Kasetsart University, Bangkok 10900, Thailand, and Institute of Ion Physics and Applied Physics, University of Innsbruck, A-6020 Innsbruck, Austria

Received: November 2, 2008; Revised Manuscript Received: February 16, 2009

The mechanisms of ethene methylation with methanol and dimethyl ether have been investigated using a 128T cluster of ZSM-5 zeolite modeled by ONIOM(B3LYP/6-31G(d,p):UFF) and ONIOM(M06-2X/6-311+G(2df,2p):UFF) calculations. The effects of the infinite zeolitic framework on the model of the zeolite nanopocket, which consisted of a quantum cluster of 34 tetrahedral units and of 128 tetrahedral units modeled on the UFF level, were also included. The zeolitic Madelung potential was reproduced by a set of point charges generated by the SCREEP method. The energies for the adsorption of methanol and dimethyl ether on H-ZSM-5 from an ONIOM2(M06-2X/6-311+G(2df,2p):UFF)+SCREEP calculation are −26.3 and −29.4 kcal/mol, respectively, which are in good agreement with the experimental data. Dissociative and associative mechanisms of the ethene methylation by methanol and dimethyl ether have been considered. For the dissociative mechanism, the methylation reaction of ethene starts with the protonation of methanol or dimethyl ether by the acidic zeolite proton to form a surface methoxide intermediate, which subsequently reacts with an ethene molecule forming a propoxide intermediate. The propoxide intermediate is then deprotonated to form the propene product. The activation energies for the first step are computed to be 41.2 and 42.9 kcal/mol for methanol and dimethyl ether, respectively. The activation energies for the subsequent second and third reaction steps are 21.4 and 26.5 kcal/mol, respectively. For the associative mechanism, protonation and methylation take place simultaneously without formation of a surface methoxide. The calculated activation barriers are 29.0 and 33.0 kcal/mol for methanol and dimethyl ether, respectively, suggesting that methanol should be slightly more reactive than dimethyl ether for the methylation of ethene. The final step in the associative mechanism, the deprotonation of the propoxide intermediate to give the adsorbed propene product, has an activation energy of 25.4 kcal/mol. The results indicate that the associative pathway is favored over the dissociative one and that the rate-determining step of this reaction is the ethene methylation step.

1. Introduction

Methylation is one of a number of reactions that increase the number of C atoms in a hydrocarbon chain. Methyl halides (CH_3I, CH_3Br, and CH_3Cl), dimethyl ether, and methanol are important conventional methylating agents. Among these, methanol is the one used most frequently in the petrochemical industry. It is supplied as a feedstock in the conversion process of methanol to hydrocarbons (MTH),[1,2] an industrial process making use of heterogeneous catalysis invented by Chang and Silvestri[3] in 1977. Presently, the MTH technology is the most interesting process besides the transformation of natural gas or coal into olefins or gasoline because the synthesis gas (CO and H_2) generated from the transformation processes of natural gas or coal can be reused in the synthesis of methanol.

The mechanistic aspects of the MTH process have been reported in many publications.[2,4−15] More than 20 different mechanisms have been suggested. However, during the past decade, the conversion mechanism of methanol to hydrocarbons over acidic zeolites through "the hydrocarbon pool mechanism" has been verified as the dominating route. This mechanism was originally proposed by Dahl and Kolboe.[16−18] The reaction proceeds via repeated methylations and dealkylations of carbonaceous compounds. Light alkenes are formed from these compounds via an elimination process. It is observed that the initial C−C bond formation leading to the formation of organic compounds is one of the important steps in the hydrocarbon pool mechanism. Therefore, this work studies the C−C bond formation between methanol and ethene, which is one of the hydrocarbon pool species.

Experimental and theoretical efforts have been carried out to gain an understanding of the methylation reaction of small olefins with methanol over the zeolite catalysts. Experimental studies[19−23] found that the methoxide intermediate can be observed inside the cavity of zeolites during the conversion of methanol. This species is generated from methanol dissociation on the acid site of zeolites. The surface methoxide intermediate is able to act as a reactive species for the C−C bond formation in the hydrocarbon-pool mechanism and could thus react directly with alkanes, alkenes, and aromatics molecules.[14,19−23] However, some studies[14,24−26] indicated that the coadsorption of methanol (end-on adsorption) and the alkene molecule on the acid site of zeolite is responsible for the methylation. Recently, Svelle et al.[10,11] have studied the methylation of ethene, propene, and

* Corresponding author. Tel.: +66-2-562-5555 ext 2159. E-mail: jumras.l@ku.ac.th.
[†] Department of Chemistry, Kasetsart University.
[‡] National Nanotechnology Center, Kasetsart University.
[§] University of Innsbruck.

10.1021/jp809746a CCC: $40.75
Published on Web 03/31/2009

n-butylene with methanol on acidic ZSM-5 by means of an isotopic label technique. They found that the intrinsic activation energies for the methylation of ethene, propene, and *n*-butene are 32.3, 26.3, and 21.5 kcal/mol, respectively. In theoretical studies,[4,9,27−31] it was shown that the methylation reaction proceeds via either a stepwise or a concerted mechanism. In the stepwise mechanism, the intermediates are consecutively generated along the reaction path. The formation of methoxide species is the first step of the reaction, followed by the methylation of alkenes and arenes. In the concerted mechanism, the methylation takes place in a single step. The C−O bond dissociation of methanol occurs simultaneously with the C−C bond formation without the formation of an intermediate. Vos et al.[31] have studied the methylation of benzene and toluene theoretically using a 4T quantum cluster model of H-ZSM-5 at the B3LYP/6-31G(d,p) level of theory. They found that the reaction occurs preferably via the concerted mechanism rather than via the stepwise mechanism. However, the stepwise pathway was found to be entropically favored over the concerted mechanism because only one molecule is required to interact with the active site. In other works, the methylation of some alkenes and arenes with methanol and dimethylether was investigated by a quantum chemical cluster model at the MP2/6-311G(d)//B3LYP/6-31G(d) level of theory via the concerted pathway only.[9,30] However, in these works, the acidic zeolite lattice was represented by an unconstrained 4T cluster model, and therefore the short- and long-range effects of the zeolite framework were neglected. Previously, it had been found[32−34] that the long-range effect of the zeolite framework must be taken into account for accurate results.[35] To account for the effects of the zeolite framework, various techniques such as periodic ab initio calculations and quantum mechanics/molecular mechanics (QM/MM) hybrid methods have been widely used. The former approach is computationally too expensive and impractical for studying the large unit cell zeolites. The recent development of QM/MM hybrid methods, such as the embedded cluster methods,[36−41] QM/MM methods with coupling Hamiltonians,[32,42−44] as well as the ONIOM methods,[45−57] were employed to keep the calculations feasible. These methods can properly describe the effect of the zeolite framework. Especially, the ONIOM method has been used successfully to investigate the adsorption of hydrocarbons such as ethene, benzene, and ethylbenzene[45−47] and the reactions of organic molecules over zeolites.[48−54]

In the present study, the ONIOM2 method was employed for investigating the formation of propene via the methylation of ethene with methanol and dimethyl ether over H-ZSM-5 zeolite. This reaction can, in principle, proceed via a dissociative (stepwise) or an associative (concerted) mechanism, and both mechanisms are considered. We have investigated the effects of the zeolite framework on the energetic profiles of both the dissociative and the associative routes. Dimethyl ether was chosen as a reactant in this work because it can be generated easily by the reversible condensation of two methanol molecules.

2. Models and Methods

The crystal lattice of the acidic ZSM-5 zeolite is represented by a 128T (127 tetrahedral atoms of Si and 1 tetrahedral atom of Al) cluster model, which covers the intersection of the straight and zigzag channels, as shown in Figure 1a. One silicon atom at the T12 site is replaced with an aluminum atom to generate the Brønsted acid site. For computational efficiency, the 128T cluster model is subdivided into two layers according to the ONIOM2 scheme. The inner layer comprises 12T atoms and is considered as the active region and is treated at the B3LYP/6-31G(d,p) level of theory. The outer layer, which is the rest of the 128T cluster, is treated with a computationally less expensive method, the universal force field (UFF) to represent the confinement effect[58−60] of the zeolite pore structure. This force field has been reported to give a good description of the short-range van der Waals interactions. During geometry optimizations, only the 5T cluster of the active region, [(≡SiO)$_3$Al(OH)Si≡], and the adsorbing molecules are relaxed. The frequency calculations are performed at the same level of theory to ensure that transition state structure has only one imaginary frequency that corresponds to the desired reaction coordinate. We have made attempts to cover the dispersion interaction in the zeolite system. Some test calculations on adsorbing molecules (methanol and dimethyl ether) over the Brønsted acid site of MFI zeolite have been performed using MP2 and the newly developed density functional, M06-2X,[61−64] which we expected to be able to reproduce adsorption on zeolites. Single-point calculations with M06-2X and MP2 at B3LYP-optimized complex geometries yield very similar results (27.7 vs 29.8 kcal/mol for adsorption energies of dimethyl ether and 25.2 vs 26.5 for methanol complexes; see Table S1 of the Supporting Information). This indicates that the M06-2X functional can indeed recover the dispersion interaction in these zeolite systems as reliably as the MP2 method with the benefit of feasible computational costs. To cover both the active Brønsted acid site and the nanopocket surrounding the reactive center, 34T QM clusters were employed in the ONIOM scheme: 34T/128T (see Figure 1b and c).

To include the electrostatic effect of the infinite zeolitic framework, the zeolite nanopockets were embedded in a set of point charges, generated by the SCREEP method, that reproduce the zeolitic Madelung potential. A detailed description of the method to optimized magnitude and positions of the point charges that accurately reproduce the electrostatic effect of the infinite lattice has been given previously.[65,66] This embedded scheme (see Figure 1d) has been successfully used in our previous studies on unsaturated hydrocarbons adsorption[54,57,67] and on the mechanisms of the Beckmann rearrangement over H-MFI zeolites.[68] With 34T/128T single point calculation using the ONIOM2(M06-2X/6-311+G(2df,2p):UFF)+SCREEP combination, the adsorption energies of methanol and dimethyl ether over the H-ZSM-5 zeolite were computed to be −26.3 and −29.4 kcal/mol, respectively, in good agreement with the experimental data.[69] While the adsorption energy of methanol is insensitive to the size of the QM region, the confinement effects from the zeolite framework significantly affect the adsorption energy of dimethyl ether. This is due mainly to the size of the adsorbing molecule inside the nanocavity of zeolite. Hence, ONIOM2(M06-2X/6-311+G(2df,2p):UFF) seems to be well suited to investigate adsorption properties and reaction mechanisms of the methylation of ethene with methanol and dimethyl ether over H-ZSM-5. All calculations were performed using the Gaussian 03 code.[70]

3. Results and Discussion

The catalytic methylation of ethene with methanol and dimethyl ether over H-ZSM-5 was systematically investigated, and the results were compared to experimentally established facts whenever possible.[10] Two previously proposed mechanisms, dissociative and associative, were theoretically investigated within the model described above. The side-on structure, the weak adsorption mode (cf., Figure 2b), was taken as the starting geometry for the dissociative mechanism, while the end-

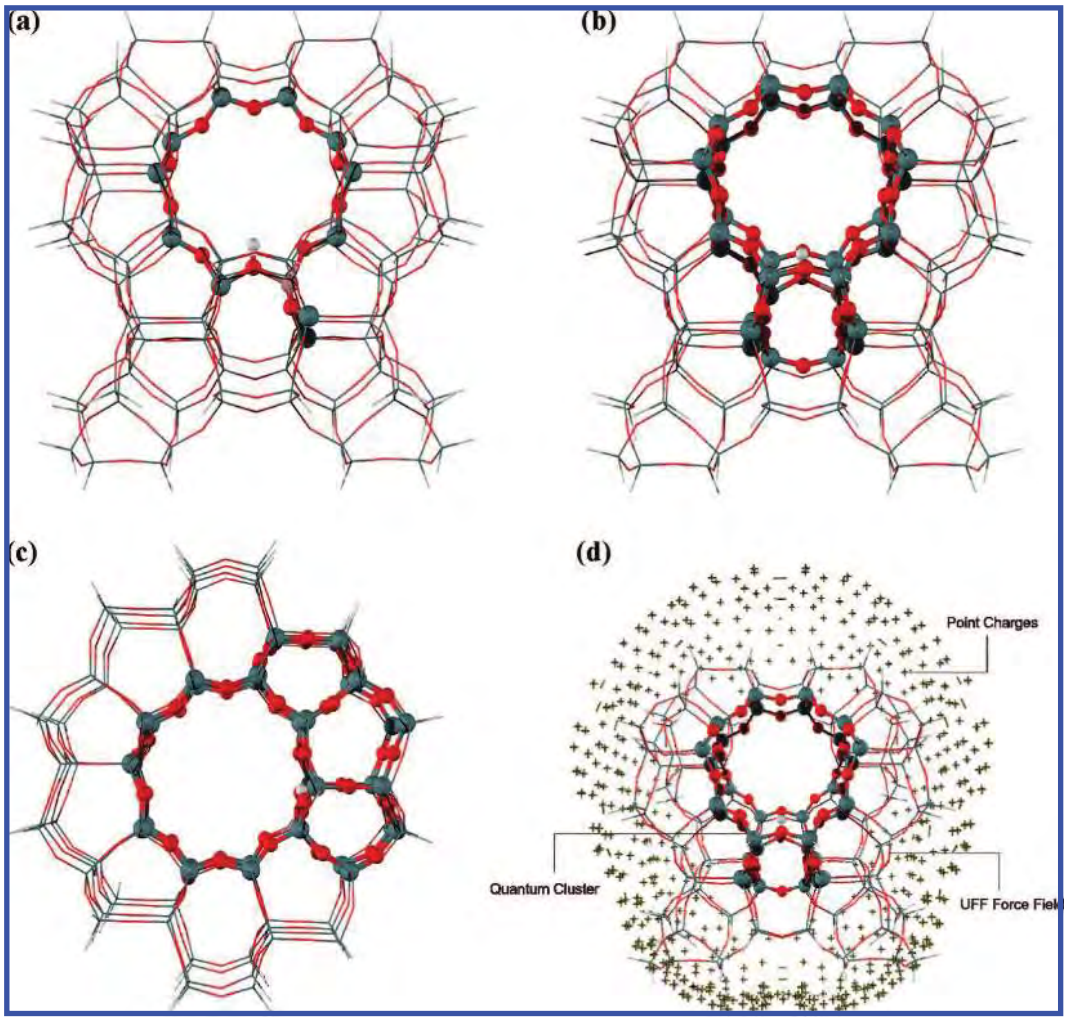

Figure 1. ONIOM2 model of the 128T cluster from H-ZSM-5 zeolite. Atoms belonging to the quantum region in the ONIOM2 scheme are drawn as bond and stick models: (a) 12T/128T ONIOM model, (b) sinusoidal channel view, and (c) straight channel view of 34T/128T ONIOM model and (d) SCREEP embedded model.

on structure, the strong adsorption mode (cf., Figure 2a), was used to describe the initial step of the associative mechanism.

3.1. Structures and Energetics of Methanol and Dimethyl Ether Adsorption. The optimized adsorption structures of methanol on the Brønsted acid site of H-ZSM-5 are shown in Figure 2a and b. It can be seen that methanol is adsorbed on the acid site by either the end-on (Ads1_M_S) or the side-on (Ads2_M_S) hydrogen-bond complex structure, in agreement with the theoretical studies mentioned above.[4,31,53,71−74] In the side-on structure, there is only one strong hydrogen bond between the OH group of methanol and the OH group of zeolite, whereas in the end-on geometry methanol is stabilized by two strong hydrogen bonds. The adsorption energies, for the side-on and end-on structures, are calculated to be 24.2 and 26.3 kcal/mol, respectively, which are consistent with the experimental observation that methanol adsorbed by the side-on structure is weaker than that by the end-on structure.[14] The later estimated adsorption energy is in good agreement with the reported experimental adsorption heat of end-on adsorption of methanol in H-ZSM-5 of 27.5 ± 1 kcal/mol.[69] The acidic O−H bond of zeolite is stretched upon adsorption of methanol by 0.07 and 0.10 Å for the weak and strong adsorption modes, respectively (O···H−O intermolecular distance: 2.53 and 2.48 Å). The O−H bond of methanol is virtually unaffected by the adsorption. It is stretched from the isolated gas phase by 0.01 and 0.02 Å, for side-on and end-on adsorption, respectively.

Figure 2c shows the adsorption structure of dimethyl ether (Ads_D_S) on the Brønsted acid site of H-ZSM-5, which resembles the end-on adsorption structure of methanol. Two methyl groups are weakly bound to the zeolite oxygen framework. No stable side-on structure could be obtained from the ONIOM2(12T/128T) scheme. The end-on adsorption energy is calculated to be −29.4 kcal/mol. The interatomic distance between the oxygen atom of dimethyl ether and the acidic hydrogen atom of zeolite (O3···H1 = 1.51 Å) is longer than that of the corresponding O3···H1 distances in the methanol case (1.49 and 1.41 Å for side-on and end-on structures, respectively), and, consequently, also the elongation of the zeolite O−H bond (1.03 Å) is less. These overall consistent results make it likely that the structures from the 12T/128T ONIOM2(B3LYP/6-31G(d,p)//UFF) model with the single point calculation at the 34T/128T embedded-ONIOM2(M06-2X/6-311+G(2df,2p)//UFF) model constitute a suitable QM/MM hybrid method for studying the adsorption of small polar molecules in zeolites, to be used to study ethene methylation, as discussed in the following sections.

3.2. Reaction and Mechanism of Ethene Methylation with Methanol and Dimethyl Ether. Experimental reports seem to indicate that the methylation of toluene by methanol and dimethyl ether that are adsorbed side-on onto the Brønsted acid site of zeolite takes place through the dissociative mechanism, while the methylation of end-on adsorbed molecules proceeds

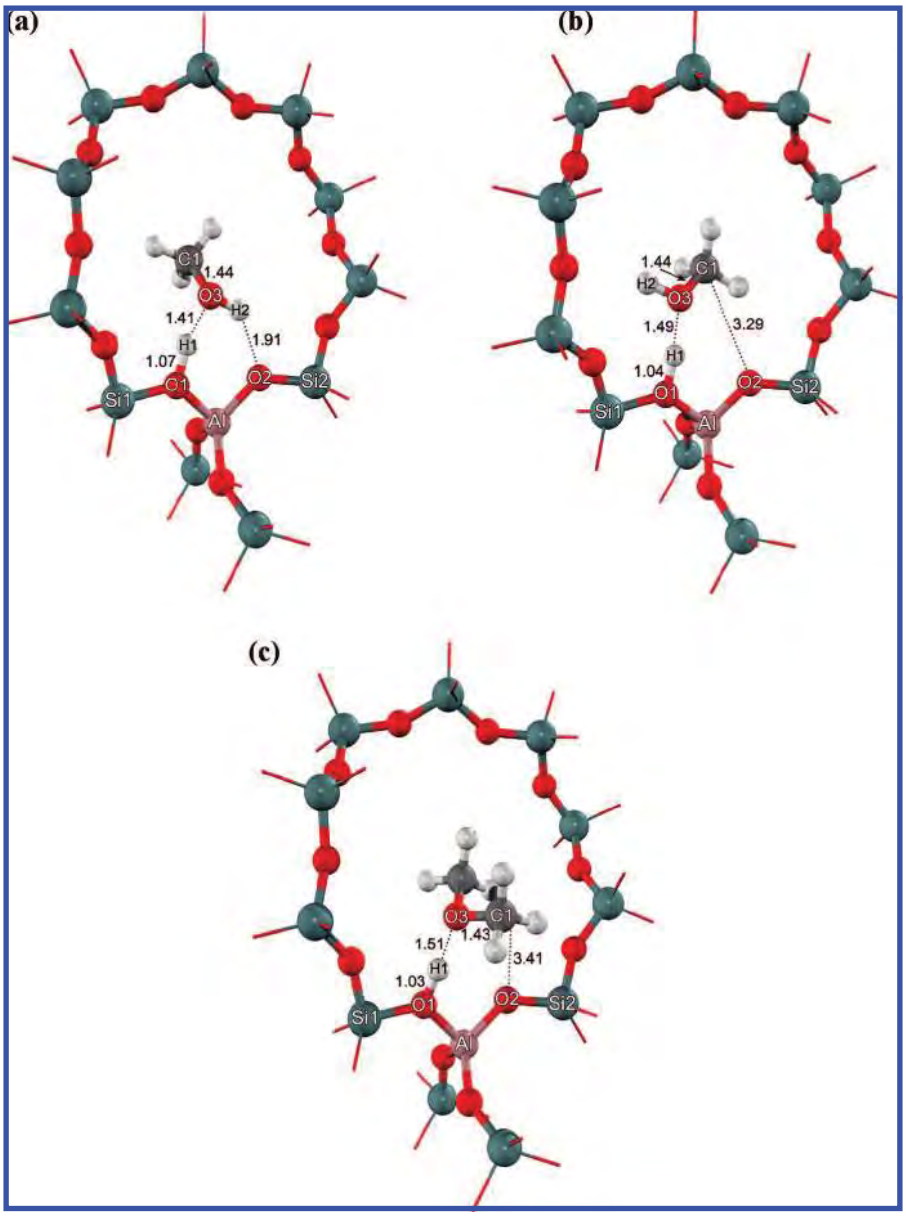

Figure 2. Optimized geometries of the adsorption complexes on 12T/128T ONIOM model: (a) end-on methanol adsorption, (b) side-on methanol adsorption, and (c) dimethyl ether adsorption.

through the associative mechanism.[14] In the dissociative mechanism, the surface methoxide species is generated as the key intermediate prior to the methylation process. This species was found to react with water and methanol at room temperature.[19−23] However, in the absence of other species, it remains stable up to a temperature of 523 K.[19−23]

3.2.1. Dissociative Reaction Pathway. *3.2.1.1. Surface Methoxide Intermediate Formation.* The surface methoxide intermediate formed by methanol is illustrated in Figure 3a, and selected geometrical parameters are listed in Table S2 (Supporting Information). This reaction is initiated by the adsorption of methanol on the active acidic site of ZSM-5 through the formation of a strong hydrogen bond between the alcoholic oxygen atom of methanol and the OH group of zeolite ("side-on" adsorption complex, Ads2_M_S). Here, its adsorption energy is −24.2 kcal/mol. The O1−H1 bond of ZSM-5 is lengthened from 0.97 to 1.04 Å. In the methanol molecule, the C1−O3 length increases by 0.02 Å because it is weakened by the hydrogen-bond formation and the subsequent electron transfer from O3 to H1.

The H-bonded adsorption complex reacts to form the surface methoxide intermediate via the transition state TS1_M_S shown in Figure 2c. In this transition state, the Brønsted proton H1 is transferred to the methanol oxygen atom O, and the C−O bond of methanol is cleaved leading to the formation of a water molecule. The leaving methyl group is stabilized by the bridging oxygen O2 of the zeolite. This results in an elongation of the C1−O3 bond distance from 1.44 to 1.94 Å. The C1···O2 distance is reduced to 2.16 Å, while the O2−C1−O3 angle stays nearly linear (171°). The activation energy for this transition state is 41.2 kcal/mol, considerably lower than what has been reported for the bare cluster models (51−54 kcal/mol).[4,71,75−77] This shows that the transition state is stabilized by the confinement effect of the zeolitic framework. Relative to the methanol end-on adsorption complex, the transition state is 43.2 kcal/mol higher in energy.

TS1_M_S proceeds then by the formation of a covalent C1−O2 bond (bond length 1.50 Å) to the surface methoxide product (Int1_M_S). In it, the Si−O2 and Al−O2 bonds are shortened by 0.08 and 0.13 Å, respectively, as are the Si1−O1

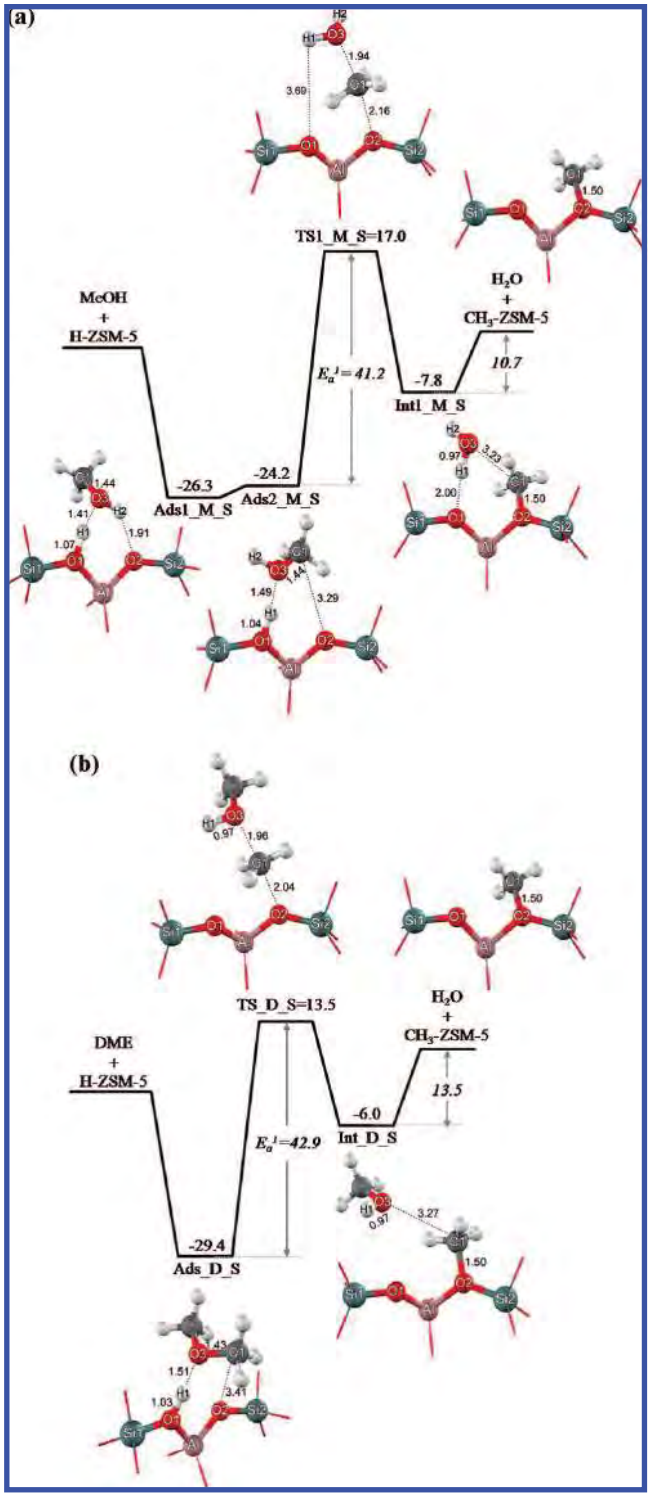

Figure 3. Energy profiles for the surface methoxide intermediate formation step of the dissociative mechanism for the embedded 34T/128T cluster calculated with the ONIOM2(M06-2X/6-311+G(2df,2p):UFF) model: (a) methanol protonation and (b) dimethyl ether protonation (energies in kcal/mol).

and Al−O1 bonds (0.06 and 0.13 Å, respectively). The Al−O1−Si1 angle decreases by 4.6°. The adsorption energy of the methoxide−water complex with respect to the isolated reactants is −7.8 kcal/mol, significantly less than the adsorption energy of methanol. The fact that the covalent bond between the methoxide intermediate and the zeolite is weak is also in agreement with experiments[19] and has been related to the steric forces of the zeolite pore walls in previous studies.[78−81] It is an active, unstable species that can easily interact with incoming molecules such as ethene.

If we consider now the corresponding surface methoxide formation from dimethyl ether, the reaction starts with the adsorption of dimethyl ether on the Brønsted acid active site of ZSM-5 zeolite, as the end-on adsorption complex. The energy profile for this reaction is shown in Figure 3b, and selected geometrical parameters are listed in Table S3 (Supporting Information). The dimethyl ether adsorbs on the acidic site through the hydrogen-bonding interaction between its oxygen and H1. The H1−O1 distance, therefore, increases from 0.97 to 1.03 Å (Ads_D_S). Similar to the methanol case, electron density is transferred from the O3 to the H1 atom, and C1−O3 is slightly lengthened by 0.02 Å. The adsorption energy of this complex is −29.4 kcal/mol. Next, the C1−O3 bond of the adsorbed dimethyl ether is cleaved and the H1−O3 bond is formed. Again, the surface methoxide species and a methanol molecule are generated on the zeolite framework. In the transition state TS_D_S, the proton (H1) is transferred to the oxygen of dimethyl ether to form the leaving methanol molecule. Its oxygen atom O3, C1, and the surface oxygen atom, O2, are aligned in a linear way (173.4° for the O3−C1−O2 bond angle). The breaking C1−O3 bond is elongated from 1.43 to 1.96 Å, and the C1···O2 distance decreases to 1.37 Å. The activation energy for the protonation step is 42.9 kcal/mol, which is close to the one for the methanol protonation reported above. The surface C1−O2 distance in the surface methoxide species is 1.50 Å (Int_D_S). Again, the calculated adsorption energy of the methoxide−methanol complex calculated is quite small, −6.0 kcal/mol, even less than for methanol. We can summarize that the reaction of dimethyl ether proceeds in the same way as for methanol and also that the energetics are similar.

3.2.1.2. Methylation and Deprotonation Reaction Step. Subsequently, the surface methoxide species in the zeolite pore structure acts as a methylating agent. It is assumed that an ethene molecule diffuses into the zeolite pore and adsorbs on the reactive methoxide intermediate, enabling the formation of an ethene−methoxide coadsorption complex (Ads3_M_S). The calculated energy profile of this part of the overall reaction is shown in Figure 4; geometric parameters are listed in Table S4 (Supporting Information). Ethene and the methoxide coadsorption complex are interacting only weakly (−10.5 kcal/mol) in this coadsorption complex. Next, the reaction proceeds via the transition state TS2_M_S that involves the concerted bond breaking of the C1−O2 bond and the formation of the C1−C2 bond. The C1−O2 distance increases from 1.50 to 2.19 Å. The length of the newly formed C1−C2 bond in Ads3_M_S is 2.23 Å, and the C2−C3 bond distance is slightly increased by 0.02 Å. The activation energy is 21.4 kcal/mol. The small primary carbocation $CH_3CH_2CH_2^+$, which is produced by the methylation of ethene, has the opportunity to stay in the zeolite nanocavity. However, theoretical studies indicate that carbocation intermediates formed by catalytic processes in zeolite are short-lived when the positive charge of the carbon atom can be approached by atoms of the framework.[82]

The propoxide intermediate produced for methylation of ethene by the methyl group is formed with a covalent bond to the O1 oxygen bridging atom of the zeolite framework (Int2_M_S). The C3−O1 bond length is 1.54 Å. The C1−C2 and C2−C3 bond distances of 1.53 and 1.52 Å, respectively, are typical for C−C single bonds. The adsorption energy of the propoxide intermediate is −36.8 kcal/mol. In the last step, the propene product is formed via the deprotonation transition state (TS3_M_S) in which the breaking of the C3−O1 bond

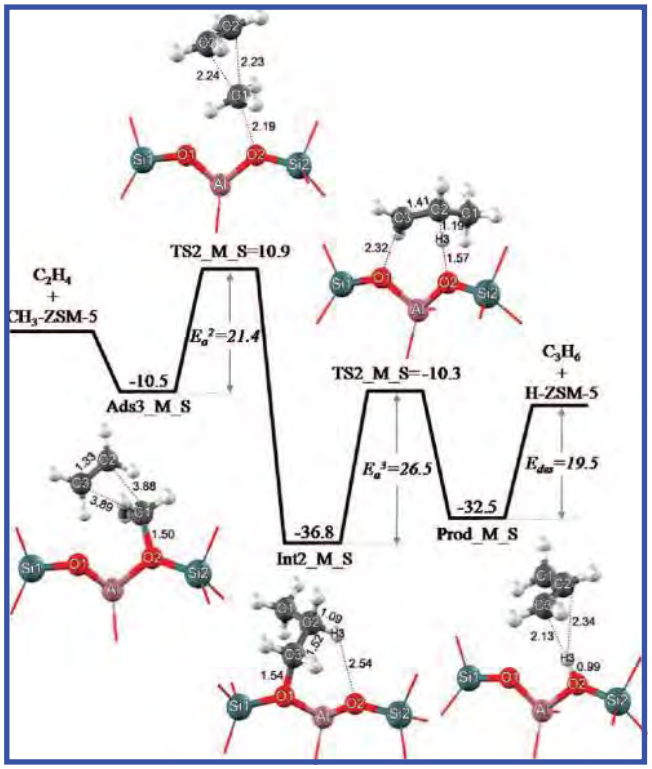

Figure 4. Energy profiles for the ethene methylation and deprotonation reaction step of the dissociative mechanism for the embedded 34T/128T cluster calculated with the ONIOM2(M06-2X/6-311+G(2df,2p):UFF model (energies in kcal/mol).

and the H3 proton transfer from propoxide to the oxygen bridging atom of zeolite begin. This transition state is very similar to the carbenium−ion complex. The C3−O1 and C2−H3 bond distances are elongated by 0.78 and 0.10 Å, respectively, while the O2···H3 distance decreases to 1.57 Å. The predicted activation energy of this step of 26.5 kcal/mol is again lower than the one obtained with a small 10T cluster model (33.4 kcal/mol)[83] due to the effects of the zeolite framework. After the back-migration of the proton to the zeolite framework, the propene product is formed (Prod_M_S). It is adsorbed on the acidic site of the zeolite through a π-bond interaction with an adsorption energy of −32.5 kcal/mol. Finally, the propene product is desorbed. This endothermic step requires 19.5 kcal/mol.

3.2.2. Associative Reaction Pathway. An associative reaction mechanism is an alternative for the ethene methylation with methanol or dimethyl ether. For the ethene methylation with methanol, the energy profile is shown in Figure 5a, and selected geometrical parameters are listed in Table S5 (Supporting Information). This reaction is also initialized by the coadsorption complex between methanol and ethene over the Brønsted acid site (Ads_M_C). Next, however, ethene is methylated directly by methanol without the formation of the methoxide intermediate. Methanol is adsorbed on the acidic proton in the end-on formation via two hydrogen bonds. The neighboring ethene molecule is adsorbed weakly. The O1−H1 distance increases from 0.97 to 1.08 Å upon absorption, and the C1−O3 bond distance increases by approximately 0.03 Å. The C1···C2 and C1···C3 intermolecular distances between the methanol and the ethene molecule are 3.99 and 4.05 Å, respectively. The coadsorption energy of the methanol and ethene on the acidic site of ZSM-5 zeolite with respect to isolated reactants is calculated to be −36.6 kcal/mol. In the transition state (TS1_M_C) of this step, methanol is protonated by the H1 of zeolite and

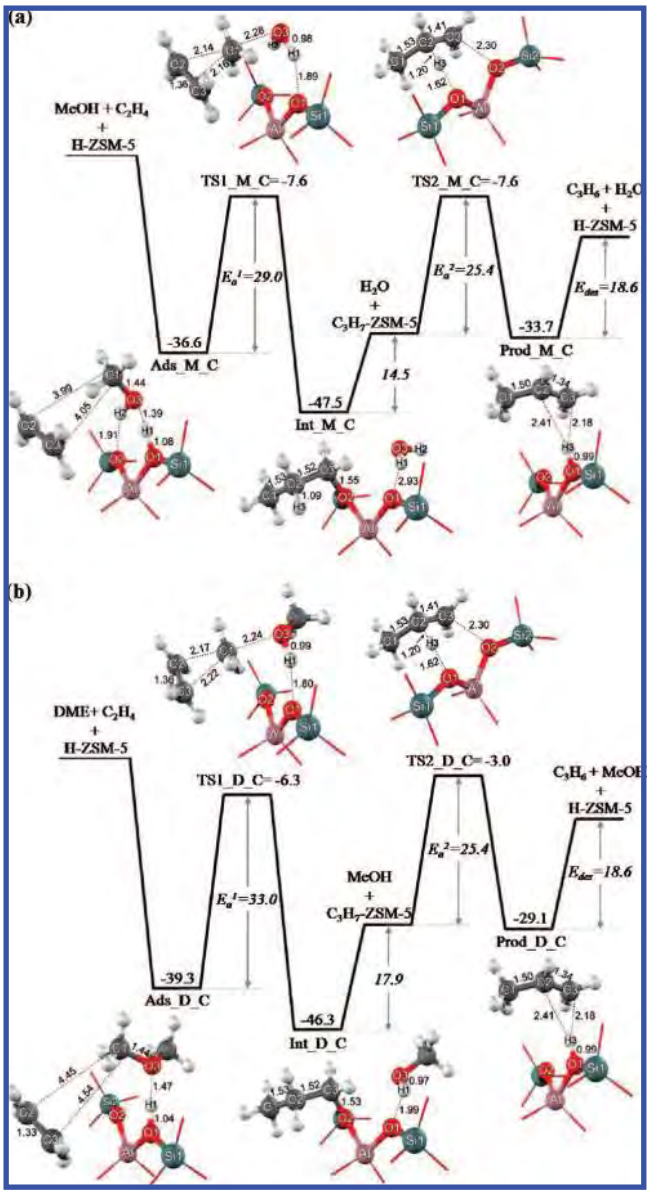

Figure 5. Energy profiles for the associative ethene methylation pathway. The calculations on the embedded 34T/128T cluster were performed with the ONIOM2(M06-2X/6-311+G(2df,2p):UFF) method: (a) methanol and (b) dimethyl ether (energies in kcal/mol).

simultaneously the C1−O3 bond is broken to give a methoxonium cation, which at the same time reacts with the C2 of ethene to form the primary alkoxide. As a result, the methanol C1−O3 bond is broken, while the C1···C2 and C1···C3 distances decrease (2.14 and 2.16 Å, respectively). The activation energy of this step is 29.0 kcal/mol, which compares well with the experimental results of Svell et al.[10] (approximately 32.3 kcal/mol). On the product side, the primary propoxide is formed with a neighboring water molecule adsorbed in the zeolite pore with the C3−O2 distance of 1.55 Å (Int_M_C). This propoxide−water complex is even more strongly adsorbed (−47.5 kcal/mol) than methanol at the beginning of the process. Finally, the desorbtion of the water molecule requires 14.5 kcal/mol.

The energy profile of the equivalent ethene methylation with dimethyl ether is shown in Figure 5b, and selected geometrical parameters are listed in Table S6 (Supporting Information). This reaction proceeds like the one with methanol discussed above. Ads_D_C shows the dimethyl ether−ethene coadsorption complex. In this complex, the O1−H1 bond length increases

slightly less (0.08 Å) than when interacting with methanol. The adsorption energy of this complex is −39.3 kcal/mol. Next, the adsorbed dimethyl ether is protonated at the O3 atom, and the free methyl group is transferred to react with the C2 of the ethene molecule leading to the formation of the propoxide intermediate (TS1_D_C). The H1−O1 bond and C1−O3 distances are elongated to 1.80 and 2.24 Å, respectively, and the O3···H1 distance is shortened to 0.99 Å. These and the other geometrical changes follow the trends found for methanol. The calculated activation energy of 33.0 kcal/mol is slightly higher than the activation energy of the methanol reaction (29.0 kcal/mol). After the transition state, TS1_D_C, the propoxide−methanol complex (Int_D_C) is formed with a C3−O2 bond length of 1.53 Å and an adsorption energy of −46.3 kcal/mol. Finally, desorption of the methanol molecule from propoxide requires 17.9 kcal/mol.

After the active primary propoxide is generated by eliminating water or methanol, the H3 proton connects to O1. This reaction to the final propene product is formed via the transition state TS2_M_C. In the reaction as well, the breaking of the C2−H3 and C3−O2 bonds starts by an increase of their lengths from 1.54 to 2.30 and 1.09 to 1.20 Å, respectively. The C2−C3 bond distance is shortened by 0.11 Å, reflecting its double bond character. The activation energy of this step is 25.4 kcal/mol. −33.7 and −29.1 kcal/mol are then gained by formation of the final product bound to the zeolite for ethene methylation with methanol and dimethyl ether, respectively. The desorption of the π-complexed product requires 18.6 kcal/mol.

4. Comparison of Dissociative and Associative Pathways

From the energetic profiles for the dissociative and associative reaction pathways of ethene methylation with methanol and dimethyl ether, it can be seen that the protonation of methanol and dimethyl ether to form the active methoxide intermediate is found to be the rate-determining step in the stepwise mechanism with activation energies of 41.2 and 42.9 kcal/mol, respectively. The methoxide intermediate is stabilized by the framework of zeolite that is active for the incoming molecule as ethene. Therefore, the methylation of ethene with the methoxide intermediate and the deprotonation step of the subsequent reaction are more facile than the methanol protonation step with lower activation energy barriers of 21.4 and 26.5 kcal/mol, respectively. However, considering the energy barrier for the ethene methylation reaction and for the hydrolysis reaction of the methoxide species, it is found that the hydrolysis reaction, reversing the methoxide complex to the methanol molecule, is kinetically and thermodynamically favored over the ethene methylation. Furthermore, the water molecule is more strongly adsorbed on the methoxide than is the ethene molecule. Therefore, an ethene molecule cannot easily be inserted into the methoxide active site. For the associative mechanism of ethene methylation with methanol or dimethyl ether, the simultaneous protonation and C−C bond formation reaction is regarded as the rate-determining step with activation energies of 29.0 and 33.0 kcal/mol, respectively. These results indicate that methanol is more reactive than dimethyl ether (DME) as a methylating agent in our system. This is in disagreement with a previous study,[9] which was performed on a cluster consisting of only four tetrahedral units, showing that such a model is too small. In this work, we found that the zeolite lattice has an important effect on both the reaction mechanism and the energetic profile. The coadsorption of the dimethyl ether and ethene molecules is stronger than that of methanol (MeOH) and ethene molecules. Considering the transition state (TS) structure of the ethene methylation with methanol as compared to that of ethene methylation with DME, it was found that the TS of the ethene + MeOH complex forms two hydrogen bonds between the leaving water and the bridging oxygens of zeolite (H1···O1 and H2···O2), while the TS structure of the ethane + DME complex forms only one hydrogen bond between the leaving water and the oxygen of zeolite (H1···O1). This indicates that the TS of the ethene + methanol complex is more stable than the TS of the other complex. The weaker coadsorption in the adsorption step and the more stable TS state both lead to the lower activation energy of the methylation of ethene with MeOH as compared to that of the methylation of ethene with DME. However, experimentally an activation energy of DME that is about 1.2 kcal/mol lower than the one for the methanol complex has been found.[9] Also, the conversion of methanol into DME in the methanol + propene system is observed to be around 20%, which is higher than the conversion of methylation process. This implies that the coadsorption of methanol can occur in the MFI zeolite favorably. As results, it might be expected that, although the methanol is more reactive than the DME in methylation reaction, the sizable turnover of a reaction catalyzed by the methanol might be delayed by the coadsorption of methanol over the acid sites of zeolite. In fact, the nature of the methanol coadsorption complex is found to strongly interact with the Brønsted acid sites and is stronger than the coadsorption of the methanol and ethene molecules. From this behavior, it leads to obstruct the methylation process of alkenes. That might be one of the reasons why the activity of DME is higher than that of methanol in experiments.

5. Conclusions

The reaction mechanism of ethene methylation with methanol or with dimethyl ether over H-ZSM-5 zeolite has been investigated by applying two ONIOM schemes: one with a popular density functional, ONIOM2(B3LYP/6-31G(d,p):UFF), and one with a newly developed density functional, ONIOM2(M06-2X/6-311+G(2df,2p):UFF). Two different pathways, the dissociative and associative mechanism, were considered in this study. For the dissociative mechanism, the methylation of ethene initiates from the protonation of methanol or dimethyl ether leading to the surface methoxide intermediate formation, which is followed by the C−C formation between the methoxide and the incoming ethene molecule to produce a propoxide intermediate. This intermediate is finally deprotonated to form the propene product. The calculated energy barrier for the rate-determining protonation step is 41.2 and 42.9 kcal/mol, respectively. The subsequent reactions, the methylation and the deprotonation, require the energy barriers of 21.4 and 26.5 kcal/mol, respectively.

For the associative mechanism, the simultaneous C−O bond breaking and C−C bond formation occur in the single step without the methoxide intermediate. The activation energy of this step is calculated to be 29.0 and 33.0 kcal/mol for methanol and for dimethyl ether, respectively. In the case of methylation with methanol, this is consistent with the experimental value of 32.3 kcal/mol. The deprotonation of the propoxide intermediate to give the adsorbed propene product has an activation energy of 25.4 kcal/mol.

The calculated pathways and energetics suggest that the ethene methylation reaction with methanol and the one with dimethyl ether proceeded preferably via the dissociative mechanism. Our calculations also demonstrated the important effect of the zeolite framework in lowering the activation barriers for these reactions.

Acknowledgment. This work was supported in part by grants from the National Science and Technology Development Agency (NSTDA Chair Professor and NANOTEC Center of Excellence), the Thailand Research Fund and the Kasetsart University Research and Development Institute (KURDI), the Commission on Higher Education, Ministry of Education, under the Postgraduate Education and Research Programs in Petroleum and Petrochemicals, and Advanced Materials, as well as the Sandwich Program (CHE-PhD-SW-INDV to T.M.). We are grateful to Donald G. Truhlar and Yan Zhao for support with the M06-2X functional.

Supporting Information Available: Table S1: Comparison of the calculated adsorption energies of methanol and dimethyl ether with the different methods and basis sets, SCREEP contributions not included. Tables S2−S6: Selected geometric parameters for the ethene methylation with methanol and dimethyl ether. This material is available free of charge via the Internet at http://pubs.acs.org.

References and Notes

(1) Stocker, M. *Microporous Mesoporous Mater.* **1999**, *29*, 3.
(2) Haw, J. F.; Song, W.; Marcus, D. M.; Nicholas, J. B. *Acc. Chem. Res.* **2003**, *36*, 317.
(3) Chang, C. D.; Silvestri, A. J. *J. Catal.* **1977**, *47*, 249.
(4) Andzelm, J.; Govind, N.; Fitzgerald, G.; Maiti, A. *Int. J. Quantum Chem.* **2003**, *91*, 467.
(5) Keil, F. J. *Microporous Mesoporous Mater.* **1999**, *29*, 49.
(6) Fougerit, J. M.; Gnep, N. S.; Guisnet, M. *Microporous Mesoporous Mater.* **1999**, *29*, 79.
(7) Cui, Z. M.; Liu, Q.; Song, W. G.; Wan, L. J. *Angew. Chem., Int. Ed.* **2006**, *45*, 6512.
(8) Svelle, S.; Joensen, F.; Nerlov, J.; Olsbye, U.; Lillerud, K. P.; Kolboe, S.; Bjorgen, M. *J. Am. Chem. Soc.* **2006**, *128*, 14770.
(9) Svelle, S.; Kolboe, S.; Swang, O.; Olsbye, U. *J. Phys. Chem. B* **2005**, *109*, 12874.
(10) Svelle, S.; Ronning, P. O.; Kolboe, S. *J. Catal.* **2004**, *224*, 115.
(11) Svelle, S.; Ronning, P. O.; Olsbye, U.; Kolboe, S. *J. Catal.* **2005**, *234*, 385.
(12) Mikkelsen, O.; Kolboe, S. *Microporous Mesoporous Mater.* **1999**, *29*, 173.
(13) Arstad, B.; Nicholas, J. B.; Haw, J. F. *J. Am. Chem. Soc.* **2004**, *126*, 2991.
(14) Ivanova, I. I.; Corma, A. *J. Phys. Chem. B* **1997**, *101*, 547.
(15) Bjørgen, M.; Svelle, S.; Joensen, F.; Nerlov, J.; Kolboe, S.; Bonino, F.; Palumbo, L.; Bordiga, S.; Olsbye, U. *J. Catal.* **2007**, *249*, 195.
(16) Dahl, I. M.; Kolboe, S. *Catal. Lett.* **1993**, *20*, 329.
(17) Dahl, I. M.; Kolboe, S. *J. Catal.* **1994**, *149*, 458.
(18) Dahl, I. M.; Kolboe, S. *J. Catal.* **1996**, *161*, 304.
(19) Wang, W.; Buchholz, A.; Seiler, M.; Hunger, M. *J. Am. Chem. Soc.* **2003**, *125*, 15260.
(20) Wang, W.; Jiang, Y.; Hunger, M. *Catal. Today* **2006**, *113*, 102.
(21) Wang, W.; Jiao, J.; Jiang, Y.; Ray, S. S.; Hunger, M. *ChemPhysChem* **2005**, *6*, 1467.
(22) Wang, W.; Seiler, M.; Hunger, M. *J. Phys. Chem. B* **2001**, *105*, 12553.
(23) Wang, W.; Hunger, M. *Acc. Chem. Res.* **2008**, *41*, 895.
(24) Vinek, H.; Derewinski, M.; Mirth, G.; Lercher, J. A. *Appl. Catal.* **1991**, *68*, 277.
(25) Mirth, G.; Lercher, J. A. *J. Phys. Chem.* **1991**, *95*, 3736.
(26) Mirth, G.; Lercher, J. A. *J. Catal.* **1991**, *132*, 244.
(27) Svelle, S.; Kolboe, S.; Olsbye, U.; Swang, O. *J. Phys. Chem. B* **2003**, *107*, 5251.
(28) Arstad, B.; Kolboe, S.; Swang, O. *J. Phys. Chem. B* **2002**, *106*, 12722.
(29) Svelle, S.; Kolboe, S.; Swang, O. *J. Phys. Chem. B* **2004**, *108*, 2953.
(30) Svelle, S.; Arstad, B.; Kolboe, S.; Swang, O. *J. Phys. Chem. B* **2003**, *107*, 9281.
(31) Vos, A. M.; Nulens, K. H. L.; Proft, F. D.; Schoonheydt, R. A.; Geerlings, P. *J. Phys. Chem. B* **2002**, *106*, 2026.
(32) Brändle, M.; Sauer, J. *J. Am. Chem. Soc.* **1998**, *120*, 1556.
(33) Sinclair, P. E.; de Vries, A. H.; Sherwood, P.; Catlow, C. R. A.; R. A., v. S. *J. Chem. Soc., Faraday Trans.* **1998**, *94*, 3401.
(34) Clark, L. A.; Sierka, M.; Sauer, J. *J. Am. Chem. Soc.* **2003**, *125*, 2136.
(35) Derouane, E. G.; Chang, C. D. *Microporous Mesoporous Mater.* **2000**, *425*, 35.
(36) Treesukol, P.; Truong, T. N.; Srisuk, K.; Limtrakul, J. *J. Phys. Chem. B* **2005**, *109*, 11940.
(37) Sirijaraensre, J.; Limtrakul, J.; Truong, T. N. *J. Phys. Chem. B* **2005**, *109*, 12099.
(38) Jungsuttiwong, S.; Truong, T. N.; Limtrakul, J. *J. Phys. Chem. B* **2005**, *109*, 13342.
(39) Hillier, I. H. *J. Mol. Struct. (THEOCHEM)* **1999**, *463*, 45.
(40) Sirijaraensre, J.; Limtrakul, J. *ChemPhysChem* **2006**, *7*, 2424.
(41) Ketrat, S.; Limtrakul, J. *Int. J. Quantum Chem.* **2003**, *94*, 333.
(42) Greatbanks, S. P.; Hillier, I. H.; Burton, N. A.; Sherwood, P. *J. Chem. Phys.* **1996**, *105*, 3770.
(43) Limtrakul, J.; Jungsuttiwong, S.; Khongpracha, P. *J. Mol. Struct.* **2000**, *525*, 153.
(44) Treesukol, P.; Lewis, J. P.; Limtrakul, J.; Truong, T. N. *Chem. Phys. Lett.* **2001**, *350*, 128.
(45) Kasuriya, S.; Namuangruk, S.; Treesukol, P.; Tirtowidjojo, M.; Limtrakul, J. *J. Catal.* **2003**, *219*, 320.
(46) Namuangruk, S.; Khongpracha, P.; Tantanak, D.; Limtrakul, J. *J. Mol. Catal. A* **2006**, *256*, 113.
(47) Pantu, P.; Boekfa, B.; Limtrakul, J. *J. Mol. Catal. A* **2007**, *277*, 171.
(48) Pabchanda, S.; Pantu, P.; Limtrakul, J. *J. Mol. Catal. A* **2005**, *239*, 103.
(49) Pantu, P.; Pabchanda, S.; Limtrakul, J. *ChemPhysChem* **2004**, *5*, 1901.
(50) Namuangruk, S.; Khongpracha, P.; Pantu, P.; Limtrakul, J. *J. Phys. Chem. B* **2006**, *110*, 25950.
(51) Namuangruk, S.; Pantu, P.; Limtrakul, J. *ChemPhysChem* **2005**, *6*, 1333.
(52) Jansang, B.; Nanok, T.; Limtrakul, J. *J. Phys. Chem. B* **2006**, *110*, 12626.
(53) Jansang, B.; Nanok, T.; Limtrakul, J. *J. Phys. Chem. C* **2008**, *112*, 540.
(54) Maihom, T.; Namuangruk, S.; Nanok, T.; Limtrakul, J. *J. Phys. Chem. C* **2008**, *112*, 12914.
(55) Panjan, W.; Limtrakul, J. *J. Mol. Struct.* **2003**, *654*, 35.
(56) Raksakoon, C.; Limtrakul, J. *J. Mol. Struct. (THEOCHEM)* **2003**, *631*, 147.
(57) Lomratsiri, J.; Probst, M.; Limtrakul, J. *J. Mol. Graphics Modell.* **2006**, *25*, 219.
(58) Derouane, E. G. *J. Catal.* **1986**, *100*, 541.
(59) Derouane, E. G.; Andre, J. M.; Lucus, A. A. *J. Catal.* **1988**, *110*, 58.
(60) Zicovich-Wilson, C. M.; Corma, A.; Viruela, P. *J. Phys. Chem.* **1994**, *98*, 10863.
(61) Zhao, Y.; Truhlar, D. G. *J. Phys. Chem. C* **2008**, *112*, 6860.
(62) Zhao, Y.; Truhlar, D. G. *Acc. Chem. Res.* **2008**, *41*, 157.
(63) Zhao, Y.; Schultz, N. E.; Truhlar, D. G. *J. Chem. Theory Comput.* **2006**, *2*, 364.
(64) Zhao, Y.; Truhlar, D. G. *Theor. Chem. Acc.* **2008**, *120*, 215.
(65) Stefanovich, E. V.; Truong, T. N. *J. Phys. Chem. B* **1998**, *102*, 3018.
(66) Vollmer, J. M.; Stefanovich, E. V.; Truong, T. N. *J. Phys. Chem. B* **1999**, *103*, 9415.
(67) Jansang, B.; Nanok, T.; Limtrakul, J. *J. Mol. Catal. A* **2006**, *264*, 33.
(68) Sirijaraensre, J.; Limtrakul, J. *Phys. Chem. Chem. Phys.* **2009**, *11*, 578.
(69) Lee, C. C.; Gorte, R. J.; Farneth, W. E. *J. Phys. Chem. B* **1997**, *101*, 3811.
(70) Frisch, M. J.; Trucks, G. W.; Schlegel, H. B.; Scuseria, G. E.; Robb, M. A.; Cheeseman, J. R.; Montgomery, J. A., Jr.; Vreven, T.; Kudin, K. N.; Burant, J. C.; Millam, J. M.; Iyengar, S. S.; Tomasi, J.; Barone, V.; Mennucci, B.; Cossi, M.; Scalmani, G.; Rega, N.; Petersson, G. A.; Nakatsuji, H.; Hada, M.; Ehara, M.; Toyota, K.; Fukuda, R.; Hasegawa, J.; Ishida, M.; Nakajima, T.; Honda, Y.; Kitao, O.; Nakai, H.; Klene, M.; Li, X.; Knox, J. E.; Hratchian, H. P.; Cross, J. B.; Adamo, C.; Jaramillo, J.; Gomperts, R.; Stratmann, R. E.; Yazyev, O.; Austin, A. J.; Cammi, R.; Pomelli, C.; Ochterski, J. W.; Ayala, P. Y.; Morokuma, K.; Voth, G. A.; Salvador, P.; Dannenberg, J. J.; Zakrzewski, V. G.; Dapprich, S.; Daniels, A. D.; Strain, M. C.; Farkas, O.; Malick, D. K.; Rabuck, A. D.; Raghavachari, K.; Foresman, J. B.; Ortiz, J. V.; Cui, Q.; Baboul, A. G.; Clifford, S.; Cioslowski, J.; Stefanov, B. B.; Liu, G.; Liashenko, A.; Piskorz, P.; Komaromi, I.; Martin, R. L.; Fox, D. J.; Keith, T.; Al-Laham, M. A.; Peng, C. Y.; Nanayakkara, A.; Challacombe, M.; Gill, P. M. W.; Johnson, B.; Chen, W.; Wong, M. W.; Gonzalez, C.; Pople, J. A. *Gaussian 03*, revision B.05; Gaussian, Inc.: Pittsburgh, PA, 2003.
(71) Blaszkowski, S. R.; van Santen, R. A. *J. Phys. Chem.* **1995**, *99*, 11728.
(72) Blaszkowski, S. R.; van Santen, R. A. *J. Am. Chem. Soc.* **1996**, *118*, 5152.

(73) Blaszkowski, S. R.; van Santen, R. A. *J. Am. Chem. Soc.* **1997**, *119*, 5020.

(74) Solans-Monfort, X.; Sodupe, M.; Mo, O.; Yanez, M.; Elguero, J. *J. Phys. Chem. B* **2005**, *109*, 19301.

(75) Blaszkowski, S. R.; van Santen, R. A. *J. Phys. Chem. B* **1997**, *101*, 2292.

(76) Zicovich-Wilson, C. M.; Viruela, P.; Corma, A. *J. Phys. Chem.* **1995**, *99*, 13224.

(77) Geerlings, P.; Vos, A. M.; Schoonheydt, R. A. *J. Mol. Struct. (THEOCHEM)* **2006**, *762*, 69.

(78) Boronat, M.; Zicovich-Wilson, C. M.; Viruela, P.; Corma, A. *J. Phys. Chem. B* **2001**, *105*, 11169.

(79) Rozanska, X.; Demuth, T.; Hutschka, F.; Hafner, J.; van Santen, R. A. *J. Phys. Chem. B* **2002**, *106*, 3248.

(80) Namuangruk, S.; Pantu, P.; Limtrakul, J. *J. Catal.* **2004**, *225*, 523.

(81) Boronat, M.; Viruela, P. M.; Corma, A. *J. Am. Chem. Soc.* **2004**, *126*, 3300.

(82) Boronat, M.; Corma, A. *Appl. Catal., A: General* **2008**, *336*, 2.

(83) Bhan, A.; Joshi, Y. V.; Delgass, W. N.; Thomson, K. T. *J. Phys. Chem. B* **2003**, *107*, 10476.

JP809746A

Mechanistic Investigation on 1,5- to 2,6-Dimethylnaphthalene Isomerization Catalyzed by Acidic β Zeolite: ONIOM Study with an M06-L Functional

Chawanwit Kumsapaya,[†,‡] Karan Bobuatong,[†,‡] Pipat Khongpracha,[†,‡] Yuthana Tantirungrotechai,[§] and Jumras Limtrakul*[,†,‡]

Laboratory for Computational and Applied Chemistry, Chemistry Department, Faculty of Science, Kasetsart University, Bangkok 10900, NANOTEC Center of Excellence, National Nanotechnology Center (NANOTEC), Kasetsart University Research and Development Institute, Bangkok 10900, and NANOTEC, National Science and Technology Development Agency, Khongluang, Pathumthani 12120, Thailand

Received: May 3, 2009; Revised Manuscript Received: July 3, 2009

The isomerization of 1,5- to 2,6-dimethylnaphthalene (DMN) over β zeolite has been investigated by applying a newly developed density functional named M06-L, incorporated into the ONIOM scheme: M06-L/6-31G(d,p): UFF. Two consecutive reaction mechanisms over the extended zeolite framework have been carefully examined: the 1,5- to 1,6-DMN isomerization followed by the 1,6- to 2,6-DMN isomerization. Both catalytic processes take place via the same mechanism. The isomerization process starts from the protonation of the DMN step, creating the naphthalynic carbocation. Subsequently, the intramolecular methyl shift occurs from the α-position to the adjacent β-position of the naphthalynic carbocation. In the final step, the anionic zeolite framework takes a proton away from the naphthalynic carbocation, yielding a desired 1,6-DMN or 2,6-DMN molecule. The methyl migrations are the rate-determining steps and require activation barriers of 25.69 and 21.05 kcal/mol for the 1,5- to 1,6-DMN and 1,6- to 2,6-DMN processes, respectively. The calculated reaction profiles are in agreement with the experimental prediction that the 1,5- to 1,6-DMN isomerization is the kinetically controlled step. The results in this study show the excellent performance of a combination of the newly developed functional and the confinement effect represented by the universal force field (M06-L/6-31G(d,p): UFF) for investigating the transformations of aromatic species in the zeolite system.

Introduction

Polyethylene naphthalate (PEN) is a thermoplastic polyester which shows very good gas barrier, mechanical, thermal, and electrical properties. These properties are indicative of promising innovative applications such as high-performance fibers and films and novel packaging, e.g., plastic beer bottles.[1−3] The current production process involves the condensation polymerization of ethylene glycol and dimethyl 2,6-napthalenedicarboxylate (2,6-NDC). The 2,6-NDC is in turn prepared from 2,6-dimethylnaphthalene (2,6-DMN).[4] However, the low availability and high production cost of 2,6-DMN result in the price of PEN being higher than that of polyethylene terephthalate (PET).[4] These, unfortunately, limit the successful commercialization of PEN, even though it shows superior properties in comparison with the widely used PET polymer. Current large-scale production (30 kton/year) of 2,6-DMN is made by BP-Amoco using its patented process. The employed process based on butadiene and *o*-xylene involves four subsequent reaction stages in four separate reactors: alkylation, cyclization, dehydrogenation, and finally catalytic isomerization from 1,5- to 2,6-DMN.[2,5] The 1,5- to 2,6-DMN isomerization step is thought to be a limiting step which leads to the low availability and the high cost of 2,6-DMN.[6] Although there are some available reports concerning the detailed investigation of this limiting step, there is no study that provides sufficient information on this reaction at the molecular level.[2,6−8] A better understanding of this reaction at the molecular level which would help increase the yield of 2,6-DMN is crucial for the improvement of the 2,6-DMN production process, hence lowering the cost of 2,6-DMN and also of PEN production.

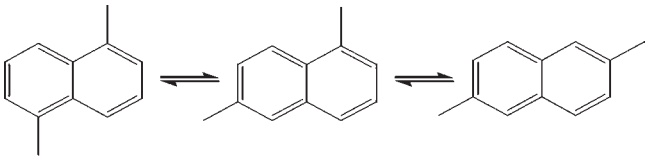

Figure 1. Isomerization reaction of 1,5-DMN to 2,6-DMN proceeding via an intramolecular 1,2-methyl shift.

The isomerization of 1,5-DMN to a more profitable 2,6-DMN molecule occurs via the intramolecular 1,2-methyl shift; i.e., the methyl group migrates one at a time from the α-position to the β-position (see Figure 1).[9−11] The intramolecular 1,2-methyl shift is widely recognized as a key mechanistic step in the rearrangements of methylbenzenes, trimethylbenzenes, tetramethylbenzenes,[9,10] methylnaphthalenes, and dimethylnaphthalenes. From the isomer distribution at the thermodynamic equilibrium sets,[1,11,12] the shift of a methyl group from the α-position to the β-position of the naphthalene nucleus in the same ring is observed to be facile. A single methyl shift of 1,5-DMN leads to 1,6-DMN. A further methyl shift of 1,6-DMN leads to 2,6-DMN. The reaction can be promoted by both Lewis and Brønsted acids. Thus, catalysts such as $BF_3 \cdot HF$ and zeolite can be used to speed up the reaction and, therefore, reduce the cost of the 2,6-DMN production.

When new "green chemistry" industrial processes are being developed, the heterogeneous catalyst is considered more

[†] Faculty of Science, Kasetsart University.
[‡] Kasetsart University Research and Development Institute.
[§] National Science and Technology Development Agency.

10.1021/jp904098t CCC: $40.75
Published on Web 08/17/2009

favorable than its homogeneous counterpart. Zeolite is a unique choice of catalyst for this purpose. Its porous structure can provide specific pathways to desirable products. Several zeolites are candidates for catalyzing this isomerization reaction.[4] Recently, Kraikul et al. conducted a catalytic activity test of three zeolites, H-β, H-mordenite, and H-ZSM-5, on the isomerization of 1,5-DMN to 2,6-DMN.[6] Among the tested catalysts, the H-β zeolite was found to be the best catalyst which provided the highest yield of 2,6-DMN. They observed that no 2,6-DMN was detected when using H-ZSM-5 as a catalyst under the testing condition. This finding demonstrates the framework selectivity of zeolitic materials. Millini et al. conducted a molecular dynamics simulation to estimate the diffusional energy barrier of DMN in zeolites.[13] The H-ZSM-5 pore structure has a very high diffusional energy barrier, rendering it difficult for DMN to move in and out of the framework. For H-mordenite and H-β zeolite, the diffusional energy barriers are much less than that of H-ZSM-5. For the porous systems considered, the diffusivity of the DMN isomer is in the order 2,6-DMN > 1,6-DMN > 1,5-DMN.[13]

At 265 °C, when using H-β zeolite as the catalyst to isomerize 1,5-DMN, the equilibrium composition of 1,5-DMN:1,6-DMN:2,6-DMN is 9.33:43.52:47.16, respectively. The percentage of 2,6-DMN is greater than that of 1,6-DMN. An analysis of the reaction quotient at 1 h and the equilibrium constant led Kraikul et al. to conclude that the 1,5- to 1,6-DMN isomerization is the kinetically limiting step for the 1,5- to 2,6-DMN conversion process.[6] However, no chemical kinetics parameter can be deduced from their study. On the other hand, Suld and Stuart studied the isomerization kinetics of several di- and monomethylnapthalenes catalyzed by $BF_3 \cdot HF$.[11] For a set of 2,6-DMN, 1,6-DMN, and 1,5-DMN molecules, they deduced the rate of isomerization to be in the temperature range of 20−50 °C. Assuming the reversible first-order kinetics, the activation energies for the 2,6- to 1,6-DMN and the 1,6- to 1,5-DMN steps were estimated to be 20.1 ± 1 and 20.3 ± 1 kcal/mol, respectively.

To our knowledge, there is no report on the activation energy of this reaction catalyzed by heterogeneous catalysts, zeolite in particular, available in the literature. In addition, although the isomerization from 1,5-DMN into 2,6-DMN over the heterogeneous catalysts is known to occur with two single methyl shift steps, the reaction mechanism has not been investigated in detail. In this paper, we report a detailed reaction mechanism of 1,5- to 2,6-DMN isomerization catalyzed by acidic β zeolite by means of the hybrid quantum mechanics/molecular mechanics (QM/MM) approach.

Computational Methods and Material Models

Computational Methods. Quantum chemical calculation is accepted nowadays by practical chemists as a very useful tool to provide insights into reaction mechanisms at the molecular level.[14] It is the only practical way to comprehend the transition states and intermediates of a complex reaction. The density functional theory (DFT) is by far the most common choice of method for chemical applications. As one deals with complex reactions taking place in a heterogeneous catalyst of infinite size, a certain approach is required to incorporate the framework effect while keeping the computational cost as low as possible. A periodic DFT is a straightforward approach, but it is very computationally demanding.[15] The typical zeolites, such as ZSM-5 and β zeolite, possess hundreds of atoms per unit cell, making a periodic calculation too expensive to be employed for these systems. At the other extreme, a bare cluster calculation, taking only the catalytic active site and the reactants, ignores all of the framework effect. A practical approach is one that incorporates the framework effect on the chemically active region in some approximate way. Examples are the embedded cluster or a combined quantum mechanics/molecular mechanics (QM/MM) approach,[16−20] as well as the more general ONIOM (our-Own-N-layered-Integrated molecular Orbital and molecular Mechanics) method.[21−27] We adopted the ONIOM approach in this work. Several reports by our groups indicate its good performance on modeling the adsorption and reaction mechanism in zeolite.[28−38]

The ONIOM scheme we adopted consists of an inner layer of the active region calculated by the M06-L/6-31G(d,p) level and a large outer layer of the framework calculated by the universal force field (UFF). The M06-L functional, as developed by the Minnesota group,[39] uses the meta generalized gradient approximation in which the density functional includes the spin densities gradient and spin kinetic energy densities and their reduced gradient.[39−41] This local functional allows the use of density fitting algorithms and plane wave algorithms that require much less computational effort than the best algorithms for the nonlocal functional; thus, it is preferred for practical computations on large systems.[41] All calculations were performed by using the Gaussian 03 code[42] incorporated with the Minnesota density functionals module 3.1 by Yan Zhao and Donald G. Truhlar.

Material Models. The extended 120T cluster, covering the active region, of the H-β zeolite is used to represent the Brønsted acid site and the zeolite framework in this investigation. This was taken from the H-β zeolite crystal lattice structures.[43,44] It includes the 12-membered ring (12MR) representing the main gateway to the intersection of two perpendicular 12MR channel systems, where the reactions normally take place (see Figure 2b). A silicon atom at a T5 position in the β zeolite is substituted by an aluminum atom. A proton is added to the bridging oxygen atoms bonded directly to the aluminum atom, conventionally called the O5 position but is designated as the O1 position in this study.[43]

In the ONIOM model, an inner layer consists of a 14T cluster including the 12-membered ring and the other two Si atoms around the Al atom and the DMN molecules. The DFT treatment in this region accounts for the interactions of the adsorbates with the Brønsted acid site of the β zeolite. A large outer layer consists of the remainder of the extended framework up to 120T. This layer takes the confinement of the extended zeolite structure and the effect of the framework into account. The UFF that is selected to represent the effect in this layer also accounts for the van der Waals interaction.[45] This interaction is the dominant contribution for adsorption−desorption mechanisms in zeolites.[45−48] During optimization, only the 5T region [$(\equiv SiO)_3Al(OH)Si\equiv$] was allowed to relax while the rest of the model was fixed along the crystallographic coordinates.

From our previous work,[49] attempts have been made to demonstrate that the geometries of reaction intermediates in the zeolite system do not influence the results. Several test calculations on zeolite models have been performed using different zeolite models: 5T, 12T, 34T, 46T, and 128T QM clusters. It was found that some important structural parameters (e.g., O1−Hz and Al···Hz) are insignificantly different on those five zeolite models. The estimates for the geometry error of the method are 0.966 ± 0.001 A for O1−Hz and 2.364 ± 0.02 Å for Al···Hz. From these findings, one could propose that the 14T QM size is reliable enough in the ONIOM model for studying such a complicated reaction mechanism in the bulk

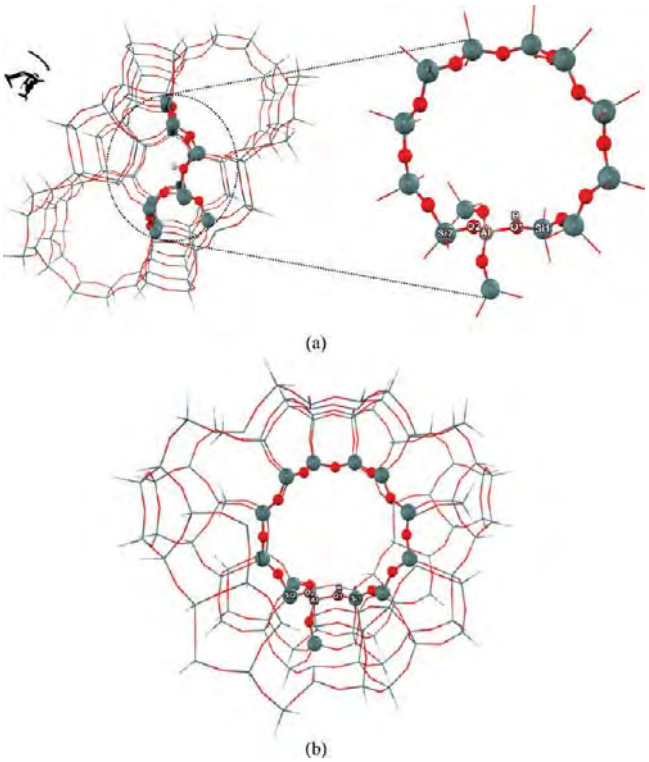

Figure 2. Extended 120T cluster model of H-β zeolite considered in this study. (a) The oval dashed line encloses an intersection of two perpendicular 12-membered ring (12MR) channel systems which serves as a nanoreactor. The ball-and-stick graphics represent the 14T active region including the main gateway to a channel intersection of H-β zeolite (12MR) where the DMN isomerization takes place. (b) View along the main channel.

catalytic system. Furthermore, to improve the energetic properties and take into account the whole zeolite framework effect, single-point energy calculations at a high level of theory on the prior optimized structures by the ONIOM method have been performed to cover the drawbacks of ONIOM models observed via the so-called *S* values,[50] being in the range of 0.00826−0.01864 au for the adsorption energy (see Table S2 of the Supporting Information). The adsorption energy computed from M06-L/6-31g(d,p) single-point calculations of 120T extended along the reaction coordinate at the ONIOM(M06-L/6-31G(d,p):UFF) optimized structures has been found to provide a good description of dispersion interactions and is also in agreement with the experimental data.[51] Consequently, the use of the 120T M06-L/6-31G(d,p)//14T ONIOM(M06-L/6-31G(d,p):UFF) approach seems to be a good strategy to model this system (see Figure 10).

The isomerization reaction from 1,5-DMN to 2,6-DMN is shown in Figure 3. This reaction mechanism is proposed on the basis of the 1,2-methyl shift in methylbenzene and dimethylnaphthalene catalyzed by acid solution.[9,11] It involves successive intramolecular 1,2-methyl shift reactions from 1,5-DMN to 1,6-DMN and finally to 2,6-DMN. Each reaction is basically a shift of a single methyl group from the α- to the β-position that is catalyzed by the acidic proton. We do not consider the situation in which the shift of two methyl groups takes place simultaneously since it is unlikely to find two acidic protons at the right position. Each reaction begins with the adsorption of DMN on the Brønsted acid site followed by the protonation, methyl shift, and proton back-donation to become the neutral adsorbed product. The geometry optimizations were performed on all important species along the reaction coordinate. These include the isolated reactant, adsorbed reactant, intermediate, transition state, adsorbed product, and isolated product.

Results and Discussion

Reaction Mechanism of 1,5- to 1,6-DMN Isomerization. Figure 3a summarizes the reaction mechanism of 1,5- to 1,6-DMN isomerization. In this mechanism, the 1,5-DMN molecule is first adsorbed at the Brønsted acid site of the acidic β zeolite. Then the adsorbed 1,5-DMN complex is protonated to form a σ-complex (Int_1). This is followed by the intramolecular methyl shift between the adjacent C5 and C6 positions. This results in the formation of a new σ-complex (Int_2) which donates a proton back to the zeolite framework, yielding the 1,6-DMN molecule in the adsorbed state (Prod_1). The following subsections describe the structural and energetic information for each step of the 1,5- to 1,6-DMN isomerization.

Protonation of the 1,5-DMN Adsorption Complex. The optimized geometric parameters of species in the 1,5-DMN protonation step are documented in Table S2 of the Supporting Information. The C5−C6 and C6−H2 bond lengths of the isolated 1,5-DMN are 1.379 and 1.088 Å, respectively. These bond lengths compare well with the corresponding experimental bond lengths of benzene of 1.397 and 1.084 Å, respectively. The adsorption mode takes place with the C5−C6 double bond interacting with the acidic proton (H1) with C5−H1 and C6−H1 distances of 2.901 and 2.576 Å, and the O1−H1 bond length increases from 0.967 to 0.980 Å (see Table S2 and Figure 4). The 1,5-DMN molecule shows few structural changes. The 1,5-DMN molecule was slightly perturbed by the zeolite cavity when adsorbed at the Brønsted acid site. The C5−C6 double bond lengthens only slightly by 0.005 Å. No change is observed in the C6−H2 bond length. Furthermore, this weak interaction does not significantly perturb the zeolite structure. Compared with the isolated zeolite, the Al−O1, Al−O2, and Si2−O2 bond distances are decreased only by 0.005, 0.004, and 0.009 Å, respectively, while the Si1−O1 bond distance is increased only by 0.002 Å. The Si1−O1−Al bond angle decreases by 2.4°, whereas the Si2−O2−Al bond angle increases by 2.0°.

The adsorption energy of 1,5-DMN is computed to be −22.13 kcal/mol. There is, unfortunately, no report of an experimental adsorption energy of this molecule in the literature. Nevertheless, this value is in accord with the experimental adsorption energy of −20.4 kcal/mol for the adsorption of ethylbenzene[51] in H-Y zeolites. Our calculated adsorption energy for the 1,5-DMN molecule is larger than the experimental report for ethylbenzene. This is due to the fact that 1,5-DMN is a more basic molecule than the ethylbenzene molecule. Therefore, the adsorption energy of 1,5-DMN on a highly acidic β zeolite should be larger than that of ethylbenzene adsorbed on a less acidic H−Y zeolite. These results show that the 120T M06-L/6-31G(d,p)//14T ONIOM(M06-L/6-31G(d,p):UFF) model is reasonable for investigating the interactions between the adsorbate and the zeolite catalyst.

In the next step, the protonation of the adsorbed 1,5-DMN complex, Ads_1, takes place at the C5 position. A new σ-bond is formed, and the original conjugation is disrupted. Figure 4 shows the calculated energy profile for the protonation step. Selected geometric parameters of the transition state and the intermediate of the first part of the isomerization are tabulated in Table S2 of the Supporting Information. The protonated 1,5-DMN is in the form of a carbenium ion in which the positive charge can delocalize over the remaining five carbon atoms of a benzene ring in DMN. At the transition state, TS_1, the zeolite proton moves toward a carbon atom of 1,5-DMN as evidenced

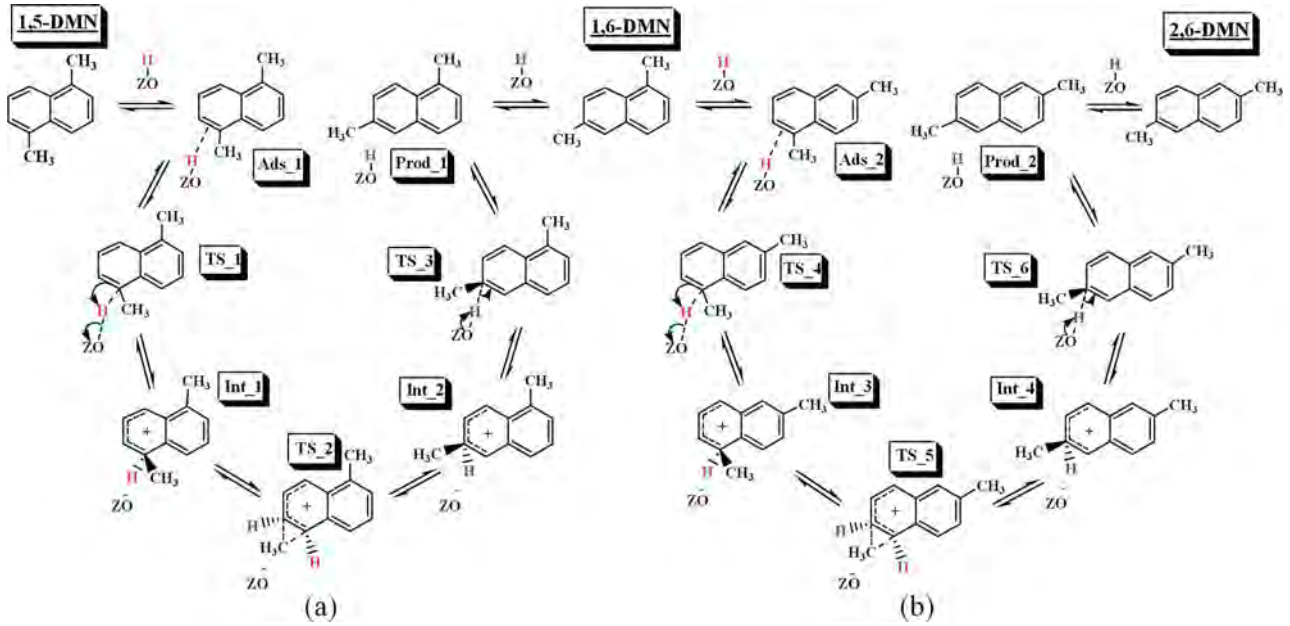

Figure 3. Reaction mechanism of (a) the 1,5- to 1,6-DMN and (b) the 1,6- to 2,6-DMN isomerizations over H-β zeolite. Schematically they consist of protonation, methyl shift, and proton back-donation of the adsorbed species.

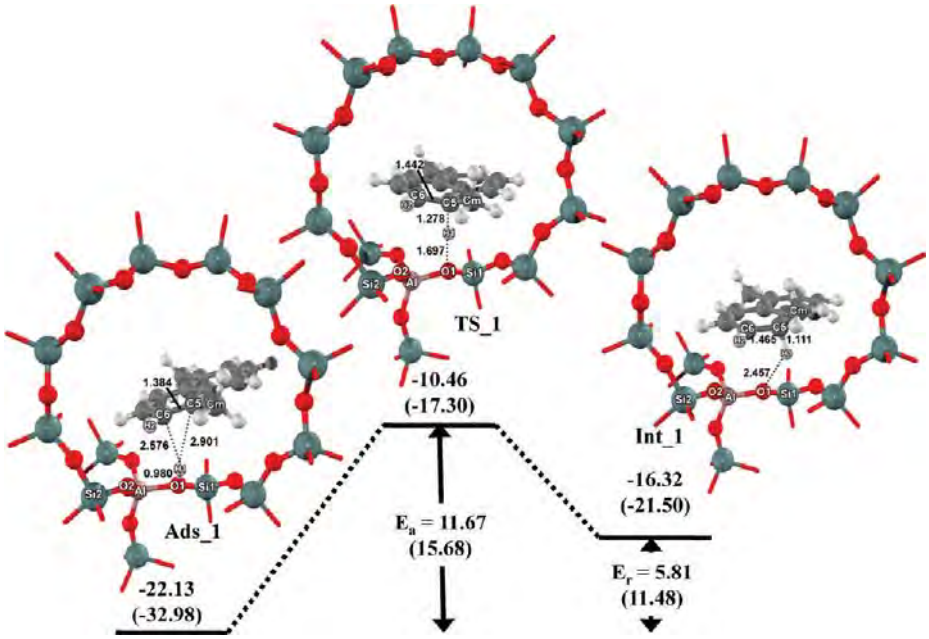

Figure 4. 120T M06-L/6-31G(d,p)//14T ONIOM(M06-L/6-31G(d,p):UFF) energy profile (kcal/mol) for the protonation step of the 1,5- to 1,6-DMN isomerization over H-β zeolite. The sum of isolated 1,5-DMN and 120T zeolite cluster energies is taken as a reference. The values in parentheses are calculated at 14T ONIOM(M06-L/6-31G(d,p):UFF). Only DMN and the 14T active region are displayed.

by a great reduction of the C5−H1 distance from 2.901 to 1.278 Å. The O1−H1 and C5−C6 bond lengths are also elongated by 0.717 and 0.058 Å with respect to those of the Ads_1 complex. It is then transformed to a stabilized intermediate, Int_1. This dimethylnaphthalenonium ion is stabilized by the resonance energy of the intact benzenoid nucleus.[11]

The energy barrier for the protonation is 11.67 kcal/mol, and the corresponding reaction energy is endothermic by 5.81 kcal/mol. The formation of the σ-bonded complex is accompanied by the structural changes of the zeolite. The Al−O1, Si1−O1, and Si2−O2 bond distances are decreased by 0.091, 0.069, and 0.009 Å, respectively, whereas the Al−O2 bond distance increases by 0.020 Å. The Si2−O2−Al angle increases by 3.3° compared with those of the adsorbed 1,5-DMN (Ads_1). We observe that the geometry of the transition state, TS_1, is more similar to that of Int_1 than to that of Ads_1. This results in the reaction tendency to proceed with the forward direction to the methyl shift step (cf Table S2 of the Supporting Information).

Methyl Shift Step of Protonated 1,5-DMN. The reversible intramolecular 1,2-methyl shift moves a methyl group from the α-position to the adjacent β-position. With reference to Figure 5, this is the formation of a second intermediate (Int_2) from the first intermediate (Int_1). The selected geometrical parameters of Int_1, the transition state (TS_2), and Int_2 are reported in Table S3 (Supporting Information), while the reaction profile is illustrated in Figure 5. The TS_2 transition structure has the shifting methyl group located in between with a C5−*Cm*−C6 bond angle of 45.4° and a C5−C6 bond distance of 1.412 Å. At this unstable tricentric transition state, the methyl group is moving slightly toward the C6 carbon atom with *Cm*−C5 and

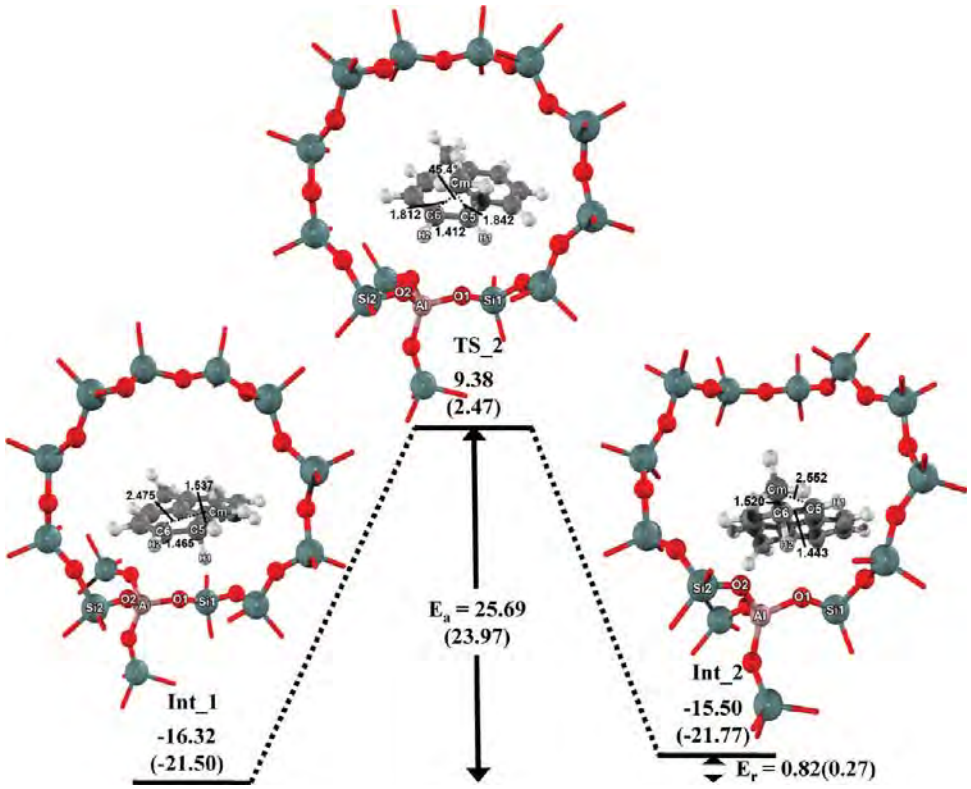

Figure 5. 120T M06-L/6-31G(d,p)//14T ONIOM(M06-L/6-31G(d,p):UFF) energy profile (kcal/mol) for the methyl shift of the 1,5- to 1,6-DMN isomerization over H-β zeolite.

Cm−C6 distances of 1.842 and 1.812 Å, respectively. In the Int_2 structure, a *Cm*−C6 bond of 1.520 Å is formed. This process causes rather insignificant perturbation on the zeolitic structure (see Table S3). The Al−O1, Al−O2, and Si2−O2 bond lengths are increased by 0.005, 0.006, and 0.004 Å, respectively, while the Si1−O1 bond length is decreased by 0.002 Å. The Si1−O1−Al bond angle increases by 0.4° and the Si2−O2−Al bond angle decreases by 1.8° with respect to those of Int_1.

The calculated binding energy of Int_2 is −15.50 kcal/mol (see Figure 5). This is slightly less stable than that of Int_1 by 0.82 kcal/mol. Therefore, the reaction energy is almost thermoneutral. This may be attributed to the reduction of steric hindrance between the methyl group in the naphthalene ring and the zeolitic pore. The activation energy for the 1,5- to 1,6-DMN methyl migration step is 25.69 kcal/mol. This actually compares well with the reported experimental activation energy of 20.3 ± 1 kcal/mol of Suld and Stuart.[11]

Proton Back-Donation to the Zeolite Framework. The final stage of the 1,5- to 1,6-DMN isomerization involves the proton back-donation from Int_2 to the zeolite framework. This leads to the 1,6-DMN molecule adsorbed on the Brønsted acid site. Figure 6 shows the energy profile for this step and the geometric parameters of all species involved: Int_2, the transition state (TS_3), and adsorbed 1,6-DMN (Prod_1) are documented in Table S4 of the Supporting Information. The H2 atom of Int_2 is transferred from C6 back to the active oxygen O1 site of the zeolite framework to form adsorbed 1,6-DMN. This is accompanied by an increase of the C6−H2 distance from 1.213 Å in TS_3 to 2.528 Å in Prod_1 and a decrease of the O1−H2 distance from 1.765 Å in TS_3 to 0.988 Å in Prod_1. The TS_3 transition-state configuration is very similar to that of Int_2. This proton back-donation occurs very fast as evidenced by the predicted energy barrier being only 2.64 kcal/mol. The reaction energy for this step is exothermic by 12.95 kcal/mol. This indicates that the proton prefers to sit on the zeolite framework.

The proton back-donation process has a slight impact on the zeolite framework. With reference to the Int_2 configuration, the Al−O1, Si1−O1, and Si2−O2 bond distances increase by 0.012, 0.009, and 0.001 Å, respectively, while the Al−O2 bond distance and the Si1−O1−Al and Si2−O2−Al bond angles are decreased by 0.005 Å, 0.5°, and 0.4°, respectively. The back-transferred proton forms a chemical bond with the O1 atom with a distance of 0.988 Å. The C6−H2 and C5−H2 bond distances of the adsorbed product are 2.528 and 2.252 Å, respectively. The C5−C6 bond is shortened to 1.384 Å, which resembles the double bond. Finally, a desorption energy of 28.36 kcal/mol is required to remove the 1,6-DMN product from the Brønsted acid site (see Figure 6).

The energy profile for all steps of the 1,5- to 1,6-DMN isomerization is summarized in Figure 10a (see also Table 1). The results show that the rate-determining step of the isomerization from 1,5- to 1,6-DMN is the methyl shift step. This step has the highest activation energy of 25.69 kcal/mol compared with 11.67 and 2.64 kcal/mol for the protonation and the proton back-donation steps. These results are in good agreement with the experimental observation in which the acid-catalyzed intramolecular 1,2-methyl shift is the rate-determining step for this isomerization with an activation energy of 20.3 kcal/mol.[11]

Reaction Mechanism of 1,6- to 2,6-DMN Isomerization. The reaction mechanism of 1,6- to 2,6-DMN isomerization is outlined in Figure 3. Once 1,5-DMN is converted to 1,6-DMN, the 1,6-DMN molecule isomerizes further to become 2,6-DMN over the same Brønsted acid site of the β zeolite catalyst. However, 1,6-DMN must orientate itself inside the pore and point another methyl group at the α-position toward the acidic proton for the reaction to occur. The considered mechanism

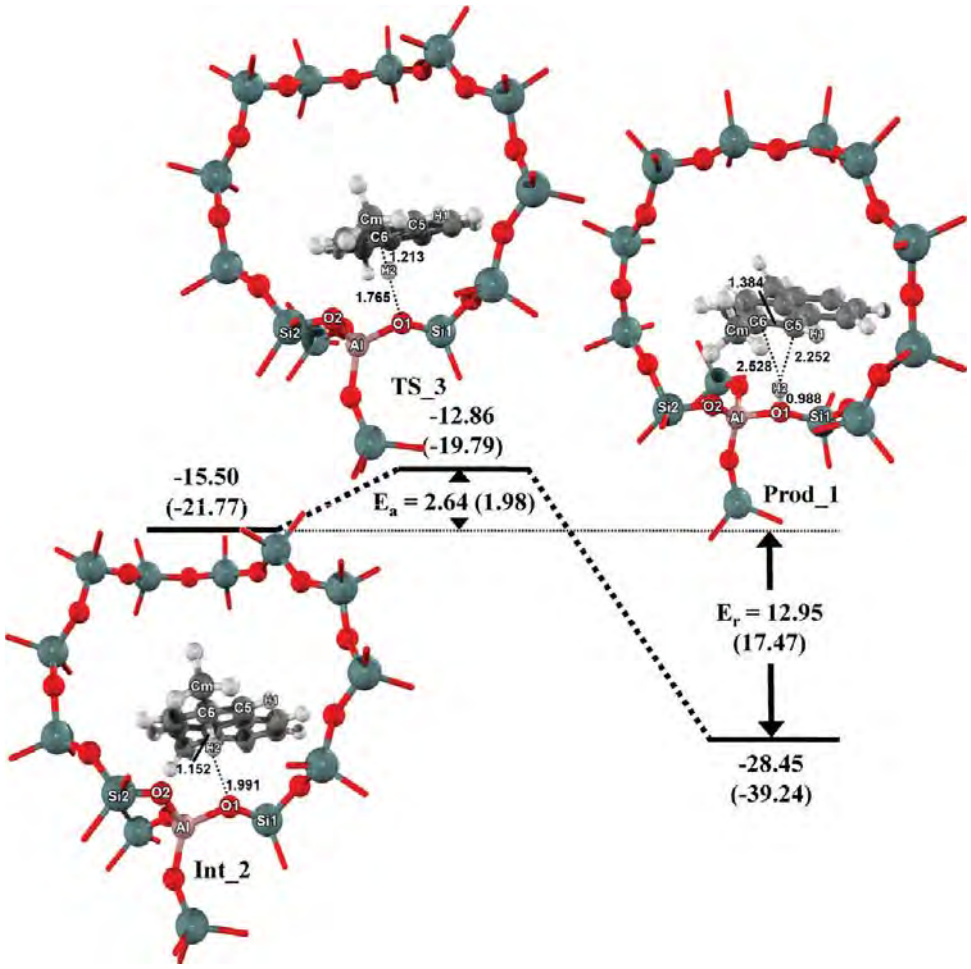

Figure 6. 120T M06-L/6-31G(d,p)//14T ONIOM(M06-L/6-31G(d,p):UFF) energy profile (kcal/mol) for the proton back-donation step of the 1,5- to 1,6-DMN isomerization over H-β zeolite.

TABLE 1: Summary of the 14T ONIOM(M06-L/6-31G(d,p):UFF) and 120T M06-L/6-31G(d,p) Energies of the Important Species along the Reaction Coordinate of the 1,5- to 2,6-DMN Isomerization over H-β Zeolite (See Figure 10)[a]

complex	ONIOM(M06-L/6-31G(d,p):UFF)	M06-L/6-31G(d,p)
Ads_1	−32.98	−22.13
TS_1	−17.30	−10.46
Int_1	−21.50	−16.32
TS_2	2.47	9.38
Int_2	−21.77	−15.50
TS_3	−19.79	−12.86
Prod_1	−39.24	−28.45
Ads_2	−33.12	−21.43
TS_4	−18.36	−11.37
Int_3	−20.44	−13.90
TS_5	0.44	7.14
Int_4	−23.13	−16.89
TS_6	−19.45	−12.95
Prod_2	−38.78	−27.72

[a] The 120T M06-L/6-31G(d,p) energies reported are the single-point energies at the ONIOM(M06-L/6-31G(d,p):UFF)-optimized structures.

begins with the adsorption of orientated 1,6-DMN over the acid site (Ads_2). Then the acidic proton is transferred to form the σ-complex (Int_3) followed by the intramolecular 1,2-methyl shifts from the adjacent C_α to C_β positions. This step leads to a new σ-complex (Int_4) which can transfer a proton back to the zeolite framework, yielding the adsorbed 2,6-DMN (Prod_2). Finally the adsorbed 2,6-DMN desorbs from the zeolite framework to become an isolated 2,6-DMN molecule.

Protonation of the 1,6-DMN Adsorption Complex. Within a β micropore, the 1,6-DMN molecule orientates its α-methyl group toward a Brønsted proton at the 12-membered ring channel intersection. The adsorbed complex Ads_2 has its geometric parameters given in Table S5 of the Supporting Information. The C1−C2 double bond of the 1,6-DMN molecule interacts with the acidic proton (H3) with C1−H3 and C2−H3 distances of 3.272 and 3.528 Å. Upon adsorption, the Brønsted O1−H3 bond is weakened with the bond length lengthened by 0.005 Å. The structure of the β zeolite is slightly perturbed upon interacting with 1,6-DMN. With reference to the isolated zeolite framework, the Al−O1 and Si1−O1 bond distances increase by 0.837 and 0.006 Å, respectively, as the Si2−O2−Al bond angle is increased by 1.4°. The Al−O2 and Si2−O2 bond distances are decreased by 0.156 and 0.087 Å, respectively, and the Si1−O1−Al bond angle is decreased by 1.7°.

The calculated adsorption energy for the adsorbed 1,6-DMN complex prior to isomerization is −21.43 kcal/mol. This is close to the −22.13 kcal/mol energy of 1,5-DMN and approximately close to the −20.4 kcal/mol energy of ethylbenzene[51] in H-Y zeolite. The adsorbed 1,6-DMN complex, Ads_2, is protonated to initiate the second isomerization. The protonation step leads to dimethylnaphthalenonium ion (Int_3) via the transition state (TS_4). For this transition-state (TS_4) configuration, the C1−H3 bond distance is significantly decreased from 3.272 to 1.222 Å, as the O1−H3 and C1−C2 bond distances increase by 0.955 and 0.073 Å, respectively. The TS_4 transition state has its structure closer to that of Int_3 than to that of Ads_2

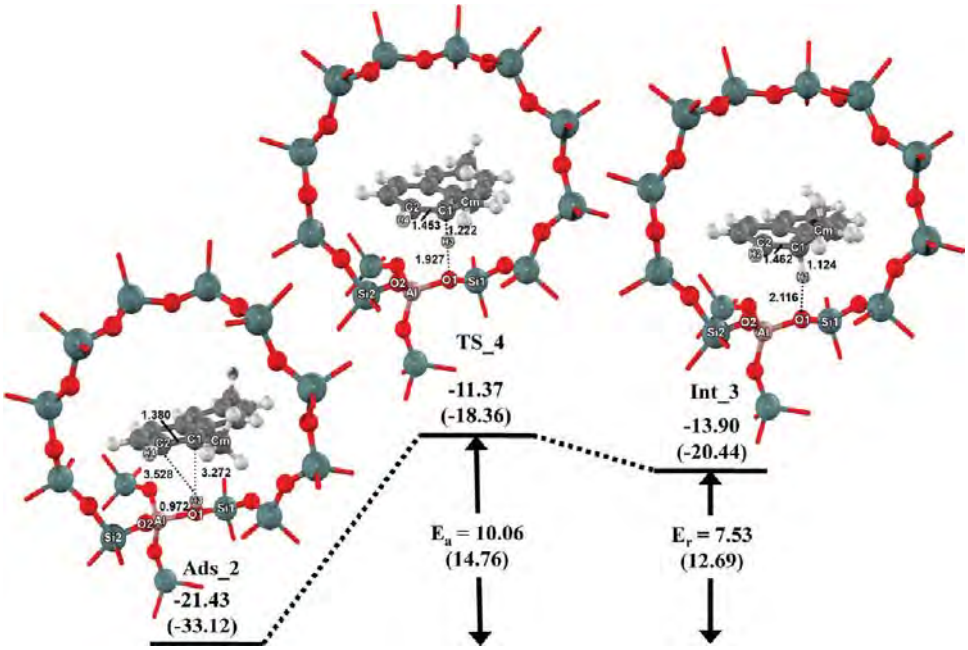

Figure 7. 120T M06-L/6-31G(d,p)//14T ONIOM(M06-L/6-31G(d,p):UFF) energy profile (kcal/mol) for the protonation step of the 1,6- to 2,6-DMN isomerization over H-β zeolite. The sum of isolated 1,6-DMN and 120T zeolite cluster energies is taken as a reference. The values in parentheses are calculated at 14T ONIOM(M06-L/6-31G(d,p):UFF). Only DMN and the 14T active region are displayed.

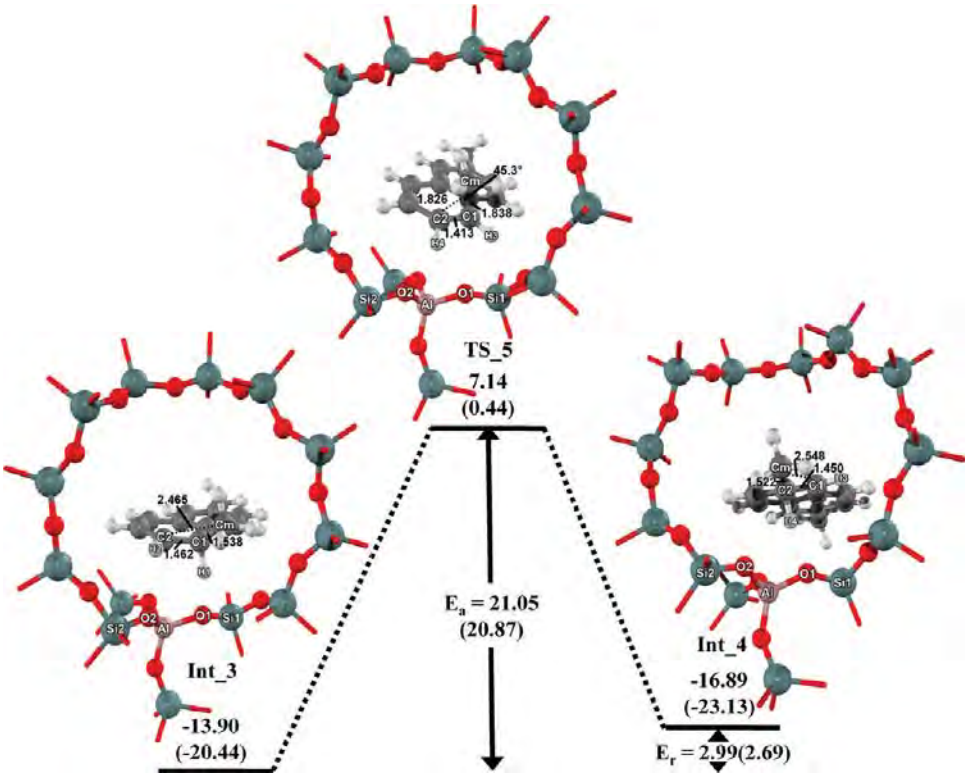

Figure 8. 120T M06-L/6-31G(d,p)//14T ONIOM(M06-L/6-31G(d,p):UFF) energy profile (kcal/mol) for the methyl shift step of the 1,6- to 2,6-DMN isomerization over H-β zeolite.

(see Figure 7 and Table S5, Supporting Information). The activation energy for the protonation step is 10.06 kcal/mol, and the reaction energy is endothermic by 7.53 kcal/mol. In comparison with the protonation step in the earlier reaction, the protonation step of Ads_2 takes up less energy than that of Ads_1 because of the steric hindrance inside the zeolite of the two methyl groups at the α-positions of 1,5-DMN.[13]

Methyl Shift Step of Protonated 1,6-DMN. The formation of the fourth intermediate (Int_4) via the intramolecular 1,2-methyl shift follows the protonation step. The optimized geometric parameters of all species in this step, Int_3, transition state (TS_5), and Int_4, are reported in Table S6 of the Supporting Information together with the reaction profile shown in Figure 8. This step shares common features with the methyl shift step of the 1,5- to 1,6-DMN isomerization. At the TS_5 transition state, the *Cm*−C1 distance increases from 1.538 to 1.838 Å, while the *Cm*−C2 distance decreases from 2.465 to 1.826 Å. The tricentric transition state also has a C1−C2 bond

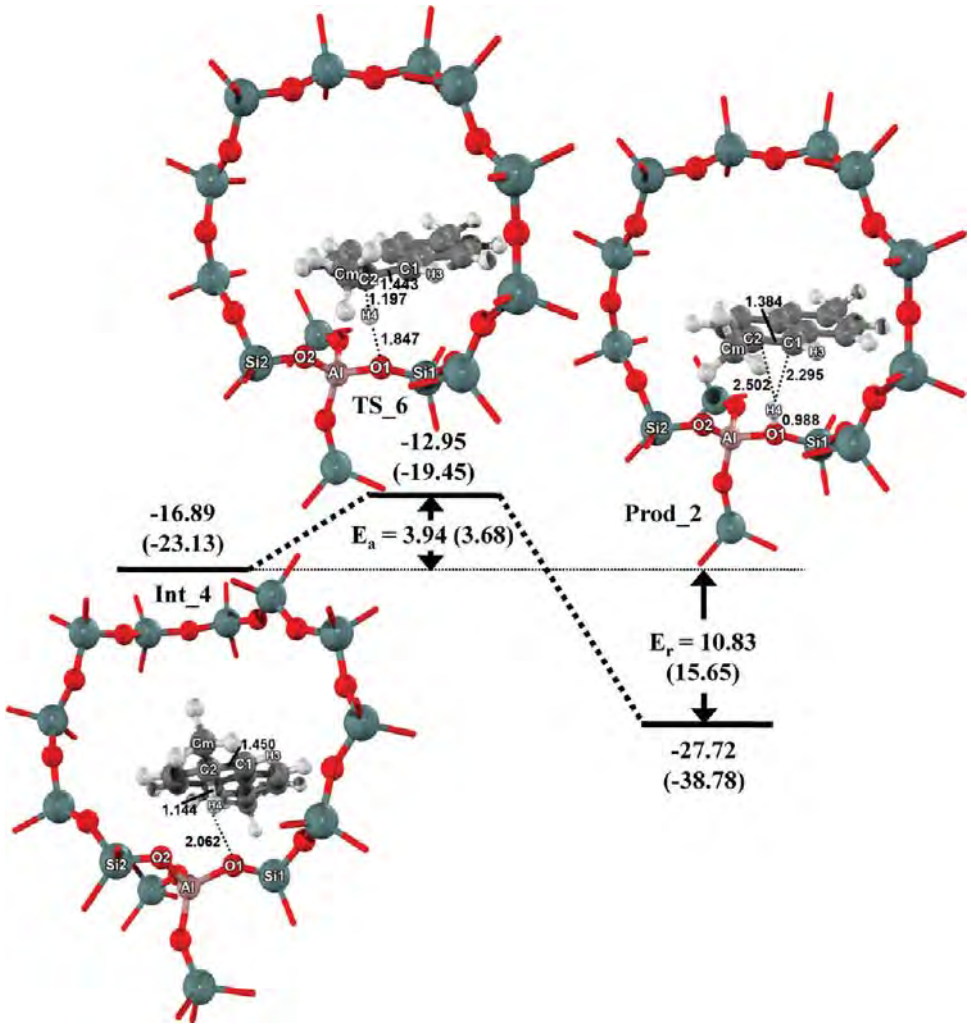

Figure 9. 120T M06-L/6-31G(d,p)//14T ONIOM(M06-L/6-31G(d,p):UFF) energy profile (kcal/mol) for the proton back-donation step of the 1,6- to 2,6-DMN isomerization over H-β zeolite.

distance of 1.413 Å and a C1−*Cm*−C2 bond angle of 45.3°. Most of the structure constraints seen in this tight transition state are relieved when a σ-complex (Int_4) is formed.

The zeolitic structure is slightly changed when Int_4 is formed. The Al−O1 and Si1−O1 bond distances are incresed by 0.003 and 0.002 Å, while both Al−O2 and Si2−O2 bond distances decrease by 0.001 Å. The Si2−O2−Al bond angle increases by 0.5°, whereas the Si1−O1−Al bond angle decreases by 0.1°. The Int_4 structure has a binding energy of −16.89 kcal/mol; it is more stable than the Int_3 intermediate by 2.99 kcal/mol. The energy barrier for the methyl shift step is 21.05 kcal/mol. This is less than that of 25.69 kcal/mol of the 1,5 to 1,6-DMN isomerization. The reaction energy is exothermic by 2.99 kcal/mol. Although there is no report of an experimental activation energy for the 1,6- to 2,6-DMN reaction, the activation energy of 19.2 kcal/mol can be estimated from the experimental activation energy of the reverse 2,6- to 1,6-DMN reaction (20.1 kcal/mol).[11] Our activation energy agrees well with this estimated activation energy. Both experimental and theoretical results agree with the fact that the activation energy for the methyl shift step in 1,5- to 1,6-DMN is greater than that in 1,6- to 2,6-DMN.

Proton Back-Donation to the Zeolite Framework. The proton is transferred back to the zeolite framework from protonated 2,6-DMN in this step. The optimized geometric parameters of species involved in this proton back-donation step are listed in Table S7 of the Supporting Information. The corresponding reaction profile is shown in Figure 9. In this step, a proton of Int_4 is transferred back to a zeolite-bridging oxygen (O1) at the acid site, hence leading to the adsorbed 2,6-DMN (Prod_2). This differs from the data obtained in the 1,5- to 1,6-DMN isomerization. The energy profile indicates that this proton back-donation step is very fast. The calculated activation energy in this second isomerization process is 3.94 kcal/mol, which is greater than that in the first isomerization. This proton back-donation step releases an energy of 10.83 kcal/mol. With reference to the Int_4 configuration, this proton back-donation step does not perturb the zeolite structure significantly. The Al−O1, Si1−O1, and Si2−O2 bond lengths increase by 0.106, 0.082, and 0.011 Å, respectively. The Al−O2 bond length and the Si1−O1−Al and Si2−O2−Al bond angles decrease by 0.027 Å, 0.6°, and 4.0°, respectively. For the geometry of 2,6-DMN, the C2−H4 distance increases from 1.144 to 2.502 Å, indicating C2−H4 bond breaking and O1−H4 bond formation. The O1−H4 bond length is now 0.988 Å. The C1−C2 bond shows double bond character as supported by the reduced bond length of 1.384 Å from 1.450 Å. The 2,6-DMN is now in the adsorbed state with the Brønsted acid site. The adsorbed 2,6-DMN product is subsequently separated from the framework by a desorption energy of 27.48 kcal/mol.

For convenient discussion, the energetic profiles for the overall steps of the 1,6- to 2,6-DMN isomerization are sum-

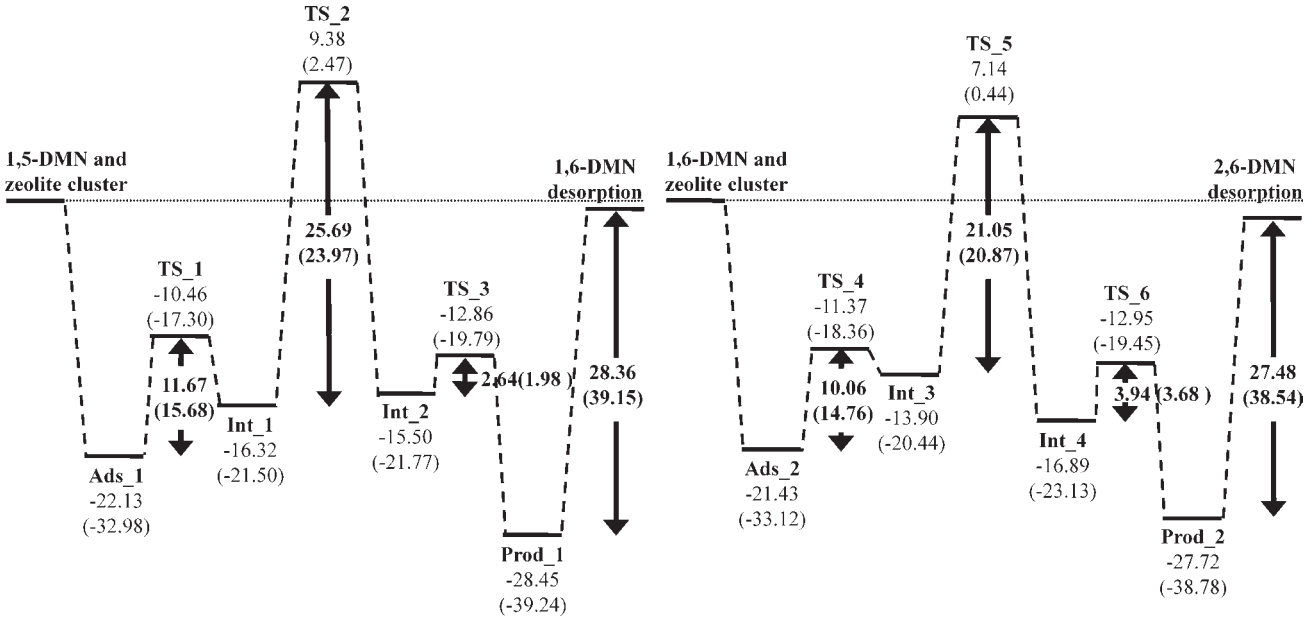

Figure 10. Summary of the overall 120T M06-L/6-31G(d,p)//14T ONIOM(M06-L/6-31G(d,p):UFF) energy profile (kcal/mol) of the (a) 1,5- into 1,6-DMN and (b) 1,6- into 2,6-DMN isomerizations over H-β zeolite. The values in parentheses are calculated at 14T ONIOM(M06-L/6-31G(d,p):UFF).

marized in Figure 10b (see also Table 1). The reaction starts with 1,6-DMN adsorbed on the acidic proton of zeolite (Ads_2). The subsequent step is the protonation to form the Int_3 intermediate with an activation barrier of 10.06 kcal/mol. The following step is the 1,2-methyl shift within bonded C−C atoms, leading to Int_4 with an energy barrier of 21.05 kcal/mol. This is followed by the proton back-donation step to generate the adsorbed 2,6-DMN product (Prod_2) with a rather low reaction barrier of 3.94 kcal/mol. The methyl shift step is considered to be the rate-determining step for the 1,6- to 2,6-DMN isomerization. This finding corresponds well with the work of Suld and Stuart.[11]

Comparison between the complete energy profiles of the 1,5- to 1,6-DMN and subsequent 1,6- to 2,6-DMN isomerization reactions can be made with the data from Figure 10 and Table 1. The methyl migration step is the rate-determining step in both reactions. The activation energy of the 1,5- to 1,6-DMN reaction is 25.69 kcal/mol, which is greater than the 21.05 kcal/mol energy of the 1,6- to 2,6-DMN reaction. This suggests that, for successive 1,5- to 1,6-DMN and 1,6- to 2,6-DMN reactions, the former isomerization reaction takes place more slowly than in the latter. This conclusion is in line with the thermodynamic view observed by Kraikul et al. that the 1,6-DMN to 2,6-DMN isomerization occurs rapidly with a higher isomerization rate.[6]

These results agree with the observation that the catalytic 1,5- to 1,6-DMN isomerization over H-β zeolite is the kinetically limiting step for the production of 2,6-DMN from 1,5-DMN. Under a thermodynamic condition as performed by Kraikul et al., the ratio of 2,6-DMN to 1,6-DMN product can be rationalized from the Boltzmann distribution of the two species. Our M06-L/6-31G(d,p) calculation indicates that the 2,6-DMN:1,6-DMN ratio is greater than 1, which agrees with the experimental observation that 2,6-DMN is obtained in a higher percentage than 1,6-DMN.[6] Although only the 14T cluster representing the active site of zeolite and the adsorbate are allowed to relax in this 120T M06-L/6-31G(d,p)//14T ONIOM(M06-L/6-31G(d,p):UFF) model, the energetic information of the isomerization reaction such as the adsorption energies and the activation energies are rational and compared well with experimental data reports in the literature.[6,9,11,13,51,52]

Conclusion

The isomerization of 1,5-DMN into 2,6-DMN over the acidic β zeolite is investigated at the molecular level by using the 120T M06-L/6-31G(d,p)//14T ONIOM(M06-L/6-31G(d,p):UFF) method. The isomerization reaction involves two consecutive methyl shift processes through the conversion of 1,5- into 1,6-DMN and of 1,6- into 2,6- DMN, respectively. The reaction mechanism begins with the adsorption of the reactant on a Brønsted acid site of the β zeolite followed by the protonation, 1,2-methyl shift, and proton back-donation steps and the product desorption. The methyl shift is shown to be the rate-determining step, with the 1,5- to 1,6-DMN isomerization reaction having a greater activation barrier than the 1,6- to 2,6-DMN reaction (25.69 vs 21.05 kcal/mol). The predicted activation barriers are in agreement with the available experimental data. Under thermodynamic control, 2,6-DMN is expected to be the main product of the isomerization reaction.

The present work is another successful example for the ONIOM approach, with proper selection of each layer that can be used to study the chemical reaction catalyzed by acidic zeolite. The M06-L/6-31G(d,p)//ONIOM(M06-L/6-31G(d,p):UFF) method of the 120T cluster is recommended to be used as an accurate and practical model to explore the structure, adsorption, and reaction mechanisms of β zeolite.

Acknowledgment. This work was supported in part by grants from the National Science and Technology Development Agency (NSTDA Chair Professor and NANOTEC Center of Excellence), the Thailand Research Fund, the Kasetsart University Research and Development Institute (KURDI), and the Commission on Higher Education, Ministry of Education, under the Postgraduate Education and Research Programs in Petroleum and Petrochemicals and Advanced Materials as well as the Sandwich Program (Grant CHE-PhD-SW-INDV to C.K.). We are grateful to Donald G. Truhlar and Yan Zhao for supporting us with the M06-L functional.

Supporting Information Available: Table S1 containing substituent values (*S* values) and their differences between the

real and model systems at the M06-L/6-31G(d,p) and UFF levels for the partitioning schemes in the isomerization of 1,5- to 2,6-DMN on H-β zeolite and Tables S2−S7 giving the selected geometric parameters for the mechanistic investigation on 1,5- to 2,6-dimethylnaphthalene isomerization catalyzed by acidic β zeolite. This material is available free of charge via the Internet at http://pubs.acs.org.

References and Notes

(1) Pu, S. B.; Inui, T. *Appl. Catal., A* **1996**, *146*, 305.
(2) Lillwitz, L. D. *Appl. Catal., A* **2001**, *221*, 337.
(3) *2,6-Dimethylnaphthalene (2,6-DMN)*; ChemSystems Report 99/00S7; Nexant: White Plains, NY, 2000.
(4) Song, C. *CATTECH* **2002**, *6*, 64.
(5) Tanabe, K.; Holderich, W. F. *Appl. Catal., A* **1999**, *181*, 399.
(6) Kraikul, N.; Rangsunvigit, P.; Kulprathipanja, S. *Chem. Eng. J.* **2005**, *114*, 73.
(7) Kraikul, N.; Rangsunvigit, P.; Kulprathipanja, S. *Appl. Catal., A* **2006**, *312*, 102.
(8) Ferino, I.; Monaci, R.; Pedditzi, L.; Rombi, E.; Solinas, V. *React. Kinet. Catal. Lett.* **1996**, *58*, 307.
(9) McCaulay, D. A.; Lien, A. P. *J. Am. Chem. Soc.* **1952**, *74*, 6246.
(10) Kilpatrick, M.; Bett, J. A. S.; Kilpatrick, M. L. *J. Am. Chem. Soc.* **1963**, *85*, 1038.
(11) Suld, G.; Stuart, A. P. *J. Org. Chem.* **1964**, *29*, 2939.
(12) Glaeser, R.; Li, R.; Hunger, M.; Ernst, S.; Weitkamp, J. *Catal. Lett.* **1998**, *50*, 141.
(13) Millini, R.; Frigerio, F.; Bellussi, G.; Pazzuconi, G.; Perego, C.; Pollesel, P.; Romano, U. *J. Catal.* **2003**, *217*, 298.
(14) Dykstra, C. E.; Frenking, G.; Kim, K. S.; Scuseria, G. *Theory and Applications of Computational Chemistry*; Elsevier: New York, 2005.
(15) van Santen, R. A.; Neurock, M. *Molecular Heterogeneous Catalysis*; Wiley-VCH: New York, 2006.
(16) Braendle, M.; Sauer, J. *J. Am. Chem. Soc.* **1998**, *120*, 1556.
(17) Hillier, I. H. *J. Mol. Struct.: THEOCHEM* **1999**, *463*, 45.
(18) Limtrakul, J.; Jungsuttiwong, S.; Khongpracha, P. *J. Mol. Struct.: THEOCHEM* **2000**, *525*, 153.
(19) Khaliullin, R. Z.; Bell, A. T. *J. Phys. Chem. A* **2001**, *105*, 10454.
(20) Limtrakul, J.; Nanok, T.; Khongpracha, P.; Jungsuttiwong, S.; Truong, T. N. *Chem. Phys. Lett.* **2001**, *349*, 161.
(21) Maseras, F.; Morokuma, K. *J. Comput. Chem.* **1995**, *16*, 1170.
(22) Humbel, S.; Sieber, S.; Morokuma, K. *J. Chem. Phys.* **1996**, *105*, 1959.
(23) Matsubara, T.; Sieber, S.; Morokuma, K. *Int. J. Quantum Chem.* **1996**, *60*, 1101.
(24) Svensson, M.; Humbel, S.; Froese, R. D. J.; Matsubara, T.; Sieber, S.; Morokuma, K. *J. Phys. Chem.* **1996**, *100*, 19357.
(25) Svensson, M.; Humbel, S.; Froese, R. D. J.; Matsubara, T.; Sieber, S.; Morokuma, K. *J. Chem. Phys.* **1996**, *105*, 3654.
(26) Dapprich, S.; Komaromi, I.; Byun, K. S.; Morokuma, K.; Frisch, M. J. *J. Mol. Struct.: THEOCHEM* **1999**, *461*, 1.
(27) Vreven, T.; Morokuma, K. *J. Comput. Chem.* **2000**, *21*, 1419.
(28) Bobuatong, K.; Limtrakul, J. *Appl. Catal., A* **2003**, *253*, 49.
(29) Panjan, W.; Limtrakul, J. *J. Mol. Struct.: THEOCHEM* **2003**, *654*, 35.
(30) Raksakoon, C.; Limtrakul, J. *J. Mol. Struct.: THEOCHEM* **2003**, *631*, 147.
(31) Namuangruk, S.; Pantu, P.; Limtrakul, J. *J. Catal.* **2004**, *225*, 523.
(32) Sirijaraensre, J.; Truong, T. N.; Limtrakul, J. *J. Phys. Chem. B* **2005**, *109*, 12099.
(33) Namuangruk, S.; Khongpracha, P.; Pantu, P.; Limtrakul, J. *J. Phys. Chem. B* **2006**, *110*, 25950.
(34) Jansang, B.; Nanok, T.; Limtrakul, J. *J. Phys. Chem. B* **2006**, *110*, 12626.
(35) Panyaburapa, W.; Nanok, T.; Limtrakul, J. *J. Phys. Chem. C* **2007**, *111*, 3433.
(36) Pantu, P.; Boekfa, B.; Limtrakul, J. *J. Mol. Catal. A* **2007**, *277*, 171.
(37) Jansang, B.; Nanok, T.; Limtrakul, J. *J. Phys. Chem. C* **2008**, *112*, 540.
(38) Maihom, T.; Namuangruk, S.; Nanok, T.; Limtrakul, J. *J. Phys. Chem. C* **2008**, *112*, 12914.
(39) Zhao, Y.; Truhlar, D. G. *J. Chem. Phys.* **2006**, *125*, 194101.
(40) Zhao, Y.; Truhlar, D. G. *Acc. Chem. Res.* **2008**, *41*, 157.
(41) Zhao, Y.; Truhlar, D. G. *Theor. Chem. Acc.* **2008**, *120*, 215.
(42) Frisch, M. J.; Trucks, G. W.; Schlegel, H. B.; Scuseria, G. E.; Robb, M. A.; Cheeseman, J. R.; Montgomery, J. J. A.; Vreven, T.; Kudin, K. N.; Burant, J. C.; Millam, J. M.; Iyengar, S. S.; Tomasi, J.; Barone, V.; Mennucci, B.; Cossi, M.; Scalmani, G.; Rega, N.; Petersson, G. A.; Nakatsuji, H.; Hada, M.; Ehara, M.; Toyota, K.; Fukuda, R.; Hasegawa, J.; Ishida, M.; Nakajima, T.; Honda, Y.; Kitao, O.; Nakai, H.; Klene, M.; Li, X.; Knox, J. E.; Hratchian, H. P.; Cross, J. B.; Bakken, V.; Adamo, C.; Jaramillo, J.; Gomperts, R.; Stratmann, R. E.; Yazyev, O.; Austin, A. J.; Cammi, R.; Pomelli, C.; Ochterski, J. W.; Ayala, P. Y.; Morokuma, K.; Voth, G. A.; Salvador, P.; Dannenberg, J. J.; Zakrzewski, V. G.; Dapprich, S.; Daniels, A. D.; Strain, M. C.; Farkas, O.; Malick, D. K.; Rabuck, A. D.; Raghavachari, K.; Foresman, J. B.; Ortiz, J. V.; Cui, Q.; Baboul, A. G.; Clifford, S.; Cioslowski, J.; Stefanov, B. B.; Liu, G.; Liashenko, A.; Piskorz, P.; Komaromi, I.; Martin, R. L.; Fox, D. J.; Keith, T.; Al-Laham, M. A.; Peng, C. Y.; Nanayakkara, A.; Challacombe, M.; Gill, P. M. W.; Johnson, B.; Chen, W.; Wong, M. W.; Gonzalez, C.; Pople, J. A. *Gaussian 03*, revision C.02; Gaussian, Inc.: Wallingford, CT, 2004.
(43) de Vries, A. H.; Sherwood, P.; Collins, S. J.; Rigby, A. M.; Rigutto, M.; Kramer, G. J. *J. Phys. Chem. B* **1999**, *103*, 6133.
(44) Rungsirisakun, R.; Jansang, B.; Pantu, P.; Limtrakul, J. *J. Mol. Struct.: THEOCHEM* **2005**, *733*, 239.
(45) Derouane, E. G.; Chang, C. D. *Microporous Mesoporous Mater.* **2000**, *35*, 425–36.
(46) Pelmenschikov, A.; Leszczynski, J. *J. Phys. Chem. B* **1999**, *103*, 6886.
(47) Clark, L. A.; Sierka, M.; Sauer, J. *J. Am. Chem. Soc.* **2003**, *125*, 2136.
(48) Rozanska, X.; van Santen, R. A.; Hutschka, F.; Hafner, J. *J. Am. Chem. Soc.* **2001**, *123*, 7655.
(49) Boekfa, B.; Choomwattana, S.; Maitarad, P.; Limtrakul, P.; Limtrakul, J. *NSTI-Nanotech 2009* **2009**, *3*, 268.
(50) Morokuma, K. *Bull. Korean Chem. Soc.* **2003**, *24*, 797.
(51) Ruthven, D. M.; Goddard, M. *Zeolites* **1986**, *6*, 275.
(52) Barthomeuf, D.; Ha, B. H. *J. Chem. Soc., Faraday Trans.* **1973**, *69*, 2158.

JP904098T

Langmuir
Article
pubs.acs.org/Langmuir

Effects of the Zeolite Framework on the Adsorptions and Hydrogen-Exchange Reactions of Unsaturated Aliphatic, Aromatic, and Heterocyclic Compounds in ZSM-5 Zeolite: A Combination of Perturbation Theory (MP2) and a Newly Developed Density Functional Theory (M06-2X) in ONIOM Scheme

Bundet Boekfa,[†,‡,§] Saowapak Choomwattana,[†,‡,§] Pipat Khongpracha,[†,‡,§] and Jumras Limtrakul*[,†,‡,§]

[†]*Laboratory for Computational and Applied Chemistry, Chemistry Department, Faculty of Science, Kasetsart University, Bangkok 10900, Thailand,* [‡]*Center of Nanotechnology, Kasetsart University Research and Development Institute, Kasetsart University, Bangkok 10900, Thailand, and* [§]*NANOTEC Center of Excellence, National Nanotechnology Center, Bangkok 10900, Thailand*

Received May 22, 2009. Revised Manuscript Received July 10, 2009

The confinement effect on the adsorption and reaction mechanism of unsaturated aliphatic, aromatic and heterocyclic compounds on H-ZSM-5 zeolite has been investigated by the four ONIOM methods (MP2:M06-2X), (MP2:B3LYP), (MP2:HF), and (MP2:UFF). The H-ZSM-5 'nanoreactor' porous intersection, where chemical reactions take place, is represented by a quantum cluster of 34 tetrahedral units. Ethene, benzene, ethylbenzene, and pyridine are chosen to represent reactions of various adsorbates of aliphatic, aromatic and heterocyclic compounds. Among the four combined methods, (MP2:M06-2X) outperforms the others. The results confirm that the method that takes weak interactions, especially the van der Waals interaction, into account is essential for describing the confinement effect from the zeolite framework. The effects of the infinite zeolitic framework on the cluster model are also included by a set of point charges generated by the embedded ONIOM model. The energies for the adsorption of ethene, benzene, ethylbenzene, and pyridine on H-ZSM-5 from an embedded ONIOM(MP2:M06-2X) calculation are predicted to be −14.0, −19.8, −24.7, and −48.4 kcal/mol, respectively, which are very close to available experimental observations. The adsorption energy of pyridine agrees well with the experiment data of −47.6 kcal/mol. We also applied the same computational methodology on the systematic investigation of the H/H exchange reaction of benzene and ethylbenzene with the acidic H-ZSM-5 zeolite. The H/H exchange reaction was found to take place in a single concerted step. The calculated apparent activation energies for benzene and ethylbenzene are 12.6 and 4.9 kcal/mol, which can be compared to the experimental estimates of 11.0 and 6.9 kcal/mol, respectively. The confinement effect of the extended zeolite framework has been clearly demonstrated not only to stabilize the adsorption complexes but also to improve their corresponding activation energies to approach the experimental benchmark.

1. Introduction

Zeolite, one of the industrially important microporous catalysts, is of great interest for its range of applications in adsorption and separation, particularly for catalysis. One of the most notable catalyst zeolites for modern petrochemical processes is ZSM-5. With its size- and shape-selectivity, thermal stability and the ability of ion-exchange, ZSM-5 is the catalyst of choice for important hydrocarbon reactions such as cracking, isomerization, and oligomerization.[1−8]

Theoretical study can offer a practical tool that provides clear insight to the reaction mechanism complementing experimental investigations or, in certain cases, offering an understanding that is not possible by experimental investigations. Most of the theoretical studies of chemical reactions on heterogeneous catalysts are based on the use of wave function methods and density functional theory (DFT). Wave function methods, especially post-Hartree−Fock methods such as configuration interaction, coupled cluster, and Møller−Plesset perturbation theory, certainly give accurate results. However, the high accuracy comes with the price of higher computational cost. DFT has gained increasing interest by providing good predictions of important properties for a wide range of applications in chemistry with a lower required computational demand. However, the conventional DFT functionals are not able to properly describe van der Waals effects, which are very important in the interactions of host/guest systems. The selection of the functional in DFT is crucial for correctly exploring the properties and reaction mechanisms of chemical reactions. Considerable effort has been invested to overcome this severe deficiency of DFT. Grimme[9] has proposed a new semiempirical functional by introducing atom-pairwise dispersion corrections to the generalized gradient

*Corresponding author.

(1) Smit, B.; Maesen, T. L. M. *Nature* (*London, U. K.*) **2008**, *451*, 671.
(2) Bhan, A.; Iglesia, E. *Acc. Chem. Res.* **2008**, *41*, 559.
(3) Luzgin, M. V.; Rogov, V. A.; Arzumanov, S. S.; Toktarev, A. V.; Stepanov, A. G.; Parmon, V. N. *Angew. Chem., Int. Ed.* **2008**, *47*, 4559.
(4) Corma, A. *J. Catal.* **2003**, *216*, 298.
(5) Chen, C. S. H.; Bridger, R. F. *J. Catal.* **1996**, *161*, 687.
(6) Yaluris, G.; Rekoske, J. E.; Aparicio, L. M.; Madon, R. J.; Dumesic, J. A. *J. Catal.* **1995**, *153*, 65.
(7) Andy, P.; Gnep, N. S.; Guisnet, M.; Benazzi, E.; Travers, C. *J. Catal.* **1998**, *173*, 322.
(8) Venuto, P. B. *Microporous Mater.* **1994**, *2*, 297.
(9) Grimme, S. *J. Comput. Chem.* **2006**, *27*, 1787.

approximation (GGA) part of the B97 functional. Zhao and Truhlar[10−13] have recently developed the M06 family of local (M06-L) and hybrid (M06, M06-2X) meta-GGA functionals that show promising performance for studying main group thermochemistry, kinetics, noncovalent interactions, excited states, and transition elements.

Nevertheless, zeolites that have high impacts in industrial processes usually possess hundreds of atoms per unit cell, making the use of sophisticated methods, such as periodic ab initio calculations, computationally too expensive and even impractical when very large zeolites are concerned. Therefore, the electronic properties of zeolites are usually modeled with quantum chemical methods for relatively small clusters where only the most important part of the zeolites is focused on.[14−19] Such limited models do not take into account the effect of the framework, which can significantly change the structure and energetics of the system and has been shown to lead to discrepancies between the cluster results and the actual zeolite behaviors.[20,21]

The confinement effect was proposed to explain the interactions between the zeolite framework and the adsorbed molecule, which is confined within the pore of the zeolite.[22,23] The confinement effects play an important role on the sorption and catalytic properties of zeolites by stabilizing adsorbed molecules, intermediates, and reaction transition states. The quantum mechanics/molecular mechanics (QM/MM) scheme was successfully applied to study the interactions and reactions of hydrocarbon molecules on zeolites.[14−19] Those calculated adsorption and activation energies are very close to the available experimental benchmarks. One of the successful combined approaches in our previous works is the ONIOM(B3LYP:UFF). This method usually gives surprisingly good results for studying systems in which confinement effects play a significant role on adsorptions and reactions in the zeolite pore.[16] However, it is due to the fact that the overestimated van der Waals interactions represented by the universal force field compensate for the weak interactions from small quantum cluster calculations treated by the B3LYP method. One could expect worse results by increasing the size of the quantum cluster. In order to avoid these unfavorable errors, we have to find another method that is more reliable and also economically viable for studying the chemistry of zeolites.

We performed the quantum chemical calculation to study (1) the adsorption of chosen molecules not only to represent various industrially important hydrocarbons and heterocyclic compounds, but also because they are known to be common failures for conventional DFT calculations: unsaturated aliphatic (ethene), aromatics (benzene and ethylbenzene), and heterocycles (pyridine) and (2) the hydrogen exchange reaction of aromatics (benzene and ethylbenzene). The hydrogen exchange is chosen because of its simplicity; it consists of a single concerted step, and

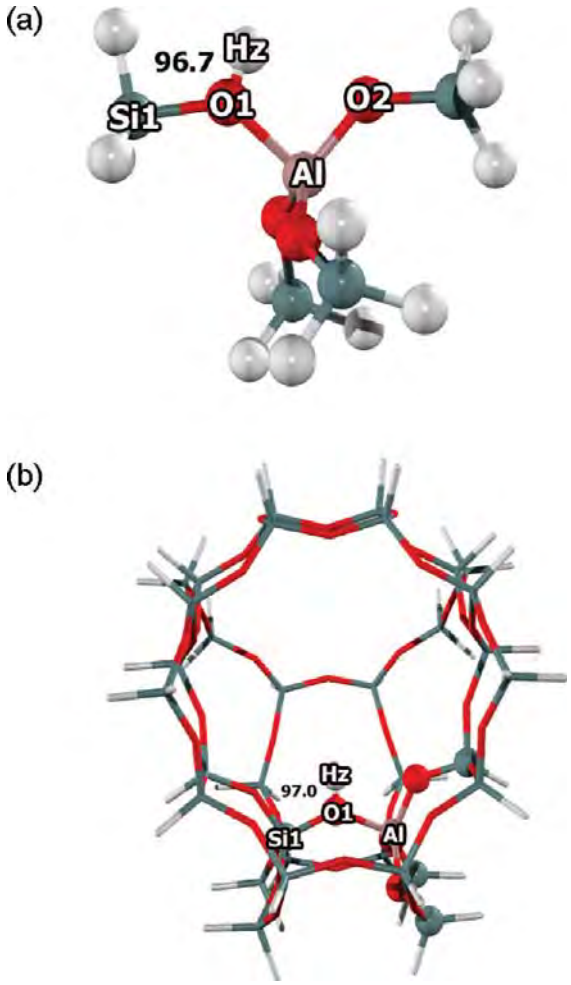

Figure 1. Presentation of H-ZSM-5 models in different sizes: (a) 5T quantum cluster and (b) 5T:34T ONIOM model. Atoms treated with the MP2 level of theory are shown in balls, whereas the area treated with a lower level of calculation is symbolized with wireframes.

the availability of experimental data. To investigate the confinement effect, the ONIOM scheme on the widely used 34T model was chosen specifically. The active site is calculated with the MP2 method, whereas the outer part is treated with different approaches: M06-2X, B3LYP, HF methods and UFF force field. The discrepancy between the benchmark of experimental data and our calculated results in the adsorption and reaction energies of probe molecules are discussed below.

2. Method

The adsorption and reaction of ethene, benzene, ethylbenzene, and pyridine on H-ZSM-5 have been initially studied with a five tetrahedral unit (5T) model. The Al atom is selected to substitute a Si atom at the T12 position, which is the most energetically favored position.[15,17,19] Afterward, the zeolite framework is expanded to become the 34T quantum cluster ($AlSi_{33}O_{46}H_{45}$) to cover the so-called "nanocavity", which is the intersection between straight and zigzag channels. For computational cost efficiency, the ONIOM scheme[24] is applied on this 34T model. The 5T quantum region of the Brønsted acid site, illustrated in Figure 1a, is assigned to be the inner layer, whereas the extended

(10) Zhao, Y.; Schultz, N. E.; Truhlar, D. G. *J. Chem. Theory Comput.* **2006**, *2*, 364.
(11) Zhao, Y.; Truhlar, D. G. *Theor. Chem. Acc.* **2008**, *120*, 215.
(12) Zhao, Y.; Truhlar, D. G. *Acc. Chem. Res.* **2008**, *41*, 157.
(13) Zhao, Y.; Truhlar, D. G. *J. Phys. Chem. C* **2008**, *112*, 6860.
(14) Kasuriya, S.; Namuangruk, S.; Treesukol, P.; Tirtowidjojo, M.; Limtrakul, J. *J. Catal.* **2003**, *219*, 320.
(15) Lomratsiri, J.; Probst, M.; Limtrakul, J. *J. Mol. Graphics Modell.* **2006**, *25*, 219.
(16) Pantu, P.; Boekfa, B.; Limtrakul, J. *J. Mol. Catal. A: Chem.* **2007**, *277*, 171.
(17) Raksakoon, C.; Limtrakul, J. *THEOCHEM* **2003**, *631*, 147.
(18) Namuangruk, S.; Pantu, P.; Limtrakul, J. *ChemPhysChem* **2005**, *6*, 1333.
(19) Panjan, W.; Limtrakul, J. *J. Mol. Struct.* **2003**, *654*, 35.
(20) Sinclair, P. E.; de Vries, A.; Sherwood, P.; Catlow, C. R. A.; van Santen, R. A. *J. Chem. Soc., Faraday Trans.* **1998**, *94*, 3401.
(21) Braendle, M.; Sauer, J. *J. Am. Chem. Soc.* **1998**, *120*, 1556.
(22) Derouane, E. G. *J. Mol. Catal. A Chem.* **1998**, *134*, 29.
(23) Zicovich-Wilson, C. M.; Corma, A.; Viruela, P. *J. Phys. Chem.* **1994**, *98*, 10863.
(24) Dapprich, S.; Komiromi, I.; Byun, K. S.; Morokuma, K.; Frisch, M. J. *THEOCHEM* **1999**, *461−462*, 1.

34T model is the outer layer. Only the active region ($AlSi_4O_4H$) and the probe molecule are allowed to relax while the rest is kept fixed with the crystallographic structure.[25] The various combinations of methods for the ONIOM scheme are compared to find the best approach for the best prediction. The full quantum calculation of the 5T inner layer of the ONIOM model is optimized with the MP2 method. A lower level of calculation for the outer layer is varied with M06-2X, B3LYP, HF, and UFF approaches. Therefore, the four combined ONIOM schemes, (MP2:M06-2X), (MP2:B3LYP), (MP2:HF), and (MP2:UFF) methods, are compared. All geometry optimizations in each method were performed by using the 6-31G(d,p) basis set. Curtiss et al. reported the close agreement between the adsorption results of MP2/6-31G(d,p) and the more accurate G2(MP2, SVP) [effectively QCISD(T)/6-311+G(3df,2p)+ ZPVE] for the adsorption complex of ethane and small 3T and 5T clusters of zeolite, which appears to be a cancellation of the high level effects: correlation, basis set and zero-point energies.[26,27] Thus, the MP2/6-31G(d,p) adsorption energy may be reasonably reliable. To obtain more reliable interaction energies, the single-point energy calculations at the 5T quantum cluster with the MP2/6-311+G(2df,2p)//MP2/6-31G(d,p) level and the 5T:34T with the ONIOM(MP2/6-311+G(2df,2p):M06−2X/6-31G(d,p)//MP2/6-31G(d,p):M06−2X/6-31G(d,p)) method are carried out. However, the long-range effects from the extended framework that is neglected in any truncated finite quantum cluster are essential for exploring adsorption and reaction properties in the zeolite systems. We have also incorporated the long-range electrostatic potential from the infinite zeolite lattice to our systems by performing single-point calculations with the electronic embedding approach. The Madelung potential from the extended lattice is reproduced by well-calibrated point charges enclosed around the 34T quantum cluster.[28−31] The ONIOM and optimized point charges embedded method called the embedded-ONIOM (e-ONIOM) approach has been successfully applied to predict adsorptions and reaction mechanisms in several zeolite systems.[15,30−34] All calculations were carried out using the Gaussian 03 program[35] incorporated with the Minnesota Density Functionals module 3.1 by Zhao and Truhlar.

3. Results and Discussion

3.1. Molecular Cluster and Nanocluster Models of Zeolites. Before giving details on the molecular adsorptions of our chosen adsorbates, we first clarify how the Brønsted acid in H-ZSM-5 is modeled. It is known that the proton can reside on any of the four nonequivalent neighboring oxygen atoms at a given Al T-site.[36] From the total of 96 tetrahedral centers and 12 topologically distinct sites in a unit cell of ZSM-5, T12 is found to be the most favored for an aluminum (Al) substitution.[37] One proton, known as Brønsted acid, is required to compensate the charge of the Al-substituted framework. From the Al position, the proton then points to the 10T ring, thus providing a catalytic cavity for acid-mediated reactions.[17,38,39] The Brønsted active site is therefore chemically composed of $AlSi_4O_4H_{13}$, called a 5T cluster, illustrated in Figure 1a. The zeolite model is further expanded to represent the more realistic system, i.e., the 34T cluster for the components of zigzag and straight channels connected with the intersection, shown in Figure 1b. With the extended framework, dominant interactions for adsorbate molecules can be taken into account. From our previous studies,[17,19] the adsorption site for small molecules such as ethene is in the zigzag channel, whereas a larger molecule such as benzene is generally located at the intersection of the channel system.

For our theoretical study of the effects of the framework on the adsorption and H/H exchange of hydrocarbons on the nanostructured zeolite, we evaluate the method combined into the ONIOM scheme to find the approach that gives the best prediction. The quantum calculation of the 5T cluster optimized with the MP2 method is performed to analyze the energy contribution from the high level of calculation in ONIOM schemes with four combined computational methods: (MP2:M06-2X), (MP2:B3LYP), (MP2:HF), and (MP2:UFF).

From the bare H-ZSM-5, the optimized structural parameters of the 5T cluster and ONIOM model with different approaches [the (MP2:M06-2X), (MP2:B3LYP), (MP2:HF), and (MP2:UFF) methods] are listed in Table S1 in the Supporting Information. It is found that a different lower level of calculation leads to a different result on the acidity of the zeolite active site. As was expected, the 5T cluster gives an underestimated Brønsted O1-Hz bond length of 96.7 pm, which is smaller than the value from all of the ONIOM approaches. The bond distance is predicted with the ONIOM methods to be in the range of 96.8−97.0 pm. The difference of those calculated bond lengths reveals the influence of the extended framework on the optimized structure and the effective reactivity of the acid site. In this case, the framework is found to enhance the acidity. To evaluate the quality of the method combination, the computed values of the Al···Hz distances are compared to the experimental observation (238.0−248.0 ± 4 pm).[40,41] The Al···Hz distance from the MP2:B3LYP (235.9 pm), MP2:HF (235.7 pm), and MP2:UFF (228.5 pm) ONIOM approaches are underestimated. The most comparable computed value is from the ONIOM(MP2:M06-2X) (236.4 pm) method.

3.2. Adsorptions of Aliphatic (Ethene), Aromatic (Benzene, Ethylbenzene) and Heterocyclic Compounds (Pyridine) with H-ZSM-5. Adsorption is one of the most important chemical

(25) Van Koningsveld, H.; Van Bekkum, H.; Jansen, J. C. *Acta Crystallogr., Sect. B: Struct. Sci.* **1987**, *B43*, 127.
(26) Curtiss, L. A.; Zygmunt, S. A.; Iton, L. E. *Proc. Int. Zeolite Conf., 12th* **1999**, *1*, 415.
(27) Zygmunt, S. A.; Curtiss, L. A.; Zapol, P.; Iton, L. E. *J. Phys. Chem. B* **2000**, *104*, 1944.
(28) Stefanovich, E. V.; Truong, T. N. *J. Chem. Phys.* **1996**, *104*, 2946.
(29) Allavena, M.; Seiti, K.; Kassab, E.; Ferenczy, G.; Angyan, J. G. *Chem. Phys. Lett.* **1990**, *168*, 461.
(30) Dungsrikaew, V.; Limtrakul, J.; Hermansson, K.; Probst, M. *Int. J. Quantum Chem.* **2003**, *96*, 17.
(31) Injan, N.; Pannorad, N.; Probst, M.; Limtrakul, J. *Int. J. Quantum Chem.* **2005**, *105*, 898.
(32) Boekfa, B.; Pantu, P.; Limtrakul, J. *J. Mol. Struct.* **2008**, *889*, 81.
(33) Maihom, T.; Boekfa, B.; Sirijaraensre, J.; Nanok, T.; Probst, M.; Limtrakul, J. *J. Phys. Chem. C* **2009**, *113*, 6654.
(34) Sirijaraensre, J.; Limtrakul, J. *Phys. Chem. Chem. Phys.* **2009**, *11*, 578.
(35) Frisch, M. J.; Trucks, G. W.; Schlegel, H. B.; Scuseria, G. E.; Robb, M. A.; Cheeseman, J. R.; Montgomery, J. A., Jr.; Vreven, T.; Kudin, K. N.; Burant, J. C.; Millam, J. M.; Iyengar, S. S.; Tomasi, J.; Barone, V.; Mennucci, B.; Cossi, M.; Scalmani, G.; Rega, N.; Petersson, G. A.; Nakatsuji, H.; Hada, M.; Ehara, M.; Toyota, K.; Fukuda, R.; Hasegawa, J.; Ishida, M.; Nakajima, T.; Honda, Y.; Kitao, O.; Nakai, H.; Klene, M.; Li, X.; Knox, J. E.; Hratchian, H. P.; Cross, J. B.; Adamo, C.; Jaramillo, J.; Gomperts, R.; Stratmann, R. E.; Yazyev, O.; Austin, A. J.; Cammi, R.; Pomelli, C.; Ochterski, J. W.; Ayala, P. Y.; Morokuma, K.; Voth, G. A.; Salvador, P.; Dannenberg, J. J.; Zakrzewski, V. G.; Dapprich, S.; Daniels, A. D.; Strain, M. C.; Farkas, O.; Malick, D. K.; Rabuck, A. D.; Raghavachari, K.; Foresman, J. B.; Ortiz, J. V.; Cui, Q.; Baboul, A. G.; Clifford, S.; Cioslowski, J.; Stefanov, B. B.; Liu, G.; Liashenko, A.; Piskorz, P.; Komaromi, I.; Martin, R. L.; Fox, D. J.; Keith, T.; Al-Laham, M. A.; Peng, C. Y.; Nanayakkara, A.; Challacombe, M.; Gill, P. M. W.; Johnson, B.; Chen, W.; Wong, M. W.; Gonzalez, C.; Pople, J. A. *Gaussian 03, revision B.05*; Gaussian, Inc.: Pittsburgh, PA, 2003.
(36) Derouane, E. G.; Fripiat, J. G. *J. Phys. Chem.* **1987**, *91*, 145.
(37) Lonsinger, S. R.; Chakraborty, A. K.; Theodorou, D. N.; Bell, A. T. *Catal. Lett.* **1991**, *11*, 209.
(38) Brand, H. V.; Curtiss, L. A.; Iton, L. E. *J. Phys. Chem.* **1993**, *97*, 12773.
(39) Simperler, A.; Bell, R. G.; Foster, M. D.; Gray, A. E.; Lewis, D. W.; Anderson, M. W. *J. Phys. Chem. B* **2004**, *108*, 7152.
(40) Klinowski, J. *Chem. Rev.* **1991**, *91*, 1459.
(41) Freude, D.; Klinowski, J.; Hamdan, H. *Chem. Phys. Lett.* **1988**, *149*, 355.

processes that lead to numerous chemical reactions. Ethene, the simplest molecule with π-bonding, thus representing intermolecular π interaction, was studied to represent the unsaturated hydrocarbon adsorption. Benzene and ethylbenzene were chosen to study aromatic hydrocarbons adsorption on H-ZSM-5. Ethylbenzene was considered for the influence of the substitution on the aromatics adsorption. Finally, the acidity of the zeolite is observed with pyridine, which is known as the basic probe molecule.

3.2.1. Unsaturated Hydrocarbon Adsorption: Ethene. The ethene molecule weakly adsorbs over the Brønsted acid site forming a π-adsorption complex. The ONIOM(MP2:M06-2X) optimized structure of the adsorption is illustrated in Figure 2. The key geometrical parameters of the adsorption complexes are shown in Table S2 in the Supporting Information. Almost symmetrical distances between Hz···C1 (218.8 pm) and Hz···C2 (218.1 pm) can be found in the optimized 5T adsorption complex. When the framework is extended to be the 34T in the ONIOM scheme, the unsymmetrical impact on the Hz···C distance from the framework is observed (216.3 pm vs 220.5 pm). In all models, the structures of Brønsted acid sites and the ethene molecule have little perturbation upon the adsorption. Focusing on the O−Hz parameter, the acid bond length is elongated during the adsorption, corresponding with the slightly elongated C1═C2 bond of ethene, from 133.5 to 134.3 pm. From the MP2 optimization for the 5T model, the O−Hz distance was extended from 96.7 to 98.1 pm. The structural change from other methods is found to have the same trend.

As for the MP2 calculation on the 5T quantum cluster, the predicted adsorption energy is just −8.7 kcal/mol. The values from the ONIOM scheme are −13.3, −10.5, −10.4, and −16.6 kcal/mol for ONIOM(MP2:M06-2X), (MP2:B3LYP), (MP2:HF) and (MP2:UFF) methods, respectively. Due to the lack of information for ethene adsorption on H-ZSM-5 zeolite, we select the ethene adsorption on H-FAU zeolite to make a validation for our calculated values. Ethene adsorbs on H-FAU with the adsorption energy of −9.0 kcal/mol.[42] It is known that the acidity of H-ZSM-5 is higher than that of H-FAU. The interaction energy of ethene on H-ZSM-5 is expected to be stronger than that on H-FAU and should be greater than a value of 10 kcal/mol. Since then, the (MP2:M06-2X) and (MP2:UFF) methods are found to give reasonable results.

3.2.2. The Aromatic Hydrocarbon Adsorption: Benzene and Ethylbenzene. Benzene and ethylbenzene also interact with the zeolite acid site via π-interaction, illustrated in Figures 3 and 4. Selected structural parameters of the benzene and ethylbenzene molecules are shown in Tables S3 and S4 in the Supporting Information. In order to discuss this in a concise manner, only the structure complexes at the most reliable and well-calibrated ONIOM(MP2: M06-2X) scheme will be the main focus . The C═C double bond in the benzene ring that forms the π-interaction with the zeolite is slightly increased and the acidic O1−Hz bond distance is slightly increased from 97.0 to 98.4 and 98.3 pm for both benzene and ethylbenzene adsorption complexes, respectively. Similar to the adsorption of ethene, the zeolite structural parameters are slightly changed by the weak interactions (changes in bond distances and bond angles are less than 0.02 Å, and 2°, respectively).

As for the bare 5T quantum cluster, the interaction of benzene calculated with the MP2 method is −12.1 kcal/mol. Considering the surrounding framework, the calculation with the ONIOM scheme gives adsorption energies of −18.4, −12.9, −11.8, and

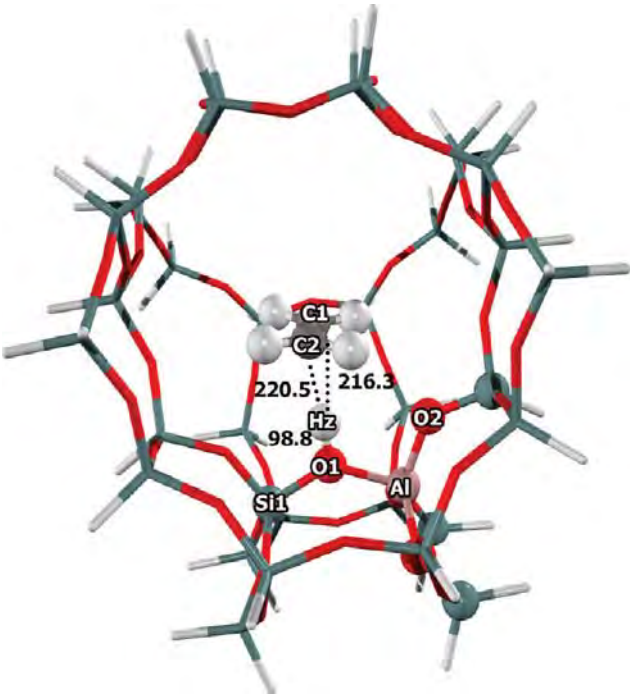

Figure 2. Presentation of an ethene molecule adsorbed on the 5T:34T model of H-ZSM-5 zeolite. Atoms treated with the MP2 level of theory are shown in balls, whereas the area treated with a lower level of calculation is symbolized with wireframes. Bond lengths are in picometers.

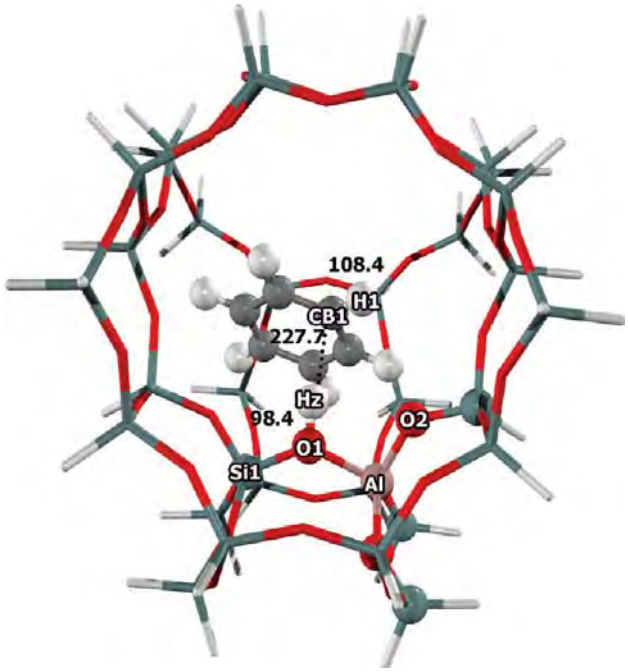

Figure 3. Presentation of a benzene molecule adsorbed on the 5T:34T model of H-ZSM-5 zeolite. Atoms treated with the MP2 level of theory are shown in balls, whereas the area treated with a lower level of calculation is symbolized with wireframes. Bond lengths are in picometers.

−26.0 kcal/mol for the ONIOM(MP2:M06-2X), (MP2:B3LYP), (MP2:HF), and (MP2:UFF) methods, respectively. The energies that are larger than those from the quantum cluster are mainly attributed to "nonlocal interactions", which are the van der Waals

(42) Cant, N. W.; Hall, W. K. *J. Catal.* **1972**, *25*, 161.

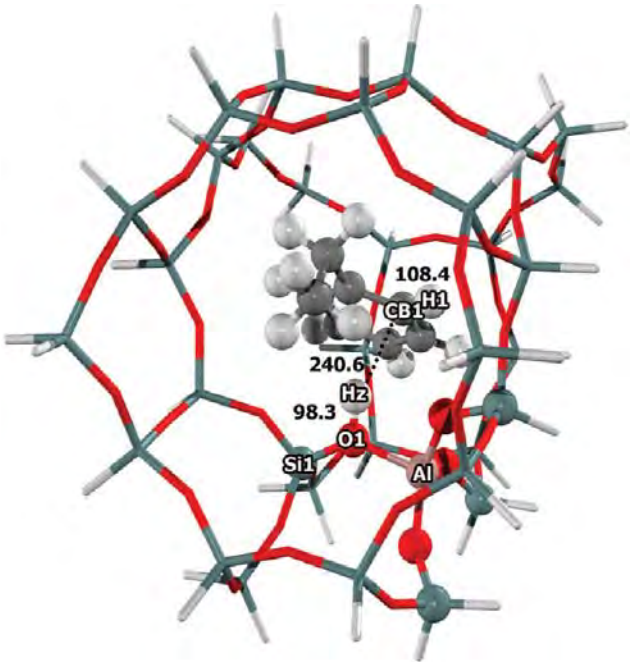

Figure 4. Presentation of an ethylbenzene molecule adsorbed on the 5T:34T model of H-ZSM-5 zeolite. Atoms treated with the MP2 level of theory are shown in balls, whereas the area treated with a lower level of calculation is symbolized with wireframes. Bond lengths are in picometers.

interactions, due to confinement of the zeolite. According to the nonpolarity of benzene, only the van der Waals interactions are expected to be significant. Since only the adsorption energy, measured as −15.3 kcal/mol for H-FAU zeolite, is available[43] and the ZSM-5 zeolite pore is smaller, the interaction inside its pore should be stronger than the value in the H-FAU system. Only the energy from the ONIOM(MP2:M06-2X) gives a reasonable adsorption energy.

The adsorption energies for ethylbenzene on H-ZSM-5 were calculated to be −13.9, −23.3, −13.3, −11.6, and −35.3 kcal/mol with the full 5T quantum MP2 and ONIOM(MP2:M06−2X), (MP2:B3LYP), (MP2:HF), and (MP2:UFF) methods, respectively. Obviously, the van der Waals interaction for the case of benzene is weaker than for the ethylbenzene adsorption and, hence, the corresponding adsorption energies at ONIOM(MP2:M06-2X) are −18.4 and −23.3 kcal/mol for benzene and ethylbenzene, respectively. These values compare well with the experimental values of −15.3 and −19.6 kcal/mol[43] for the adsorption of benzene and ethylbenzene in a weaker acid zeolite, and H−Y zeolite, respectively. This discrimination of adsorption energies is due partly to the confinement effect of H-ZSM-5 being larger than the H−Y zeolite. The accurately predicted adsorption energies clearly demonstrate that the ONIOM(MP2:M06-2X) model used in this work can represent the interactions between the adsorbates and zeolite very well. The combination of the MP2 method at the active region embedded in the extended structure modeled by the M06-2X apparently works well in representing van der Waals interactions in the zeolite system as compared to B3LYP and HF. The adsorption results of the ONIOM(MP2:UFF) tend to yield overestimated values (see Table 1).

3.2.3. Heterocyclic Compounds Adsorption: Pyridine. The acidity of the H-ZSM-5 zeolite can be studied with pyridine, known as the basic probe molecule. The molecule also has been widely studied as the representative for the heterocyclic molecule. Pyridine is held over the Brønsted acid site of the H-ZSM-5 zeolite with the ion pair intermolecular interaction, illustrated in Figure 5a. Selected structural parameters of the pyridine molecule on H-ZSM-5 are shown in Table S5 in the Supporting Information. From the calculation of the 5T model, the nitrogen atom of pyridine is spontaneously protonated by the zeolite proton. The formation of an ion pair consisting of a pyridinium cation and the deprotonated zeolite can be seen by the bond distance between N and the acidic proton Hz of 110.2 pm, concurrently with the increase of its distance to O1 from 96.7 to 144.5 pm. The results are in accordance with Gutmann's rules,[44] i.e., a lengthening of the O1−Hz bond, a shortening of Al−O1, and a lengthening of Al−O2 (not adjacent to the bridging O1−Hz). Similar structural changes are also found from the ONIOM calculation on the model with the extended framework. The intermolecular O1···N distance of the pyridine/zeolite adduct increases on the model expansion from 253.7 pm (5T) to 257.4−274.7 pm (ONIOM).

The experimentally determined adsorption energy of pyridine on the acidic H-ZSM-5 zeolite of 47.6 kcal/mol[45] is considered as the benchmark. We computed the adsorption energy on the 5T model with the MP2/6-31G(d,p) level of theory to be −24.9 kcal/mol. Once the model is expanded up to 34T, the adsorption energies are considerably increased to −43.7, −39.1, −38.7, and −38.6 kcal/mol for the ONIOM(MP2:M06−2X), (MP2:B3LYP), (MP2:HF), and (MP2:UFF) methods, respectively. As in the former cases, the ONIOM(MP2:M06−2X) result most closely approaches the benchmark. As expected, this result is due to the M06-2X method

Table 1. The Contribution Analysis on Adsorption Energies of Ethene, Benzene, Ethylbenzene, and Pyridine Molecules on 5T Models Calculated with MP2 Full Quantum Calculation and the 5T:34T Model with Different ONIOM Approaches[a]

model	method	ethene	benzene	ethylbenzene	pyridine
5T	MP2[b]	−8.7	−12.1	−13.9	−24.9
5T:34T	ONIOM(MP2:M06−2X)[c]	−13.3	−18.4	−23.3	−43.7
	high level	−8.8	−11.7	−12.8	−23.6
	low level	−4.5	−6.7	−10.5	−20.1
5T:34T	ONIOM(MP2:B3LYP)[d]	−10.5	−12.9	−13.3	−39.1
	high level	−9.1	−11.0	−12.0	−24.2
	low level	−1.4	−1.9	−1.3	−14.9
5T:34T	ONIOM(MP2:HF)[e]	−10.4	−11.8	−11.6	−38.7
	high level	−9.0	−10.7	−11.8	−23.9
	low level	−1.4	−1.1	0.2	−14.8
5T:34T	ONIOM(MP2:UFF)[f]	−16.6	−26.0	−35.3	−38.6
	high level	−8.5	−10.9	−11.8	−26.3
	low level	−8.1	−15.1	−23.5	−12.3
Expt	H-ZSM-5				−47.6
	FAU	−9	−15.3	−19.6	−43.1

[a] Energies are in kcal/mol. (high level means contribution from a high level of theory: $\triangle E$(model,high); low level means contribution from a low level of theory: $\triangle E$(real, low) − $\triangle E$(model, low)). [b] MP2/6-311+G(2df,2p)//MP2/6-31G(d,p). [c] ONIOM(MP2/6-311+G(2df,2p):M06−2X/6-31G(d,p)//MP2/6-31G(d,p):M06−2X/6-31G(d,p)). [d] ONIOM(MP2/6-311+G(2df,2p):B3LYP/6-31G(d,p)//MP2/6-31G(d,p):B3LYP/6-31G(d,p)). [e] ONIOM(MP2/6-311+G(2df,2p):HF/6-31G(d,p)//MP2/6-31G(d,p):HF/6-31G(d,p)). [f] ONIOM(MP2/6-311+G(2df,2p):UFF//MP2/6-31G(d,p):UFF).

(43) Coker, E. N.; Jia, C.; Karge, H. G. *Langmuir* **2000**, *16*, 1205.

(44) Gutmann, V. *The Donor-Acceptor Approach to Molecular Interactions*; Plenum Press: New York, 1978.

(45) Parrillo, D. J.; Lee, C.; Gorte, R. J. *Appl. Catal., A* **1994**, *110*, 67.

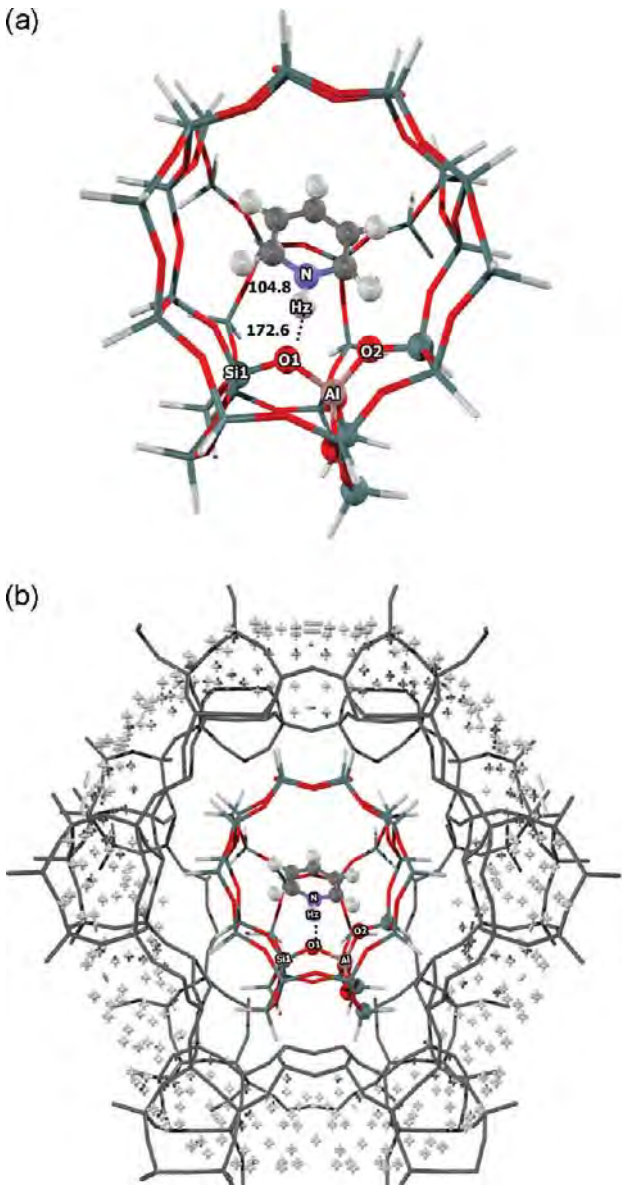

Figure 5. Presentation of a pyridine molecule adsorbed on the 5T:34T model of H-ZSM-5 zeolite (a) without charge embedding and (b) with well-calibrated charge embedding. Atoms treated with the MP2 level of theory are shown in balls, whereas the area treated with a lower level of calculation is symbolized with wireframes. Bond lengths are in picometers.

including the nonlocal interactions, which are a vital contribution from the outer framework, into the calculation.

By using the ONIOM(MP2:M06-2X) scheme in combination with the embedded approach, referred to here as the "embedded ONIOM", we demonstrate that the electrostatic potential from the extended framework plays a much larger role in the stabilization of the adsorption complex of the ion-pair of pyridine cation interacted with anionic zeolite than at the other neutral complexes. Consequently, the zeolite framework effects bring the adsorption energy of the ion-pair complex close to the experimental observation.

Confirmation of the convergence of the model size is listed in Table 2. The ONIOM(5T:128T) calculations were performed for all nonpolar adsorbates and found to give no difference in the energy (−13.3 vs −13.6 kcal/mol for ethene, −18.4 vs −19.0 kcal/mol for benzene, and −23.3 vs −23.6 kcal/mol for ethylbenzene). Therefore, the ONIOM(5T:34T) model is large enough for the chemical prediction. From the table, we also found that adsorption energies derived from those of the ONIOM(5T:128T) (−47.0 kcal/mol) and embedded ONIOM (−48.4 kcal/mol), where long-range electrostatic interactions have been included, can be compared well with the experimental data (−47.6 kcal/mol) for the case of the ion-pair system. Moreover, it should be noted that adsorption energies from M06-2X/6-31G(d,p) with the 34T quantum cluster and the ONIOM(MP2:M06-2X) with the 5T:34T are in good agreement with each other.

3.3. Benzene and Ethylbenzene Hydrogen Exchange in ZSM-5 Reaction. The well thought-out combined method of ONIOM(MP2:M06-2X) with the 34T model is used to study the H/H exchange reaction of the adsorbates. Generally, the H/D exchange can be described as an electrophilic aromatic substitution.[46−49] The reaction mechanism is composed of (1) the attack of the Brønsted proton at the aromatic ring, which is protonated to yield a σ complex, and (2) the decomposition of the complex by transferring a proton to the negatively charged framework oxygen in the local structure. One can also consider that the adsorbates and the zeolite active site exchange their protons, as presented in the chemical eq 1.

$$\mathrm{RCH} + \mathrm{Z(O\mathbf{Hz})} \rightarrow \mathrm{RC\mathbf{Hz}} + \mathrm{Z(OH)} \qquad (1)$$

where RCH in our study represents benzene and ethylbenzene, Z(O**Hz**) is the active site, and **Hz** is the Brønsted proton.

Since ethene and pyridine proceed differently for further chemical steps, only the reactions of benzene and ethylbenzene are investigated. Our prediction is then evaluated with the benchmark of experimental data.[47]

The proton exchange reaction takes place at the bridging OH group of the zeolite. Considering the transition state of the reaction between benzene and the active site, the sp^3 hybridized CB1 atom can be generated from the orginal sp^2 carbon of the benzene. The CB1−H1 bond dissociation is found to correspond to the O2−H1 bond formation. The Brønsted proton (Hz) is leaving the zeolite acid site (O1) for the three-coordinated carbon (CB1). The transition structure is proposed to be in the benzenium cation ($C_6H_7^+$).[48] Receiving the hydrogen atom from benzene, the O2 oxygen acts as a Lewis base. For the orbital insight, it is the sp^3 hybridized carbon (CB1) that proceeds to full aromatization restoration. Similar to the methane case,[49−51] the protonated carbon (CB1) stays in the main plane of the active site and becomes a six-membered transition structure, as shown in Scheme 1.

Figure 6 illustrates the optimized structures of the adsorption, the transition state, and the product for the hydrogen exchange reaction of benzene on the zeolite model. From the normal-mode analysis, one imaginary frequency is identified to confirm the transition structure. Key structural parameters for these structures are shown in Tables S6 and S7 in the Supporting Information.

The reaction starts with the benzene adsorption (AD) over the Brønsted acid site of H-ZSM-5 zeolite, demonstrated in Figure 6. The structural parameters are shown in Table S6. From the

(46) Goncalves, V. L. C.; Rodrigues, R. C.; Lorencato, R.; Mota, C. J. A. *J. Catal.* **2007**, *248*, 158.
(47) Huang, J.; Jiang, Y.; Marthala, V. R. R.; Wang, W.; Sulikowski, B.; Hunger, M. *Microporous Mesoporous Mater.* **2007**, *99*, 86.
(48) Nicholas, J. B. *Top. Catal.* **1997**, *4*, 157.
(49) Ryder, J. A.; Chakraborty, A. K.; Bell, A. T. *J. Phys. Chem. B* **2000**, *104*, 6998.
(50) Zheng, X.; Blowers, P. *J. Mol. Catal. A: Chem.* **2005**, *242*, 18.
(51) Zheng, X.; Blowers, P. *J. Mol. Catal. A: Chem.* **2006**, *246*, 1.

Table 2. Comparison of Model Size and Computational Approach on Adsorption Energies of Ethene, Benzene, Ethylbenzene, and Pyridine Molecule on H-ZSM-5 Zeolite[a]

model	method	ethene	benzene	ethylbenzene	pyridine
5T:34T	ONIOM(MP2:M06-2X)[b]	−13.2	−17.7	−22.2	−43.2
5T:34T	ONIOM(MP2:M06-2X)[c]	−13.3	−18.4	−23.3	−43.7
5T:128T	ONIOM(MP2:M06-2X)[c]	−13.6	−19.0	−23.6	−47.0
5T:34T	embedded ONIOM(MP2:M06-2X)[c]	−14.0	−19.8	−24.7	−48.4
34T	M06-2X[d]	−14.0	−18.2	−22.8	−41.5
Expt	H-ZSM-5				−47.6
	FAU	−9	−15.3	−19.6	−43.1

[a] The ONIOM(MP2:M06-2X) method on the 5T:34T and 5T:128T models, the embedded ONIOM(MP2:M06-2X) method on the 5T:34T model, and the M06-2X quantum calculation on the 34T model. Energies are in kcal/mol. [b] ONIOM(MP2/6-31G(d,p):M06−2X/6-31G(d,p)). [c] ONIOM(MP2/6-311+G(2df,2p):M06-2X/6-31G(d,p)//MP2/6-31G(d,p):M06-2X/6-31G(d,p)). [d] M06-2X/6-31G(d,p)//ONIOM(MP2/6-31G(d,p):M06−2X/6-31G(d,p)).

Scheme 1

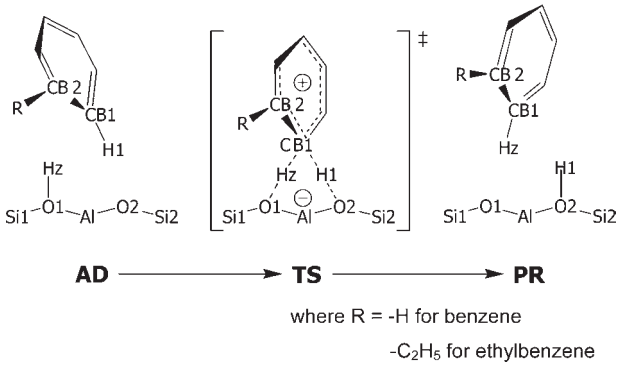

adsorption state, the acidic proton points to the benzene ring. The intermolecular distances were measured from the CB1 and CB2 of benzene to the zeolite acid. From the optimized structure with the ONIOM calculation, the adsorption distances grow significantly larger to 227.7 and 246.5 pm. Moreover, the acidity of the framework-included model in the adsorption state is more pronounced as the acid bond length is increased from 97.8 to 98.4 pm. The O−Hz bond length in the adsorption complex is barely changed from the bare model (97.0 pm). From the transition structure (TS), the optimized geometry is consistent with the asymmetric exchange of the protons. Hz···CB1 was found to be 118.2 pm long, whereas the H1···CB1 distance is 122.4 pm. The extended O1−Hz bond of 151.4 pm corresponds to the shortened Hz−CB1 intermolecular distance of 118.2 pm. The aromaticity of the benzene remains the same as the CB1−CB2 distance and is constant along the reaction. From a frequency calculation of the transition state geometry, the imaginary frequency of 605i cm^{-1} corresponds to the exchange. In the product formation (PR) shown in Figure 6, CB1···H1 becomes the definition of the intermolecular distance for the product/zeolite complex. It is calculated to be 234.0 pm, similar to the Hz···CB1 and Hz···CB2 values in the adsorption state. Like the reactant adsorption, benzene in the product state is located at the nanocavity, close to the zigzag channel, owing to the influence from the zeolite framework.

Now we will discuss the energetics of the reaction. The calculated energies are reported in Table 3. As mentioned in the previous section, the adsorption energies, before and after the framework addition, are −12.1 and −18.4 kcal/mol, respectively. The framework inclusion not only stabilizes the molecular adsorption, but also the transition structure. Thus, the reaction energies from both the quantum cluster and the ONIOM scheme are insignificantly different. The relative energy of the transition is also found to be greatly reduced from 22.7 to 12.6 kcal/mol while the surrounding framework is considered with the ONIOM calculation. The calculated apparent activation energy of 12.6 kcal/mol corresponds with the experimental apparent activation energy of 11.0 kcal/mol.[47] Because of the lack of information for adsorption energy from experiment, we could not compare the calculated actual activation energy with the experimental one. From the energies of the adsorption and transition, the actual activation energy is found to be 31.0 kcal/mol. It is logical that less energy is required for the reaction of benzene than methane and ethane since the electron delocalization of the benzene ring stabilizes the transition state structure. The reaction is found to be 4.1 kcal/mol endothermic. From the accurate apparent activation energy, it is obvious that using the M06-2X method for taking the framework effect into account for the calculation remarkably improves the computational prediction.

For the reactant with a larger molecular size, ethylbenzene is studied. Its adsorption and reaction are analogous with the benzene case. It was reported that *meta*-substituted alkylbenzenes showed noticeably less exchange than the *ortho* or *para* isomers.[52] Further considering the steric hindrance, the *ortho* postition is the most preferential for the proton exchange. At the site, the H1 transfer from ethylbenzene to zeolite oxygen (O2) is simultaneous with the Hz transfer back to the adsorbate (CB1). The mechanism is illustrated in Scheme 1.

Upon the adsorption (AD), the zeolite acid bond length is elongated as in the previous cases and becomes even more elongated when the framework is taken into account. From Table S7 in the Supporting Information, the distances are 97.9 pm for the 5T cluster (from 96.7 pm) and 98.3 pm for the ONIOM model (from 97.0 pm). A more distinct change is found compared to the benzene adsorption. A less asymmetric exchange of the protons is observed from the transition structure (TS), compared to the benzene case. Optimized with the ONIOM calculation, the Hz···CB1 was found to be 117.2 pm long, whereas the H1···CB1 distance is 119.5 pm. We found that the O1−Hz bond (153.6 pm) is more extended than the one in the benzene reaction (151.4 pm). This leads us to expect that both the activation energy and the energy barrier will be lower than the values of the previous reaction. Other structural changes correspond to the reaction coordinate. During the transition, the aromaticity of ethylbenzene is stable as the CB1−CB2 distance hardly changes. The imaginary frequency of 282i cm^{-1} of the transition geometry corresponds to the exchange. When the product is completely formed (PR), the intermolecular distance (CB1···H1) was predicted to be 296.4 pm, which is slightly larger than the value in the first step (240.6 pm). The illustration of the product adsorption at the active site is presented in Figure 7. Like the reactant adsorption, the product is held over the intersection close to the zigzag channel.

(52) Hawthorne, S. B.; Miller, D. J. *Anal. Chem.* **1985**, *57*, 694.

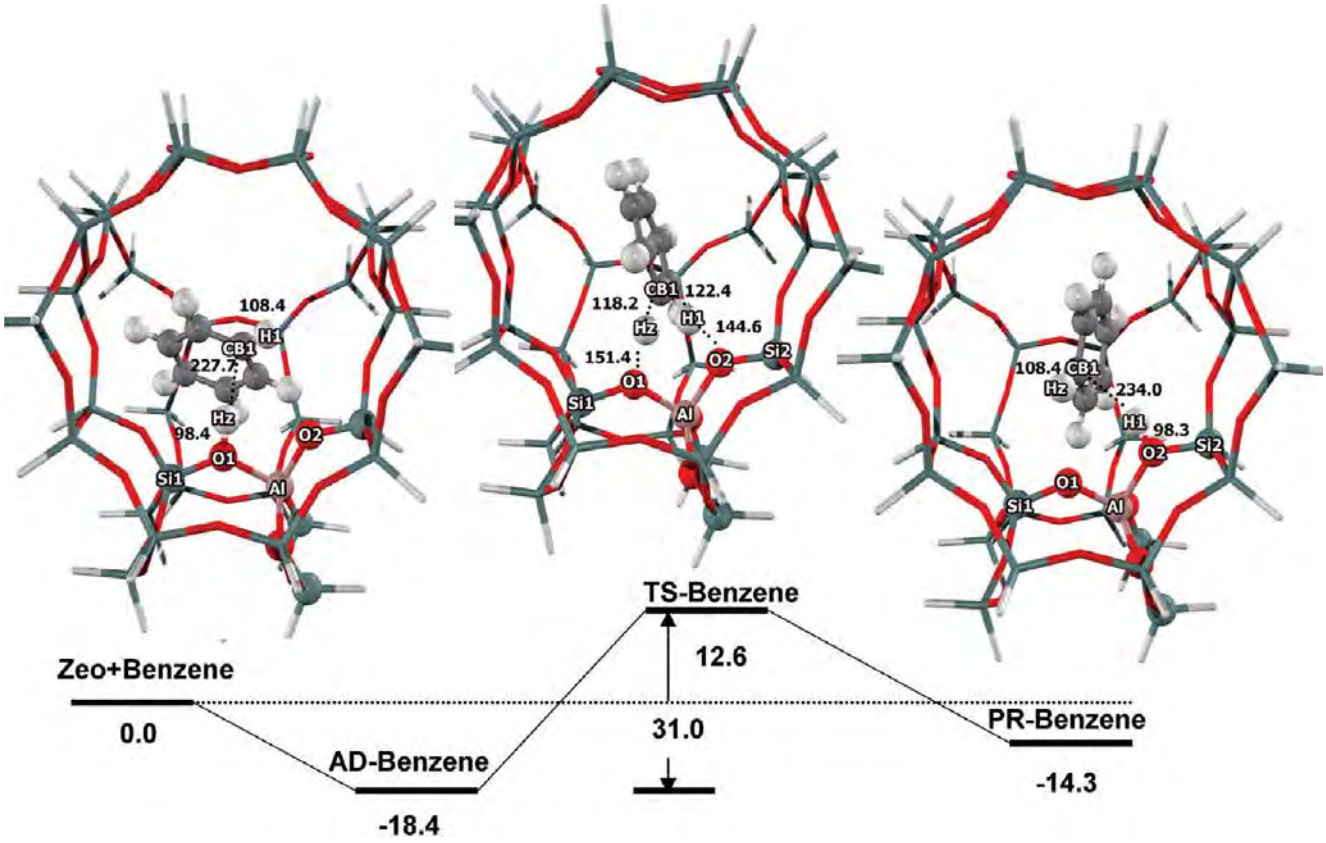

Figure 6. Energy profile for the proton exchange of benzene on the 5T:34T model of H-ZSM-5 zeolite calculated by the ONIOM(MP2/6-311+G(2df,2p):M06-2X/6-31G(d,p)//MP2/6-31G(d,p):M06-2X/6-31G(d,p)) method. Atoms treated with the MP2 level of theory are shown in balls, whereas the area treated with a lower level of calculation is symbolized with wireframes. Bond lengths are in picometers and energies are in kcal/mol.

Table 3. Reaction Energies for the H/H Exchange Reaction of Benzene and Ethylbenzene on Various Models of H-ZSM-5 Zeolite Calculated with Different Methodologies[a]

		benzene			ethyl benzene		
model	method	AD	TS	PR	AD	TS	PR
5T	MP2[b]	−12.1	**22.7** (34.8)	−8.6	−13.9	**19.8** (33.7)	−10.4
5T:34T	ONIOM(MP2:M06-2X)[c]	−18.4	**12.6** (31.0)	−14.3	−23.3	**4.6** (27.9)	−20.6
5T:128T	ONIOM(MP2:M06-2X)[c]	−19.0	**12.6** (31.6)	−13.7	−23.6	**4.9** (28.5)	−20.6
5T:34T	embedded ONIOM(MP2:M06-2X)[c]	−19.8	**10.4** (30.2)	−14.1	−24.7	**1.9** (26.6)	−21.9
34T	M06-2X[d]	−18.2	**13.5** (31.7)	−14.2	−22.8	**4.9** (27.7)	−20.0
Expt	H-ZSM-5		**11.0**			**6.9**	

[a] Apparent activation energies are presented in bold type, while intrinsic activation energies are in parentheses. Energies are in kcal/mol. [b] MP2/6-311+G(2df,2p)//M06-2X/6-31G(d,p). [c] ONIOM(MP2/6-311+G(2df,2p):M06-2X/6-31G(d,p)//MP2/6-31G(d,p):M06-2X/6-31G(d,p)). [d] M06-2X/6-31G(d,p)//ONIOM(MP2/6-31G(d,p):M06-2X/6-31G(d,p)).

The calculated energies for the reaction are reported in Table 3. The adsorption energy almost doubled as a result of the framework effect, from −13.9 to −23.3 kcal/mol, as previously discussed. The explanation of this is given in the discussion on the benzene reaction. The relative energy for the transition structure is found to be 19.8 and 4.6 kcal/mol for bare quantum 5T and ONIOM(5T:34T) models, respectively. Considering the experimental estimate of the apparent activation energy (6.9 kcal/mol), the ONIOM(MP2:M06−2X) method gives us the prediction for the value of 4.6 kcal/mol, which is comparable to the benchmark. The energy barrier is calculated to be 27.9 kcal/mol. Compared to the predicted barrier of the benzene reaction (31.0 kcal/mol), it is

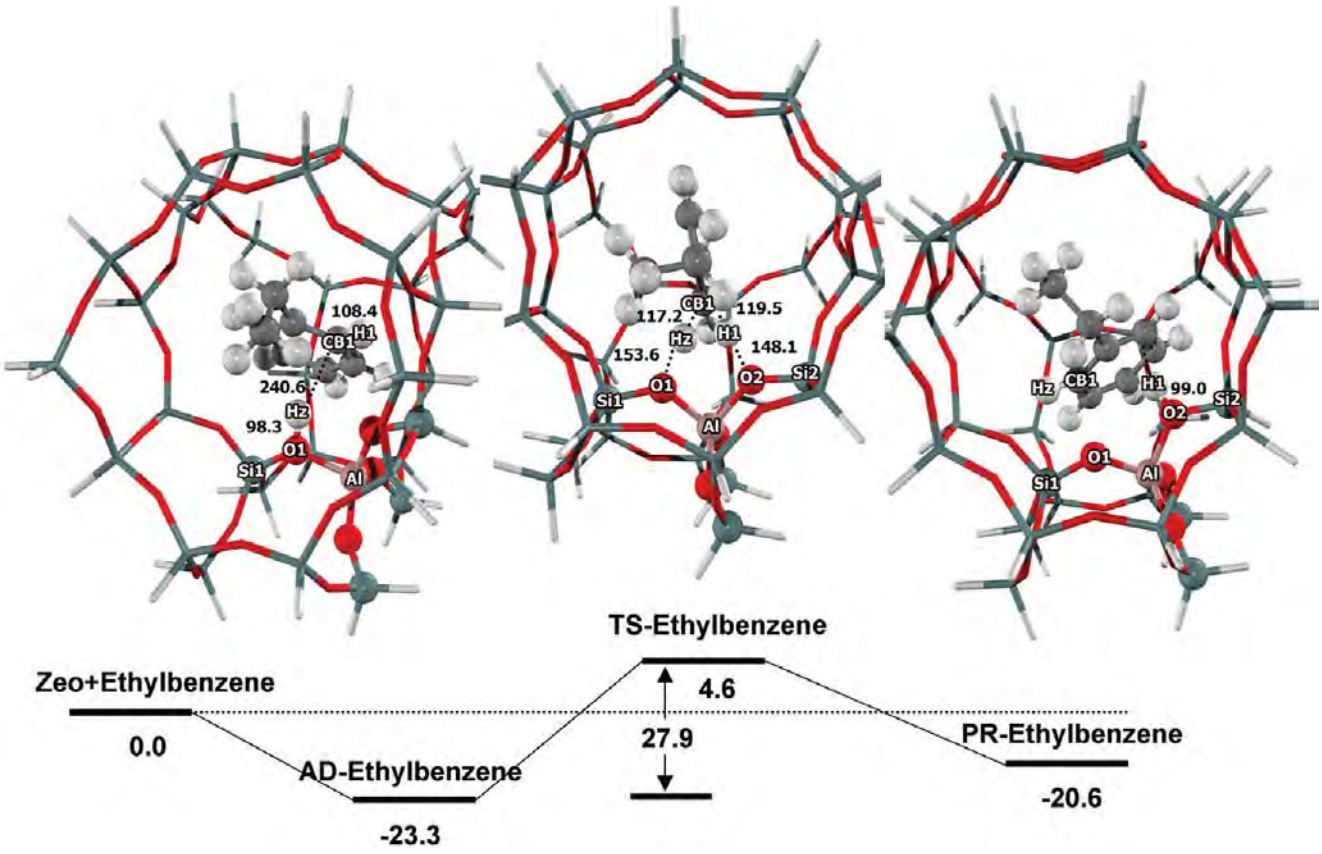

Figure 7. Energy profile for the proton exchange of ethylbenzene on the 5T:34T model of H-ZSM-5 zeolite calculated using the ONIOM-(MP2/6-311+G(2df,2p):M06-2X/6-31G(d,p)//MP2/6-31G(d,p):M06-2X/6-31G(d,p)) method. Atoms treated with the MP2 level of theory are shown in balls, whereas the area treated with a lower level of calculation is symbolized with wireframes. Bond lengths are in picometers and energies are in kcal/mol.

in good agreement with an alkyl group bound to aromatic rings that decrease the energy barrier for the ring protonation or methylation.[46,53]

The energy prediction for the proton exchange reactions of benzene and ethylbenzene to the H-ZSM-5 zeolite with the ONIOM(MP2:M06-2X) approach successfully reproduced the experimental observations. The energies for the adsorption, transition state, and product are computed to be −18.4, 12.6, and −14.3 kcal/mol for benzene (see Figure 6) and −23.3, 4.6, and −20.6 kcal/mol for ethylbenzene (see Figure 7), respectively. The apparent activation energy (the same as the transition structure's relative energy) agrees well with the experimental data for both reactions.[47] We therefore propose that the combined methodology of the ONIOM(MP2:M06-2X) method and the 5T:34T model is practical for the study of the framework effect on the adsorption and the reaction for such molecules in the zeolite pore.

4. Conclusions

Chemical insight on the adsorption and the H/H exchange reaction of ethene, benzene, ethylbenzene, and pyridine on H-ZSM-5 zeolite were investigated with the ONIOM scheme associated with the combination of the MP2 method and various lower level approaches including M06-2X, B3LYP, HF, UFF. This is the first time that a newly developed density functional, M06-2X, is combined with the MP2 method to perform the ONIOM calculation. The H-ZSM-5 model was carefully calibrated to be 5T:34T for the ONIOM(MP2:M06-2X) calculation. The adsorption energies of ethene, benzene, ethylbenzene, and pyridine on H-ZSM-5 from the ONIOM(MP2:M06-2X) plus long-range electrostatic contributions corrected, are predicted to be −14.0, −19.8, −24.7, and −48.4 kcal/mol, respectively, which are very close to experimental observations if available. The adsorption energy of pyridine agrees well with the experiment data of −47.6 kcal/mol. The ONIOM(MP2:M06-2X) approach can well describe the reaction mechanisms for the proton exchange reactions of benzene and ethylbenzene on H-ZSM-5 zeolite and successfully reproduce experimental observations. Energies for adsorption, transition state, and product are computed to be −18.4, 12.6, and −14.3 kcal/mol for benzene and −23.3, 4.6, and −20.6 kcal/mol for ethylbenzene, respectively. Therefore, the ONIOM(MP2:M06-2X) approach is recommended to represent the framework effect on the reacting molecule within the zeolite pore for both studies of adsorption and reaction.

Acknowledgment. This work was supported in part by grants from the National Science and Technology Development Agency, (NSTDA Chair Professor and NANOTEC Center of Excellence), the Thailand Research Fund and the Kasetsart University Research and Development Institute (KURDI), the Commission on Higher Education as well as the Ministry of Education, under the Postgraduate Education and Research Programs in Petroleum and Petrochemicals, and Advanced Materials. The authors are grateful to Donald G. Truhlar and Yan Zhao for their support with the M06-2X functional.

(53) March, J. *Advanced Organic Chemistry: Reactions, Mechanisms, and Structure*, 4th ed.; McGraw-Hill Press: New York, 1992.

Supporting Information Available: Tables S1−S7: Selected geometrical parameters for adsorption and reaction mechanism of ethene, benzene, ethylbenzene, and pyridine on H-ZSM-5 zeolite with various methods. Tables S8−S11: The adsorption and reaction energies of ethene, benzene, ethylbenzene, and pyridine on H-ZSM-5 zeolite with various methods. Table S12: comparison of CPU time for different zeolite models at different levels of theory. This material is available free of charge via the Internet at http://pubs.acs.org.

Adsorption and Tautomerization Reaction of Acetone on Acidic Zeolites: The Confinement Effect in Different Types of Zeolites

Bundet Boekfa,[†,‡,§] Piboon Pantu,[†,‡,§] Michael Probst,[⊥] and Jumras Limtrakul*[,†,‡,§]

Laboratory for Computational and Applied Chemistry, Department of Chemistry, Faculty of Science, Kasetsart University, Bangkok 10900, Thailand, Center of Nanotechnology, Kasetsart University Research and Development Institute, Kasetsart University, Bangkok 10900, Thailand, NANOTEC Center of Nanotechnology, National Nanotechnology Center, Kasetsart University, Bangkok 10900, Thailand, and Institute of Ion Physics and Applied Physics, University of Innsbruck, A-6020 Innsbruck, Austria

Received: June 26, 2010; Revised Manuscript Received: August 4, 2010

The adsorption and tautomerization reaction of acetone in H-FER, H-ZSM-5, and H-MCM-22 zeolites has been studied using full quantum calculations at the M06-2X/6-311+G(2df,2p) level of theory. The combination of a large quantum cluster and this meta-hybrid density functional results in reasonably accurate adsorption energies of −26.9, −28.1, and −23.9 kcal/mol for acetone adsorption in H-FER, H-ZSM-5, and H-MCM-22, respectively. Due to the acidity of the zeolite and the framework confinement effect, the tautomerization of acetone proceeds through a much lower activation barrier than in the isolated gas phase or in the presence of water molecules alone. The activation energies are calculated to be 24.9, 20.5, and 16.6 kcal/mol in H-FER, H-ZSM-5 and H-MCM-22, respectively. The endothermic reaction energy decreases with increasing of the zeolite pore sizes and amounts to 22.7, 17.6, and 15.9 kcal/mol for the reaction in H-FER, H-ZSM-5 and H-MCM-22, respectively. In addition, the adsorbed acetone enol is found to be highly unstable in the zeolite framework and readily reverse-transforms to adsorbed acetone with a very small activation energy. The activity trend and relative stabilities of the adsorbed keto and enol forms are well correlated with the interactions within the Brønsted acid site.

1. Introduction

Aldol condensation is one of the most important C−C bond forming reactions for organic synthesis.[1−3] Aldol condensation of acetone can be readily catalyzed by acidic or basic reagents. In a confined space of microporous zeolites, reactions of acetone over the Brønsted acid site selectively produce mesityl oxide.[4−7] The mesityl oxide can be hydrogenated to produce methyl isobutyl ketone, which is widely used as a solvent for paints, lacquers, and certain types of polymers and resins. The process can be carried out in a single step over bifunctional catalysts (e.g., Pt/H-ZSM-5,[8] Pd/H-MCM-22,[9] etc.). Aldol condensation is very important for the transformation of acetone to methyl isobutyl ketone.[4−6]

Acetone tautomerization to the enol form is an important initial step of aldol condensation and many reactions of acetone.[1−3] The activity of tautomerization dependents on the acidity and the ionic strength of the reaction media. The fundamental steps of the aldol condensation in acidic zeolites are believed to be similar to the reaction in solution.[4−7] The mechanism consists of the acid-catalyzed tautomerization of acetone. Acetone is transformed to an α,β-unsaturated carbonyl compound. A number of theoretical studies on keto−enol tautomerization of acetaldehyde and acetone have been reported.[10−15] Previous theoretical calculations reported that in the gas phase, acetone tautomerization requires a high activation energy of 64.0−69.2 kcal/mol.[11−15] In solvent-assisted systems, the presence of water molecules can greatly reduce the energy barrier by about 20−30 kcal/mol.[12−15] Theoretical results for the tautomerization reaction over a zeolite catalyst have also been reported[15,16] with the synergistic functions of Brønsted acid and Lewis basic sites on H-ZSM-5, drastically reducing the barrier height for the tautomerization of acetaldehyde to 20.2 kcal/mol.[15]

The interaction between the zeolite framework and an adsorbed molecule, which is generally called the confinement effect,[17,18] also plays an important role for the adsorptions and reactions on zeolites.[17−23] Therefore, the details of the interactions between the reactants and the active site in the zeolite's framework and the influence of the topology close to the active site are important to completely understand the reaction mechanism inside zeolite pores. Recently, the role of the zeolite confinement effect on reactions of unsaturated aliphatic, aromatic and heterocyclic compounds has been successfully studied[24] by using full quantum calculations with the new density functional M06-2X.[25−27]

In this work, we study the mechanism of acetone tautomerization and relative stabilities of the keto and enol form in the isolated phase, in the presence of assisting water molecules, and in zeolite-catalyzed environments. Our aim is to investigate the effects of confinement in different zeolite structures on the tautomerization of acetone. Three different zeolites (H-FER, H-ZSM-5, and H-MCM-22) with different dimensions of pores and cavities are selected for this investigation. Sufficiently large clusters are used to represent the zeolite structures, and the full quantum chemical calculations using the M06-2X method are performed to attempt to account for all interactions between

* Corresponding author. Phone: +66-2-562-5555 ext 2159. E-mail: jumras.l@ku.ac.th.
† Department of Chemistry, Kasetsart University.
‡ Kasetsart University Research and Development Institute, Kasetsart University.
§ National Nanotechnology Center, Kasetsart University.
⊥ Institute of Ion Physics and Applied Physics, University of Innsbruck.

10.1021/jp1058947
Published on Web 08/19/2010

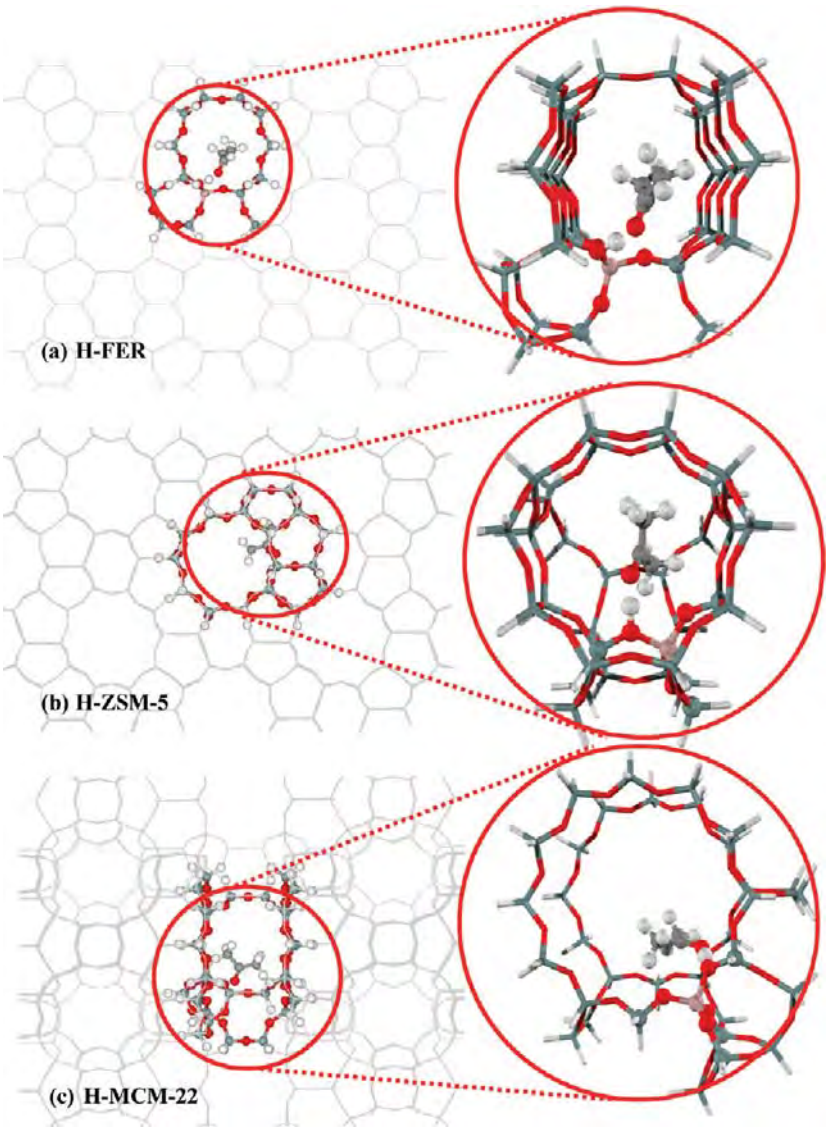

Figure 1. Optimized structures of acetone adsorbed on the 34T model of (a) H-FER, (b) H-ZSM-5, and (c) H-MCM-22 zeolites.

the reactive intermediates and the zeolite acid site and surrounding pore walls.

2. Methodology

34T clusters were taken from crystallographic data of H-FER, H-ZSM-5, and H-MCM-22 zeolites.[28−30] The cluster model of H-FER zeolite covers the 10-membered ring main channel (4.2 × 5.4 Å) that is intersected with the 8-membered ring channel (3.5 × 4.8 Å), as shown in Figure 1a. One silicon atom at the T2 site[31] is replaced with an aluminum atom to represent the Brønsted acid site. The model of H-ZSM-5 represents the intersection cavity where the straight channel (5.4 × 5.6 Å) and the zigzag channel cross (5.1 × 5.4 Å), as shown in Figure 1b. A silicon atom was substituted with an aluminum atom at the most favorable position (T12).[32] The cluster model of H-MCM-22 represents the 12-membered ring channels of the supercage (7.1 × 7.1 × 18.4 Å), as shown in Figure 1c. The substituted aluminum atom is located at the T1 site.[33]

The M06-2X density functional is used in all calculations. During geometry optimizations, only the 5T active region of ≡SiOHAl(OSi)$_2$OSi≡ and the reacting molecule are allowed to relax, while the rest of the structure is kept fixed at the crystallographic coordinates. We also study the reaction of an isolated acetone molecule and the reaction in the presence of water molecules. For geometry optimizations, the 6-31G(d,p) basis set was used. To obtain more accurate interaction energies, single-point calculations with the 6-311+G(2df,2p) basis set were carried out. Transition states were located with the Berny algorithm[34,35] and were checked to confirm that they had one imaginary frequency corresponding to the reaction coordinate. We did not include the zero-point vibrational contributions (ZPVE) to the energies, since the systems are too large to calculate the matrix of second energy derivatives with the M06-2X functional in reasonable time. We are also not aware that this has been performed on systems of similar size. Curtis et al. have performed a study on ethane absorbed on small 3T and 5T clusters.[36,37] They found close agreement between results from G2(MP2) (including ZPVE) and MP2/6-31G(d,p) calculations not including ZPVE, due to cancellation of various effects. We assume that also in our work, the relative changes caused by inclusion of the ZPVE are less than the errors inherent in the functional and basis set. All calculations were performed with the Gaussian 03 code[38] modified to incorporate the Minnesota Density Functionals module 3.1 by Zhao and Truhlar.

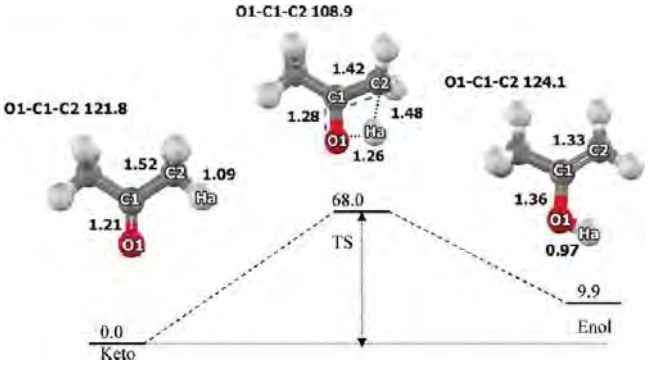

Figure 2. Molecular structures and energy profile of the tautomerization of acetone in an uncatalyzed gas phase environment (M06-2X/6-311+G(2df,2p)//M06-2X/6-31G(d,p) calculations). Distances and energies are given in Å and kcal/mol.

3. Results and Discussion

3.1. Tautomerization of Acetone in the Gas Phase. The uncatalyzed tautomerization of acetone has been extensively studied and was found to occur via a concerted mechanism.[11−15] In this study, we therefore examine the concerted tautomerization mechanism of acetone to validate the applicability of the new density functional M06-2X. Figure 2 shows the potential energy profile and the geometries of acetone, the transition state, and the enol product computed at the M06-2X/6-311+G(2df,2p)//M06-2X/6-31G(d,p) level of theory. At the transition state, the intramolecular proton transfer from the methyl group to the carbonyl oxygen atom takes place. The C2−Ha bond distance increases to 1.48 Å and the O1−Ha decreases to 1.26 Å. At the same time, the C1−O1 carbonyl bond increases from 1.21 to 1.28 Å and the C1−C2 bond length decreases from 1.52 to 1.42 Å. The activation energy is calculated to be 68.0 kcal/mol, and the reaction energy is 9.9 kcal/mol. The computed activation energy and reaction energy agree well with previous theoretical studies that employed the Møller−Plesset perturbation theory.[12,14] In those studies, the activation energies were found to be 64.0 and 69.2 kcal/mol, and the reaction energies were 11.6 and 13.1 kcal/mol. The reaction energies computed in this study are also in reasonable agreement with the experimental results of 12 ± 2 kcal/mol.[39,40]

3.2. Tautomerization of Acetone in Aqueous Solution. For aqueous solutions, it has previously been reported that water molecules can reduce the energy barrier by stabilizing the transition state with hydrogen bonds.[11−15] The tautomerization reaction occurs via cyclic proton transfer networks with water molecules acting as proton donors and acceptors facilitating the reaction. The optimized geometries and energy profiles are presented in Figure 3. The reaction is considered to proceed via the concerted mechanism similar to the reaction in the isolated gas phase. In the presence of a water molecule, acetone interacts with the water molecule by forming 2 hydrogen bonds. Then two protons are transferred simultaneously through the hydrogen bonding network. With two and three additional water molecules, stronger and larger hydrogen bonding networks are formed, as indicated by shorter hydrogen bond distances and angles that are closer to the linear angles of the hydrogen bonds (O···H···O). The addition of water molecules results in a significant reduction of activation energy. The computed activation energies at the M06-2X/6-311+G(2df,2p)//M06-2X/6-31G(d,p) level of theory are 40.2, 32.7, and 33.6 kcal/mol and the reaction energies are 9.7, 7.8, and 8.2 kcal/mol, for the presence of 1, 2, and 3 water molecules, respectively. These results agree well with a previous theoretical study[14] at the MP2/cc-pVTZ//MP2/6-31G(d,p) level, which included the zero-point vibrational energy correction and reported activation energies of 37.5, 30.4, and 29.1 kcal/mol for the presence of 1, 2, and 3 water molecules, respectively. The computed reaction energies in the presence of water molecules were reported to be similar to the reaction energy in the gas phase. The measured reaction enthalpy in aqueous solution was reported as 10.3 ± 0.4 kcal/mol,[41] very close to the gas phase value. Therefore, we conclude that the M06-2X method can give reasonably accurate results for the activation energy and reaction energy of acetone tautomerization as compared with the high level of calculations.

3.3. Tautomerization of Acetone in Zeolites. ***3.3.1. Structure of the Zeolites.*** In this study, we examine the tautomerization of acetone in three different zeolites.[25−27] These three zeolites can be synthesized with a high Si/Al ratio. Therefore, for the sake of model simplicity, we use a single Brønsted acid as an active site for these high silica zeolites. The Brønsted acid is placed on the favorable sites predicted by previous theoretical studies.[31−33] H-FER zeolite has a two-dimensional pore structure with a main straight channel and a smaller channel. The two channels are perpendicular and intersected. In the model used in this study, the Brønsted acid is located at the most favorable position (T2)[31] at the intersection of the 10T main channel (4.2 × 5.4 Å in diameter) and the 8T channel (3.5 × 4.8 Å in diameter) (see Figure 1a). The O1−Hz bond leans toward the middle of the small 8T channel with an angle of about 30° to the axial direction of the 10T main channel.

H-ZSM-5 zeolite is a three-dimensional pore zeolite. The Brønsted acid is located at the T12 position[32] on the window of the zigzag channel that is connected to the intersection cavity. The employed model represents the intersection cavity of ∼9 Å in diameter where the straight channel (10-membered ring, 5.4 × 5.6 Å in diameter) and the zigzag channel (10-membered ring, 5.1 × 5.4 Å in diameter) intersect (see Figure 1b).

H-MCM-22 is also a three-dimensional pore zeolite. The main straight channel is a 10-membered ring having dimensions of 4.0 × 5.5 Å in diameter. It opens to a large cavity called the supercage (7.1 × 7.1 × 18.4 Å). In this study, we consider the acid site to be located on the 12-membered ring in the supercages.

Despite different pore structures, the O1−Hz Brønsted acid bond distance is approximately the same at 0.97 Å in all three zeolite models. The Al···Hz distances are in the range of 2.30−2.43 Å, which compared well with the experimental values of 2.38−2.48 ± 0.04 Å.[42,43]

3.3.2. Acetone Adsorption on H-FER, H-ZSM-5 and H-MCM-22. The optimized structures of acetone adsorbed on the three zeolites are shown in Figure 1, and selected geometric parameters are given in Table 1. In H-FER, an acetone molecule forms a hydrogen bond between its carbonyl oxygen (O3) and the Brønsted acidic proton (Hz). The adsorbed acetone molecule is located in the 10T main channel. The O1−Hz−O3 hydrogen bond angle is 165.8°. This deviation from the linear hydrogen bond angle is due to the alignment of the Brønsted O−H that initially leans toward the small 8T window. The adsorption energy is computed to be −26.9 kcal/mol. In the H-ZSM-5 zeolite, the acetone molecule adsorbs by forming a strong hydrogen bond with the Brønsted acid site. The O1−Hz−O3 bond angle (177.6°) is close to linear, and the adsorption energy is computed to be −28.1 kcal/mol. This value agrees reasonably with an experimental report of the adsorption energy of acetone in H-ZSM-5 of −31.1 kcal/mol.[44] In the large cavity of H-MCM-22, acetone also forms a strong hydrogen bond with the Brønsted acid site on the 12T-membered ring of the

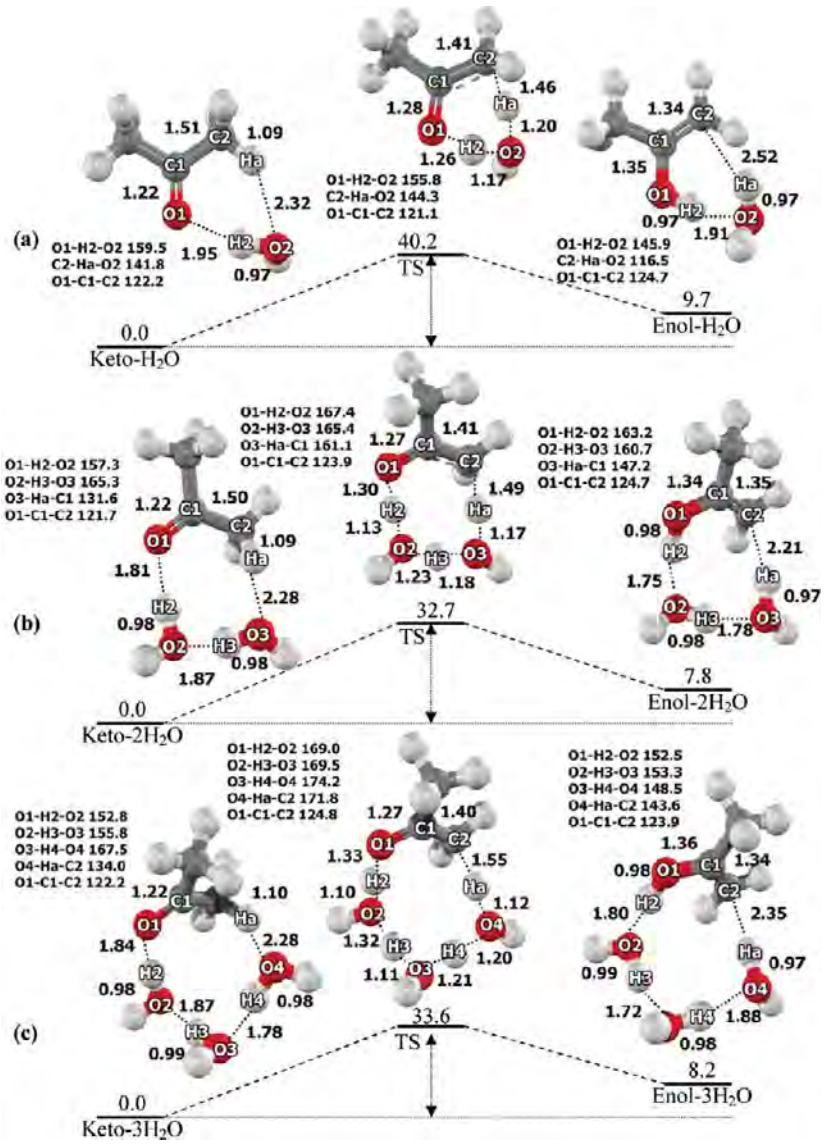

Figure 3. Energy profile and complex geometries in the water-assisted tautomerization of acetone from M06-2X/6-311+G(2df,2p)//M06-2X/6-31G(d,p) calculations: (a) one, (b) two, and (c) three water molecules.

supercage. The O1−Hz−O3 bond angle (171.7°) is also close to linear. The adsorption energy is −23.9 kcal/mol.

The computed adsorption energy is found to be dependent on the pore dimension and also on the local geometry of the Brønsted acid site. H-FER is a medium-pore zeolite with a smaller pore dimension as compared with H-ZSM-5, but the geometry of the Brønsted acid site is not suitable for the adsorption of the acetone molecule. Initially, the acid site bond points toward the small 8T window that is too small to accommodate an acetone molecule. The adsorbed acetone molecule has to be located in the 10T main channel. Therefore, the O1−Hz−O3 hydrogen bond angle deviates from linearity. As a result, the interaction of acetone with the Brønsted acid site in H-FER is not as strong as in H-ZSM-5. The adsorption energy in the medium pore H-ZSM-5 is higher than the large pore H-MCM-22 mainly due to the pore confinement effect.

In our previous work,[20] we demonstrated that in studies of the adsorption of carbonyl compounds in zeolites both van der Waals and electrostatic interactions have to be carefully accounted for. We were able to calculate the adsorption energies of acetaldehyde and acetone in H-ZSM-5 by using the embedded ONIOM(B3LYP:UFF) method. With small cluster models, the computed adsorption energy is underestimated by as much as 16 kcal/mol. In the embedded ONIOM(B3LYP:UFF) method, the UFF force field was used to explicitly account for the short-range van der Waals interactions with the surrounding pore walls, and the embedded Madelung potential was used to account for the long-range electrostatic interactions with the zeolite framework. It has been demonstrated that the short-range van der Waals interactions and the long-range electrostatic interactions with the zeolite framework are both very important to the stabilization of the adsorbed carbonyl compounds in zeolite.

In this work, aiming at higher accuracy, we decided to use a large quantum cluster (34T) model calculated with the meta-hybrid M06-2X method that can account for those two important interactions in the zeolite framework simultaneously. The computed results compared well with the experimental measurement, especially in the case of H-ZSM-5. Therefore, we believe that the combination of models and methods presented here is appropriate for investigation of the interactions and reactions of acetone with the Brønsted acid site of zeolites.

TABLE 1: Optimized Structural Parameters of the Acetone/Zeolite Cluster Complexes in the Three Zeolites As Obtained from M06-2X/6-31G(d,p) Calculations

	H-FER				**H-ZSM-5**				H-MCM-22			
	bare	AD	TS	PR	bare	AD	TS	PR	bare	AD	TS	PR
						Distance						
Si1−O1	1.67	1.64	1.59	1.59	1.65	1.63	1.59	1.58	1.67	1.63	1.60	1.60
Si2−O2	1.58	1.57	1.64	1.66	1.59	1.57	1.62	1.64	1.60	1.59	1.64	1.65
O1−Al	1.87	1.81	1.72	1.71	1.82	1.78	1.71	1.69	1.80	1.75	1.69	1.68
O2−Al	1.67	1.67	1.79	1.82	1.68	1.69	1.77	1.80	1.67	1.68	1.76	1.77
Al ··· Hz	2.30	2.44	2.93	3.01	2.35	2.45	3.19	3.52	2.43	2.43	3.06	3.08
O1−Hz	0.97	1.10	1.74	1.83	0.97	1.11	1.80	2.08	0.97	1.16	1.90	1.94
Hz ··· O3		1.36	0.99	0.98		1.32	0.99	0.97		1.24	0.98	0.97
O1 ··· O3		2.43	2.71	2.80		2.42	2.74	2.91		2.39	2.70	2.73
O3−C1	1.21	1.23	1.32	1.34	1.21	1.23	1.31	1.33	1.21	1.24	1.31	1.32
C1−C2	1.52	1.50	1.38	1.36	1.52	1.49	1.38	1.36	1.52	1.49	1.38	1.37
C2−Ha	1.09	1.09	1.56	1.92	1.09	1.10	1.43	1.76	1.09	1.09	1.50	1.60
C1 ··· Ha	2.14	2.14	2.24	2.46	2.14	2.10	2.07	2.25	2.14	2.14	2.19	2.23
Ha ··· O2		2.36	1.14	1.02		2.67	1.20	1.04		2.81	1.14	1.09
O1 ··· O2	2.56	2.59	2.65	2.66	2.49	2.52	2.54	2.52	2.60	2.63	2.62	2.61
C1 ··· O1		3.23	3.30	3.37		3.23	3.27	3.37		3.20	3.21	3.23
C1 ··· O2		3.60	3.20	3.31		3.09	3.09	3.19		3.64	3.18	3.18
C2 ··· O2		3.33	2.67	2.89		2.99	2.63	2.79		3.03	2.63	2.68
						Angle						
Al−O1−Si1	141.8	139.5	141.5	141.1	130.6	128.4	127.6	127.4	125.0	123.5	123.4	123.2
Al−O2−Si2	150.7	153.0	146.3	146.8	133.3	135.8	133.0	133.0	124.5	125.8	126.0	126.2
O1−Hz−O3		165.8	167.1	167.8		177.6	156.8	142.0		171.7	137.3	136.1
O1−Al−O2	92.5	95.8	98.0	97.8	90.4	93.1	93.7	92.4	97.2	100.0	98.8	98.4

3.3.3. Tautomerization of Acetone on H-FER, H-ZSM-5 and H-MCM-22. The tautomerization of acetone on the Brønsted acid site of zeolite starts by the adsorption of acetone on the active site shown in Figure 4. The acetone molecule is stabilized by forming a hydrogen bond complex with the zeolite acid site. The computed adsorption energies are in the following order: −23.9, −26.9, and −28.1 for H-MCM-22, H-FER, and H-ZSM-5, respectively. These adsorption energies would suggest that the hydrogen bond between the adsorbed acetone and zeolite acid site on H-ZSM-5 is the strongest and on the H-MCM-22 is the weakest. However, when looking at the structural parameters of the optimized complex, it is observed that the hydrogen bond distance (O1···O3) in the H-MCM-22 is the shortest at 2.39 Å and the hydrogen bond angle (O1-Hz-O3) is also close to the linear angle (171.7°), indicating a very strong hydrogen bond interaction. In H-MCM-22, the adsorption causes the Brønsted O1−Hz bond distance to be significantly lengthened from 0.97 to 1.16 Å. The carbonyl double bond (O3−C1) is lengthened from 1.21 to 1.24 Å, and the C1−C2 single bond distance is decreased from 1.52 to 1.49 Å, indicating that the adsorbed acetone is activated. In H-ZSM-5, the hydrogen bond distance (O1···O3) is longer than in H-MCM-22 (2.42 Å). Therefore, the adsorbed acetone is somewhat less activated. The carbonyl double bond (O3−C1) is lengthened to 1.23 Å, and the C1−C2 single bond distance is decreased to 1.49 Å. The hydrogen bond complex in H-FER is observed to have the weakest hydrogen bond interaction. The hydrogen bond angle (O1−Hz−O3) is 165.8°, and the hydrogen bond distance (O1···O3) is 2.43 Å. The adsorbed acetone is, thus, least activated. The O3−C1 bond distance is lengthened to 1.23 Å and the C1−C2 bond distance is slightly decreased to 1.50 Å. At the transition state, the Brønsted proton is completely transferred to the carbonyl oxygen atom. For example, in the case of H-MCM-22, the O1−Hz bond elongates from 1.16 to 1.90 Å. The O3−C1 bond distance increases to 1.31 Å as the O3−Hz hydroxyl bond is formed with a bond length of 0.98 Å. The C1−C2 bond distance is reduced to 1.38 Å, indicating the double bond formation.

The activation energy of acetone tautomerization on the zeolite acid site is much smaller than in the isolated gas phase and in the water-assisted system. The zeolite acid site can greatly reduce the activation barrier. The computed activation energies are 16.6, 20.5, and 24.9 kcal/mol for the reaction in H-MCM-22, H-ZSM-5, and H-FER, respectively. The activation energies for acetone enolization in zeolites are in the same range with the free energy of activation for the reaction catalyzed by diluted mineral acid in aqueous solutions of 23.6 kcal/mol (at 298 K).[41] The activation energy trend is directly related to the strength of the hydrogen bond interactions between the adsorbed acetone and the Brønsted acid site but not to the overall adsorption interactions.

In these three representative cases, the adsorbed acetone molecule can get closer to the acid site in a geometry with larger pores and, thus, form a stronger hydrogen bonds and more activated adsorption complexes. The reaction energies for the transformation of adsorbed keto to enol of acetone are found to be 15.9, 17.6, and 22.7 kcal/mol in H-MCM-22, H-ZSM-5, and H-FER, respectively. These values are significantly higher than the reaction energy observed in diluted solutions of mineral acids (10.3 kcal/mol).[41] The higher endothermic reaction energy is due to the fact that the adsorbed acetone is highly stabilized by a strong hydrogen bond with the acid site but the produced acetone enol is weakly adsorbed on the acid site by a weak π interaction. Among these three zeolites, the difference in the energies between adsorbed acetone and acetone enol decrease with the increase of pore dimensions. However, the observed reaction energy trend is not simply due to the confinement effect of the zeolite walls. It is more likely to be related to the local interaction of the adsorbed enol form with the Brønsted acid site. The large cavity of H-MCM-22 can better accommodate the bulkier acetone enol, as reflected by a closer intermolecular distance of the C2 carbon atom of the adsorbed enol to the Ha proton of the acid site. The distances are 1.60, 1.76, and 1.92 Å for H-MCM-22, H-ZSM-5, and H-FER, respectively.

It is noticed that the structures of the transition state and the product are very similar and the reverse reaction to transform

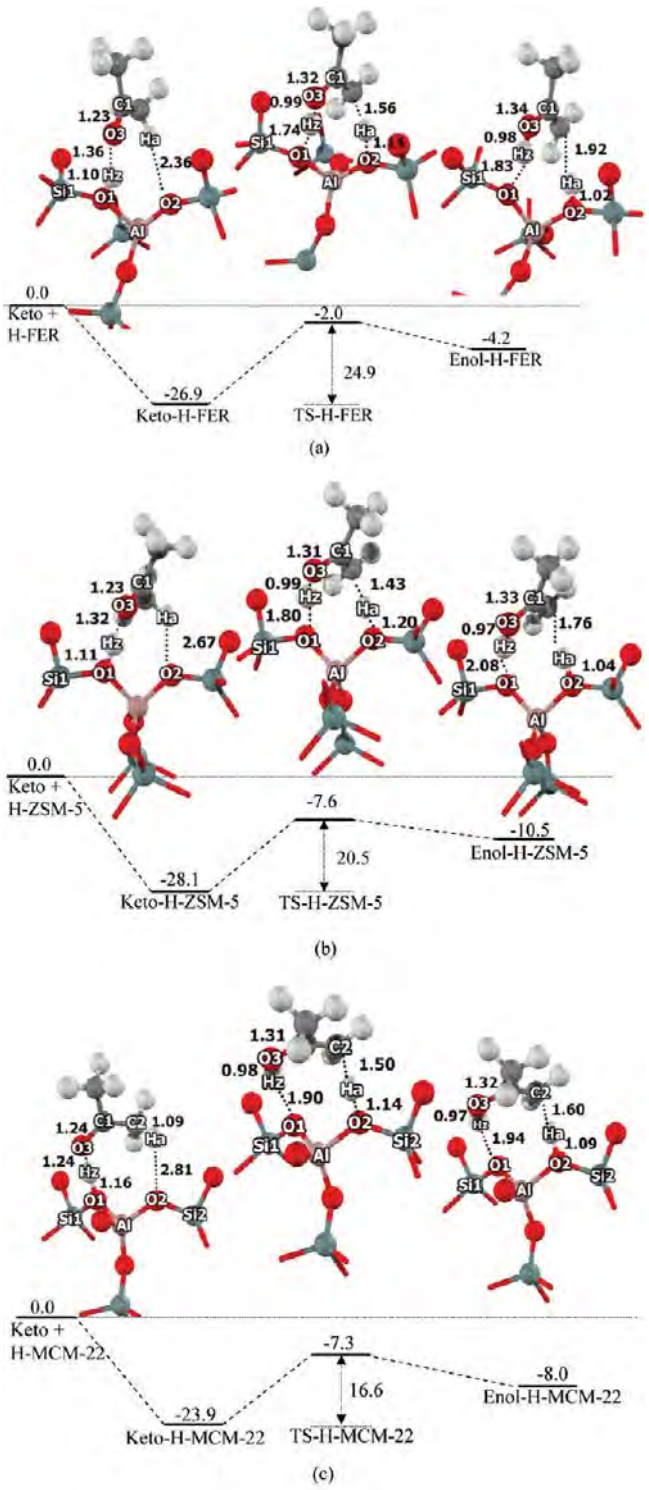

Figure 4. Molecular structures and energy profile of the tautomerization of acetone in a 34T model of (a) H-FER, (b) H-ZSM-5 and (c) H-MCM-22 as obtained from M06-2X/6-31+G(2df,2p)//M06-2X/6-31G(d,p) calculations. Distances and energies are given in Å and kcal/mol.

the adsorbed enol to the adsorbed keto form is very facile on zeolite surfaces with a small activation barrier. The activation energy of the ketonization process in these zeolites is calculated to be 0.7, 2.9, and 2.2 kcal/mol for H-MCM-22, H-ZSM-5, and H-FER, respectively, although the activation barrier for acetone ketonization in diluted mineral acid was experimentally measured to be 12.3 kcal/mol.[41] The reason for the small reverse activation energies and their trend among these three zeolites should be due to the relative stability of the adsorbed enol compared with the adsorbed acetone on the zeolite acid site. Acetone enol is much less stabilized than the adsorbed acetone on the zeolite acid site. This observation is in agreement with several experimental studies of reactions of carbonyl compounds in zeolites in which the enol form could not be detected.[4,5,45] The involvement of the enol form in carbonyl transformations was experimentally suggested by the observation of H/D exchange[45] and chlorination of acetone on the Brønsted acid site of zeolites.[5] These experimental results would indicate that the reaction of acetone would be processed through the enol form, which, however, is highly unstable in the zeolite framework. Our results clearly illustrate the relative stabilities of keto and enol forms of acetone in these three zeolites. The energies of reactants, transition states and products have also been calculated with the B3LYP functional. As expected, these adsorption energies are much smaller or there is no binding at all. Their values are given in the Supporting Information.

4. Conclusions

The effect of zeolite pore confinement on the tautomerization of acetone has been studied on three zeolites with different pore sizes. The use of a large cluster model with M06-2X/6-311+G(2df,2p)//M06-2X/6-31G(d,p) level of theory is found to be sufficient to account for interactions of acetone with the zeolite acid site and pore environments. The adsorption energies are calculated to be −26.9, −28.1, and −23.9 kcal/mol for H-FER, H-ZSM-5, and H-MCM-22, respectively, which agree well with the available experimental data for H-ZSM-5. Due to the involvement of the zeolite Brønsted acid site and the confinement effect, the tautomerization of acetone in zeolite proceeds through a much lower activation barrier than in the isolated gas phase and in the presence of water molecules. The activation energies and reaction energies decrease with the increase in the zeolite pore sizes, which are 24.9, 20.5, and 16.6 kcal/mol and 22.7, 17.6, and 15.9 kcal/mol, for the reaction in H-FER, H-ZSM-5, and H-MCM-22, respectively. The fact that the adsorption energy and activation energy trends are not correlated but rather in opposite directions indicates that the interaction with the acid site and the confinement effect of the pore walls are equally important and must be carefully accounted for to understand this reaction in zeolites. These trends are more related to the relative strength of the interactions of the active intermediates with the Brønsted acid site than to the confinement effect of the zeolite walls. The large pore of H-MCM-22 allows the adsorbed acetone and acetone enol to be closer to the acid site for stronger interactions. Therefore, both acetone enolization and (reverse) ketonization are very facile in this large-pore zeolite.

Acknowledgment. This work was supported in part by grants from the National Science and Technology Development Agency (2009 NSTDA Chair Professor funded by the Crown Property Bureau under the management of the National Science and Technology Development Agency and NANOTEC Center of Excellence funded by the National Nanotechnology Center), The Thailand Research Fund, the Commission of Higher Education, Ministry of Education ("the National Research University Project of Thailand (NRU)" and "Postgraduate Education and Research Programs in Petroleum and Petrochemicals and Advanced Materials"). Support from the Kasetsart University Research and Development Institute (KURDI) and Graduate School Kasetsart University are also acknowledged. The authors are grateful to Donald G. Truhlar and Yan Zhao

for their support with the M06-2X functional. M.P. acknowledges support from the Austrian Ministry of Science BMWF as part of the Uni-Infrastrukturprogramm of the research platform Scientific Computing at LFU Innsbruck.

Supporting Information Available: Table S1: Selected geometrical parameters for adsorption and reaction mechanism of acetone on H-FER, H-ZSM-5, and H-MCM-22 zeolites. Table S2: The adsorption and reaction energies of acetone on H-FER, H-ZSM-5, and H-MCM-22 zeolites with various methods. This material is available free of charge via the Internet at http://pubs.acs.org.

References and Notes

(1) Evans, D. A.; Nelson, J. V.; Vogel, E.; Taber, T. R. *J. Am. Chem. Soc.* **1981**, *103*, 3099.
(2) Salvapati, G. S.; Ramanamurty, K. V.; Janardanarao, M. *J. Mol. Catal.* **1989**, *54*, 9.
(3) Li, C. J. *Chem. Rev. (Washington, DC)* **1993**, *93*, 2023.
(4) Xu, T.; Munson, E. J.; Haw, J. F. *J. Am. Chem. Soc.* **1994**, *116*, 1962.
(5) Biaglow, A. I.; Sepa, J.; Gorte, R. J.; White, D. *J. Catal.* **1995**, *151*, 373.
(6) Panov, A. G.; Fripiat, J. J. *J. Catal.* **1998**, *178*, 188.
(7) Dumitriu, E.; Hulea, V.; Fechete, I.; Auroux, A.; Lacaze, J. F.; Guimon, C. *Microporous Mesoporous Mater.* **2001**, *43*, 341.
(8) Melo, L.; Giannetto, G.; Cardozo, L.; Llanos, A.; Garcia, L.; Magnoux, P.; Guisnet, M.; Alvarez, F. *Catal. Lett.* **1999**, *60*, 217.
(9) Yang, P.; Shang, Y.; Yu, J.; Wang, J.; Zhang, M.; Wu, T. *J. Mol. Catal. A: Chem.* **2007**, *272*, 75.
(10) Rodriguez-Santiago, L.; Vendrell, O.; Tejero, I.; Sodupe, M.; Bertran, J. *Chem. Phys. Lett.* **2001**, *334*, 112.
(11) Wu, C.-C.; Lien, M.-H. *J. Phys. Chem.* **1996**, *100*, 594.
(12) Lee, D.; Kim, C. K.; Lee, B.-S.; Lee, I.; Lee, B. C. *J. Comput. Chem.* **1997**, *18*, 56.
(13) Cucinotta, C. S.; Ruini, A.; Catellani, A.; Stirling, A. *ChemPhysChem* **2006**, *7*, 1229.
(14) Zakharov, M.; Masunov, A. E.; Dreuw, A. *J. Phys. Chem. A* **2008**, *112*, 10405.
(15) Solans-Monfort, X.; Bertran, J.; Branchadell, V.; Sodupe, M. *J. Phys. Chem. B* **2002**, *106*, 10220.
(16) Rattanasumrit, A.; Ruangpornvisuti, V. *J. Mol. Catal. A: Chem.* **2005**, *239*, 68.
(17) Zicovich-Wilson, C. M.; Corma, A.; Viruela, P. *J. Phys. Chem.* **1994**, *98*, 10863.
(18) Derouane, E. G. *J. Mol. Catal. A: Chem.* **1998**, *134*, 29.
(19) Derouane, E. G.; Chang, C. D. *Microporous Mesoporous Mater.* **2000**, *35*−*36*, 425.
(20) Boekfa, B.; Sirijareansre, J.; Pantu, P.; Limtrakul, J. *Stud. Surf. Sci. Catal.* **2004**, *154B*, 1582.
(21) Pantu, P.; Boekfa, B.; Limtrakul, J. *J. Mol. Catal. A: Chem.* **2007**, *277*, 171.
(22) Namuangruk, S.; Khongpracha, P.; Pantu, P.; Limtrakul, J. *J. Phys. Chem. B* **2006**, *110*, 25950.
(23) Namuangruk, S.; Pantu, P.; Limtrakul, J. *ChemPhysChem* **2005**, *6*, 1333.
(24) Boekfa, B.; Choomwattana, S.; Khongpracha, P.; Limtrakul, J. *Langmuir* **2009**, *25*, 12990.
(25) Zhao, Y.; Truhlar, D. G. *Theor. Chem. Acc.* **2008**, *120*, 215.
(26) Zhao, Y.; Truhlar, D. G. *J. Phys. Chem. C* **2008**, *112*, 6860.
(27) Maihom, T.; Boekfa, B.; Sirijaraensre, J.; Nanok, T.; Probst, M.; Limtrakul, J. *J. Phys. Chem. C* **2009**, *113*, 6654.
(28) Morris, R. E.; Weigel, S. J.; Henson, N. J.; Bull, L. M.; Janicke, M. T.; Chmelka, B. F.; Cheetham, A. K. *J. Am. Chem. Soc.* **1994**, *116*, 11849.
(29) Van Koningsveld, H.; Van Bekkum, H.; Jansen, J. C. *Acta Crystallogr., Sect. B: Struct. Sci.* **1987**, *B43*, 127.
(30) Kennedy, G. J.; Lawton, S. L.; Rubin, M. K. *J. Am. Chem. Soc.* **1994**, *116*, 11000.
(31) Nieminen, V.; Sierka, M.; Murzin, D. Y.; Sauer, J. *J. Catal.* **2005**, *231*, 393.
(32) Lonsinger, S. R.; Chakraborty, A. K.; Theodorou, D. N.; Bell, A. T. *Catal. Lett.* **1991**, *11*, 209.
(33) Zhou, D.; Bao, Y.; Yang, M.; He, N.; Yang, G. *J. Mol. Catal. A: Chem.* **2006**, *244*, 11.
(34) Schlegel, H. B. *J. Comput. Chem.* **1982**, *3*, 214.
(35) Gonzalez, C.; Bernhard Schlegel, H. *J. Chem. Phys.* **1989**, *90*, 2154.
(36) Curtiss, L. A.; Zygmunt, S. A.; Iton, L. E. *Proc. Int. Zeolite Conf.* **1999**, *1*, 415.
(37) Zygmunt, S. A.; Curtiss, L. A.; Zapol, P.; Iton, L. E. *J. Phys. Chem. B* **2000**, *104*, 1944.
(38) Frisch, M. J.; Trucks, G. W.; Schlegel, H. B.; Scuseria, G. E.; Robb, M. A.; Cheeseman, J. R.; Montgomery, J. A., Jr.; Vreven, T.; Kudin, K. N.; Burant, J. C.; Millam, J. M.; Iyengar, S. S.; Tomasi, J.; Barone, V.; Mennucci, B.; Cossi, M.; Scalmani, G.; Rega, N.; Petersson, G. A.; Nakatsuji, H.; Hada, M.; Ehara, M.; Toyota, K.; Fukuda, R.; Hasegawa, J.; Ishida, M.; Nakajima, T.; Honda, Y.; Kitao, O.; Nakai, H.; Klene, M.; Li, X.; Knox, J. E.; Hratchian, H. P.; Cross, J. B.; Adamo, C.; Jaramillo, J.; Gomperts, R.; Stratmann, R. E.; Yazyev, O.; Austin, A. J.; Cammi, R.; Pomelli, C.; Ochterski, J. W.; Ayala, P. Y.; Morokuma, K.; Voth, G. A.; Salvador, P.; Dannenberg, J. J.; Zakrzewski, V. G.; Dapprich, S.; Daniels, A. D.; Strain, M. C.; Farkas, O.; Malick, D. K.; Rabuck, A. D.; Raghavachari, K.; Foresman, J. B.; Ortiz, J. V.; Cui, Q.; Baboul, A. G.; Clifford, S.; Cioslowski, J.; Stefanov, B. B.; Liu, G.; Liashenko, A.; Piskorz, P.; Komaromi, I.; Martin, R. L.; Fox, D. J.; Keith, T.; Al-Laham, M. A.; Peng, C. Y.; Nanayakkara, A.; Challacombe, M.; Gill, P. M. W.; Johnson, B.; Chen, W.; Wong, M. W.; Gonzalez, C.; Pople, J. A. *Gaussian 03, revision B.05*; Gaussian, Inc.: Pittsburgh, PA, 2003.
(39) Holmes, J. L.; Lossing, F. P. *J. Am. Chem. Soc.* **1982**, *104*, 2648.
(40) Turecek, F.; Havlas, Z. *J. Org. Chem.* **1986**, *51*, 4066.
(41) Chiang, Y.; Kresge, A. J.; Schepp, N. P. *J. Am. Chem. Soc.* **1989**, *111*, 3977.
(42) Klinowski, J. *Chem. Rev.* **1991**, *91*, 1459.
(43) Freude, D.; Klinowski, J.; Hamdan, H. *Chem. Phys. Lett.* **1988**, *149*, 355.
(44) Sepa, J.; Lee, C.; Gorte, R. J.; White, D.; Kassab, E.; Evleth, E. M.; Jessri, H.; Allavena, M. *J. Phys. Chem.* **1996**, *100*, 18515.
(45) Xu, M.; Wang, W.; Hunger, M. *Chem. Commun. (Cambridge, U. K.)* **2003**, 722.

JP1058947

Effect of the Zeolite Nanocavity on the Reaction Mechanism of *n*-Hexane Cracking: A Density Functional Theory Study

T. Maihom,[†,‡] P. Pantu,[†,‡] C. Tachakritikul,[§] M. Probst,[||] and J. Limtrakul*[,†,‡]

Laboratory for Computational and Applied Chemistry, Department of Chemistry, Faculty of Science and Center of Nanotechnology, Kasetsart University Research and Development Institute, Kasetsart University, Bangkok 10900, Thailand, NANOTEC Center of Excellence, National Nanotechnology Center, Kasetsart University, Bangkok 10900, Thailand, PTT Research and Technology Institute, PTT Public Company Limited, Wang Noi, Phra Nakhon Si Ayutthaya, Thailand, and Institute of Ion Physics and Applied Physics, University of Innsbruck, A-6020 Innsbruck, Austria

Received: December 11, 2009; Revised Manuscript Received: February 9, 2010

The effects of the zeolite framework on the mechanism of *n*-hexane monomolecular cracking have been investigated with M06-2X/6-311+G(2df,2p)//M06-2X/6-31G(d,p) calculations. M06-2X is a recently developed hybrid-meta functional that is parametrized to include the London dispersion energy. The 38T H-FAU and 34T H-ZSM-5 nanocluster models where T atoms are either Si or Al atoms are used to represent H-FAU and H-ZSM-5 zeolites. The adsorption energies of hexane are predicted to be −10.8 and −18.2 kcal/mol for H-FAU and H-ZSM-5, respectively, in good agreement with experimental measurements. This indicates that the confinement effects on different types of zeolites can be well represented by the M06-2X functional. The reaction is assumed to proceed in two steps. In the first step, the central C−C bond of adsorbed *n*-hexane is protonated to form a hexonium intermediate. The adsorbed 3-C-hexonium is highly unstable and can be rapidly decomposed to produce the products. The first step is found to be the rate-determining step with activation energies of 45.7 and 45.8 kcal/mol for H-FAU and H-ZSM-5, respectively. For step two, the activation energies are calculated to be 8.6 and 9.9 kcal/mol for H-FAU and H-ZSM-5, respectively. The results clearly demonstrate that the reaction of *n*-hexane cracking is intrinsically the same in these large- and medium-pore zeolites. The different apparent activities can be explained by the different adsorption energies which are mainly due to the van der Waals interactions with the zeolite walls.

1. Introduction

The catalytic cracking of hydrocarbons is an important reaction in the petrochemical industry. It is used to break down large hydrocarbons in crude oil into light hydrocarbons for the production of fuels. Zeolite catalysts, especially Y and ZSM-5, are widely used in cracking processes due to their advantages of high catalytic activity and selectivity. Because of the molecular shape selectivity, zeolites are also widely used in many other petrochemical processes, for example, hydrocracking, isomerization, and alkylation of hydrocarbons and aromatics.[1,2]

The catalytic cracking of hydrocarbons is proposed to occur via a bimolecular and a monomolecular mechanism.[3–5] The classical bimolecular mechanism involves hydride transfer between an alkane and an adsorbed carbenium ion followed by isomerization and β-scission. This mechanism prevails under high partial pressure of hydrocarbons and low reaction temperature. Monomolecular cracking is believed to be an important mechanism for the cracking reaction of hydrocarbons under low partial pressure of hydrocarbons and high reaction temperature.[3,4] In this mechanism, the reaction proceeds through a high-energy carbonium ion which is formed by the direct protonation of Brønsted acid to the C−C bond.[3,4] Subsequently, the carbonium ion collapses, leading to the scission of the C−C bond to produce alkane and alkene products. Many theoretical studies[6–12] have attempted to explain monomolecular cracking of alkanes in zeolites and reported that the nonclassical two-electron three-center carbonium ions are the transition states of the reactions. Collins and O'Malley[6,7] have suggested that a pathway involving a carbenium ion intermediate could also exist for the protolytic cracking of alkanes. Kazansky et al.[13] were able to locate adsorbed carbonium ions as local minima in hydride transfer between methyl and methane and between ethyl and ethane on the zeolite surface. However, for hydride transfer involving secondary and tertiary alkyl cations, carbonium ions are only present as transition states. The adsorbed carbonium ions are highly unstable and easily decomposed to give products with a very small activation energy or presumably without an energy barrier. Boronat et al.[14,15] have reported that the C−H−C bridged carbonium ions, for example, 1-C-butonium and 2-C-butonium, can be reaction intermediates for hydride transfer, alkylation, and cracking of alkanes on zeolites. They have concluded that only carbonium ions whose positive charges are delocalized and inaccessible to oxygen atoms on the zeolite surface can exist as true reaction intermediates.

To understand hydrocarbon reactions, it is of particular interest to study the reactivity and stability of the carbonium ions as transition states or reaction intermediates on the zeolite surface. It is expected that the zeolite framework should have profound effects on reactive intermediates and the reaction

* To whom correspondence should be addressed. E-mail: jumras.1@ku.ac.th. Telephone: +66-2-562-5555 ext 2159.
[†] Laboratory for Computational and Applied Chemistry, Department of Chemistry, Faculty of Science and Center of Nanotechnology, Kasetsart University Research and Development Institute, Kasetsart University.
[‡] NANOTEC Center of Excellence, National Nanotechnology Center, Kasetsart University.
[§] PTT Research and Technology Institute, PTT Public Company Limited.
[||] Institute of Ion Physics and Applied Physics, University of Innsbruck.

10.1021/jp911732p
Published on Web 04/13/2010

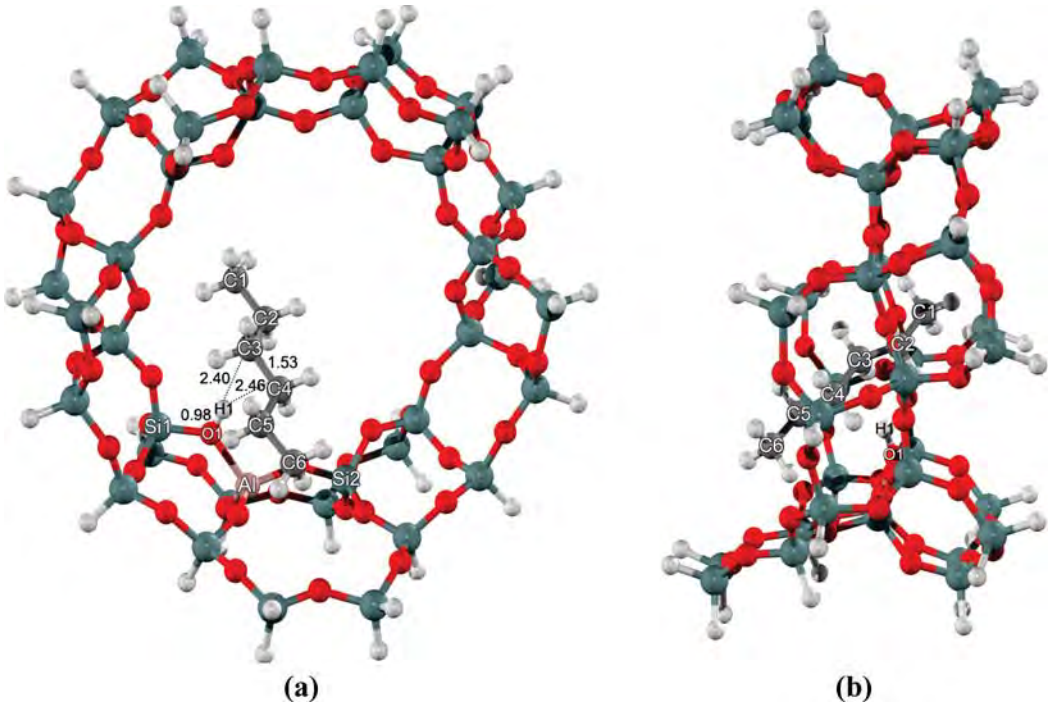

Figure 1. 38T cluster model of H-FAU zeolite with adsorbed *n*-hexane: (a) front view and (b) side view.

mechanism for catalytic reactions over zeolite catalysts.[16,17] Recently, Hansen et al.[18] have indicated that to be able to locate highly reactive intermediates, carbenium or carbonium ions, it is necessary to use a sufficiently large model. In that report, they have found protonated ethyl benzene as a stable intermediate only when a large cluster of zeolite (33T) was used for the calculations. That finding emphasizes that both short-range van der Waals interactions and long-range electrostatic interactions with the zeolite pore walls can significantly affect relative stabilities of intermediates and transition states of reactions and, thus, the overall reaction mechanisms. Due to a large number of atoms per unit cell of zeolites, the periodic ab initio calculations usually are computationally too expensive and even impractical when very large zeolites are concerned. Conventional density functional methods are known to be unable to describe dispersion (van der Waals) forces.[19] Therefore, it is not certain that density functional theory (DFT) calculations on large zeolite clusters will give the right answer. Previously, we have successfully used the ONIOM method[20] to study several reaction mechanisms in zeolites.[21–26] The success of the ONIOM method is, however, strongly dependent on the right partition of the active region and the environment, and the right combination of high and low level methods. Recently, the new meta-hybrid density functional M06 series[27,28] have been developed and shown to accurately compute binding energies of adsorbates covalently and noncovalently interacting with the zeolite acid site. The results were comparable to MP2 calculations at a high basis set but at much more affordable computer times. Recently, we have demonstrated that the zeolite confinement effect on reactions of unsaturated aliphatic, aromatic, and heterocyclic compounds could be successfully studied[29] by performing full quantum calculations on sufficiently large clusters using the M06-2X method. This approach is, in principle, not only more accurate compared to the ONIOM method, but it also makes the selection of zeolite models more general and systematic.

In this work, we report the theoretical investigation on the mechanism of *n*-hexane protolytic cracking of H-ZSM-5 and H-FAU zeolites by employing relatively large cluster models to realistically represent the framework of zeolites and using the M06-2X method. The reaction mechanism and relative energies and structures of intermediates and transition states are discussed to understand the effect of the zeolite pore confinement on the protolytic cracking reaction. *n*-Hexane is chosen as a reactant in this work because it is widely used experimentally as a benchmark in cracking reactions to study the zeolite acidity and the effect of different zeolite frameworks.[30,31] Theoretical studies of the protolytic cracking of *n*-hexane on different types of zeolites utilizing realistic models have not been performed previously.

2. Models and Method

38T H-FAU and 34T H-ZSM-5 cluster zeolite models were generated from their lattice structures.[32,33] The 38T cluster model of H-FAU, illustrated in Figure 1, covers the 12-membered-ring window connecting two supercages of faujasite. It is symmetrically extended from the 12T of the 12-membered-ring to include 38 tetrahedral atoms. Silicon at the T2 position was replaced by aluminum to model a Brønsted acid site. For the ZSM-5 zeolite, the 34T quantum cluster model (see Figure 2) covers the intersection at the interconnection between the straight channel and the zigzag channel. One aluminum atom was substituted for a silicon atom at the T12 site to generate the Brønsted acid site.

The M06-2X density functional is used in all calculations. During geometry optimizations, only the 5T active region of "$SiOHAl(OSi)_2OSi$" and the reacting molecule are allowed to relax while the rest of the structure is kept fixed at the crystallographic coordinates. For geometry optimizations, the 6-31G(d,p) basis set was used. In order to obtain more accurate interaction energies, single point calculations with the 6-311+G(2df,2p) basis set were carried out. Transition states were confirmed to have one imaginary frequency corresponding to the reaction coordinate. Furthermore, the internal reaction coordinate (IRC) method[34,35] was used to verify that the transition states are

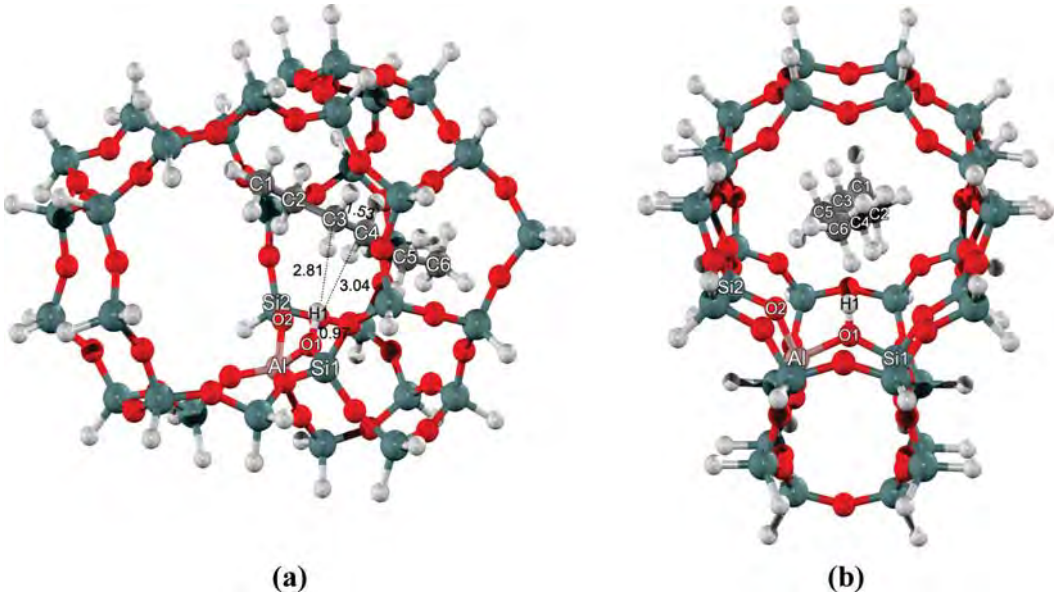

Figure 2. 34T cluster model of H-ZSM-5 zeolite with adsorbed *n*-hexane via the two methylene carbon atoms: (a) straight channel view and (b) sinusoidal channel view.

TABLE 1: Optimized Geometrical Parameters of the Species Involved in the *n*-Hexane Cracking on FAU Zeolite

parameter	isolated cluster	hexane adsorption (Ads_FAU)	transition state (TS1_FAU)	3-C-hexonium intermediate (Int_FAU)	transition state (TS2_FAU)	product (Prod_FAU)
			distances (Å)			
O1−H1	0.97	0.98	1.79	2.15	2.45	
Al−O1	1.97	1.96	1.83	1.81	1.79	1.74
Al−O2	1.72	1.72	1.77	1.78	1.80	1.94
H1−C3		2.40	1.25	1.24	1.71	
H1−C4		2.46	1.39	1.26	1.13	1.09
C2−C3	1.53	1.53	1.52	1.51	1.43	1.34
C3−C4	1.53	1.53	1.72	1.91	2.70	4.06
O2−H2		3.85	4.02	4.32	1.81	1.01
C2−H2		1.10	1.10	1.09	1.14	2.11
C3−H2		2.16	2.14		2.01	1.98
C3−O1		3.37	2.93	3.14	2.90	3.23
C3−O2		4.47	2.89	4.40	3.57	2.98
C4−O1		3.32	2.89	3.04	3.15	3.17
C4−O2		3.53	3.12	3.10	3.61	4.53
			angles (deg)			
O2−Al−O1	106.2	107.1	109.3	109.6	109.1	104.8
Si1−O1−Al	132.3	131.5	128.3	129.9	133.1	132.3
C3−H1−C4		35.0	81.2	100.1	144.0	138.7

connected with the minima. In order to reduce the computational cost of the frequency and IRC calculations, 14T H-FAU and 12T H-ZSM-5 models based on 38T H-FAU and 34T H-ZSM-5 optimized structures were employed. Profiles of the energy and of important distances along the reaction coordinate are given as Supporting Information. All calculations were performed with the Gaussian 03 code[36] modified to incorporate the Minnesota Density Functionals module 3.1 by Zhao and Truhlar.

3. Results and Discussion

3.1. Adsorption of *n*-Hexane on H-FAU and H-ZSM-5 Zeolites. Optimized structures of *n*-hexane adsorption on H-FAU and H-ZSM-5 zeolites obtained from the M06-2X/6-31G(d,p) calculations are shown in Figures 1 and 2, respectively. Selected geometrical structures for the adsorption complexes are tabulated in Tables 1 and 2. An *n*-hexane molecule is weakly adsorbed on zeolite through interactions between two methylene carbon atoms and the Brønsted acid site (O1−H1). In this study, we focus only on the adsorption on the central C−C bond of *n*-hexane because the protolytic cracking of this bond will lead to the formation of propane and propene molecules which are the main products of *n*-hexane cracking.[37–40] The adsorption interactions are weak so that the structures of the zeolites and the adsorbed *n*-hexane are not significantly changed. The bond distance in the acidic O−H bond and the C−C bond of *n*-hexane differ slightly from the isolated molecules. In H-FAU, the distances between the carbon atoms of the adsorbed *n*-hexane and the zeolite proton are 2.40 and 2.46 Å for H1···C3 and H1···C4, respectively. The calculated adsorption energy is −10.8 kcal/mol, which agrees well with an experimental measurement of −12.7 kcal/mol.[41] In the ZSM-5 zeolite, the calculated adsorption energy is −18.2 kcal/mol. This computed adsorption energy is also in good agreement with the experimental measurement of −19.6 kcal/mol.[41]

Analogous calculations were also performed with the widely used B3LYP density functional. Selected geometrical parameters of the complexes and the corresponding adsorption energies obtained from B3LYP are listed in Table S1 in the Supporting

TABLE 2: Optimized Geometrical Parameters of All Species Involved in the *n*-Hexane Cracking on H-ZSM-5 Zeolite

parameter	isolated cluster	hexane adsorption (Ads_ZSM-5)	transition state (TS1_ ZSM-5)	3-C-hexonium intermediate (Int_ZSM-5)	transition state (TS2_ZSM-5)	product (Prod_ZSM-5)
			distances (Å)			
O1−H1	0.97	0.97	1.74	2.01	2.31	
Al−O1	1.82	1.82	1.73	1.72	1.71	1.68
Al−O2	1.68	1.68	1.70	1.71	1.72	1.81
H1−C3		2.81	1.31	1.26	1.88	
H1−C4		3.04	1.32	1.26	1.11	1.09
C2−C3	1.53	1.53	1.52	1.52	1.42	1.34
C3−C4	1.53	1.53	1.76	1.86	2.72	3.38
O2−H2		2.90	2.53	2.67	1.87	1.01
C2−H2		1.10	1.09	1.09	1.15	2.10
C3−H2		2.15	2.14		1.95	2.03
C3−O1		3.77	2.87	2.96	3.01	3.32
C3−O2		3.96	3.34	3.31	3.47	3.03
C4−O1		3.95	2.85	3.00	3.21	3.46
C4−O2		3.81	2.98	2.99	3.18	3.57
			angles (deg)			
O2−Al−O1	90.4	90.5	94.3	94.2	95.0	91.6
Si1−O1−Al	130.5	130.1	126.1	127.5	128.8	128.8
C3−H1−C4		30.0	83.7	95.0	129.3	115.1

Information. While the geometric differences are small, B3LYP leads to adsorption energies of −1.65 and 1.06 kcal/mol for H-FAU and H-ZSM-5, respectively, which are much too low compared to the experimental values given above. This is not surprising, given the lack of dispersion interactions in B3LYP which leave exchange repulsion as the only short-range *n*-hexane/zeolite interaction.

3.2. Reaction Mechanism of *n*-Hexane Protolytic Cracking. The adsorbed *n*-hexane molecule is considered to undergo a two-step protolytic cracking, consisting of the protonation of *n*-hexane and the decomposition of the hexonium intermediate to produce propane and propene products.

3.2.1. Protonation of n-Hexane. In the first step, the adsorbed *n*-hexane molecule is protonated by the acidic proton at the central C−C bond to form the adsorbed 3-C-hexonium intermediate. Selected geometrical parameters for this reaction step are shown in Tables 1 and 2, and optimized structures are shown in Figures 3 and 4 for reactions in H-FAU and H-ZSM-5, respectively. The energy profiles are shown in Figure 5. At the transition state, the H1 proton is protonated to the C3−C4 bond of *n*-hexane. In H-FAU, the Brønsted O1−H1 bond distance is elongated from 0.98 to 1.79 Å while the C3−C4 bond distance is increased to 1.72 Å. The C3−H1 and C4−H1 distances are 1.25 and 1.39 Å, respectively. The activation energy of this step is 45.7 kcal/mol. The transition state structure in H-ZSM-5 is very similar to that in H-FAU. The activation energy for *n*-hexane protonation in H-ZSM-5 is also almost the same (45.8 kcal/mol). The existence of true transition states has been confirmed by frequency calculations resulting in one imaginary frequency at −548.3i and −470.2i cm^{-1} for H-FAU and H-ZSM-5 zeolites, respectively, related to the movement of the acidic proton of zeolite (H1) to the *n*-hexane C3−C4 bond and the breaking of the C3−C4 bond. IRC calculations (see Figures S1 and S2 in the Supporting Information) were performed to illustrate the continuous change from products to the transition state. They also confirm that the C3−C4 bond of *n*-hexane is broken by the attacking of the zeolite H1 proton leading to the formation of the 3-C-hexonium intermediates.

The 3-C-hexonium intermediate is adsorbed on the zeolite surface by forming hydrogen bond interactions with the negatively charged oxygen atom (O1) of the zeolite. The distance H1···O1 is at 2.15 and 2.01 Å in H-FAU and H-ZSM-5, respectively. The structure of the adsorbed C3−H1−C4 bridge hexonium intermediate becomes symmetrical. The C3−H1 and C4−H1 bond distances are almost equal at 1.24 and 1.26 Å, respectively. The C3−C4 bond distance is 1.91 Å and the C3−H1−C4 angle is 100.1° in H-FAU. In H-ZSM-5, the C3−H1−C4 bridge angle is narrower at 95.0° and, consequently, the C3−C4 bond distance is shorter at 1.86 Å. The C3−H1 and C4−H1 bond distances are the same at 1.26 Å. Kazansky et al.[13] have pointed out that the C3−H1−C4 bridge angle is related to the hydride character of the central H atom. The Mulliken population analysis for the partial atomic charge of the H1 atom is 0.294 and 0.322 in H-FAU and H-ZSM-5, respectively, and in agreement with the Kazansky et al.[13] report.

The formation of the adsorbed 3-C-hexonium intermediate is highly endothermic. The reaction energies with respect to the isolated reactants are 33.6 and 26.9 kcal/mol, in H-FAU and H-ZSM-5, respectively. The adsorbed 3-C-hexonium intermediate is only 1.3 and 0.7 kcal/mol more stable than its preceding transition state, in H-FAU and H-ZSM-5, respectively.

3.2.2. Decomposition of the Hexonium Intermediate. The adsorbed 3-C-hexonium intermediates in both zeolites are unstable and highly reactive. They can be decomposed back to adsorbed *n*-hexane with a very small activation barrier. Therefore, it would be extremely difficult to locate this intermediate experimentally. The conversion to produce propane and propene products proceeds through a more energetic transition state (TS2). At the transition state, the H1 atom is moved toward a carbon atom (C4) and the C3−C4 bond is dissociated. The Mulliken population analysis indicates that at the transition state the H1 atom has a higher hydride character than in its previous adsorption complex. The partial atomic charge of the H1 atom is 0.051 and 0.115 in H-FAU and H-ZSM-5, respectively. At this transition state, the H2 proton on the carbon next to the C3 atom is elongated to be transferred to the oxygen atom of the zeolite framework. Simultaneously, the C3−C2 bond is contracted. In H-FAU, the C4−H1 distance is reduced to 1.13 Å while the C3−C4 bond is increased to 2.70 Å. The C2−H2 is elongated from 1.09 to 1.14 Å, and the C2−C3 bond distance is decreased from 1.51 to 1.43 Å. The TS2 structure in H-ZSM-5 is also similar but a little bit closer to the product state. The C2−C3 and C4−H1 are a little bit shorter while the C3−C4 and C2−H2 distances are slightly longer than what was observed in the TS2 of H-FAU. Normal mode analysis reveals one

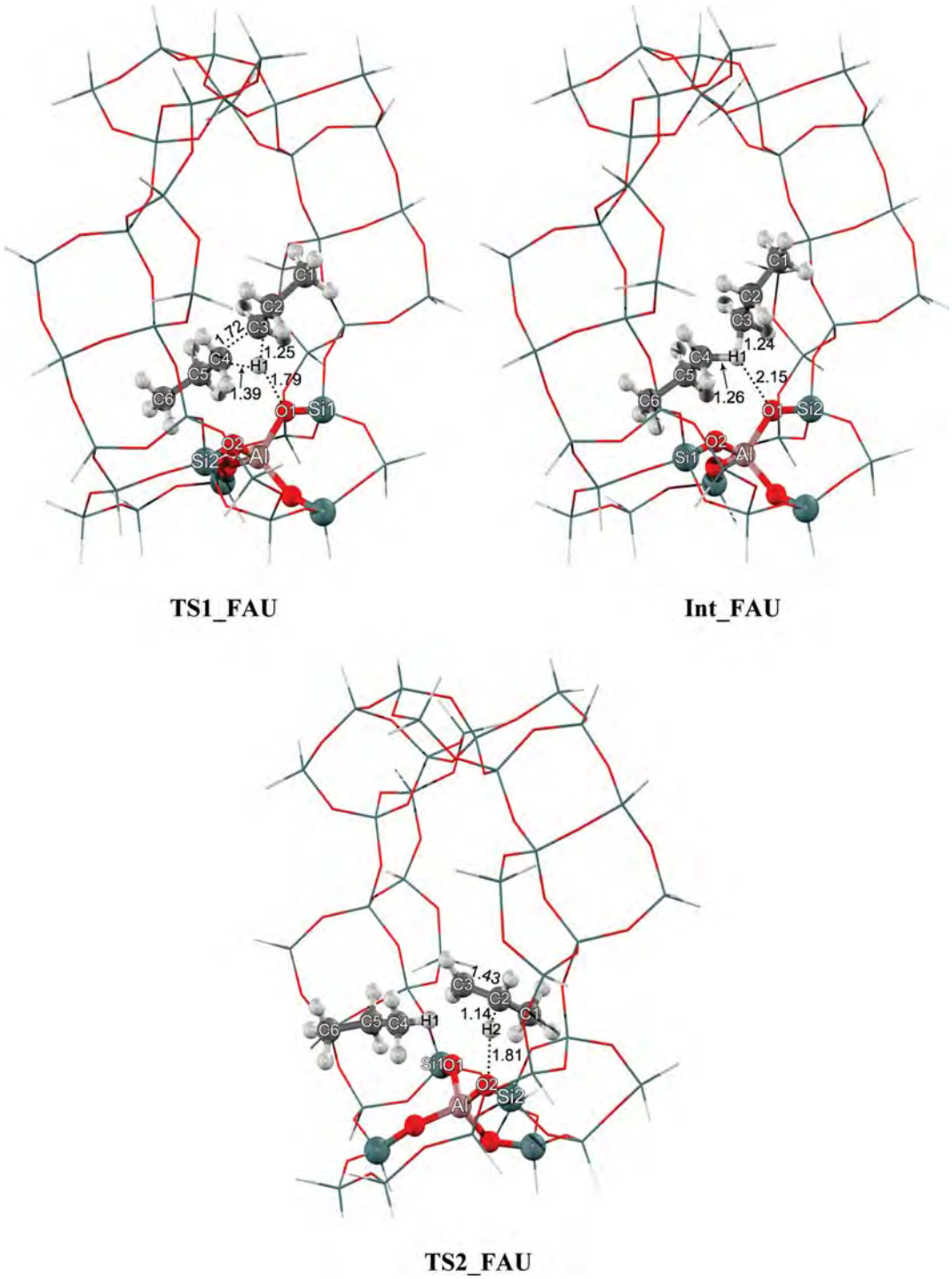

Figure 3. Optimized structures of transition states and intermediates involved in the protolytic cracking of *n*-hexane over H-FAU.

imaginary frequency at −294.9i and −197.7i cm^{-1} associated with the TS2 of H-FAU and H-ZSM-5 zeolites, respectively, which corresponds to movement along the reaction coordinate in which the C2−H2 bond breaks and the H2−O2 bond forms simultaneously. The energy barriers for this step are 8.6 and 9.9 kcal/mol for the reaction in H-FAU and H-ZSM-5, respectively. After the decomposition is completed, a propane molecule and a propene molecule are produced. The propene molecule remains adsorbed on the acidic site of the zeolite through a π-bond interaction. The desorption of products requires an amount of energy of 20.4 and 26.2 kcal/mol in H-FAU and H-ZSM-5, respectively.

The intrinsic activation energies for the protonation of *n*-hexane and the decomposition of the 3-C-hexonium intermediate are found to be almost the same in both zeolites (cf. Figure 5). The overall reaction barrier is considered to be the energy difference between the adsorbed *n*-hexane and the TS2 and is found to be 53.0 and 55.0 kcal/mol for the reaction in H-FAU and H-ZSM-5, respectively. These values are very close to the experimentally estimated intrinsic activation energies of about 56 kcal/mol in these two zeolites.[39,40] The energy profiles of the reactions in these two zeolites contain very similar features. However, due to the confinement effect, the reaction intermediates and transition states in H-ZSM-5 are 6−8 kcal/mol lower in energies than those stationary points in H-FAU. Therefore, the apparent reaction barrier would be 36.8 and 42.2 kcal/mol for the reaction in H-ZSM-5 and H-FAU, respectively. The predicted apparent reaction barriers are also very close to the

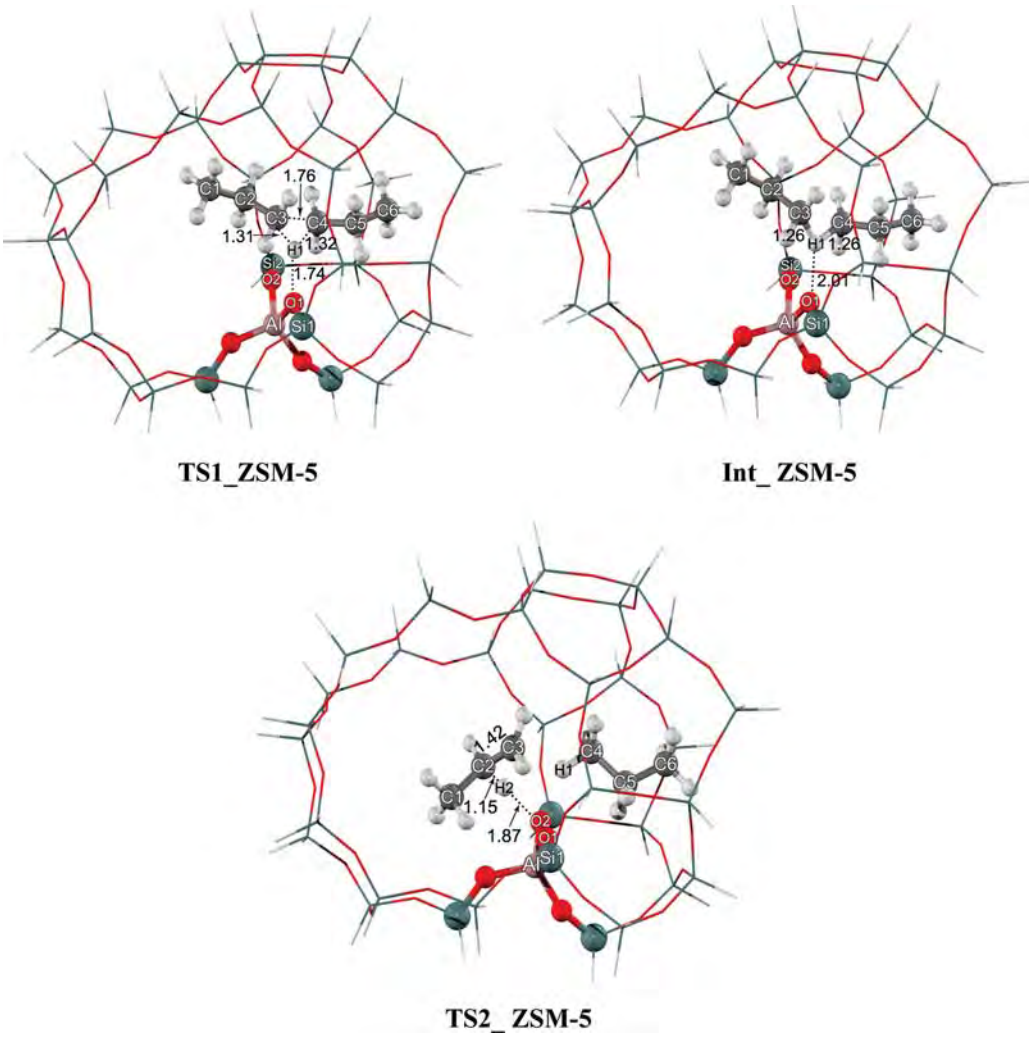

Figure 4. Optimized structures of transition states and intermediates involved in the protolytic cracking of *n*-hexane over H-ZSM-5.

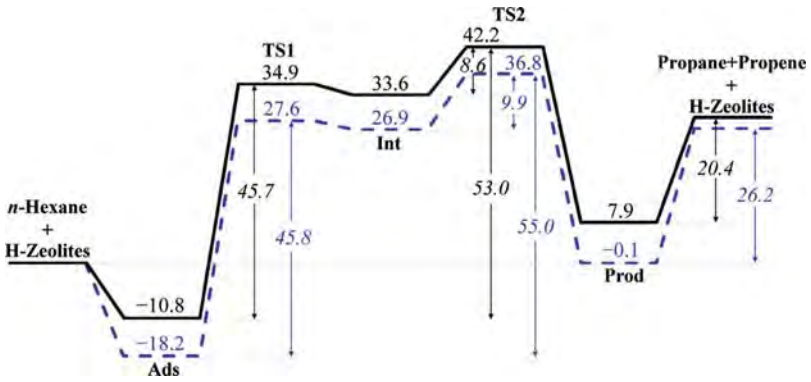

Figure 5. Energy profile for the *n*-hexane cracking mechanisms for both zeolites: H-FAU zeolite (solid line) and H-ZSM-5 zeolite (dashed line) (energies are in kcal/mol).

values reported in recent experimental studies[39,40] which reported the apparent activation energies of 35.5 and 44.4 kcal/mol for the monomolecular cracking of *n*-hexane in H-ZSM-5 and H-FAU, respectively. Since the computed intrinsic activation energies of the two reaction steps are very similar in these two zeolites, the different cracking activity on these two zeolites can only be explained by the different adsorption energies of the *n*-hexane reactant. The computed deprotonation energies of these two models of zeolites are also comparable (295.9 and 293.8 kcal/mol, for H-ZSM-5 and H-FAU, respectively). Therefore, the intrinsic catalytic activity of zeolites for *n*-hexane cracking is not dependent on the type of zeolites, even if their pores are quite different in shape and size. This confirms previous experimental results,[37–40] and the mechanism underlying this unexpected behavior can now be better understood.

4. Conclusion

The cracking reaction of *n*-hexane over two different types of zeolite has been investigated by utilizing the 38T H-FAU and 34T H-ZSM-5 cluster models calculated at the M06-2X/6-311+G(2df,2p)//M06-2X/6-31G(d,p) level of theory. These

calculations give adsorption energies which are in good agreement with experimental data. After the adsorption, the acidic proton of the zeolites is directly protonated to a C−C bond of *n*-hexane and the 3-C-hexonium intermediate is formed in the nanocavity. In the second step, the 3-C-hexonium is readily decomposed to form propane and propene molecules. The computational results indicate the plausible existence of 3-C-hexonium intermediates in the zeolites for the protolytic cracking of *n*-hexane. The structures and relative stabilities of the 3-C-hexonium intermediates in these two zeolites are very similar. The protonation step is found to be the rate-determining step. The apparent activation energies are computed to be 42.2 and 36.8 kcal/mol in H-FAU and H-ZSM-5, respectively, which are very close to the apparent activation energies for monomolecular cracking of *n*-hexane reported in literature.[39,40] The results confirm that relatively large quantum clusters are needed for the study of hydrocarbon reactions in zeolites. The M06-2X method is well-suited for this case, while reference calculations show that functionals such as B3LYP are not. The different activities of the two zeolites can only be explained by the different adsorption energies which are mainly due to the van der Waals interactions between *n*-hexane and the zeolite walls.

Acknowledgment. This work was supported in part by grants from the National Science and Technology Development Agency (NSTDA Chair Professor and NANOTEC Center of Excellence), the Thailand Research Fund (to J.L.), the Kasetsart University Research and Development Institute (KURDI), the Commission on Higher Education, Ministry of Education ("National Research University of Thailand" and "Postgraduate Education and Research Programs in Petroleum and Petrochemicals and Advanced Materials"), under the program Strategic Scholarships for Frontier Research Network for the Joint Ph.D. Program Thai Doctoral degree from the Office of the Higher Education Commission, Thailand (to T.M.), as well as PTT Research and Technology Institute, PTT Public Company Limited. The authors are grateful to Donald G. Truhlar and Yan Zhao for supporting them with the code for the M06-2X functional.

Supporting Information Available: Table S1: Selected geometric parameters and adsorption energies of the *n*-hexane adsorption obtained from B3LYP. Figures S1 and S2: IRC calculation for protonation of *n*-hexane over H-ZSM-5 and H-FAU zeolites, respectively. This material is available free of charge via the Internet at http://pubs.acs.org.

References and Notes

(1) Weitkamp, J. *Solid State Ionics* **2000**, *131*, 175.
(2) Stocker, M. *Microporous Mesoporous Mater.* **2005**, *82* (3), 257.
(3) Haag, W. O.; Dessau, R. M. In *Proceedings, 8th International Congress on Catalysis Berlin, 1984*; Ertl. G., Ed.; Dechema: Frankfurt-am-Main, 1984; Vol. 2, p 305.
(4) Kotrel, S.; Knözinger, H.; Gates, B. C. *Microporous Mesoporous Mater.* **2000**, *35*−*36*, 11.
(5) Corma, A.; Orchilles, A. V. *Microporous Mesoporous Mater.* **2000**, *35*−*36*, 21.
(6) Collins, S. J.; O'Malley, P. J. *J. Catal.* **1995**, *153*, 94.
(7) Collins, S. J.; O'Malley, P. J. *Chem. Phys. Lett.* **1995**, *246*, 555.
(8) Kazansky, V. B.; Senchenya, I. N.; Frash, M. V.; van Santen, R. A. *Catal. Lett.* **1994**, *27*, 345.
(9) Blaszkowski, S. R.; Nascimento, M. A. C.; van Santen, R. A. *J. Phys. Chem. A* **1996**, *100* (9), 3463.
(10) Frash, M. V.; van Santen, R. A. *Top. Catal.* **1999**, *9*, 191.
(11) Zheng, X.; Blowers, P. *J. Phys. Chem. A* **2005**, *109*, 10734.
(12) Zheng, X.; Blowers, P. *J. Mol. Catal. A: Chem.* **2005**, *229*, 77.
(13) Kazansky, V. B.; Frash, M. V.; van Santen, R. A. *Catal. Lett.* **1997**, *48*, 61.
(14) Boronat, M.; Viruela, P.; Corma, A. *J. Phys. Chem. B* **2000**, *104*, 1944.
(15) Boronat, M.; Corma, A. *Appl. Catal., A* **2008**, *336*, 2.
(16) Zicovich-Wilson, C. M.; Corma, A.; Viruela, P. *J. Phys. Chem. B* **1994**, *98*, 10863.
(17) Derouane, E. G. *J. Mol. Catal. A: Chem.* **1998**, *134*, 29.
(18) Hansen, N.; Brüggemann, T.; Bell, A. T.; Keil, F. J. *J. Phys. Chem. C* **2008**, *112*, 15402.
(19) Wesolowski, T. A.; Parisel, O.; Ellinger, Y.; Weber, J. *J. Phys. Chem. A* **1997**, *101* (42), 7818.
(20) Svensson, M.; Humbel, S.; Froese, R. D. J.; Matsubara, T.; Sieber, S.; Morokuma, K. *J. Phys. Chem. A* **1996**, *100*, 19357.
(21) Namuangruk, S.; Pantu, P.; Limtrakul, J. *J. Catal.* **2004**, *225*, 523.
(22) Namuangruk, S.; Pantu, P.; Limtrakul, J. *ChemPhysChem* **2005**, *6* (7), 1333.
(23) Maihom, T.; Namuangruk, S.; Nanok, T.; Limtrakul, J. *J. Phys. Chem. C* **2008**, *112*, 12914.
(24) Maihom, T.; Boekfa, B.; Sirijaraensre, J.; Nanok, T.; Probst, M.; Limtrakul, J. *J. Phys. Chem. C* **2009**, *113*, 6654.
(25) Jansang, B.; Nanok, T.; Limtrakul, J. *J. Phys. Chem. B* **2006**, *110*, 12626.
(26) Namuangruk, S.; Khongpracha, P.; Pantu, P.; Limtrakul, J. *J. Phys. Chem. B* **2006**, *110* (51), 25950.
(27) Zhao, Y.; Truhlar, D. G. *J. Phys. Chem. C* **2008**, *112*, 6860.
(28) Zhao, Y.; Truhlar, D. G. *Acc. Chem. Res.* **2008**, *41*, 157.
(29) Boekfa, B.; Choomwattana, S.; Khongpracha, P.; Limtrakul, J. *Langmuir* **2009**, *25* (22), 12990.
(30) Bourdillon, G.; Gueguen, C.; Guisnet, M. *Appl. Catal.* **1990**, *61*, 123.
(31) Lercher, J. A.; Jentys, A.; Brait, A. *Mol. Sieves Sci. Technol.* **2008**, *6*, 153.
(32) Alberti, A.; Davoli, P.; Vezzalini, G. Z. *Z. Kristallogr.* **1986**, *175*, 249.
(33) van Koningsveld, H.; Bekkum, H. v.; Jansen, J. C. *Acta Crystallogr., Sect. B: Struct. Sci.* **1987**, *43*, 127.
(34) Gonzalez, C.; Schlegel, H. B. *J. Chem. Phys.* **1989**, *90*, 2154.
(35) Gonzalez, C.; Schlegel, H. B. *J. Phys. Chem.* **1990**, *94*, 5523.
(36) Frisch, M. J.; Trucks, G. W.; Schlegel, H. B.; Scuseria, G. E.; Robb, M. A.; Cheeseman, J. R.; Montgomery, J. A., Jr.; Vreven, T.; Kudin, K. N.; Burant, J. C.; Millam, J. M.; Iyengar, S. S.; Tomasi, J.; Barone, V.; Mennucci, B.; Cossi, M.; Scalmani, G.; Rega, N.; Petersson, G. A.; Nakatsuji, H.; Hada, M.; Ehara, M.; Toyota, K.; Fukuda, R.; Hasegawa, J.; Ishida, M.; Nakajima, T.; Honda, Y.; Kitao, O.; Nakai, H.; Klene, M.; Li, X.; Knox, J. E.; Hratchian, H. P.; Cross, J. B.; Adamo, C.; Jaramillo, J.; Gomperts, R.; Stratmann, R. E.; Yazyev, O.; Austin, A. J.; Cammi, R.; Pomelli, C.; Ochterski, J. W.; Ayala, P. Y.; Morokuma, K.; Voth, G. A.; Salvador, P.; Dannenberg, J. J.; Zakrzewski, V. G.; Dapprich, S.; Daniels, A. D.; Strain, M. C.; Farkas, O.; Malick, D. K.; Rabuck, A. D.; Raghavachari, K.; Foresman, J. B.; Ortiz, J. V.; Cui, Q.; Baboul, A. G.; Clifford, S.; Cioslowski, J.; Stefanov, B. B.; Liu, G.; Liashenko, A.; Piskorz, P.; Komaromi, I.; Martin, R. L.; Fox, D. J.; Keith, T.; Al-Laham, M. A.; Peng, C. Y.; Nanayakkara, A.; Challacombe, M.; Gill, P. M. W.; Johnson, B.; Chen, W.; Wong, M. W.; Gonzalez, C.; Pople, J. A. *Gaussian 03*, revision B.05; Gaussian, Inc.: Pittsburgh, PA, 2003.
(37) Narbeshuber, T. F.; Vinek, H.; Lercher, J. A. *J. Catal.* **1995**, *157*, 388.
(38) Kotrel, S.; Rosynek, M. P.; Lunsford, J. H. *J. Phys. Chem. B* **1999**, *103*, 818.
(39) Babitz, S. M.; Williams, B. A.; Miller, J. T.; Snurr, R. Q.; Haag, W. O.; Kung, H. *Appl. Catal., A* **1999**, *179*, 71.
(40) van Bokhoven, J. A.; Williams, B. A.; Ji, W.; Koningsberger, D. C.; Kung, H. H.; Miller, J. T. *J. Catal.* **2004**, *224*, 50.
(41) Eder, F.; Stockenhuber, M.; Lercher, J. A. *J. Phys. Chem. B* **1997**, *101*, 5414.

JP911732P

CHEMPHYSCHEM

DOI: 10.1002/cphc.201000586

Oxidative Dehydrogenation of Propane over a VO_2-Exchanged MCM-22 Zeolite: A DFT Study

Sippakorn Wannakao,[a, b] Bundet Boekfa,[b, c] Pipat Khongpracha,[a, b, c] Michael Probst,[d] and Jumras Limtrakul*[a, b, c]

The adsorption and the mechanism of the oxidative dehydrogenation (ODH) of propane over VO_2-exchanged MCM-22 are investigated by DFT calculations using the M06-L functional, which takes into account dispersion contributions to the energy. The adsorption energies of propane are in good agreement with those from computationally much more demanding MP2 calculations and with experimental results. In contrast, B3LYP binding energies are too small. The reaction begins with the movement of a methylene hydrogen atom to the oxygen atom of the VO_2 group, which leads to an isopropyl radical bound to a HO–V–O intermediate. This step is rate determining with the apparent activation energy of 30.9 kcal mol^{-1}, a value within the range of experimental results for ODH over other silica supports. In the propene formation step, the hydroxyl group is the more reactive group requiring an apparent activation energy of 27.7 kcal mol^{-1} compared to that of the oxy group of 40.8 kcal mol^{-1}. To take the effect of the extended framework into account, single-point calculations on 120T structures at the same level of theory are performed. The apparent activation energy is reduced to 28.5 kcal mol^{-1} by a stabilizing effect caused by the framework. Reoxidation of the catalyst is found to be important for the product release at the end of the reaction.

1. Introduction

Propene is one of the most important starting materials for many processes in the chemical industry. It is, for example, used for polymer production and the scarcity of natural resources will most likely lead to a significant increase in the demand for propene in the near future.[1] However, the conventional propene production processes exhibit many disadvantages. For example, due to thermodynamic constraints, larger amounts of ethylene than propene are produced in the steam cracking process even though the demand for ethylene is not growing as much as that for propene. Moreover, industrial steam cracking is a high energy-consuming process that also produces CO_2.[2] Dehydrogenation also has the problem of rapid deactivation of the catalyst by coke production. Thus, finding competitive ways to produce propene has high priority and the oxidative dehydrogenation (ODH) of propane has, in principle, the advantages of low energy consumption, lower coke and CO_x by-products, and high selectivity of the desired product compared to the conventional dehydrogenation process.[3]

Vanadia-supported catalysts have proven to be active and selective for this reaction.[1,3,4] Silica-supported vanadium oxide catalysts especially are highly selective because they do not favor direct combustion of the propane reactant to CO_x species, compared to alumina and titania supports.[1,4j] Zeolites and mesoporous silicas, which are industrially important catalysts, can also be used as the silica support catalysts.[1,5] To understand the mechanistic scheme of the reaction, many theoretical studies of the propane ODH over vanadium oxides and silica-supported catalysts have been conducted. Engeser et al. found a product allyl complex (η^3-C_3H_5)V(O)–(OH)$^+$ when they studied alkane oxidation by VO_2^+ in a gas-phase system.[6] Systems consisting of clusters systematically selected from the bulk structure have also been studied theoretically.[7] Rozanska et al. identified possible reaction pathways for ODH of propane by vanadium oxide sites on a silica support cluster.[7b] They found that the first hydrogen abstraction at the O=V site was the rate-limiting step. In another study on a (001) periodic surface of V_2O_5, Fu et al. found that the propene formation step was rate limiting.[8] From these observations, one can say that different systems cause different controls of the rate-determining step even when they have the same active species. Although porous silica supports have been widely used in many experimental studies, to the best of our knowledge their atom-

[a] S. Wannakao, Dr. P. Khongpracha, Prof. Dr. J. Limtrakul
Laboratory for Computational and Applied Chemistry
Department of Chemistry, Faculty of Science and Center of Nanotechnology
Kasetsart University Research and Development Institute
Kasetsart University, Bangkok 10900 (Thailand)
Fax: (+66) 2-562-5555
E-mail: Jumras.l@ku.ac.th

[b] S. Wannakao, Dr. B. Boekfa, Dr. P. Khongpracha, Prof. Dr. J. Limtrakul
NANOTEC Center of Excellence, National Nanotechnology Center
Kasetsart University, Bangkok 10900 (Thailand)

[c] Dr. B. Boekfa, Dr. P. Khongpracha, Prof. Dr. J. Limtrakul
Center for Advanced Studies in Nanotechnology and its Applications in Chemical, Food, and Agricultural Industries
Kasetsart University, Bangkok 10900 (Thailand)

[d] Prof. Dr. M. Probst
Institute of Ion Physics and Applied Physics
University of Innsbruck, 6020 Innsbruck (Austria)

Supporting information for this article is available on the WWW under http://dx.doi.org/10.1002/cphc.201000586.

istic details have never been studied computationally. In reactions such as adsorption and catalysis processes in confined spaces, van der Waals interactions play an important role. In previous calculations on various reactions in zeolites, ONIOM (B3LYP:UFF) was found to be an economical method,[9] able to reproduce experimental data for such systems. Its good performance is, however, partially due to the compensation between the overestimated framework confinement effect and the underestimated interaction in the active region. Recently, Zhao and Truhlar have developed a new type of density functional (M06 series) in which London dispersion is taken into account in the parameterization.[10] This method has been shown to be very useful for studying adsorption and reaction mechanisms in zeolite and metal oxide systems in which van der Waals interactionspredominate.[11]

To understand such a reaction in a confined space, we used a well-calibrated VO_2-exchanged MCM-22 (VO_2-MCM22) model that has been recently studied experimentally.[5c] We studied propane adsorption and the reaction mechanism of the propane ODH reaction over the catalyst by means of DFT calculations with the M06-L functional, which Zhao and Truhlar have shown to be both accurate for transition metals and practical for large-system studies. The reaction can be divided into three main steps: 1) methylene ($-CH_2-$) hydrogen activation, 2) propene formation, and 3) reoxidation of the catalyst by using N_2O as an oxidizing agent.

2. Results and Discussion

2.1. Propane Adsorption over the Catalyst

A VO_2-MCM-22 cluster, the vanadium oxide component of which acts as an active site and is embedded in the intersection cavity at the 12T-membered ring of the supercage, was used in this study (Figure 1). The cluster model is similar to

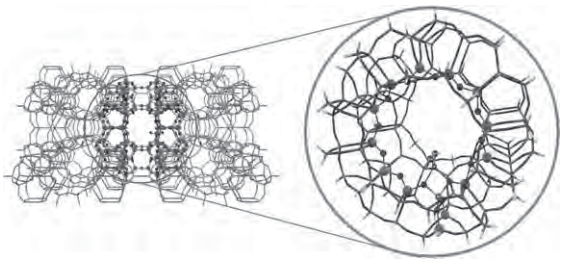

Figure 1. Structure of VO_2-MCM-22. Balls represent the 14T optimized site and sticks represent the extended framework on which single-point calculations were performed.

that used in our previous study on isolated metal oxide on zeolite.[12] The [VO_2] ionic group lies between the two bridging oxygen atoms of the zeolite framework forming a tetrahedral arrangement at the vanadium atom, which is the most stable configuration. With the M06-L functional and the 6-31G(d,p) basis set, the optimized V–O bond lengths are 1.59, 1.59, 1.98, and 1.98 Å for V–O1, V–O2, V–Oa, and V–Ob, respectively. The distance between V and the Al atoms is 2.78 Å. With the B3LYP functional, V–O and V–Al distances were the same as those obtained from the M06-L functional. Geometry optimizations with the MP2 method gave longer V–O distances, that is, V–O1 and V–O2 are 1.66 Å and V–Oa and V–Ob are 2.03 Å with a V–Al distance of 2.82 Å.

Although the M06-L functional leads to nearly the same structure of the active site as the B3LYP functional, when the van der Waals probe molecule propane was interacting with the site the relation of the structure obtained with each method was different. Optimized geometries of the adsorption complexes and their energies obtained from M06-L and B3LYP functional and MP2 calculations are illustrated in Figure 2. The

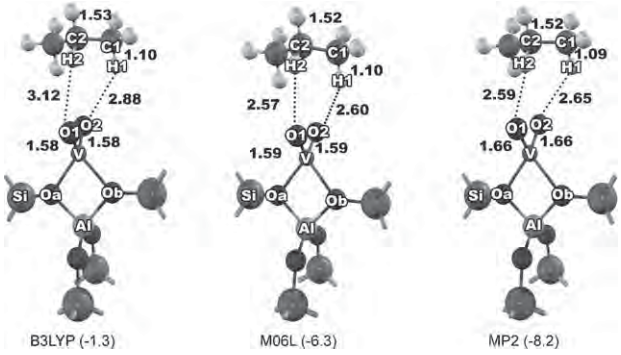

Figure 2. Optimized adsorption structures from the three methods. The adsorption energies are given in parentheses [kcal mol^{-1}].

propane molecule is weakly adsorbed on the catalyst with H2 binding to O1 and H1 to O2. The M06-L and MP2 methods lead to about the same O1–H2 and O2–H1 distances (2.57 and 2.59 Å, respectively). The weaker interaction from the B3LYP functional leads to a longer O1–H2 distance of 3.12 Å.

Not only the structure but also the energies from M06-L (-6.3 kcal mol^{-1}) are close to those obtained from the (much more CPU time-consuming) MP2 calculations (-8.2 kcal mol^{-1}). The adsorption energy from B3LYP is, in contrast, very small (-1.3 kcal mol^{-1}). The experimental value for the heat of propane adsorption over supported vanadium oxide material is about -8 kcal mol^{-1}.[5d,13] These results indicate that M06-L is suitable for studying systems of transition metals in which the van der Waals interaction plays an important role, as originally suggested.[10b]

2.2. Methylene Hydrogen Abstraction

The M06-L functional was used to study the reaction mechanism of the propane ODH over VO_2-MCM-22. The reaction begins with the activation of the methylene C–H bond by an oxygen atom of the VO_2 group. The transition structure shows distortion from the original tetrahedral one (Figure 3). At the transition state (TS1), the O1–H2 and C2–H2 distances are 1.21 and 1.45 Å, respectively. The V–O1 distance changes from 1.59 Å in the bare catalyst to 1.68 Å. The imaginary frequency of 1372i cm^{-1} of the transition state corresponds to the move-

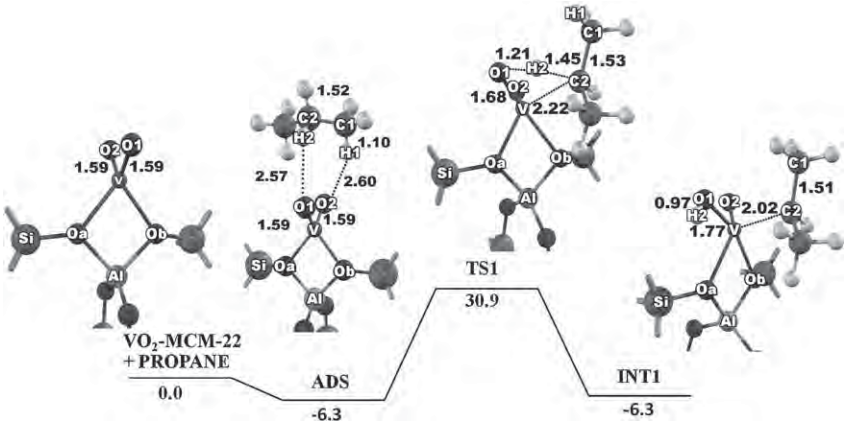

Figure 3. Energy profile for the first hydrogen abstraction step of the ODH of propane over VO_2-MCM-22 (M06-L/6-31G(d,p) calculations on a 14T model).

ment of the H2 atom between the O1 and C2 atoms. This step requires an intrinsic activation energy of 37.2 kcal mol^{-1} while the apparent activation energy is 30.9 kcal mol^{-1} (see Figure 3). The product of this step, the isopropyl radical intermediate (INT1), has a relative energy of −6.3 kcal mol^{-1}. It is closely coordinated to the vanadium atom with a V–C2 distance of 2.02 Å. It is interesting to note that in V_2O_5 bulk[8] and clusters,[7a,b] the intermediate was found to be not coordinated to the vanadium atom but that our intermediate is rather similar to the one predicted for gas-phase VO_2^+,[6] thus indicating the flexibility of the active site.

2.3. Propene Formation

The isopropyl radical intermediate (INT1) can be converted to propene via abstraction of the hydrogen atom from C1 to the hydroxyl group (O1H2) or to the O2 oxygen atom on the vanadium atom, to yield an adsorbed water molecule and dihydroxy vanadium intermediates (INT2-O2), respectively. For the former, the C1–H1 bond of the isopropyl radical is elongated from 1.09 to 1.37 Å and correspondingly, H1–O1 decreases from 2.74 to 1.32 Å. The normal-mode analysis shows one imaginary frequency at 1445i cm^{-1} corresponding to the movement of H1 in the formation of the O1–H1 bond and the breaking of the C1–H1 bond.

The second pathway proceeds through the transition state TS2-O2, and H1 is transferred towards O2 and the C1–H1 and H1–O2 bond lengths become 1.46 and 1.26 Å, respectively. The associated imaginary frequency at the transition state is 1529i cm^{-1}. The first pathway is kinetically preferred over the second one with a required apparent activation energy of 27.7 kcal mol^{-1}, which is 13.1 kcal mol^{-1} lower than that for the second pathway. Moreover, the water formation intermediate (INT2) is more stable than the dihydroxy vanadium one (see Figure 4). During this step, the isopropyl radical intermediate can react with the hydroxyl group (O1H2) of the active site to

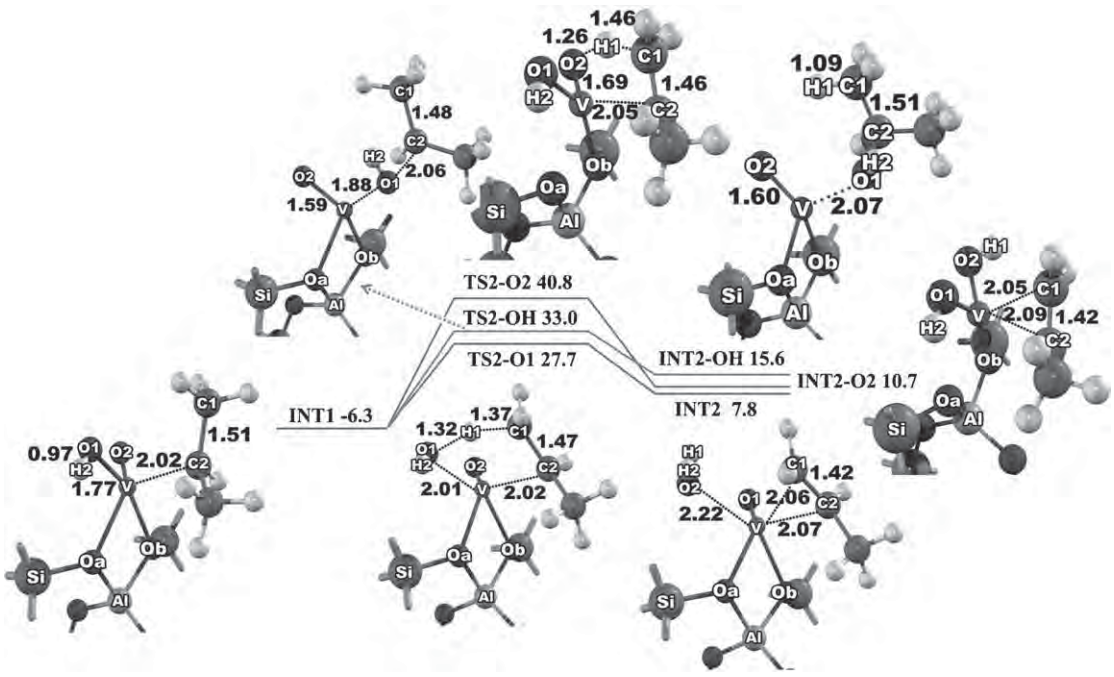

Figure 4. Energy profiles of the three possible reactions at the propene formation step (M06-L/6-31G(d,p) calculations on a 14T model).

form an oxygenated product, which leads to a reduced selectivity towards propene. This step was found to proceed via a triplet state, consistent with the literature.[7b] However, the calculation shows that propene formation is favored by 5.3 kcal mol^{-1} energy and thus this pathway is kinetically and thermodynamically preferred. This agrees with observations from Fu et al. in which the formation of isopropoxide at the vanadyl oxygen site was found to be unlikely.[8] The driving force of this step is the highly endothermic change of the V oxidation state from +5 (d^0) to +3 (d^2), thus overcompensating the exothermic conversion of propane and oxygen to propene and water.[14] It is noted that for the transition structure TS2-OH, the oxygen atoms are tetrahedrally coordinated to the V atom, which is different from the distorted square-planar structure for the other transition states (TS2-O2 and TS2-O1).

2.4. Reoxidation of the Catalyst

Nitrous oxide (N_2O) was used as the reoxidizing agent for the catalyst recovery step because it has been proven that it provides a higher selectivity than molecular oxygen.[7c] After the propene formation step, the water molecule needs 24.9 kcal mol^{-1} to desorb while propene is even more strongly coordinated at the vanadia site (41.9 kcal mol^{-1}).

The reaction profile for this step is shown in Figure 5. In the beginning of the reoxidation step, N_2O adsorbs on the vanadium atom with N2–O3 and O3–V distances of 1.20 and 2.47 Å, respectively. Its adsorption sets 8.5 kcal mol^{-1} free. After that, the O3 of N_2O interacts with vanadium causing elongation of the N2–O3 bond to 1.35 Å while O3–V contracts to 1.90 Å. This requires an intrinsic activation energy of 15.9 kcal mol^{-1}. The intermediate is stabilized by a relative energy of −37.5 kcal mol^{-1}. This indicates that the active site strongly prefers the fivefold coordination over the fourfold one. Finally, removal of nitrogen and propene from the catalyst requires 5.3 and 14.0 kcal mol^{-1}, respectively. From these results, it can be implied that the reoxidation step is not rate limiting but that the reduction of the product desorption energy is needed to recover the active site.

2.5. The Framework Effect

The 120T nanocluster model was used for single-point calculations, to evaluate how the MCM-22 framework affects reaction energies during the ODH process. It was found that all structures are stabilized by the extended framework. The adsorption energy of propane over the catalyst increases from −6.3 kcal mol^{-1} for the 14T cluster to −7.0 kcal mol^{-1} for the 120T model. In the methylene hydrogen abstraction step, which is considered to be a rate-limiting step for this reaction, the apparent activation energy was reduced from 30.9 to 28.5 kcal mol^{-1}. This is in accordance with the 20–30 kcal mol^{-1} from experiments on propane ODH over supported vanadia catalysts.[4i,15] However, when the reduction of the adsorption energy is considered, the true activation energy of this system remains nearly unchanged by the confinement effect of the MCM-22 framework. This overall shift is similar to the propene formation step (see Table 1).

Single-point calculations were also performed for the structures without the whole zeolitic framework. Three model structures containing VO_2^+ and the probe molecule were formed from the 14T optimized geometries (see Figure 6). In these models VO_2^+ was neutralized by OH^- (**1**), (H_2O)(OH^-) (**2**), and $Al(OH)_4^-$ (**3**) and each structure was fixed at the 14T optimized geometry. The adsorption energies of the three models were similar to each other (−2.4, −2.6, and −2.2 kcal mol^{-1} for models **1**–**3**, respectively). Taking into account the value of −6.3 kcal mol^{-1} for the cluster with the framework, one can estimate that the framework contribution to the adsorption energy of propane on the catalyst is about 60%. The desorption energy of the propene product is 8.1 and 8.2 kcal mol^{-1} for models **2** and **3**, respectively, and 16.4 kcal mol^{-1} for model **1**. The strong interaction obtained for model **1** might be due to the unsaturated fourfold coordination that is found to be the same as in the initial desorption of propene before the reconstruction of the active site takes place. When considering only models **2** and **3**, one can state

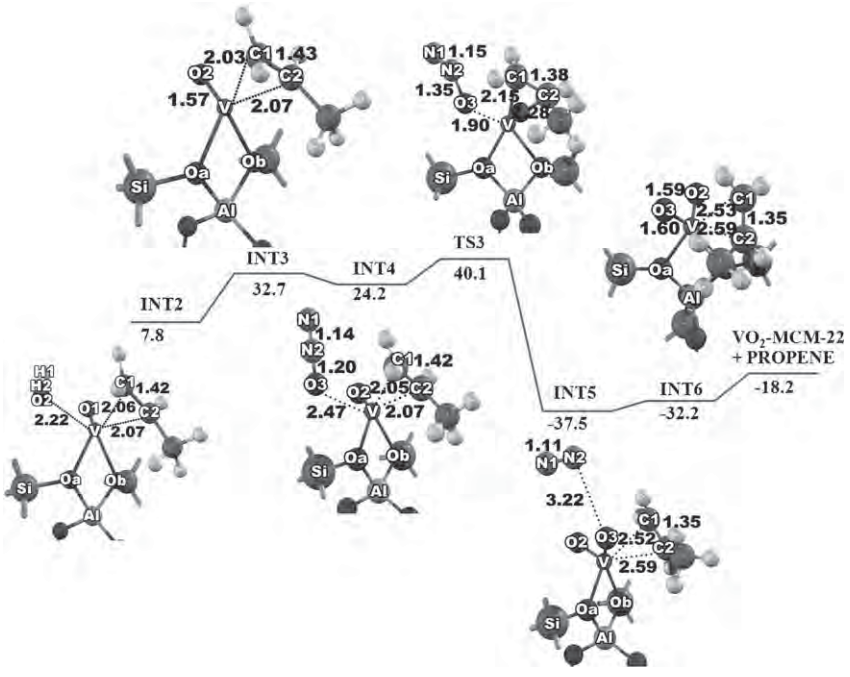

Figure 5. Reaction profile for the reoxidation step.

Table 1. Energies of the components in the ODH process, given relative to the energy of the reactants.

System	Relative Energy [kcal mol^{-1}] 14T M06-L/6-31G(d,p) (Optimized)	120T M06-L/6-31G(d,p) (Single Point)
VO2-MCM-22 + propane + N_2O	0.0	0.0
ADS	−6.3	−7.0
TS1	30.9	28.5
INT1	−6.3	−10.8
TS2	27.7	23.1
INT2	7.8	1.1
INT3	32.7	28.1
INT4	24.2	19.9
TS3	40.1	36.9
INT5	−37.5	−42.4
INT6	−32.2	−36.8
VO_2-MCM-22 + propene + N_2	−18.2	−18.2

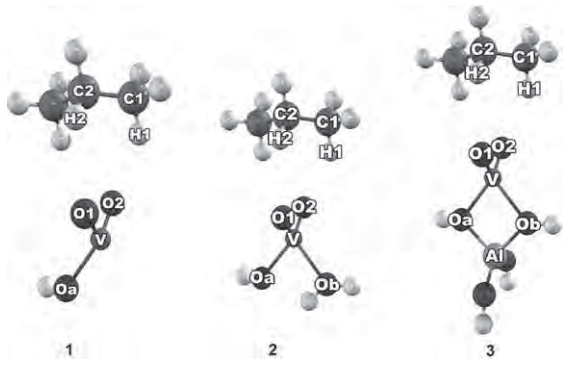

Figure 6. Three small models of the active site saturated and neutralized by OH^- (**1**), $(H_2O)(OH^-)$ (**2**), and $Al(OH)_4^-$ (**3**). See text for explanation.

that the framework contribution for the propene desorption energy is less than about 40%, a result of the strong π bond between alkene and the metal.

Finally, to obtain additional information about the interactions in our system we performed an approximate energy decomposition[16] of the zeolite–adsorbate system. In this scheme, the self-consistent field (SCF) energy between the zeolite model and propane is "deconstructed" into: 1) the interaction between the two parts, each with its own frozen wavefunction, 2) the mutual polarization due to orbital relaxation, still with independent wavefunctions, 3) charge transfer, and 4) the change due to orbital delocalization after the wavefunctions are allowed to mix. Since in M06-L the dispersion-like interactions are parameterized into the basic energy expression of the functional, they ought to appear in part (1). Indeed, the zeolite–propane interaction energy (1) between the frozen parts is −9 kcal mol^{-1} for M06-L and +2 kcal mol^{-1} for B3LYP in their respective geometries (partially optimized as described above). The small overall attractive energy in the case of B3LYP is mostly a result of SCF delocalization (4). The energy decomposition analysis thus confirms the nature of the improvements resulting from M06-L. The calculations were performed with the Q-Chem 3.22 program[17] and, for technical reasons, the SBKJC basis set.[18]

2.6. Rate Constants

Rate constants (k_r) and equilibrium constants (K_{eq}) were calculated for the rate-limiting C–H activation step and are summarized in Table 2. Values of k_r and K_{eq} were calculated in the range of 300–800 °C, a typical temperature range for experiments. It was found that k_r for the forward reaction increases dramatically when the temperature increases; K_{eq} increases gradually from 0.255 to 0.418. This finding is consistent with the experimentally observed temperature dependence of the propane conversion rate.[5c]

Table 2. Kinetic and equilibrium constants of the reaction in the temperature range between 300 and 800 °C.

Temperature [°C]	k_r (FWD)	k_{-r} (REV)	K_{eq}
300	4.27×10^{-1}	1.67×10^{0}	0.255
350	5.33×10^{0}	1.99×10^{1}	0.268
400	4.63×10^{1}	1.65×10^{2}	0.281
450	3.01×10^{2}	1.02×10^{3}	0.296
500	1.55×10^{3}	4.96×10^{3}	0.312
550	6.56×10^{3}	2.00×10^{4}	0.328
600	2.37×10^{4}	6.87×10^{4}	0.345
650	7.51×10^{4}	2.07×10^{5}	0.363
700	2.12×10^{5}	5.56×10^{5}	0.381
750	5.43×10^{5}	1.36×10^{6}	0.399
800	1.28×10^{6}	3.06×10^{6}	0.418

3. Conclusions

The adsorption and the ODH reaction mechanism of the propane/VO_2-MCM-22 system have been investigated by DFT calculations with the M06-L functional. The adsorption energies of propane are comparable to those derived from computationally much more demanding MP2 calculations and to experimental results while, as expected, the values from the B3LYP functional are too small.

For the reaction mechanism, two main steps were considered. The reaction begins with the rate-determining step, the abstraction of the methylene hydrogen. The calculated apparent activation energy for this system is 30.9 kcal mol^{-1}, which is within the range of the experimental values reported for propane ODH over supported vanadium catalysts. We find that the formation of propene is indeed preferred over the competing oxygenated product on the VO_2-MCM-22 nanocatalyst. A single-point calculation showed that the activation energy with a larger 120T model is 2.4 kcal mol^{-1} lower than it is in the 14T cluster, which indicates the amount of stabilization due to the framework.

For the propane adsorption step the framework dominates the energetics, while for the propene desorption the metal site dominates. As a consequence, the reoxidation of the vanadium

site by N_2O greatly reduces the amount of energy needed for propene desorption due to the strong interaction of the unsaturated active site. From the very different adsorption energies of propane and propene, one can suggest this catalyst to be usable for separating the alkene product from the alkane. A subsequent study will consider the activity and selectivity of this reaction on further modified catalysts.

Computational Methods

The geometry of the MCM-22 zeolite cluster was obtained from the crystal structure,[19] represented by a cluster of 14 tetrahedrally coordinated Si or Al atoms (14T). The cluster covers the 12-membered ring at the intersection of two channels, which is considered to be an appropriate active site of the catalyst (see Figure 1). An Al atom is located at the T1 position, its most stable configuration in this model.[20] The vanadium oxide species $[VO_2]^+$ is adsorbed at the highly accessible Brønsted acid site. All geometry optimizations were performed by the M06-L functional using the 6-31G(d,p) basis set for H, C, O, Al, and Si atoms, whereas the Stuttgart effective core potentials (ECPs)[21] were employed for the V atom. Calculations with the B3LYP functional and with Møller–Plesset perturbation theory (MP2) with the same basis set were performed for comparison. During geometry optimization, only the active sites of the catalyst ($VO_2/AlSi_4O_4$) and the probe molecule were allowed to relax, while the rest were kept fixed at the original crystal structure. A normal-mode analysis of the transition states shows only one imaginary frequency, the mode of which corresponds to the designated reaction. The total spin state was assumed to be a singlet, which was found to be the most stable state.[6] Rate constants were calculated by classical transition-state theory (TST) using Equation (1):

$$k_r = \frac{k_B T}{h}\frac{q_{TS}}{q_{Int}}\exp(-\Delta E_a/RT) \quad (1)$$

where ΔE_a is the activation energy, k_B is Boltzmann's constant, h is Plank's constant, T is the temperature, R is the universal gas constant, and q_{TS} and q_{Int} are the total partition functions for the transition state and intermediate complex, respectively.

Finally, to cover the confinement effect from the zeolite framework, the model was extended to a 120T structure which included a supercage of MCM-22. All calculations were performed by the Gaussian 03 package[22] modified to incorporate the Minnesota Density Functionals module 3.1 by Zhao and Truhlar.

Acknowledgements

This work was supported in part by grants from the National Science and Technology Development Agency (NSTDA Chair Professor and NANOTEC Center of Excellence), the Thailand Research Fund (to J.L.), the Kasetsart University Research and Development Institute (KURDI), the Commission on Higher Education, Ministry of Education ("the National Research University Project of Thailand (NRU)" and "Postgraduate Education and Research Programs in Petroleum and Petrochemicals and Advanced Materials"), under the Royal Golden Jubilee Ph.D. program from the Thailand Research Fund (to S.W.). The authors are grateful to Donald G. Truhlar and Yan Zhao for supplying them with the code for the M06-L functional. M.P. acknowledges an infrastructure grant of the Austrian Ministry of Science to the LFU scientific computing platform.

Keywords: density functional calculations · oxidative dehydrogenation · propene · vanadium oxide · zeolites

[1] F. Cavani, N. Ballarini, A. Cericola, *Catal. Today* **2007**, *127*, 113 – 131.
[2] T. Ren, M. Patel, K. Blok, *Energy* **2006**, *31*, 425 – 451.
[3] a) G. Centi, F. Cavani, F. Trifirò, *Selective Oxidation by Heterogeneous Catalysis*, Kluwer Academic, New York, **2001**; b) T. Blasco, J. M. Lopez Nieto, *Appl. Catal. A* **1997**, *157*, 117 – 142; c) E. A. Mamedov, V. Cortés Corberán, *Appl. Catal. A* **1995**, *127*, 1 – 40.
[4] a) M. A. Chaar, D. Patel, H. H. Kung, *J. Catal.* **1988**, *109*, 463 – 467; b) A. Corma, J. M. Lopez Nieto, N. Paredes, *J. Catal.* **1993**, *144*, 425 – 438; c) F. D. Hardcastle, I. E. Wachs, *J. Mol. Catal.* **1988**, *46*, 173 – 186; d) I. E. Wachs, B. M. Weckhuysen, *Appl. Catal. A* **1997**, *157*, 67 – 90; e) J. G. Eon, R. Olier, J. C. Volta, *J. Catal.* **1994**, *145*, 318 – 326; f) A. Khodakov, B. Olthof, A. T. Bell, E. Iglesia, *J. Catal.* **1999**, *181*, 205 – 216; g) A. Khodakov, J. Yang, S. Su, E. Iglesia, A. T. Bell, *J. Catal.* **1998**, *177*, 343 – 351; h) E. V. Kondratenko, M. Baerns, *Appl. Catal. A* **2001**, *222*, 133 – 143; i) M. D. Argyle, K. Chen, A. T. Bell, E. Iglesia, *J. Catal.* **2002**, *208*, 139 – 149; j) E. V. Kondratenko, M. Cherian, M. Baerns, *Catal. Today* **2006**, *112*, 60 – 63.
[5] a) A. Julbe, D. Farrusseng, J. C. Jalibert, C. Mirodatos, C. Guizard, *Catal. Today* **2000**, *56*, 199 – 209; b) S. A. Karakoulia, K. S. Triantafyllidis, G. Tsilomelekis, S. Boghosian, A. A. Lemonidou, *Catal. Today* **2009**, *141*, 245 – 253; c) A. A. Teixeira-Neto, L. Marchese, G. Landi, L. Lisi, H. O. Pastore, *Catal. Today* **2008**, *133–135*, 1 – 6; d) A. Dinse, S. Khennache, B. Frank, C. Hess, R. Herbert, S. Wrabetz, R. Schlögl, R. Schomäcker, *J. Mol. Catal. A* **2009**, *307*, 43 – 50.
[6] M. Engeser, M. Schlangen, D. Schröder, H. Schwarz, T. Yumura, K. Yoshizawa, *Organometallics* **2003**, *22*, 3933 – 3943.
[7] a) M. J. Cheng, K. Chenoweth, J. Oxgaard, A. Van Duin, W. A. Goddard III, *J. Phys. Chem. C* **2007**, *111*, 5115 – 5127; b) X. Rozanska, R. Fortrie, J. Sauer, *J. Phys. Chem. C* **2007**, *111*, 6041 – 6050; c) X. Rozanska, E. V. Kondratenko, J. Sauer, *J. Catal.* **2008**, *256*, 84 – 94.
[8] H. Fu, Z. P. Liu, Z. H. Li, W. N. Wang, K. N. Fan, *J. Am. Chem. Soc.* **2006**, *128*, 11114 – 11123.
[9] a) T. Maihom, S. Namuangruk, T. Nanok, J. Limtrakul, *J. Phys. Chem. C* **2008**, *112*, 12914 – 12920; b) B. Jansang, T. Nanok, J. Limtrakul, *J. Phys. Chem. C* **2008**, *112*, 540 – 547; c) S. Choomwattana, T. Maihom, P. Khongpracha, M. Probst, J. Limtrakul, *J. Phys. Chem. C* **2008**, *112*, 10855 – 10861; d) B. Jansang, T. Nanok, J. Limtrakul, *J. Mol. Catal. A* **2007**, *264*, 33 – 39; e) S. Namuangruk, D. Tantanak, J. Limtrakul, *J. Mol. Catal. A* **2006**, *256*, 113 – 121; f) S. Namuangruk, P. Khongpracha, P. Pantu, J. Limtrakul, *J. Phys. Chem. B* **2006**, *110*, 25950 – 25957; g) J. Lomratsiri, M. Probst, J. Limtrakul, *J. Mol. Graphics Modell.* **2006**, *25*, 219 – 225; h) S. Kasuriya, S. Namuangruk, P. Treesukol, M. Tirtowidjojo, J. Limtrakul, *J. Catal.* **2003**, *219*, 320 – 328; i) K. Bobuatong, J. Limtrakul, *Appl. Catal. A* **2003**, *253*, 49 – 64.
[10] a) Y. Zhao, D. G. Truhlar, *Theor. Chem. Acc.* **2008**, *120*, 215 – 241; b) Y. Zhao, D. G. Truhlar, *Acc. Chem. Res.* **2008**, *41*, 157 – 167.
[11] a) T. Maihom, B. Boekfa, J. Sirijaraensre, T. Nanok, M. Probst, J. Limtrakul, *J. Phys. Chem. C* **2009**, *113*, 6654 – 6662; b) B. Boekfa, S. Choomwattana, P. Khongpracha, J. Limtrakul, *Langmuir* **2009**, *25*, 12990 – 12999; c) C. Kumsapaya, K. Bobuatong, P. Khongpracha, Y. Tantirungrotechai, J. Limtrakul, *J. Phys. Chem. C* **2009**, *113*, 16128 – 16137; d) R. Valero, J. R. B. Gomes, D. G. Truhlar, F. Illas, *J. Chem. Phys.* **2008**, *129*, 124710; e) R. Valero, J. R. B. Gomes, D. G. Truhlar, F. Illas, *J. Chem. Phys.* **2010**, *132*, 104701.
[12] P. Pantu, S. Pabchanda, J. Limtrakul, *ChemPhysChem* **2004**, *5*, 1901 – 1906.
[13] A. Kämper, A. Auroux, M. Baerns, *Phys. Chem. Chem. Phys.* **2000**, *2*, 1069 – 1075.
[14] J. Sauer, J. Döbler, *Dalton Trans.* **2004**, 3116 – 3121.
[15] a) K. Chen, A. T. Bell, E. Iglesia, *J. Phys. Chem. B* **2000**, *104*, 1292 – 1299; b) E. Heracleous, M. Machli, A. A. Lemonidou, I. A. Vasalos, *J. Mol. Catal. A* **2005**, *232*, 29 – 39.

[16] R. Z. Khaliullin, E. A. Cobar, R. C. Lochan, A. T. Bell, M. Head-Gordon, *J. Phys. Chem. A* **2007**, *111*, 8753 – 8765.
[17] Y. Shao, L. F. Molnar, Y. Jung, J. Kussmann, C. Ochsenfeld, S. T. Brown, A. T. B. Gilbert, L. V. Slipchenko, S. V. Levchenko, D. P. O'Neill, R. A. DiStasio, Jr., R. C. Lochan, T. Wang, G. J. O. Beran, N. A. Besley, J. M. Herbert, C. Y. Lin, T. Van Voorhis, S. H. Chien, A. Sodt, R. P. Steele, V. A. Rassolov, P. E. Maslen, P. P. Korambath, R. D. Adamson, B. Austin, J. Baker, E. F. C. Byrd, H. Dachsel, R. J. Doerksen, A. Dreuw, B. D. Dunietz, A. D. Dutoi, T. R. Furlani, S. R. Gwaltney, A. Heyden, S. Hirata, C. P. Hsu, G. Kedziora, R. Z. Khalliulin, P. Klunzinger, A. M. Lee, M. S. Lee, W. Liang, I. Lotan, N. Nair, B. Peters, E. I. Proynov, P. A. Pieniazek, Y. M. Rhee, J. Ritchie, E. Rosta, C. D. Sherrill, A. C. Simmonett, J. E. Subotnik, H. L. Woodcock III, W. Zhang, A. T. Bell, A. K. Chakraborty, D. M. Chipman, F. J. Keil, A. Warshel, W. J. Hehre, H. F. Schaefer III, J. Kong, A. I. Krylov, P. M. W. Gill, M. Head-Gordon, *Phys. Chem. Chem. Phys.* **2006**, *8*, 3172 – 3191.
[18] a) T. R. Cundari, W. J. Stevens, *J. Chem. Phys.* **1993**, *98*, 5555 – 5565; b) W. J. Stevens, H. Basch, M. Krauss, *J. Chem. Phys.* **1984**, *81*, 6026 – 6033; c) W. J. Stevens, M. Krauss, H. Basch , P. G. Jasien, *Can. J. Chem.* **1992**, *70*, 612.
[19] M. E. Leonowicz, J. A. Lawton, S. L. Lawton, M. K. Rubin, *Science* **1994**, *264*, 1910 – 1913.
[20] D. Zhou, Y. Bao, M. Yang, N. He, G. Yang, *J. Mol. Catal. A* **2006**, *244*, 11 – 19.
[21] M. Dolg, U. Wedig, H. Stoll, H. Preuss, *J. Chem. Phys.* **1987**, *86*, 866 – 872.
[22] Gaussian 03, Revision B.05, M. J. Frisch, G. W. Trucks, H. B. Schlegel, G. E. Scuseria, M. A. Robb, J. R. Cheeseman, J. A. Montgomery, Jr., T. Vreven, K. N. Kudin, J. C. Burant, J. M. Millam, S. S. Iyengar, J. Tomasi, V. Barone, B. Mennucci, M. Cossi, G. Scalmani, N. Rega, G. A. Petersson, H. Nakatsuji, M. Hada, M. Ehara, K. Toyota, R. Fukuda, J. Hasegawa, M. Ishida, T. Nakajima, Y. Honda, O. Kitao, H. Nakai, M. Klene, X. Li, J. E. Knox, H. P. Hratchian, J. B. Cross, V. Bakken, C. Adamo, J. Jaramillo, R. Gomperts, R. E. Stratmann, O. Yazyev, A. J. Austin, R. Cammi, C. Pomelli, J. W. Ochterski, P. Y. Ayala, K. Morokuma, G. A.Voth, P. Salvador, J. J. Dannenberg, V. G. Zakrzewski, S. Dapprich, A. D. Daniels, M. C. Strain, O. Farkas, D. K. Malick, A. D. Rabuck, K. Raghavachari, J. B. Foresman, J. V. Ortiz, Q. Cui, A. G. Baboul, S. Clifford, J. Cioslowski, B. B. Stefanov, G. Liu, A. Liashenko, P. Piskorz, I. Komaromi, R. L. Martin, D. J Fox, T. Keith, M. A. Al-Laham, C. Y. Peng, A. Nanayakkara, M. Challacombe, P. M. W. Gill, B. Johnson, W. Chen, M. W. Wong, C. Gonzalez, J. A. Pople, Gaussian, Inc., Wallingford, CT, **2004**.

Received: July 20, 2010
Published online on October 25, 2010

Structures and Energetics of the Methylation of 2-Methylnaphthalene with Methanol over H-BEA Zeolite

Karan Bobuatong,[†,‡,§,⊥] Michael Probst,[¶] and Jumras Limtrakul*[,†,‡,§,⊥]

Laboratory for Computational and Applied Chemistry, Department of Chemistry, Faculty of Science, Kasetsart University, Bangkok 10900, Thailand, Center of Nanotechnology, Kasetsart University Research and Development Institute, Kasetsart University, Bangkok 10900, Thailand, NANOTEC Center of Nanotechnology, National Nanotechnology Center, Kasetsart University, Bangkok 10900, Thailand, Center for Advanced Studies in Nanotechnology and Its Applications in Chemical, Food and Agricultural Industries, Kasetsart University, Bangkok 10900, Thailand, and Institute of Ion Physics and Applied Physics, University of Innsbruck, A-6020 Innsbruck, Austria

Received: September 8, 2010; Revised Manuscript Received: October 24, 2010

The methylation of 2-methylnaphthalene (2-MN) with methanol to the 2,6 (2,6-DMN) and 2,7 (2,7-DMN) dimethylnaphthalenes catalyzed over nanoporous BEA zeolite has been investigated quantum chemically using the M06-2X density functional. The catalytic cycle consists of three elementary steps: (1) formation of a methoxy species from methanol that is bound to a zeolite oxygen atom, (2) methylation of 2-MN to DMN with methoxy leading to naphthalynic carbocations, and (3) formation of DMN by proton back-donation from naphthalynic carbocations. The reaction profiles are similar for both the 2,6 and the 2,7 isomer and are in agreement with the experimental observation that they are produced in equal amounts on acidic BEA zeolite. A possible side reaction, the formation of dimethyl ether via the self-activation of methanol, is also discussed. The stability of the intermediates inside the pores is, to a large extent, governed by the steric constraints and the van der Waals dispersion interactions induced by the pore structure of BEA zeolite. These are the key parameters for understanding the relationship between zeolite topology and catalytic activity.

1. Introduction

The catalytic conversion of aromatic molecules via methylation, alkylation and isomerization is a very important process in the petrochemical industry.[1] Nowadays, zeolites are used industrially for this purpose. These remarkable aluminosilicate minerals are capable of catalyzing chemical reactions that take place in their well-defined nanostructured pore cavity, and also often provide numerous advantages over the traditional Friedel−Crafts catalyst due to their high selectivity to the desired products and their thermal properties. In addition, the use of heterogeneous inorganic catalysts like zeolites facilitates the design of clean technologies and applications that have to take into consideration environmental concerns.

In the past decade, the demand for 2,6-naphthalenedicarboxylic acid (2,6-NDA) as a raw material for the manufacture of a high-performance polyethylene naphthalene (PEN)[2,3] has increased significantly. 2,6-Dimethylnaphthalene (2,6-DMN) is considered as the most suitable feedstock with its high reactivity toward oxidation into 2,6-NDA.[4] Therefore, the synthesis of 2,6-DMN from the ten DMN isomers has been studied.[4−7] The alternative process of 2,6-DMN production, the methylation of methylnaphthalene (MN), has also been investigated[8−12] intensively.

In all these studies, ZSM-5 showed a high β- and/or β,β-selectivity, approximately 80%. T. Inui et al.[13] optimized the performance of H-ZSM-5 by a mechanochemical method leading to a significant improvement in the life of the catalyst as well as the improvement of the shape-selectivity. However, the ratio of 2,6-DMN/2,7-DMN produced on ZSM-5 was almost 1, and their yields were still not high. S.-B. Pu et al.[11] studied the same reaction over MFI metallosilicates, as well as over some large-pore zeolites, to improve especially the 2,6-DMN/2,7-DMN ratio. They reported that these large-pore zeolites significantly increase the yield of 2,6-DMN. In all the zeolites used, BEA showed the highest yield of 2,6-DMN and its deactivation was more gradual than the one of ZSM- 12 and Y. A three-dimensional large-pore structure without a supercage as is present in BEA, is necessary for binuclear aromatic hydrocarbon conversion. Furthermore, the catalytic life of BEA can be prolonged markedly by using tetralin as the solvent for β-MN. This is caused by the dehydrogenation of tetralin in the vicinity of the active sites to prevent coke formation and/or remove the coke formed. However, the reaction mechanisms of this reaction inside the zeolite pores are not well understood.

Computational methods based on quantum chemistry have become reliable techniques to clarify the microstructural properties of various chemical systems.[14] Especially, the computational investigation of the catalytic mechanisms in zeolites is of considerable practical importance. Nevertheless, zeolites that have a high impact in industrial processes usually possess hundreds of atoms per unit cell, which makes the use of sophisticated methods, such as periodic DFT calculations,

* Corresponding author. E-mail: jumras.l@ku.ac.th. Telephone: +66-2-562-5555, ext 2159.
† Laboratory for Computational and Applied Chemistry, Department of Chemistry, Faculty of Science, Kasetsart University.
‡ Center of Nanotechnology, Kasetsart University Research and Development Institute, Kasetsart University.
§ NANOTEC Center of Nanotechnology, National Nanotechnology Center, Kasetsart University.
⊥ Center for Advanced Studies in Nanotechnology and Its Applications in Chemical, Food and Agricultural Industries, Kasetsart University.
¶ Institute of Ion Physics and Applied Physics, University of Innsbruck.

10.1021/jp108566c
Published on Web 11/17/2010

computationally too expensive. Most DFT calculations do not take into account the van der Waals (vdW) contributions to the interaction energy.[15] For example, the popular B3LYP functional has an unsatisfactory performance for such reactions. Besides issues such as an underestimation of reaction barrier heights, it is unable to describe van der Waals complexes bound by medium-range interactions, and it also exhibits incorrect trends in the bond energies of organometallic catalytic systems.[16,17]

Recently, Zhao and Truhlar[18−21] have developed the M06 class of hybrid functionals, and they suggest that they are suitable for general-purpose applications. Both M06-L and M06 are intended for applications in transition metal chemistry and perform markedly better than B3LYP for main-group thermochemistry, barrier heights, and noncovalent interactions. M06-2X has an improved performance in these areas as compared with M06-L and M06, but it is not suitable for describing transition metal chemistry. In recent works[22−24] it has been demonstrated that the zeolite confinement effect on reactions of unsaturated aliphatic, aromatic, and heterocyclic compounds can be studied by performing full quantum chemical calculations on sufficiently large clusters using the M06-2X method. This leads to a better overall accuracy than the somewhat arbitrary QM/MM schemes like the ONIOM method. Furthermore, it makes the selection of zeolite models more general and systematic.

The purpose of the present study is to examine the reaction mechanisms of the methylation of 2-methylnaphthalene (2-MN) in a model of a large zeolite cluster. The reaction path for the side reaction, the formation of dimethyl ether, has also been studied.

2. Computational Details

The crystal lattice structure of H-BEA was taken from the work of J. B. Higgins, et al.[25] An extended 34T (34 tetrahedral sites) zeolite cluster, covering the active region of the H-β zeolite is used to represent the Brønsted acid site and the zeolite framework. It includes the 12-membered ring representing the main gateway to the intersection of two perpendicular 12 MR channel systems, where the reactions normally take place (See Figure 1). A silicon atom at a T5 position in β zeolite is substituted by an aluminum atom. A proton is added to the bridging oxygen atoms bonded directly to the aluminum atom, conventionally called the O5 position, which is the O1 position in this study.

The M06-2X functional and the 6-31G(d,p) basis set were applied for the 34T zeolite cluster. In order to obtain more reliable results, single point calculations at the M06-2X/6-311+G(2df,2p) level of theory were also carried out. All calculations have been performed using the Gaussian 03 code.[26] During the structure optimization, the 5T portion of the active-site region [≡SiO(≡SiO)$_2$AlO(H)OSi≡] and the adsorbates are allowed to relax while the rest of the active region is kept at the crystallographic coordinates.

3. Results and Discussion

The results are organized in the following way. First, we examine the mechanism of the methylation of 2-MN to 2,6-DMN and 2,7-DMN, the main issue of the present work. Finally, we explore the possibility of dimethyl ether formation as a competitive reaction to the methylation of 2-MN.

3.1. The Methylation of 2-Methyl Naphthalene. A graph of the reaction mechanism is depicted in Scheme 1. The energy profile containing all species involved is plotted in Figure 2. In the following, we employ the notation that a postfix 'a' (as in Int_1a) denotes the 2,6-isomer, while a postfix 'b' is used for the 2,7-isomer. When energy values are followed by a second value in parentheses (as 2.6 (2.7) kcal/mol), this also refers to the 2,6- and 2.7-isomers. In addition, the optimized geometries of all species in this study are shown in the Supporting Information (Figure S1). This reaction is initiated by the adsorption of a methanol molecule on the acidic proton of H-BEA (denoted Ads in Scheme 1). The adsorption complex is stabilized by two hydrogen bonds between the OH group of methanol and the Brønsted acid site (O1−H1) of the zeolite: one between the Brønsted proton (H1) and the methanol oxygen atom (O4), and another between the methanol hydrogen atom

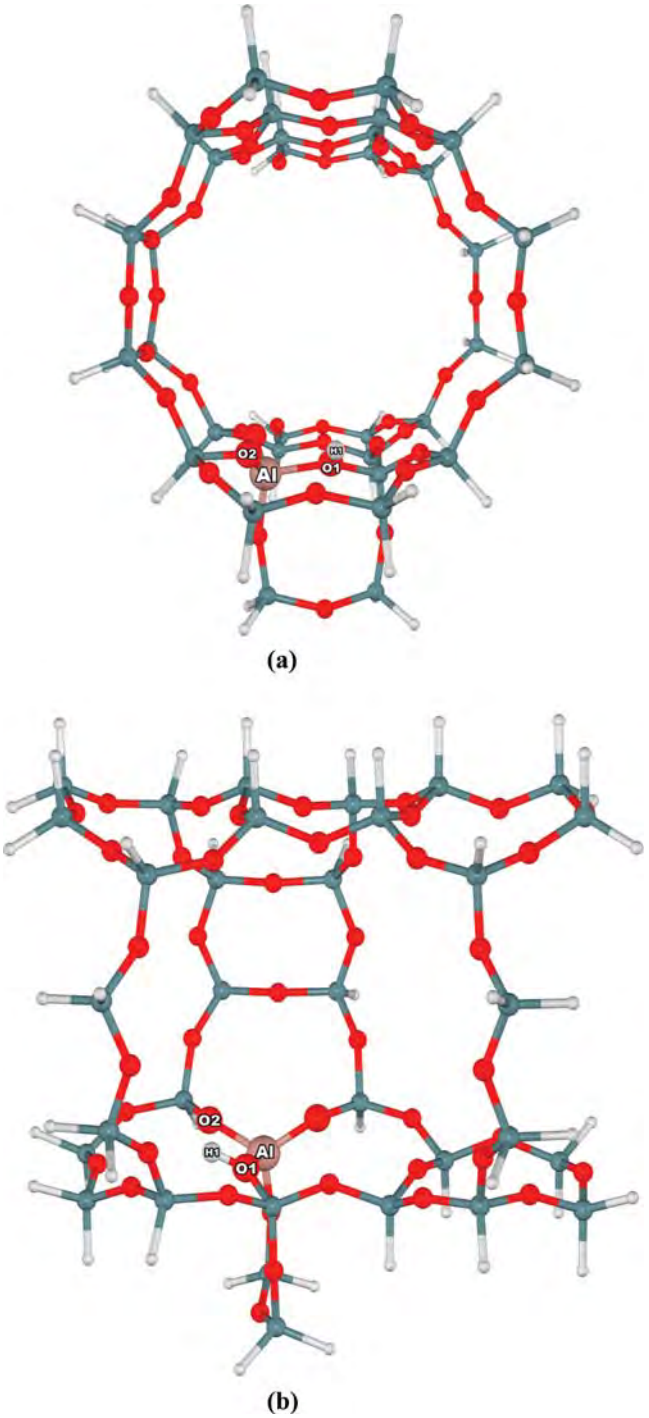

Figure 1. 34T cluster models of H-BEA. (a) 34T quantum cluster viewed from the direction of the pore axis. (b) 34T quantum cluster viewed from the direction of the side pore.

SCHEME 1: Catalytic Cycles of the Methylation of 2-MN to 2,6-DMN and 2,7-DMN over H-BEA Zeolite; Initiation Step Is the Adsorption of Methanol (Ads)

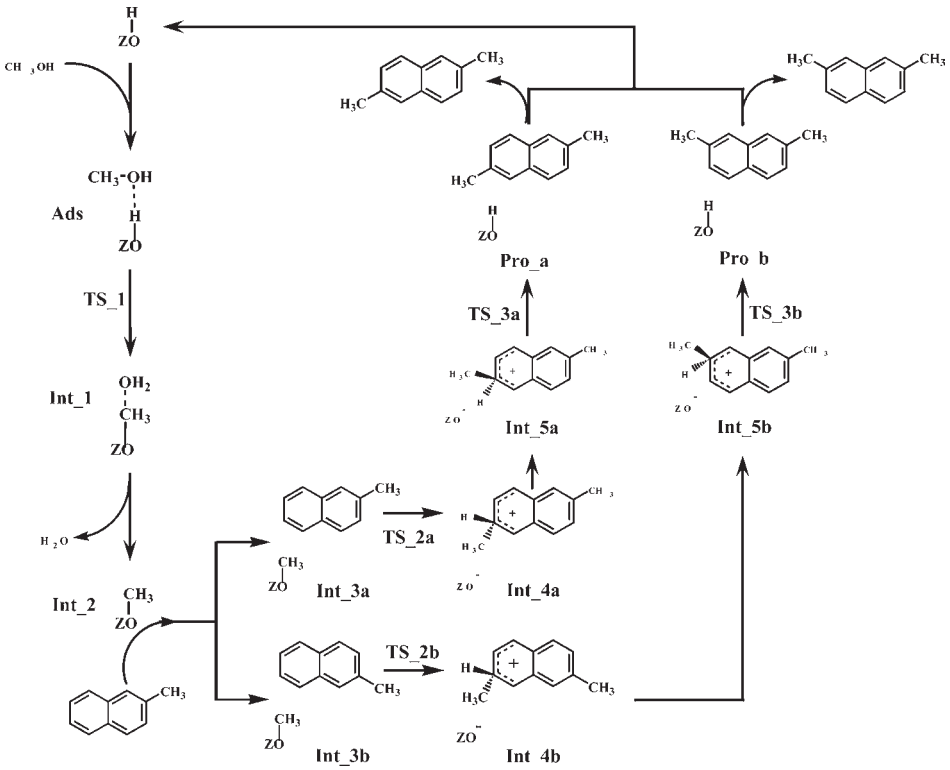

(H2) and the basic oxygen atom of the zeolite active site (O3). No protonation of methanol by the Brønsted site is observed. Similar configurations have also been described in previous studies.[27−30] The adsorption of methanol on the hydrogen form of ZSM-5 was studied in a calorimetric experiment by Gorte et al.[31] At 80% coverage of the Brønsted sites, a value of 27.5 ± 1.2 kcal/mol (115 ± 5 kJ/mol) was reported. The average acidic strength of the ZSM-5 zeolite was found to be similar to or stronger than that of the BEA zeolite, as determined by various spectroscopic techniques,[32−34] or NH_3-TPD[33] and hydrocarbon cracking.[32,34,35] The calculated adsorption energy of −24.2 kcal/mol therefore seems reliable. It is also compatible with typical van der Waals contributions inside the zeolite pore.

At the first transition state, the methanol C−O bond is activated by the attack of the Brønsted proton H1 on the methanol oxygen atom O4. The protonated methanol OH group is leaving as the methyl group is being attacked by the active zeolite O atom (Figure S1b, Supporting Information). We observe the dissociation of the C1−O4 bond and the association of the C1−O2 bond, respectively. As summarized in Table 1, the C1−O4 bond is lengthened from 1.44 to 1.91 Å, whereas the C1−O2 distance contracts to 2.05 Å. The corresponding O4−C1−O2 angle is 171.4°. In this configuration, the geometry of the methyl group is altered from tetrahedral to trigonal planar. The active-site structure of the zeolite is only slightly affected in the course of the progression of the reaction.

The activation barrier taken with respect to the adsorption of one methanol molecule at the acidic site (Ads) is predicted to be 39.8 kcal/mol (Figure 2a). This value is lower than the 51.4 kcal/mol obtained in previous calculations on smaller zeolite clusters.[36,37] The stabilizing effect of the zeolite micropore on the ionic transition state is well-known and can reach 10−30% of the activation barrier as was found for small zeolite clusters.[38] Upon methanol dehydration, methoxy species and a water molecule are created and coadsorb at the active site of BEA zeolite, Int_1. The water molecule then desorbs (Int_2) and is replaced by the incoming 2-MN. The relative energies of the coadsorption complexes are exothermic by −20.2 (Int_3a; 2,6-DMN) and −19.3 kcal/mol (Int_3b; 2,7-DMN).

After the coadsorption, the methyl group from the zeolite framework is transferred to the β-position of 2-MN via transition states TS_2a and TS_2b. The barriers for this reaction are 29.5 and 28.1 kcal/mol for 2,6-DMN and 2,7-DMN, respectively. The transition states are also shown in Figure 2a. The normal mode corresponding to the single imaginary frequency was also calculated and indicates the proceeding of the methylation of 2-MN. In the transition structures, which have the characteristics of methyl carbocations with a trigonal planar geometry, the C−C bond between CH_3 and MN starts to form. The C1−O2 bond of the methoxy species is elongated from 1.48 Å (1.49 Å) to 2.17 Å (2.12 Å) for 2,6-DMN and 2,7-DMN, respectively. Simultaneously, the lengths of the C1−C2 and C1−C3 bonds decrease from 3.77 Å to 2.20 Å and 3.35 Å to 2.20 Å for 2,6-DMN and 2,7-DMN, respectively. The transition states lead to the formation of the key intermediates, 2,6- and 2,7-naphthalenium (Int_4a and Int_4b). These are adsorbed on the active site by −14.6 (−11.3) kcal/mol. The difference of the adsorption energies can be explained by the fact that the 2,6-naphthalenium intermediate is located closer to the active site than the 2,7-isomer. The existence of aromatic cations in the zeolite cavity has been disclosed by the results of N. Hansen et al.[38] and X. Rozanska et al.[39] They found the aromatic carbocation as a reaction intermediate and concluded that large models of medium and micropore zeolites are able to stabilize the benzylic ionic intermediate.

Our results from above show that the naphthalenium intermediates will stay adsorbed to the active site and can undergo a proton back-donation process, as shown in Figure 2b. The hydrogen atoms at the carbon center of the naphthalenium intermediates are not in close proximity to the three oxygen

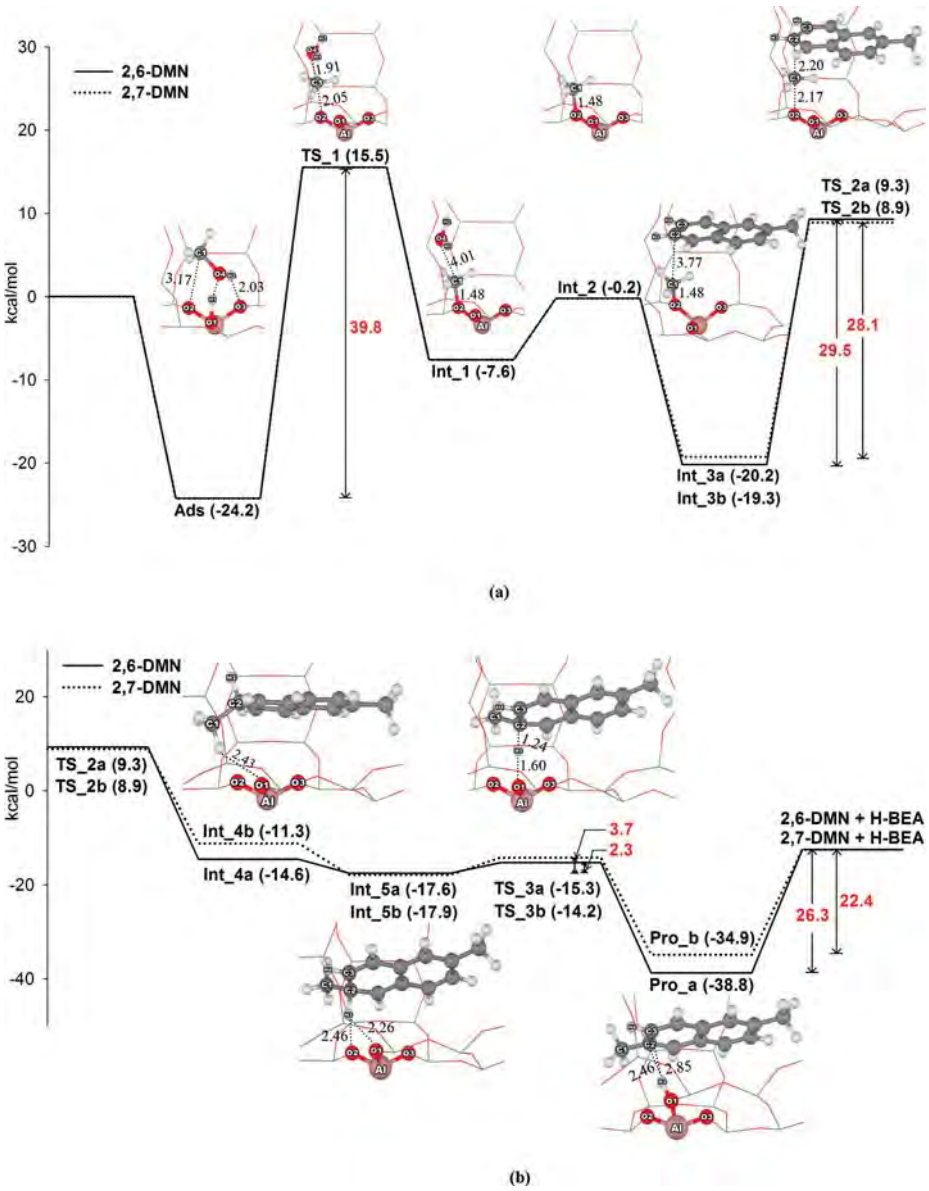

Figure 2. The calculated energy profile for the methylation of 2-MN to 2,6-DMN and 2,7-DMN (kcal/mol). Due to its size, this figure is split into parts (a) and (b).

TABLE 1: Geometrical Parameters from the 34T Model (M06-2X/6-311+G(2df,2p)//M06-2X/6-31G(d,p)) Calculations of the H-BEA Zeolite, Adsorption Complex (Ads), Transition States (TS_1 to TS_3b), Reaction Intermediates (Int_1 to Int_5b), and Products (Pro_a and Pro_b) for the Methylation of 2-MN to 2, 6-DMN and 2,7-DMN over H-BEA Zeolite[a]

parameter	H-BEA	Ads	TS_1	Int_1	Int_2	Int_3a	TS_2a	Int_4a	Int_5a	TS_3a	Pro_a	Int_3b	TS_2b	Int_4b	Int_5b	TS_3b	Pro_b
O1−H1	0.98	1.10	3.76	4.61	–	–	–	–	–	–	–	–	–	–	–	–	–
C1−O2	–	3.17	2.05	1.48	1.48	1.48	2.17	3.12	3.38	3.24	3.18	1.49	2.12	3.20	3.36	3.32	3.45
C1−O4	–	1.44	1.91	4.01	–	–	–	–	–	–	–	–	–	–	–	–	–
C1−C2	–	–	–	–	–	3.92	2.20	1.54	1.54	1.54	1.51	3.58	2.75	2.55	2.55	2.51	2.53
C1−C3	–	–	–	–	–	3.77	2.81	2.52	2.55	2.56	2.53	3.35	2.20	1.53	1.54	1.55	1.51
C2−H3	–	–	–	–	–	1.09	1.09	1.16	1.13	1.24	2.46	1.09	1.09	1.12	1.13	1.26	2.56
O1−H3	–	–	–	–	–	6.08	4.88	4.57	2.26	1.60	0.99	5.69	5.01	4.36	2.24	1.68	0.99
Al−O1	1.85	1.81	1.72	1.69	1.69	1.69	1.68	1.72	1.72	1.72	1.84	1.69	1.71	1.72	1.72	1.71	1.84
Al−O2	1.70	1.70	1.76	1.86	1.86	1.86	1.71	1.71	1.72	1.72	1.69	1.85	1.75	1.71	1.72	1.72	1.69
Al−O3	1.68	1.72	1.70	1.69	1.69	1.69	1.67	1.72	1.72	1.72	1.69	1.69	1.71	1.72	1.72	1.72	1.69
∠O1−Al−O2	93.1	97.1	97.2	94.3	94.3	94.4	96.7	100.0	99.1	98.8	94.9	94.6	97.8	99.9	99.1	99.16	94.9

[a] Distances are in Å, and angles are in degrees.

atoms around the active site. To allow for the regeneration of the active site in the final step, the naphthalenium intermediates need to rotate along the zeolite pore axis which causes these hydrogen atoms to get closer to the active site. Due to the lack of data, we use an experimentally derived approximate value of 6.9 kcal/mol[40,41] for the barriers of rotation of the protonated species around C2. The reoriented naphthalenium intermediates stick to the active site (Int_5a and Int_5b) with adsorption energies of −17.6 and −17.9 kcal/mol, respectively.

2,6-DMN and 2,7-DMN can be generated through direct proton transfer from the tetrahedral carbon center of the naphthalenium intermediates to an oxygen atom attached to the

SCHEME 2: Diagram Showing the Possible Competition between the Dimethyl Ether Formation and the Methylation of 2-MN over H-BEA Zeolite

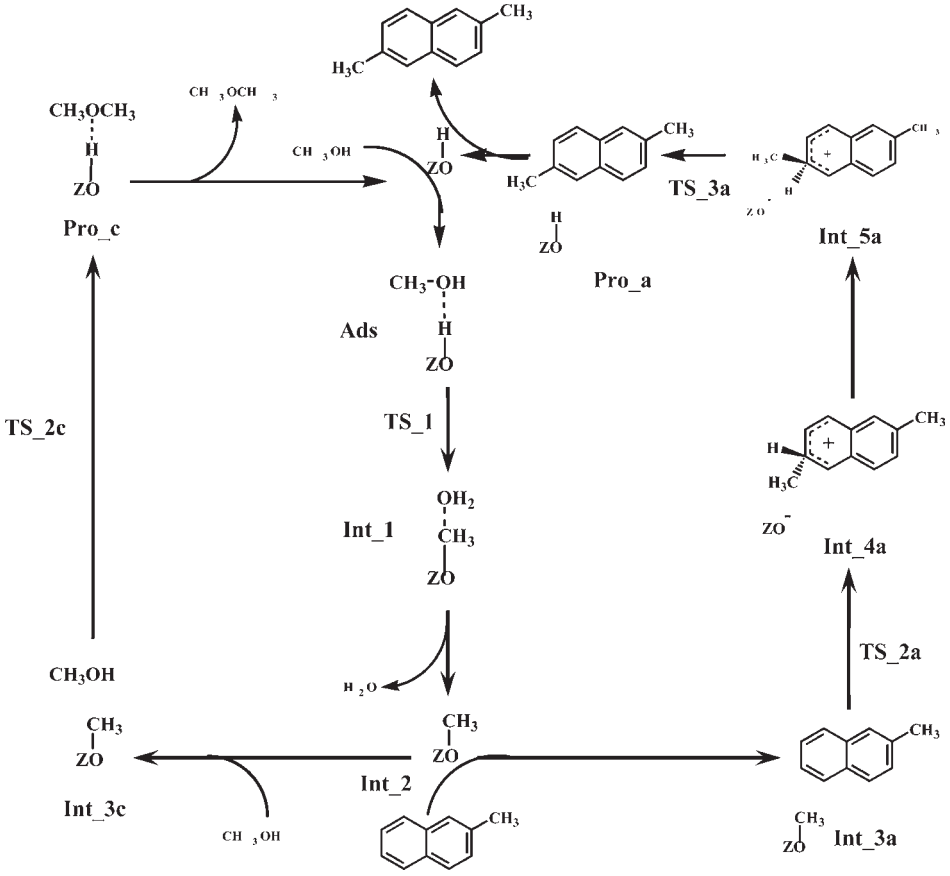

aluminum atom at the active sites (TS_3a and TS_3b) with calculated barriers of 2.3 and 3.7 kcal/mol. The transition states are slightly perturbed by the zeolite framework which causes the optimized structures to be very close to the intermediates. At the transition state TS_3 where the C−H cleavage occurs, the C−H bond distances of the naphthalenium intermediates are elongated from 1.13 Å (1.13 Å) to 1.24 Å (1.26 Å). Finally, after this third transition state, the products, 2,6-DMN and 2,7-DMN are adsorbed at the acidic active site via a π-bond interaction by −38.8 and −34.9 kcal/mol, respectively. These predicted reactions are exothermic, and finally 2,6-DMN and 2,7-DMN require desorption energies of 26.3 and 22.4 kcal/mol, respectively. Overall, the reaction profiles for the formation of 2,6-DMN and 2,7-DMN are similar to each other, in agreement with the experimental observation[11] that there is no preference for either of them when synthesized over acidic BEA zeolite.

3.2. Dimethyl Ether Formation. Finally, we consider another possible reaction of methanol over zeolite catalysts that could compete with the naphthalene methylation. It has been shown earlier[37] that at low coverage the methoxy species described above can react with a second methanol molecule to dimethyl ether (DME).

The proposed reaction mechanism of the dimethyl ether formation involves two elementary steps and is shown in Scheme 2. Its energetics are presented in Figure 3. We use the postfix 'c', when appropriate, for this reaction cycle. The first step starts with the initial adsorption of one methanol molecule at the zeolite acidic site, which is then dehydrated, leaving a methyl group attached to the basic oxygen of the zeolite. This step has been discussed already in section 3.1. The dehydration process is now followed by the activation of another methanol molecule by the methoxy species. The adsorption of the second methanol to the methoxy intermediate (Int_3c) is exothermic by −10.3 kcal/mol. The adsorption energy of this structure is 9.9 kcal/mol higher than the coadsorbed methoxy species and 2-MN (Int_3a), indicating a weaker interaction with the BEA zeolite cavity. The transition state (TS_2c) has the characteristics of a methyl carbocation with a trigonal planar geometry that leads to the formation of the C−O bond with the methanol molecule. The distance between C1 and O2 of methoxy increases from 1.49 to 1.98 Å, and the C1 and O5 distance decreases from 3.22 to 1.92 Å as their bond is formed (Table 2). Here, the zeolite framework plays an important role in stabilizing both the adsorption complex and the transition structure, with the energy barrier lowered by 3.6 kcal/mol compared to the value obtained from the 3T quantum cluster model[37] (Table 2). From the reaction profile in Figure 3 it can be seen that DME requires 26.2 kcal/mol to desorb from the active site. The rate-limiting step for DME formation according to this pathway is the dehydration of the first methanol molecule which requires 39.8 kcal/mol. The activation barrier in the latter step is 5.1 (6.4) kcal/mol higher than the methylation of 2-MN to 2,6-DMN (2,7-DMN). Therefore, also the second side reaction discussed here, the self-activation of methanol to dimethyl ether, is not supposed to be competitive with the methylation of 2-MN.

4. Conclusions

In this theoretical investigation we have shown how steric constraints and van der Waals contributions of the zeolite

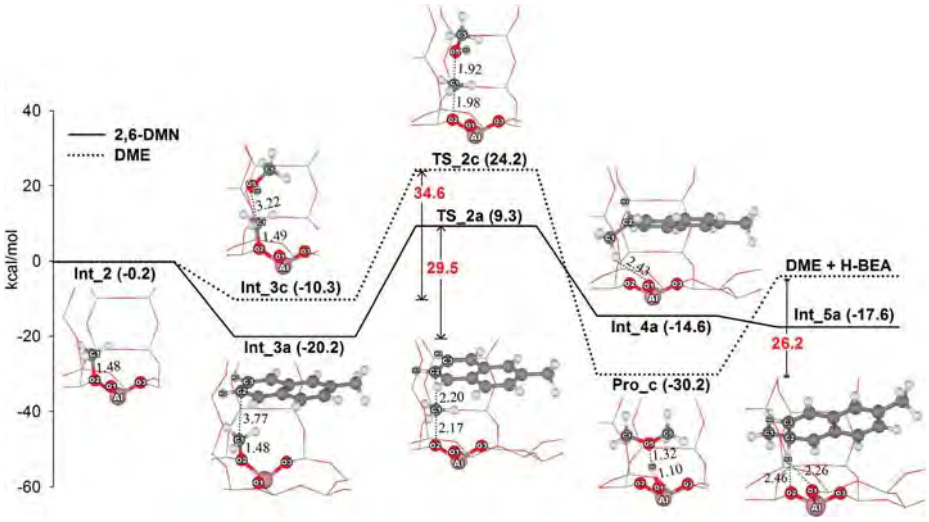

Figure 3. The energy profile comparing the methylation of 2-MN to 2,6-DMN and the dimethyl ether (DME) formation.

TABLE 2: Geometrical Parameters from the 34T Model (M06-2X/6-311+G(2df,2p)//M06-2X/6-31G(d,p)) Calculations of the Intermediates (Int_2 and Int_3c), Transition State (TS_2c), and Product (Pro_c) for the Dimethyl Ether Formation over H-BEA[a]

parameters	H-BEA	Int_2	Int_3c	TS_2c	Pro_c
O1−H1	0.98	−	−	−	−
C1−O2	−	1.48	1.49	1.98	2.99
C1−O5	−	−	3.22	1.92	1.43
C4−O5	−	−	1.41	1.44	1.43
O5−H5	−	−	0.97	0.97	1.51
O1−H5	−	−	4.05	3.97	1.10
Al−O1	1.85	1.69	1.66	1.71	1.80
Al−O2	1.70	1.86	1.80	1.77	1.70
Al−O3	1.68	1.69	1.65	1.71	1.70
∠O1−Al−O2	93.1	94.3	93.0	98.1	95.8

[a] Distances are in Å and angles are in degrees.

framework can affect the reaction pathways of the methylation of 2-methylnaphthalene and of competing reactions. Our results can be summarized as follows:

(1) The methylation of 2-MN to 2,6-DMN and 2,7-DMN is initiated by the adsorption of a methanol molecule at the zeolite acidic site, which is then dehydrated, leaving a methyl group attached to the basic oxygen of the zeolite. Subsequently, the methyl group from the zeolite framework transfers to 2-MN at the β-positions yielding naphthalenium intermediates. Eventually, 2,6- and 2,7-DMN are generated by direct proton transfer from the naphthalenium intermediates to the active site. The formation of the methoxy species is considered to be the rate-determining step.

(2) The zeolitic framework plays an important role in the stabilization of the adsorption complexes, transition states, and intermediates. The calculated adsorption energies are in good qualitative agreement with experimental results. The stabilizing effect of the zeolite micropore on the ionic transition state causes the activation barrier to be about 20% lower than what has been calculated for small clusters lacking these contributions. The 34T cluster that is used to model BEA zeolite stabilizes the key reaction intermediates, the naphthalenium cations.

(3) The energy profiles for the formation of 2,6- and 2,7-DMN formation are similar and in agreement with the experimental data that showed no preference for either of them.

(4) Considering a possibly competing process, the self-activation barrier of methanol to DME is unfavorably high for the C−O bond-formation step, compared to that for the formation of the C−C bond in 2-MN.

Acknowledgment. This work was supported in part by grants from the National Science and Technology Development Agency (2009 NSTDA Chair Professor funded by the Crown Property Bureau under the management of the National Science and Technology Development Agency and NANOTEC Center of Excellence funded by the National Nanotechnology Center), The Thailand Research Fund (to J.L.), the Commission on Higher Education, Ministry of Education (the "National Research University Project of Thailand (NRU)" and the "National Center of Excellence for Petroleum, Petrochemical and Advanced Materials (NCE-PPAM)"). The support from the Kasetsart University Research and Development Institute (KURDI) and the Graduate School Kasetsart University (to K.B.) are also acknowledged. We are grateful to Donald G. Truhlar and Yan Zhao for their support concerning the M06-2X code. M.P. acknowledges an infrastructure grant from the Austrian Ministry of Science to the LFU scientific computing platform.

Supporting Information Available: All Cartesian coordinates of the species in the paper. This material is available free of charge via the Internet at http://pubs.acs.org.

References and Notes

(1) Jacobs, P. A.; Martens, J. A. In *Studies in Surface Science and Catalysis*; van Bekkum, H., Flanigen, E. M., Jansen, J. C., Eds.; Elsevier: Amsterdam, 1991; Vol. 58, Chapter 12, pp 445−496.

(2) Lillwitz, L. D. *Appl. Catal., A* **2001**, *221*, 337.

(3) Song, C.; Schobert, H. H. *Fuel Process. Technol.* **1993**, *34*, 157.

(4) Horita, H.; Takeuchi, G. *Petrotech* **1995**, *18*, 844.

(5) Kraikul, N.; Rangsunvigit, P.; Kulprathipanja, S. *Chem. Eng. J.* **2005**, *114*, 73.

(6) Kraikul, N.; Rangsunvigit, P.; Kulprathipanja, S. *Appl. Catal., A* **2006**, *312*, 102.

(7) Sikkenga, D. Zaenger, I. C.; Williams, G. S. U.S. Patent 4,962,260, 1990.

(8) Fraenkel, D.; Cherniavsky, M.; Ittah, B.; Levy, M. *J. Catal.* **1986**, *101*, 273.

(9) Komatsu, T.; Araki, Y.; Namba, S.; Yashima, T. In *Studies in Surface Science and Catalysis*; Weitkamp, J., Karge, H. G., Pfeifer, H., Hölderich, W., Eds.; Elsevier: Amsterdam, 1994; Vol. 84, Part 3, p 1821.

(10) Popova, Z.; Yankov, M.; Dimitrov, L. In *Studies in Surface Science and Catalysis*; Weitkamp, J., Karge, H. G., Pfeifer, H., Hölderich, W., Eds.; Elsevier: Amsterdam, 1994; Vol. 84, Part 3, p 1829.

(11) Pu, S.-B.; Inui, T. *Appl. Catal., A* **1996**, *146*, 305.

(12) Weitkamp, J.; Neuber, M. In *Studies in Surface Science and Catalysis*; Tomoyuki lnui, S. N., Takashi, T., Eds.; Elsevier: Amsterdam, 1991; Vol. 60, p 291.
(13) Inui, T.; Pu, S.-B.; Kugai, J.-i. *Appl. Catal., A* **1996**, *146*, 285.
(14) Schwabe, T.; Grimme, S. *Acc. Chem. Res.* **2008**, *41*, 569.
(15) Zhang, I. Y.; Wu, J.; Xu, X. *Chem. Commun.* **2010**, *46*, 3057.
(16) Tsipis, A. C.; Orpen, A. G.; Harvey, J. N. *Dalton Trans.* **2005**, 2849.
(17) Zhao, Y.; Truhlar, D. G. *Org. Lett.* **2007**, *9*, 1967.
(18) Zhao, Y.; Truhlar, D. G. *J. Chem. Phys.* **2006**, *125*, 194101.
(19) Zhao, Y.; Truhlar, D. G. *J. Phys. Chem. A* **2006**, *110*, 13126.
(20) Zhao, Y.; Truhlar, D. *Theor. Chem. Acc* **2008**, *120*, 215.
(21) Zhao, Y.; Truhlar, D. G. *Acc. Chem. Res.* **2008**, *41*, 157.
(22) Boekfa, B.; Choomwattana, S.; Khongpracha, P.; Limtrakul, J. *Langmuir* **2009**, *25*, 12990.
(23) Maihom, T.; Boekfa, B.; Sirijaraensre, J.; Nanok, T.; Probst, M.; Limtrakul, J. *J. Phys. Chem. C* **2009**, *113*, 6654.
(24) Maihom, T.; Pantu, P.; Tachakritikul, C.; Probst, M.; Limtrakul, J. *J. Phys. Chem. C* **2010**, *114*, 7850.
(25) Higgins, J. B.; LaPierre, R. B.; Schlenker, J. L.; Rohrman, A. C.; Wood, J. D.; Kerr, G. T.; Rohrbaugh, W. J. *Zeolites* **1988**, *8*, 446.
(26) Frisch, M. J.; Trucks, G. W.; Schlegel, H. B.; Scuseria, G. E.; Robb, M. A.; Cheeseman, J. R.; Montgomery, Jr., J. A.; Vreven, T.; Kudin, K. N.; Burant, J. C.; Millam, J. M.; Iyengar, S. S.; Tomasi, J.; Barone, V.; Mennucci, B.; Cossi, M.; Scalmani, G.; Rega, N.; Petersson, G. A.; Nakatsuji, H.; Hada, M.; Ehara, M.; Toyota, K.; Fukuda, R.; Hasegawa, J.; Ishida, M.; Nakajima, T.; Honda, Y.; Kitao, O.; Nakai, H.; Klene, M.; Li, X.; Knox, J. E.; Hratchian, H. P.; Cross, J. B.; Bakken, V.; Adamo, C.; Jaramillo, J.; Gomperts, R.; Stratmann, R. E.; Yazyev, O.; Austin, A. J.; Cammi, R.; Pomelli, C.; Ochterski, J. W.; Ayala, P. Y.; Morokuma, K.; Voth, G. A.; Salvador, P.; Dannenberg, J. J.; Zakrzewski, V. G.; Dapprich, S.; Daniels, A. D.; Strain, M. C.; Farkas, O.; Malick, D. K.; Rabuck, A. D.; Raghavachari, K.; Foresman, J. B.; Ortiz, J. V.; Cui, Q.; Baboul, A. G.; Clifford, S.; Cioslowski, J.; Stefanov, B. B.; Liu, G.; Liashenko, A.; Piskorz, P.; Komaromi, I.; Martin, R. L.; Fox, D. J.; Keith, T.; Al-Laham, M. A.; Peng, C. Y.; Nanayakkara, A.; Challacombe, M.; Gill, P. M. W.; Johnson, B.; Chen, W.; Wong, M. W.; Gonzalez, C.; Pople, J. A. *Gaussian 03*, revision C.02; Gaussian, Inc.: Wallingford, CT, 2004.
(27) Haase, F.; Sauer, J.; Hutter, J. *Chem. Phys. Lett.* **1997**, *266*, 397.
(28) Stich, I.; Gale, J. D.; Terakura, K.; Payne, M. C. *Chem. Phys. Lett.* **1998**, *283*, 402.
(29) Haase, F.; Sauer, J. *Microporous Mesoporous Mater.* **2000**, *35*−*36*, 379.
(30) Svelle, S.; Tuma, C.; Rozanska, X.; Kerber, T.; Sauer, J. *J. Am. Chem. Soc.* **2008**, *131*, 816.
(31) Lee, C. C.; Gorte, R. J.; Farneth, W. E. *J. Phys. Chem. B* **1997**, *101*, 3811.
(32) Kotrel, S.; Lunsford, J. H.; Knozinger, H. *J. Phys. Chem. B* **2001**, *105*, 3917.
(33) Pinto, R. R.; Borges, P.; Lemos, M. A. N. D. A.; Lemos, F.; Védrine, J. C.; Derouane, E. G.; Ribeiro, F. R. *Appl. Catal., A* **2005**, *284*, 39.
(34) Suzuki, K.; Noda, T.; Katada, N.; Niwa, M. *J. Catal.* **2007**, *250*, 151.
(35) Kotrel, S.; Rosynek, M. P.; Lunsford, J. H. *J. Phys. Chem. B* **1999**, *103*, 818.
(36) Blaszkowski, S. R.; van Santen, R. A. *J. Am. Chem. Soc.* **1996**, *118*, 5152.
(37) Blaszkowski, S. R.; van Santen, R. A. *J. Phys. Chem. B* **1997**, *101*, 2292.
(38) Hansen, N.; Bruggemann, T.; Bell, A. T.; Keil, F. J. *J. Phys. Chem. C* **2008**, *112*, 15402.
(39) Rozanska, X.; van Santen, R. A.; Hutschka, F.; Hafner, J. *J. Am. Chem. Soc.* **2001**, *123*, 7655.
(40) Sato, T.; Kunimori, K.; Hayashi, S. *Phys. Chem. Chem. Phys.* **1999**, *1*, 5.
(41) Jobic, H.; Bee, M.; Renouprez, A. *Surf. Sci.* **1984**, *140*, 307.

JP108566C

PCCP

View Online
Dynamic Article Links

Cite this: *Phys. Chem. Chem. Phys.*, 2011, **13**, 6462–6470

www.rsc.org/pccp

PAPER

Structures and reaction mechanisms of glycerol dehydration over H-ZSM-5 zeolite: a density functional theory study†

Kanokwan Kongpatpanich,[abcd] Tanin Nanok,[abcd] Bundet Boekfa,[bcd] Michael Probst[e] and Jumras Limtrakul*[abcd]

Received 5th September 2010, Accepted 27th January 2011
DOI: 10.1039/c0cp01720e

The initial stage of glycerol conversion over H-ZSM-5 zeolite has been investigated using density functional theory (DFT) calculations on an embedded cluster model consisting of 128 tetrahedrally coordinated atoms. It is found that glycerol dehydration to acrolein and acetol proceeds favourably *via* a stepwise mechanism. The formation of an alkoxide species upon the first dehydration requires the highest activation energy (42.5 kcal mol^{-1}) and can be considered as the rate determining step of the reaction. The intrinsic activation energies for the first dehydration are virtually the same for both acrolein and acetol formation, respectively, suggesting the competitive removal of the primary and secondary OH groups. A high selectivity to acrolein at moderate temperatures can be attributed to the selective activation of the stronger adsorption mode of glycerol through the secondary OH group and the kinetically favoured subsequent consecutive steps. In addition, the less reactive nature of acrolein relative to acetol precludes it from being converted to other products upon conversion to glycerol. In accordance with typical endothermic reactions, the forward rate constant for glycerol dehydration significantly increases with increasing reaction temperature.

1. Introduction

Biomass conversion can partially replace petroleum-based chemical processes.[1] Among the biomass-based raw materials, glycerol has gained much attention because of its continuous overproduction from the biodiesel production process and its capability of being a sustainable and biodegradable raw material to synthesize various chemicals.[2]

While there are many recent attempts concerning the utilization of glycerol by means of oxidation, hydrogenolysis, pyrolysis, transesterification, esterification, polymerization and dehydration, one of the most interesting catalytic processes is the catalytic conversion of glycerol to acrolein by double dehydration. This process could offer a route to the sustainable production of acrolein, which has broad industrial and agricultural applications.[3] Acrolein is an essential and versatile starting chemical widely used in the production of DL-Methionine, acrylic acid, super absorber polymers, and detergents. Furthermore, it can be directly used as bactericides in the petroleum drilling branch. Various homogeneous and heterogeneous acid catalysts have been investigated for glycerol dehydration in the liquid phase, especially in near- or supercritical water, and in the gas phase. The main advantage of using supercritical water is the capability to adjust its physical properties by varying the pressure and temperature.[4–7] However, a heterogeneous catalyst is often more preferable because of its easy separation at the end of the process. Moreover, the use of supercritical water results in high investments because processes dealing with supercritical conditions need high-quality equipment. Therefore, the development of a high-performance heterogeneous catalyst and a practical gas phase reaction is still of great interest.

The dehydration of glycerol in the gas phase can be accomplished by three categories of solid acid catalysts:

The first one is supported inorganic acids, including heteropolyacids.[8] The properties required to design effective catalysts of that type[9] are well understood. Although their selectivity for acrolein is high, these catalysts often lose their activity quite rapidly. The second group is the mixed-oxide type catalyst.

[a] *Laboratory for Computational and Applied Chemistry, Department of Chemistry, Faculty of Science, Kasetsart University, Bangkok 10900, Thailand*
[b] *Center for Advanced Studies in Nanotechnology and Its Applications in Chemical, Food and Agricultural Industries, Kasetsart University, Bangkok 10900, Thailand*
[c] *Center of Nanotechnology, Kasetsart University Research and Development Institute, Kasetsart University, Bangkok 10900, Thailand*
[d] *NANOTEC Center of Nanotechnology, National Nanotechnology Center, Kasetsart University, Bangkok 10900, Thailand. E-mail: jumas.l@ku.ac.th; Fax: +66-2562-5555 ext 2159; Tel: +66-2562-5555 ext 2176*
[e] *Institute of Ion Physics and Applied Physics, University of Innsbruck, A-6020 Innsbruck, Austria*
† Electronic supplementary information (ESI) available: See DOI: 10.1039/c0cp01720e

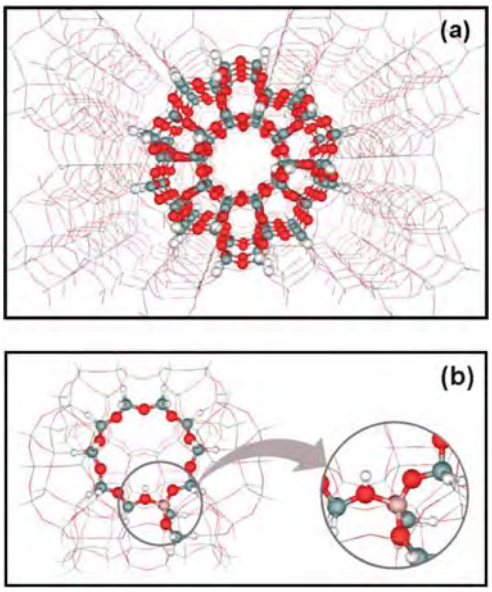

Fig. 1 (a) The model of the 128T cluster of H-ZSM-5 zeolite. Atoms belonging to the 128T region and wires represent the rest of the lattice structure. (b) Selection of the 12T active site region and the 128T clusters from the lattice structure of the H-ZSM-5 zeolite.

Mixed-oxide catalyst types are currently called into question because they have not been extensively studied.[10–12] The last group is acidic zeolites. These groups have been extensively studied for glycerol dehydration for more than three years.[13–16] Their general advantages are high catalytic activity, shape selectivity and thermal stability. The catalytic activity originates from the presence of the Brønsted acid site in the confined space.[17] Its acidity and, therefore, performance, can be controlled by tuning the Si/Al ratio. Experimental studies suggest that the H-ZSM-5 zeolite is one of the best for glycerol conversion, especially in the gas phase.

It is quite difficult to get comprehensive information about the detailed mechanism of glycerol dehydration in zeolites solely from experiments. This is due to the complexity of their nanoporous structures that prevents them from being investigated by conventional techniques. The most comprehensive study has been performed by Corma and co-workers.[14] These authors proposed a complex reaction network to explain the formation of all the observed products. The first dehydration step in glycerol dehydration leads to either acetol or 3-hydroxypropionaldehyde. The latter further dehydrates in a second dehydration step to yield acrolein. The progress of the reaction can be briefly observed experimentally by the in-situ FTIR study. IR spectra interpretation proved that acrolein is the major product of the glycerol dehydration over H-ZSM-5 zeolite. The reaction towards acrolein is found to be more favorable than towards acetol.[18]

There are theoretical studies on glycerol dehydration over homogeneous catalysts[19] but, to the best of our knowledge, there are no theoretical studies reported about the detailed reaction mechanism of glycerol dehydration over solid acid in the gas phase, which may offer a different mechanism from the conventional ones. Therefore, a computational investigation of the reaction mechanisms with a reliable method should be useful. In this work we investigate and compare the different possible reaction mechanisms and product formation pathways by means of cluster calculations using a density functional that includes dispersion energy.

2. Computational details

The cluster approach is commonly used to describe the interaction between organic molecules and the active sites of zeolites. Nevertheless, its accuracy is limited to only small polar molecules in which the effect caused by the extended zeolite lattice is negligible. For non-polar molecules, the confinement effect by the zeolite framework becomes important, particularly, when the molecular size of adsorbing molecules is comparable to the dimension of zeolite pores. To take into account the short- and medium-range effects by the zeolite framework, a 128T (T = Si and Al tetrahedral sites) cluster model of the ZSM-5 zeolite, covering the straight channel, the zigzag channel, and the channel intersection, was used in this study. The reaction was assumed to mainly take place at the cavity that emerged at the channel intersection. One silicon atom of 12 different tetrahedral sites (T1 to T12) was substituted by an aluminum atom to generate the Brønsted acidic site. An aluminum atom was chosen to reside at the T12 site located at the 10-membered ring window open to both straight and zigzag channels. In that position it is accessible to the diffusing molecules from both types of the channel. Our previous studies showed that the density functional theory using the M06-2X functional[20,21] provided quite good results compared to functionals without dispersion energy terms for the interaction energy of organic molecules in the zeolite systems.[22–26] The performance of M06-2X has also been evaluated favourably in other studies. For example, it was found[27] that short-to medium range correlation effects are well reproduced and that it's accuracy for reaction enthalpies is often comparable to much more expensive methods[28] This functional is, therefore, also used in our present study.

Because the adsorption complex between the 128T cluster model of zeolite and the adsorbing molecule constitutes a large and computationally demanding system, we considered the 12T cluster as the smallest unit required to represent the active site of zeolite (see Fig. 1). The dangling bonds created from the cluster trimming process, aligning exactly in the same direction of the corresponding Si–O bonds from the crystallographic structure, were saturated with hydrogen atoms. During the geometry optimization, all atoms of the 12T zeolite cluster model were frozen at their initial position except atoms located within the second coordination shell of the aluminum centre. The adsorbing molecule was permitted to fully relax. All stationary points along the reaction paths were located by eigenvector following and verified by performing frequency calculations at the M06-2X/6-31G(d,p) level of theory.[29] A negative frequency of the normal mode motion corresponding to the desired reaction coordinate observed in all transition states confirmed that our transition states were located at the saddle point. No negative frequency was found in the reactants and products. The optimized structure of each stationary point was then inserted in the rest of the 128T cluster to impose the realistic short- and medium-range effects of the zeolite framework. The model was further augmented

with the long-range electrostatic potential from the periodic zeolite lattice. For this, the 128T quantum cluster was surrounded with point charges derived from the surface charge representation of the electrostatic embedding potential (SCREEP)[30] method to reproduce the Madelung potential. The energy was then calculated in a single-point calculation. This embedding scheme provides a cost-effective way of treating the extended framework effects on the adsorption and reaction of organic molecules in zeolites.[22,31]

Standard enthalpies and free energy changes of all structures in the rate determining step were obtained from frequency calculations. These data were used to predict the rate and equilibrium constants for the rate determining step of the reaction. The rate constants were evaluated over the temperature range of 473–773 K with an interval of 50 K using simple transition state theory (TST). The equation for calculating the reaction rate constant is:

$$k(T) = \frac{k_B T}{h} \exp\left(-\frac{\Delta G^{\neq}}{RT}\right)$$

Where $\Delta G^{\#}$ is the free energy of activation, k_B is Boltzmann's constant, h is Plank's constant, T is the temperature in Kelvin and R is the universal gas constant. Thermodynamic data at the temperature range of 473 to 773 K were listed in Table S6 (see Supporting Information). All calculations were performed using the Gaussian 03 code[32] modified to include the Minnesota density functionals module 3.1 by Zhao and Truhlar.

3. Results and discussions

3.1 Glycerol adsorption onto the Brønsted acid site

Glycerol has a highly flexible C_3-backbone structure with three hydroxyl (OH) groups in vicinal positions. A variation in the orientation of the three OH groups leads to different conformations of its gas phase molecule. Recently, it has been reported that the most stable conformer of glycerol is the one in which all three of its OH groups form a linear-chain structure of intramolecular hydrogen bonds.[33,34]

Adsorption of glycerol onto the zeolite acid site can probably take place through either its primary or secondary OH groups. Fig. 2a and b show the optimized geometries of glycerol adsorption through primary (**ads_1**) and secondary (**ads_2**) OH groups, respectively. The nearly linear O1–Hz–O5 and O1–Hz–O4 angles (177.2° for both structures) suggest a strong hydrogen bond between glycerol and the zeolite which normally increases the proton transfer capability. As can be seen, the O1–Hz bond separation (1.07 and 1.06 Å for the primary and secondary OH groups, respectively) increases significantly from that of an isolated zeolite (0.97 Å). The close contact of one glycerol OH group with the zeolite Brønsted proton Hz results in a significant lengthening and weakening of its corresponding C–O bond (1.44 and 1.43 Å for **ads_1** and **ads_2**, respectively) with respect to the other two C–O bond distances (an average of 1.42 Å).

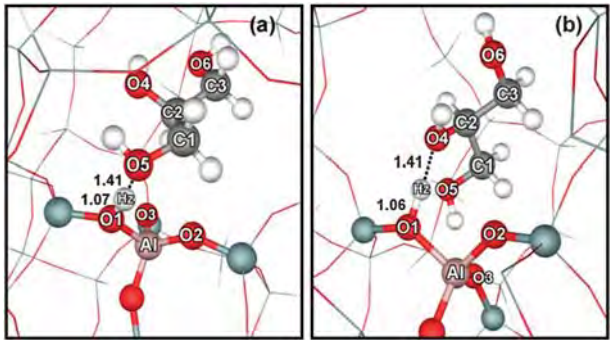

Fig. 2 Optimized structures of glycerol adsorption using (a) the primary OH group **ads_1** and (b) the secondary OH group **ads_2**.

As a result, the protonation of glycerol by the zeolite could give support to enhancing the glycerol dehydration. However, we could not locate the completely protonated form, an ion-pair complex, as a stable intermediate, even when carrying out the geometry optimization using the 34T quantum cluster at the same level of theory. This situation is similar to the monomolecular adsorption of small alcohols on the proton zeolites.[22,35] The adsorption energies for the **ads_1** and **ads_2** structures are estimated to be −39.4 and −42.5 kcal mol^{-1}, respectively.

These values are considerably higher than the experimental values for simple alcohols on the H-ZSM-5 zeolite of −27.5 and −31.1 kcal mol^{-1} for methanol and ethanol, respectively.[36] The higher value for glycerol adsorption indicates a stronger interaction with the zeolite, which results mostly from two additional hydrogen-bondings of the non-adsorbed OH groups with the partially negatively charged oxygen atoms of the zeolite framework. The dehydration of **ads_1** is believed to result in the acetol formation, while acrolein is formed upon the dehydration of **ads_2**. Statistically, from the number of primary and secondary OH groups in a glycerol molecule, the possibility for acetol formation would be twice that for acrolein formation. Recently, the product distribution[14] and FT-IR studies[18] of glycerol conversion at low temperatures (< 646 K) have revealed that the H-ZSM-5 zeolite is selective to acrolein formation, whereas the selectivity to acetol is only very small. To clarify if the removal of the secondary OH group is more favourable than that of the primary OH group, the detailed mechanisms of the initial reaction pathways for glycerol dehydration to acrolein and acetol are to be explored and discussed in the reaction mechanism sections.

3.2 Conversion of glycerol to acrolein

As mentioned above, the conversion of glycerol to acrolein is presumably initialized from **ads_2**. Based on the previous FT-IR study,[18] the reaction mechanism for acrolein formation consecutively proceeds through the three main steps: (1) the removal of the secondary OH group of glycerol by the dehydration reaction to produce an enol-intermediate, (2) the tautomerization of the enol into the keto-intermediate, and (3) the removal of the primary OH group from the keto-intermediate to form the acrolein product. Each step of the reaction is considered to take place in the monomolecular fashion. The water molecules developed in the dehydration process are assumed not to be further involved in the reaction progress. The three steps for acrolein formation are shown in Scheme 1.

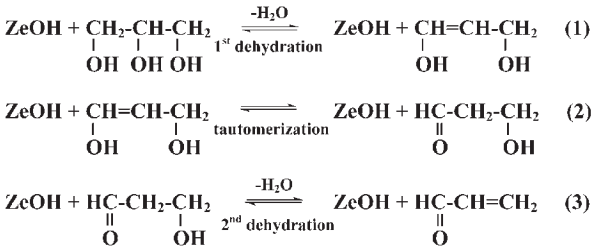

Scheme 1 The reaction pathway of glycerol dehydration: the acrolein formation pathway.

3.2.1 Dehydration at the secondary OH group (the first dehydration). In the first dehydration step, the adsorbed glycerol is protonated by the acidic proton of the zeolite at the secondary OH group. This results in the weakening of the secondary C–O bond and promotes the removal of the secondary OH group as a water molecule. The dehydration can in principle proceed through either the stepwise or the concerted mechanism.

For the stepwise mechanism, the water molecules are developed upon the formation of alkoxide species. It is noted that the attempt to locate the transition state closely related to the corresponding adsorption complex **ads_2** is discarded by the proton back donation from the adsorbed glycerol to the zeolite. The proton exchange is also expected to occur readily under normal experimental conditions. We, therefore, propose an activated complex as shown in Fig. 3a for the first transition state structure, **ts_dehyd_1**. The secondary carbon C2 is centred between the protonated OH group and the zeolite lattice oxygen O2. The protonated glycerol is ionized by the assistance of the basic zeolite oxygen to form a secondary carbocation.

However, it is found that the secondary carbocation created at the transition state does not exist as an intermediate. From the vibrational mode with an imaginary frequency, it can be seen that the transition state already indicates the formation of a water molecule and the alkoxide. The secondary surface alkoxide species, **alk_1**, and a water molecule are the stable products of the first elementary step. The transition state requires an activation energy of 42.5 kcal mol^{-1}. From the bond distance parameters, the formation of a water molecule is more advanced (C2–O4 = 2.40 Å) than the formation of the alkoxide species (C2–O2 = 2.28 Å). With respect to the adsorption complex **ads_2**, the alkoxide formation is endothermic by 27.7 kcal mol^{-1}. This is consistent with the Hammond–Leffler postulate[37] which states that for an endothermic reaction the transition state structure resembles the final products. To shift the reaction forwards, it is essential that the water molecule generated in this step is desorbed from the system. The desorption energy of a water molecule adsorbed nearby the surface alkoxide is estimated to be 16.3 kcal mol^{-1}. This value is close to the reported desorption energy of a water molecule from the Brønsted active site of about 12–14 kcal mol^{-1}.[38,39] After the water molecule is eliminated from the system, the surface alkoxide, **alk_1**, can readily desorb from the zeolite surface by undergoing the proton back donation to regenerate the zeolite Brønsted active site. The hydrogen atom attached to the alkoxy primary carbon C1 is abstracted by the basic zeolite oxygen O3 to release 1,3-dihydroxypropene, **hyd_enol_1**, as a resulting product. This elementary step proceeds through the transition state **ts_alk_1** as depicted in Fig. 3b and requires an activation energy of 19.7 kcal mol^{-1}. 1,3-dihydroxypropene has an enol-form structure and binds strongly to the zeolite Brønsted active site using its vinyl hydroxyl group. As a result, the transformation of the alkoxide species to 1,3-dihydroxypropene adsorbed onto the zeolite Brønsted active site is an exothermic elementary step.

In the concerted mechanism, the water elimination and the enol formation occur without passing through the alkoxide intermediate. 1,3-dihydroxypropene is, therefore, obtained in a single elementary step. Fig. 4a shows the transition state structure, **tsc_dehyd_1**, for the E2 mechanism. The secondary glycerol OH group is protonated by the Brønsted proton at the same time that the primary hydrogen is abstracted by the basic zeolite oxygen. In concomitance with the elongation of the C2–O4 bond distance from 1.43 to 2.20 Å upon glycerol protonation, the C1–C2 bond distance is contracted to 1.39 Å upon the primary hydrogen abstraction. Such a simultaneous action of two functions (proton donor and proton acceptor) of the zeolite active site requires an activation energy of 72.0 kcal mol^{-1}, which is higher than that required in the stepwise mechanism (42.5 and 19.7 kcal mol^{-1}). A slightly smaller amount of the energy (14.3 kcal mol^{-1}) relative to that used to desorb a water molecule from the alkoxide intermediate (16.3 kcal mol^{-1}) is necessitated for extracting a water molecule from its coadsorption with 1,3-dihydroxypropene in the zeolite pore.

3.2.2 Tautomerization of 1,3-dihydroxypropene to 3-hydroxypropionaldehyde. 1,3-dihydroxypropene can isomerize to its keto-form through the tautomerization reaction. The π-bonding interaction of the double bond with the Brønsted acid site is considered to facilitate a double proton transfer and leads to the formation of 3-hydroxypropanal. As shown in Fig. 3c, the transition state, **ts_tauto_1**, for the tautomerization involves the concerted action of the zeolite active sites. The acidic proton at the zeolite O3 transfers to the C2 of glycerol at the same time that the hydroxyl proton on the glycerol O6 transfers back to the zeolite O1 to regenerate the acidic site. A small activation energy of 3.6 kcal mol^{-1} implies that the keto-enol tautomerization of 1,3-dihydroxypropene to 3-hydroxypropionaldehyde on the acidic site occurs readily under the experimental conditions. As it is typical for the tautomerization of the enol-form to the keto-form, the reaction is exothermic. The keto-product strongly adsorbs onto the Brønsted acid site with its carbonyl group, **keto_CO**, *via* the hydrogen bonding interaction.

3.2.3 Dehydration of at the primary OH group (the second dehydration). In order to stimulate the second dehydration, the orientation of the strongly adsorbed keto-form is readjusted to the weaker adsorption mode, **keto_OH**. The interaction of its OH group with the Brønsted acid site is adopted as the starting geometry for the second dehydration step. Similar to the first dehydration step, the OH group is protonated by the zeolite and acts as a leaving group. The dehydration can proceed through either the stepwise or concerted mechanism.

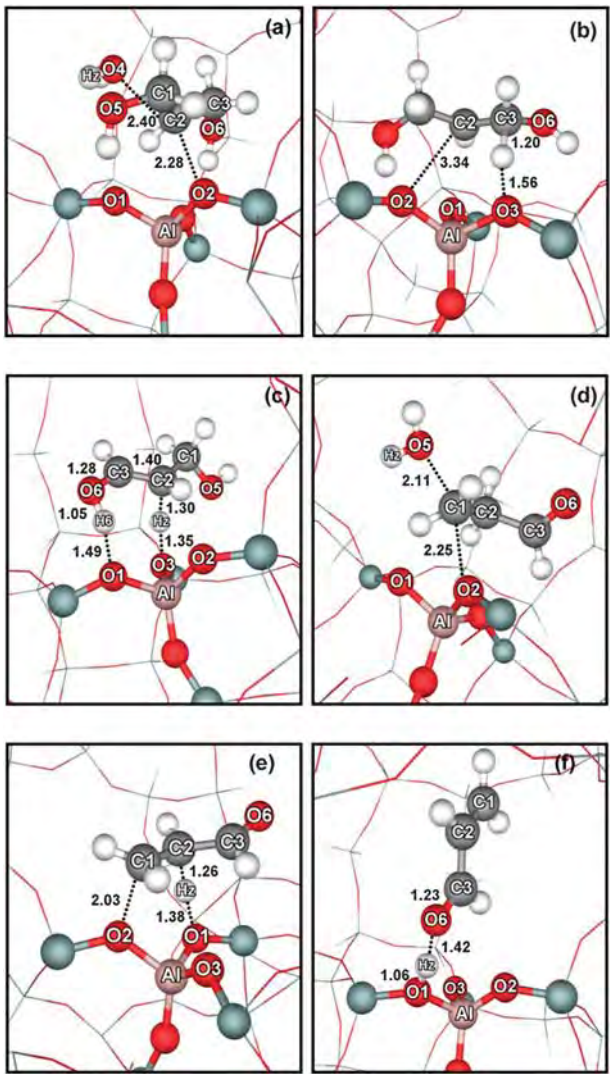

Fig. 3 Optimized structures of the transition states and a product (acrolein) along the stepwise mechanism for glycerol conversion to acrolein: (a) **ts_dehyd_1** (b) **ts_alk_1** (c) **ts_tauto_1** (d) **ts_alk_2** (e) **ts_acrolein** and (f) **acrolein**.

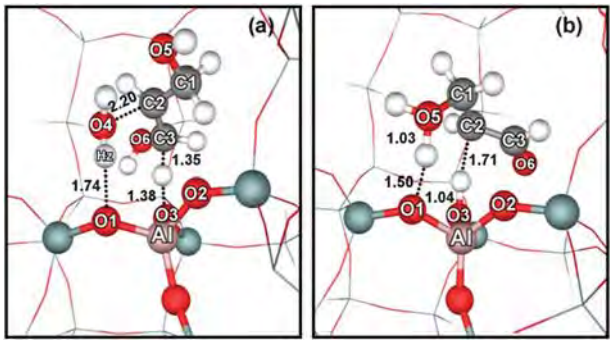

Fig. 4 Optimized structures of the transition states along the concerted mechanism for glycerol conversion to acrolein: (a) **tsc_dehyd_1** (b) **tsc_dehyd_2**.

For the stepwise mechanism, the attack of the 3-hydroxypropanal primary carbon by the basic zeolite oxygen takes place in concomitance with the elimination of a water molecule, generating the primary alkoxide intermediate **alk_2**. The transition state **ts_alk_2** (see Fig. 3d) requires an activation energy of 35.8 kcal/mol. The primary alkoxide intermediate **alk_2** generated from this step is coadsorbed by a single water molecule. To remove an adsorbed water molecule from the alkoxide species requires the desorption energy of 12.6 kcal mol^{-1}. The dehydrated alkoxide species undergoes proton back donation from the secondary carbon to the basic zeolite oxygen leading to the acrolein product formation. The corresponding transition state **ts_acrolein** (see Fig. 3e) requires an activation energy of 24.0 kcal mol^{-1}. Finally, the desorption of acrolein from the zeolite surface requires the energy of 30.5 kcal mol^{-1}.

In the concerted mechanism, the elimination of the protonated primary OH group occurs simultaneously with the hydrogen abstraction at the secondary carbon atom. The single imaginary frequency of $-1145i$ cm^{-1} indicates that at the transition state **tsc_dehyd_2** the protonation is more complete than the hydrogen abstraction. This can be confirmed by the selected bond distances depicted in Fig. 4b. The concerted activation energy for the second dehydration is estimated to be 39.3 kcal mol^{-1}, which is still higher than the activation energies in the stepwise case. The coadsorption complex of a water molecule and acrolein are the final products of this mechanism. These two constituents require the energy of 41.4 kcal mol^{-1} to desorb from the zeolite framework.

3.3 Comparison of the stepwise mechanism with the concerted mechanism

The energetic profiles for the stepwise and the concerted mechanisms are shown in Fig. 5 and 6. Elementary steps in Fig. 5 refers to the first and the second steps of Scheme 1 while Fig. 6 relates to the third step of Scheme 1. It can be seen that the production of acrolein from glycerol is an endothermic process. The first dehydration reaction requires the highest activation energy and is therefore the rate determining step for both reaction mechanisms. Since the dehydration is thermodynamically and kinetically unfavourable, it is necessary to introduce a sufficiently high temperature to the system.[14,40] The selectivity to acrolein is, however, significantly decreased when increasing the reaction temperature while the selectivity to products resulting from the combustion and cracking of the coke such as CO, CO_2, light olefins, methane, and hydrocarbons become dominant.[14] On the other hand, when the reaction is carried out under low to moderate temperatures, selectivity close to 60% can be achieved for acrolein as the major product. Therefore, the large amount of energy (39.5–42.5 kcal mol^{-1}) released by glycerol adsorption could also be an additional internal energy for driving the conversion at low and moderate temperatures. From our calculated activation energies, it is apparent that the dehydration of glycerol in a stepwise mechanism is more favoured than that in a concerted mechanism. In addition, our result is also in agreement with experiments that have detected stable alkoxide intermediates for methanol and ethanol dehydration on zeolites.[41]

The temperature dependence of the rate constants of the reaction is often useful for understanding the reaction

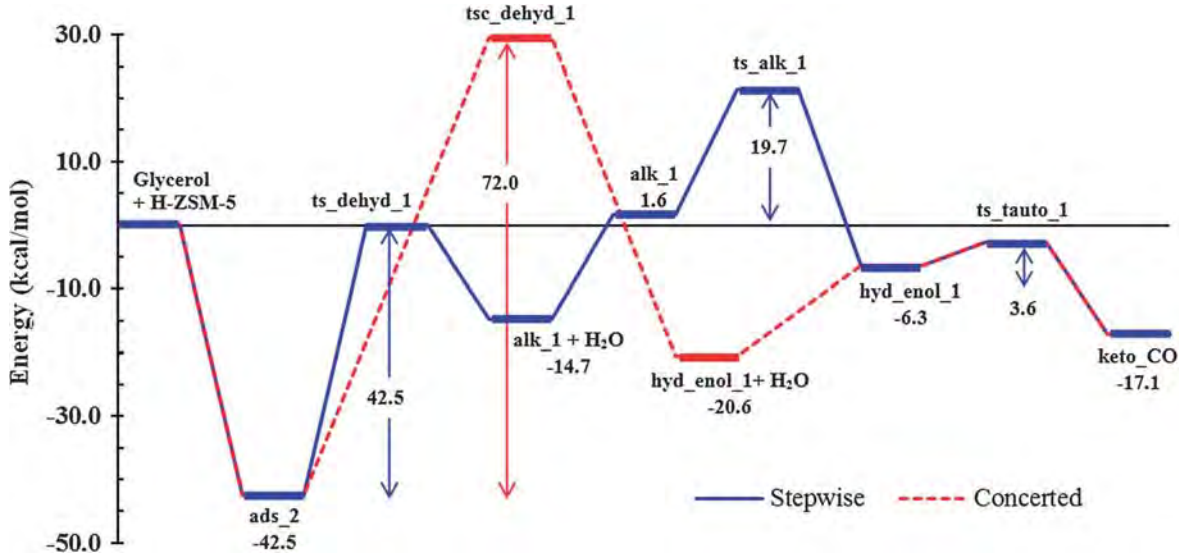

Fig. 5 Energy profile for the glycerol dehydration to acrolein calculated using the M06-2X/6-31G(d,p) method including SCREEP charges on the 128T//12T cluster of H-ZSM-5 zeolite for the first two steps (the first dehydration and the keto-enol tautomerization). Energies are in kcal mol^{-1}.

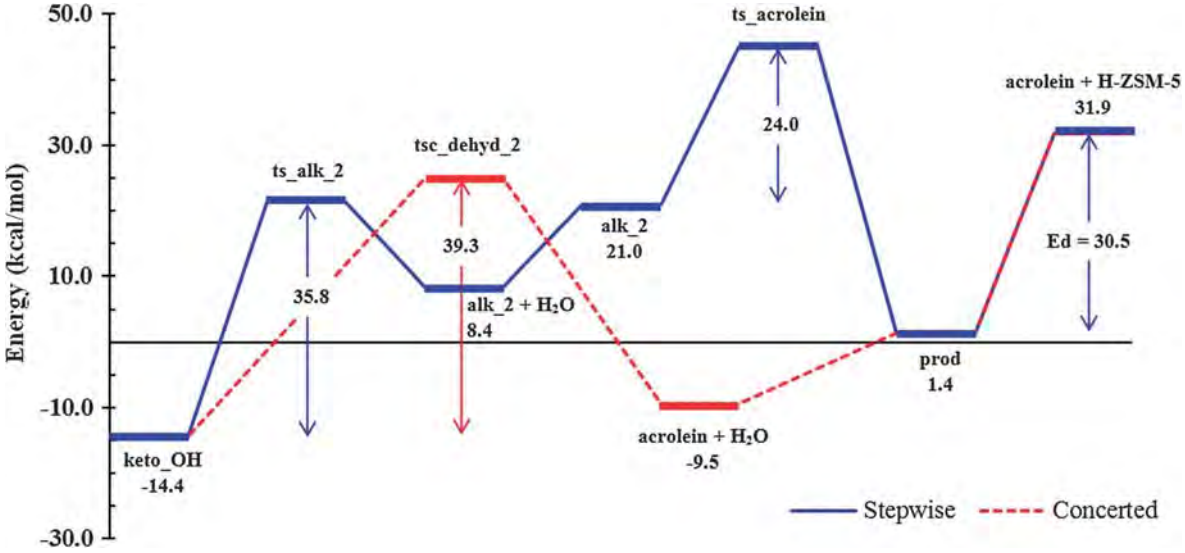

Fig. 6 Energy profile for the glycerol dehydration to acrolein calculated using the M06-2X/6-31G(d,p) method including SCREEP charges on the 128T//12T cluster of H-ZSM-5 zeolite for the first two steps (the second dehydration, and the product desorption). Energies are in kcal mol^{-1}.

mechanism. In this study, the forward and reverse rate constants (k) as well as the equilibrium constants (K) for the first dehydration step of glycerol have been calculated by using the transition state theory (TST)[42] based on thermodynamic parameters obtained from the simplified 12T cluster. Over a temperature range of 473–773 K, the rate constant for both forward and reverse reactions increases with increasing the temperature (see Fig. 7), in an accordance with the typical endothermic reaction behavior. No related experiment on reaction rates over the H-ZSM-5 zeolite has been reported and so we provide only a qualitative discussion of the results. At an optimal temperature of 563 K, we find that the reaction rate for the alkoxide formation is about eight orders of magnitude lower than the alkoxide decomposition. However, since the free energy for water desorption from the zeolite surface is −4.10 kcal mol^{-1} lower than the one for adsorption on the surface alkoxide implies that the water molecule developed from the first dehydration will be suddenly desorbed from the zeolite surface at this temperature. As a result, the hydration rate must be considerably very slow to shift the reaction backwards. This is consistent with results obtained from previous reaction optimization experiments which require a continuous feed reactor for shifting the reaction forwards.[3,14] Since the water molecule generated by the dehydration process can readily react with the active alkoxide intermediate, the continuous removal of water from the system is another crucial point. We can also note that these results can well explain why the gas phase reaction is preferred over the liquid phase.

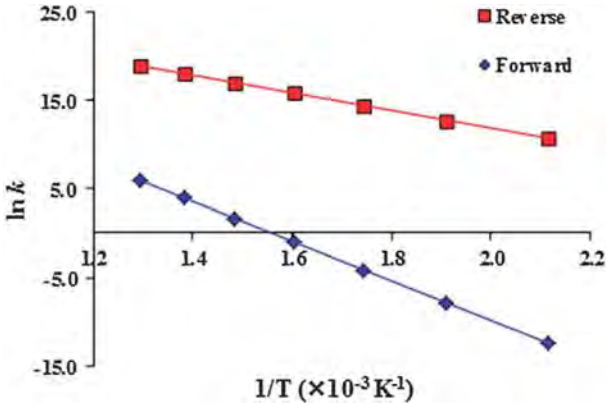

Fig. 7 Arrhenius Plot for the rate determining step.

3.4 Conversion of glycerol to acetol

The reaction pathway for glycerol conversion to acetol is proposed to consist of two main steps. The results of reaction mechanisms for acrolein formation demonstrated that the analogous dehydration of glycerol could favor the stepwise mechanism. Therefore, only the stepwise mechanism is considered for glycerol conversion to acetol. Two steps of acetol formation are shown in Scheme 2.

For the first step, the adsorbed glycerol, **ads_1**, loses its primary OH group upon the attack of the zeolite basic oxygen at the primary carbon through the transition state **TS1** shown in Fig. 8a. Similar to the removal of the secondary OH group, the water formation is more advanced than the alkoxide formation. The primary OH group is already protonated by the zeolite and readily eliminated as a water molecule while the primary carbon C1 is forming a covalent bond with the zeolite basic oxygen O2. The activation energy for the removal of the primary OH group is calculated to be 42.3 kcal mol^{-1}. Subsequently, the alkyl group is covalently bound to the basic oxygen atom of zeolite (C1–O2 = 1.49 Å) forming the alkoxide intermediate, **ALK**. The removal of a water molecule from the system requires the energy of 13.3 kcal mol^{-1}. During the alkoxide intermediate being desorbed from the zeolite surface, it returns the proton back to regenerate the zeolite active site through the transition state **TS2** (see Fig. 8b). This process requires an activation energy of 26.8 kcal mol^{-1}. The one imaginary frequency exhibits the simultaneous actions of the proton back donation to the zeolite surface and the double bond formation of the resulting enol product.

In the second step, the adsorbed enol tautomerizes to its corresponding keto-form leading to the formation of acetol. The tautermerization of the enol-form proceeds through a

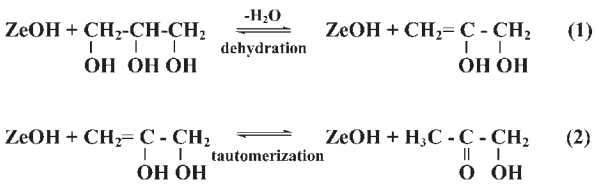

Scheme 2 The reaction pathway of glycerol dehydration: the acetol formation pathway.

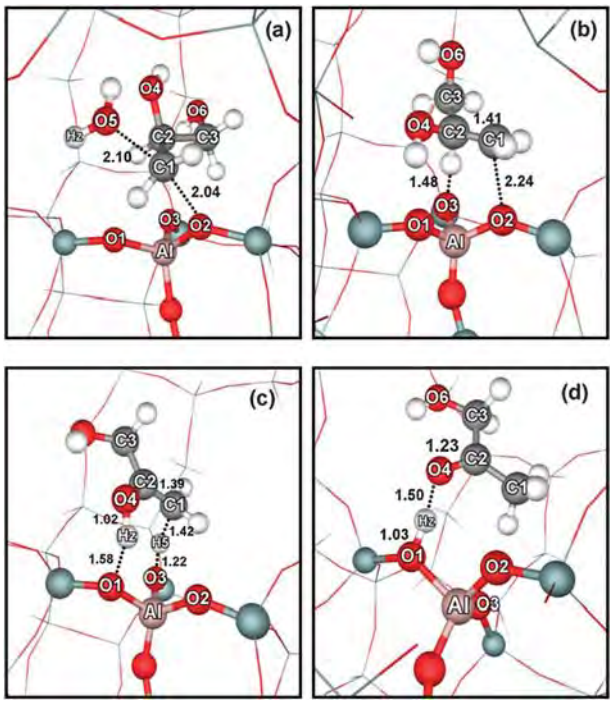

Fig. 8 Optimized structures of the transition states and a by-product (acetol) for glycerol conversion to acetol (a) **TS1** (b) **TS2** (c) **TS3** and (d) **acetol**.

transition state **TS3** (see Fig. 8c). The hydrogen abstraction by the zeolite basic oxygen occurs simultaneously with the protonation of the secondary carbon by the zeolite Brønsted proton. The activation energy for this step is 11.3 kcal mol^{-1}. Desorption of acetol from the zeolite active site requires 30.9 kcal mol^{-1}.

Fig. 9 shows the energy profiles of acrolein and acetol formation in a stepwise mechanism. The first two elementary steps in Fig. 9 are equal to the first step in Scheme 2. It can be seen that the first dehydration is the rate determining step for both acrolein and acetol formation. The removal of the primary and secondary OH groups competes with one another with virtually the same activation energy. Therefore, the selective dehydration is determined by the binding strength of the primary and secondary OH groups to the Brønsted acid site. Our adsorption results support the selective removal of the glycerol secondary OH group over H-ZSM-5.[18] The selectivity to acrolein formation becomes more noticeable after the first dehydration has taken place. Desorption of the secondary surface alkoxide to regenerate the zeolite acid site requires less energy than for the primary surface alkoxide. This is due to the smaller steric hindrance in the primary hydrogen abstraction than in the secondary hydrogen abstraction by the basic oxygen of the zeolite. In contrast to the hydrogen abstraction, upon the keto-enol tautomerization, the protonation by the zeolite proceeds more readily at the secondary carbon atom than on the primary one. These results indicate that acrolein formation is more kinetically favored over acetol formation. In addition, the study of acetol conversion reveals that, even at the moderate temperature, acetol is almost completely converted to other products.[14] From this information,

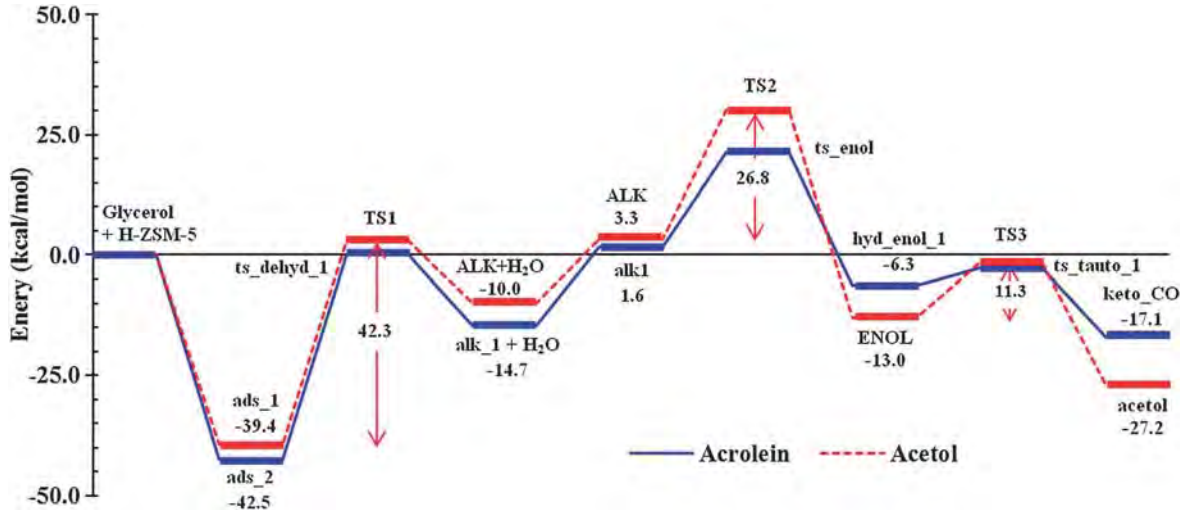

Fig. 9 Energy profile for the acetol formation calculated using the M06-2X/6-31G(d,p) method on the 128T/12T cluster of H-ZSM-5 zeolite. Energies are in kcal mol^{-1}.

one can conclude that acetol is more reactive than acrolein and it is further converted to other products during the glycerol conversion.

4. Conclusions

The structures and reaction mechanisms for the initial stage of glycerol dehydration over the H-ZSM-5 zeolite are investigated. The effects of the zeolite framework imposed on the reaction mechanism are described by using the embedded M06 approach utilizing a 128T cluster. As proposed by the recent experimental studies,[14] the glycerol dehydration mechanism is started with two different glycerol adsorption modes. The adsorption with the primary OH group leads to acetol formation, while the adsorption with the secondary OH group directs to acrolein formation. The dehydration through the alkoxide formation in the stepwise mechanism is apparently more favourable than that in the concerted mechanism. The first dehydration is considered as the rate determining step for both acrolein and acetol formation with the intrinsic activation energies of 42.5 and 42.3 kcal mol^{-1}, respectively. These results imply that the removal of the primary OH group competes with the removal of the secondary OH group in the glycerol dehydration. However, modes of glycerol adsorption onto the zeolite Brønsted site might exhibit selective dehydration. The stronger adsorption of glycerol through its secondary OH group favourably supports the secondary OH dehydration. Details of the reaction mechanism subsequent to the first dehydration reveal that acrolein formation is more kinetically favoured over the competitive formation of acetol. Also, it is expected that acrolein is less reactive than acetol and, at moderate temperatures, it is not converted to other products, thus remaining the major product for glycerol conversion. Consistent with experimental findings, conversion of glycerol to acrolein or acetol is an endothermic reaction. The increase of reaction temperature causes a more significant increase in the forward rate than that in the reverse rate. Further studies of the reaction network of acrolein and acetol conversion could lead to a better understanding of the experimental product selectivity of glycerol conversion. We believe that such information can be important as a guideline to find the best reaction conditions.

Acknowledgements

This work was supported in part by grants from the National Science and Technology Development Agency (2009 NSTDA Chair Professor funded by the Crown Property Bureau under the management of the National Science and Technology Development Agency and NANOTEC Center of Excellence funded by the National Nanotechnology Center), The Thailand Research Fund, the Commission on Higher Education, Ministry of Education (“National Research University of Thailand” and “Postgraduate Education and Research Programs in Petroleum and Petrochemicals and Advanced Materials”). The support from the Kasetsart University Research and Development Institute (KURDI) and the Graduate School Kasetsart University are also acknowledged. The authors are grateful to Donald G. Truhlar and Yan Zhao for their support concerning the M06-2X code. MP acknowledges support from the Austrian Ministry of Science *via* an infrastructure grant to the LFU scientific computing platform and from the RFBR-FWF projects 09-03-91001-a and I200-N19.

References

1 A. Corma Canos, S. Iborra and A. Velty, *Chem. Rev. (Washington, DC, U. S.)*, 2007, **107**, 2411–2502.
2 M. Pagliaro, R. Ciriminna, H. Kimura, M. Rossi and C. Della Pina, *Angew. Chem., Int. Ed.*, 2007, **46**, 4434–4440.
3 B. Katryniok, S. Paul, M. Capron and F. Dumeignil, *ChemSusChem*, 2009, **2**, 719–730.
4 S. Ramayya, A. Brittain, C. DeAlmeida, W. Mok and M. J. Antal Jr, *Fuel*, 1987, **66**, 1364–1371.
5 W. Bühler, E. Dinjus, H. J. Ederer, A. Kruse and C. Mas, *J. Supercrit. Fluids*, 2002, **22**, 37–53.
6 L. Ott, M. Bicker and H. Vogel, *Green Chem.*, 2006, **8**, 214–220.
7 V. Lehr, M. Sarlea, L. Ott and H. Vogel, *Catal. Today*, 2007, **121**, 121–129.
8 A. Alhanash, E. F. Kozhevnikova and I. V. Kozhevnikov, *Appl. Catal., A*, 2010, **378**, 11–18.

9 W. Suprun, M. Lutecki, T. Haber and H. Papp, *J. Mol. Catal. A: Chem.*, 2009, **309**, 71–78.
10 S. H. Chai, H. P. Wang, Y. Liang and B. Q. Xu, *J. Catal.*, 2007, **250**, 342–349.
11 F. Wang, J. L. Dubois and W. Ueda, *J. Catal.*, 2009, **268**, 260–267.
12 F. Wang, J. L. Dubois and W. Ueda, *Appl. Catal., A*, 2010, **376**, 25–32.
13 C. J. Zhou, C. J. Huang, W. G. Zhang, H. S. Zhai, H. L. Wu and Z. S. Chao, *Stud. Surf. Sci. Catal.*, 2007, **165**, 527–530.
14 A. Corma, G. W. Huber, L. Sauvanaud and P. O'Connor, *J. Catal.*, 2008, **257**, 163–171.
15 C. J. Jia, Y. Liu, W. Schmidt, A. H. Lu and F. Schüth, *J. Catal.*, 2010, **269**, 71–79.
16 Y. T. Kim, K. D. Jung and E. D. Park, *Microporous Mesoporous Mater.*, 2010, **131**, 28–36.
17 R. A. Van Santen and G. J. Kramer, *Chem. Rev. (Washington, DC, U. S.)*, 1995, **95**, 637–660.
18 E. Yoda and A. Ootawa, *Appl. Catal., A*, 2009, **360**, 66–70.
19 M. R. Nimlos, S. J. Blanksby, X. Qian, M. E. Himmel and D. K. Johnson, *J. Phys. Chem. A*, 2006, **110**, 6145–6156.
20 Y. Zhao and D. G. Truhlar, *Acc. Chem. Res.*, 2008, **41**, 157–167.
21 Y. Zhao and D. G. Truhlar, *J. Phys. Chem. C*, 2008, **112**, 6860–6868.
22 T. Maihom, B. Boekfa, J. Sirijaraensre, T. Nanok, M. Probst and J. Limtrakul, *J. Phys. Chem. C*, 2009, **113**, 6654–6662.
23 C. Kumsapaya, K. Bobuatong, P. Khongpracha, Y. Tantirungrotechai and J. Limtrakul, *J. Phys. Chem. C*, 2009, **113**, 16128–16137.
24 T. Maihom, P. Pantu, C. Tachakritikul, M. Probst and J. Limtrakul, *J. Phys. Chem.C*, 2010, **114**, 7850–7856.
25 B. Boekfa, P. Pantu, M. Probst and J. Limtrakul, *J. Phys. Chem. C*, 2010, **114**, 15061–15067.
26 S. Wannakao, B. Boekfa, P. Khongpracha, M. Probst and J. Limtrakul, *ChemPhysChem*, 2010, **11**, 3432–3438.
27 E. G. Hohenstein, S. T. Chill and C. D. Sherrill, *J. Chem. Theory Comput.*, 2008, **4**, 1996–2000.
28 S. Rayne and K. Forest, *THEOCHEM*, 2010, **948**, 102–107.
29 C. Peng, P. Y. Ayala, H. B. Schlegel and M. J. Frisch, *J. Comput. Chem.*, 1996, **17**, 49–56.
30 E. V. Stefanovich and T. N. Truong, *J. Phys. Chem. B*, 1998, **102**, 3018–3022.
31 B. Boekfa, S. Choomwattana, P. Khongpracha and J. Limtrakul, *Langmuir*, 2009, **25**, 12990–12999.
32 M. J. Frisch, G. W. Trucks, H. B. Schlegel, G. E. Scuseria, M. A. Robb, J. R. Cheeseman, J. Montgomery, T. J. A. Vreven, K. N. Kudin, J. C. Burant, J. M. Millam, S. S. Iyengar, J. Tomasi, V. Barone, B. Mennucci, M. Cossi, G. Scalmani, N. Rega, G. A. Petersson, H. Nakatsuji, M. Hada, M. Ehara, K. Toyota, R. Fukuda, J. Hasegawa, M. Ishida, T. Nakajima, Y. Honda, O. Kitao, H. Nakai, M. Klene, X. Li, J. E. Knox, H. P. Hratchian, J. B. Cross, V. Bakken, C. Adamo, J. Jaramillo, R. Gomperts, R. E. Stratmann, O. Yazyev, A. J. Austin, R. Cammi, C. Pomelli, J. W. Ochterski, P. Y. Ayala, K. Morokuma, G. A. Voth, P. Salvador, J. J. Dannenberg, V. G. Zakrzewski, S. Dapprich, A. D. Daniels, M. C. Strain, O. Farkas, D. K. Malick, A. D. Rabuck, K. Raghavachari, J. B. Foresman, J. V. Ortiz, Q. Cui, A. G. Baboul, S. Clifford, J. Cioslowski, B. B. Stefanov, G. Liu, A. Liashenko, P. Piskorz, I. Komaromi, R. L. Martin, D. J. Fox, T. Keith, M. A. Al-Laham, C. Y. Peng, A. Nanayakkara, M. Challacombe, P. M. W. Gill, B. Johnson, W. Chen, M. W. Wong, C. Gonzalez and J. A. Pople, *Gaussian 03, revision B.05*, Gaussian, Inc., Wallingford CT, 2004.
33 R. Chelli, F. L. Gervasio, C. Gellini, P. Procacci, G. Cardini and V. Schettino, *J. Phys. Chem. A*, 2000, **104**, 11220–11222.
34 R. Chelli, F. L. Gervasio, C. Gellini, P. Procacci, G. Cardini and V. Schettino, *J. Phys. Chem. A*, 2000, **104**, 5351–5357.
35 M. Hunger and T. Horvath, *J. Am. Chem. Soc.*, 1996, **118**, 12302–12308.
36 C. C. Lee, R. J. Gorte and W. E. Farneth, *J. Phys. Chem. B*, 1997, **101**, 3811–3817.
37 G. S. Hammond, *J. Am. Chem. Soc.*, 1955, **77**, 334–338.
38 A. Ison and R. J. Gorte, *J. Catal.*, 1984, **89**, 150–158.
39 S. A. Zygmunt, L. A. Curtiss, L. E. Iton and M. K. Erhardt, *J. Phys. Chem.*, 1996, **100**, 6663–6671.
40 Y. Izumi, *Catal. Today*, 1997, **33**, 371–409.
41 W. Wang and M. Hunger, *Acc. Chem. Res.*, 2008, **41**, 895–904.
42 D. G. Truhlar, B. C. Garrett and S. J. Klippenstein, *J. Phys. Chem.*, 1996, **100**, 12771–12800.

Characterization of Acidity in [B], [Al], and [Ga] Isomorphously Substituted ZSM-5: Embedded DFT/UFF Approach

SIRIPORN JUNGSUTTIWONG,[1] JARUN LOMRATSIRI,[1] JUMRAS LIMTRAKUL[2]

[1]*Department of Chemistry, Ubon Ratchathani University, Ubon Ratchathani 34190, Thailand*

[2]*Department of Chemistry and NANOTEC Center of Excellence, Kasetsart University, Bangkok 10900, Thailand*

Received 8 November 2009; accepted 23 November 2009
Published online 2 March 2010 in Wiley Online Library (wileyonlinelibrary.com).
DOI 10.1002/qua.22531

ABSTRACT: The structure and electronic properties of the Brønsted acid site in B, Al or Ga isomorphously substituted ZSM-5 zeolites were studied by using quantum cluster and embedded ONIOM approaches. In the former approach, zeolites are modeled by 5T and 12T quantum clusters, where T represents a Si or Al atom. In the latter model, called "Embedded ONIOM", the long-range interactions of the zeolite lattice beyond the 12T quantum cluster is included via optimized point charges added to the ONIOM(B3LYP/6-31G(d,p):UFF). Inclusion of the extended zeolitic framework covering the nanocavity has an effect on the structure and adsorption properties. We found that the OH distances and v OH of the acidic proton in zeolite obtained from both models can predict the trend of acid strength as: B-ZSM-5 < Ga-ZSM-5 < Al-ZSM-5, which is in very good agreement with the experimental sequence. Furthermore, the PA data calculated from E-ONIOM is also consistent with the experimental trend: B-ZSM-5 < Ga-ZSM-5 < Al-ZSM-5. It has, therefore, been demonstrated that our embedded ONIOM model provides accurate performance and can be one of the useful and affordable methods for future mechanistic studies involving petrochemical reactions. ©2010 Wiley Periodicals, Inc. Int J Quantum Chem 111: 2275–2282, 2011

Key words: embedded ONIOM; DFT; isomorphous substituted ZSM-5

Correspondence to: S. Jungsuttiwong; e-mail: jsiriporn_2000@yahoo.com

Contract grant sponsors: The Thailand Research Fund (TRF-CHE Research Grant for New Scholar), Ubon Ratchathani University and NANOTEC Center of Excellence, Kasetsart University.

Introduction

Since the introduction of synthetic zeolites as catalysts in fluid catalytic cracking of heavy petroleum distillates in 1962, catalysis has become the single most financially-important application of zeolites in terms of financial impact. Driven by the potential economic impact, progress in zeolite catalysis has focused largely on the synthesis, postsynthesis modification, physiochemical characterization, and testing. Much less has been achieved in improving the fundamental understanding of the structure and functions of zeolites and their catalytic roles. This is indicated by the fact that there are a very large number of zeolite topologies are known today, yet only a very limited number of such zeolites are actually used in applications [1–7]. Fundamental molecular-level understanding of structure–function relationships of the catalytic activity of zeolites and mechanisms of reactions at the active sites have a significant impacts on catalytic and process design and thus drastically improve the industrial competitive edge. The presence of Al replacing Si in zeolite structure generates a bridging hydroxyl group so called ["Brønsted acid site" (BAS)]. Many of the catalytic properties of zeolites can be directly related to this Brønsted acidity. In fact, heteroatoms such as B, Ga, Fe, and Zn can be introduced into the framework of zeolite [8–12] by the replacement of Si atoms. Many of these studies were focused on predicting the acid strength of isomorphously substituted ZSM-5. The ability to vary the acidity of the catalyst is of importance in determining the extent and selectivity of the catalytic process. In previous experiments in which results were mostly obtained by IR spectroscopy and TPD of NH_3, Chu and Chang [9] predicted that the Brønsted acidity of substituted ZSM-5 increases in the order B-ZSM-5 $\ll$ Fe-ZSM-5 $<$ Ga-ZSM-5 $<$ Al-ZSM-5, indicating that the catalytic properties can be tuned for a particular reaction. There have been several theoretical studies on zeolite structure and reactivity [3, 8, 13–16] using the cluster method.

The cluster methodology recognizes the most important region of the chemistry of the system as that surrounding the active site and the adsorbate, and treats it explicitly within full quantum mechanical formalism as an isolated system and ignoring the effects of the remaining crystal framework. Therefore the cluster methodology cannot provide information on the effects of the zeolite framework. Periodic electronic structure methods, on the other hand, provide an accurate framework to model interactions in extended systems such as crystals or surfaces [17, 18]. Zeolites often have large unit cells; for instance, the unit cell for ZSM-5 has 288 atoms (96 silicon atoms and 192 oxygen atoms). Because of the large number of reactions involved in this mechanism, the use of accurate periodic electronic structure methods is limited due to the demand of enormous computational resources and time. The only alternative is to use the embedded cluster approach. This approach recognizes the most important region of the chemistry of the system as that surrounding the active site and the adsorbate and thus treats it explicitly within full quantum mechanical formalism and adding the effects of the crystal framework in the Hamiltonian of the quantum region in an approximated manner. Some previous works employed a charge representation of the external electrostatic potential [19–23]. The electrostatic component of the Madelung potential, which makes the largest contribution, is represented by a set of surface charges. This is done by the SCREEP method [24–27]. However, in several systems, it was found to be technically difficult to obtain an accurate Madelung potential for the cluster embedded inside by means of surface charges [28]. To obtain a more accurate method, as in the study of the structure of BAS, the E-ONIOM method has been used to improve the energetic information.

In this article, the focus was on using the ONIOM embedded [29] approach in fine tuning the strength of the acid sites of the isomorphously substituted zeolites. This technique is a simple method that uses only the atomic positions of the lattice and is, therefore, easy to use while requiring a similarly small computational effort compared with periodic calculations. The structure and electronic properties of the BAS in [B], [Al], and [Ga] isomorphously substituted ZSM-5 zeolites were studied by using the ONIOM embedded approach with the B3LYP/6-31G (d,p) level of theory.

Computational Details

There are three different models that have been used to study the isomorphously substituted zeolites. The first model is the small 5T cluster model

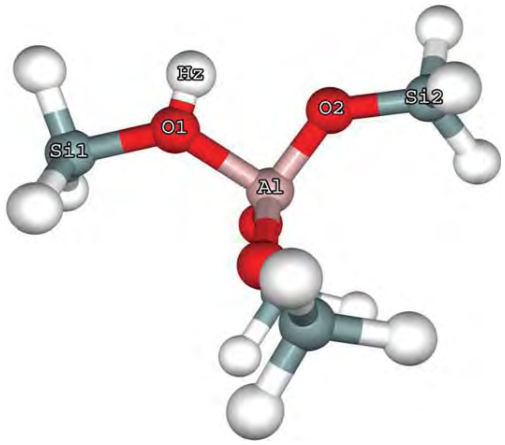

FIGURE 1. The 5T cluster model of H-ZSM-5. [Color figure can be viewed in the online issue, which is available at wileyonlinelibrary.com.]

(see Fig. 1), which are parts of the 10-membered ring of ZSM-5 zeolites, consisting of five tetrahedrally coordinated atoms (Si, Al). They were taken from the crystal structure of the ZSM-5 lattice [30]. These rings are at the intersections of the channels and are accessible to the adsorbates. Hydrogen atoms were used to cap the dangling bonds. These capped hydrogen atoms are located along the direction of corresponding Si—O bonds. The resulting 5T clusters, Si4AlO4H13, have a total of 22 atoms. The second models are a larger 12T clusters, Si11AlO12H25, consisting of a total of 49 atoms (see Fig. 2). They were selected to study the effects of unphysical interactions between small adsorbates and capped hydrogen atoms. These effects were remarkably observed in 5T cluster models. The T12 site was selected to represent the active site of ZSM-5 because it was found to be among the most stable sites for Al substitution [29, 31], and this site provides sufficient space and can be accessed easily by small adsorbates. Most previous theoretical works have also chosen the T12 site as the Al substitution site for ZSM-5.

The third model is termed "embedded ONIOM"[29] and is used to include the long-range interactions of the zeolite lattice beyond 12T (see Fig. 3). As point charges close to the quantum region can easily cause problems, we place our point charges only in a region defined by a minimal distance to the center of the quantum region and a maximal distance that determines the number of point charges. This finite number of point charges is further divided into an inner and an

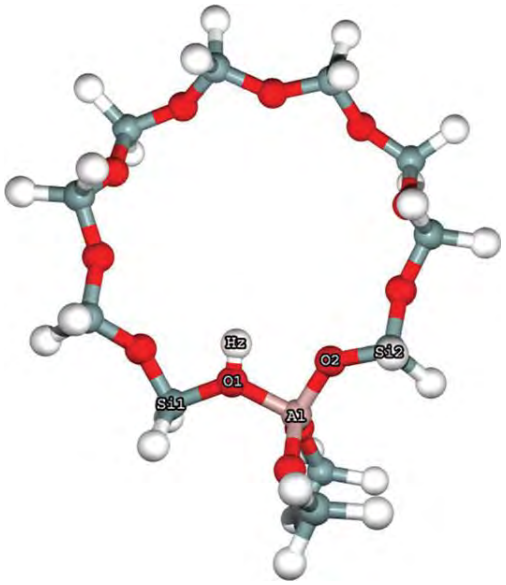

FIGURE 2. 12T-[Al]-ZSM-5 cluster model. [Color figure can be viewed in the online issue, which is available at wileyonlinelibrary.com.]

outer zone. Point charges in the inner zone (which might be a shell with a typical thickness of 5–10 Å and a few hundred point charges) are not optimized and have values one-half the formal charges of the zeolite atoms. Such "effective" charges $Q_{Si} = +2$ and $Q_O = -1$ are often used for a supermolecule such as zeolite and appear to be more realistic than the formal charges. The point charges in the outer region, which is a shell region immediately adjacent to the zone of the fixed charges, are

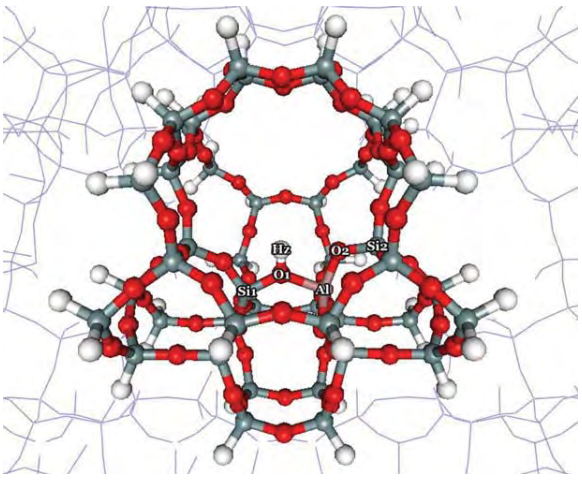

FIGURE 3. Embedded ONIOM 12T-[Al]-ZSM-5 model. [Color figure can be viewed in the online issue, which is available at wileyonlinelibrary.com.]

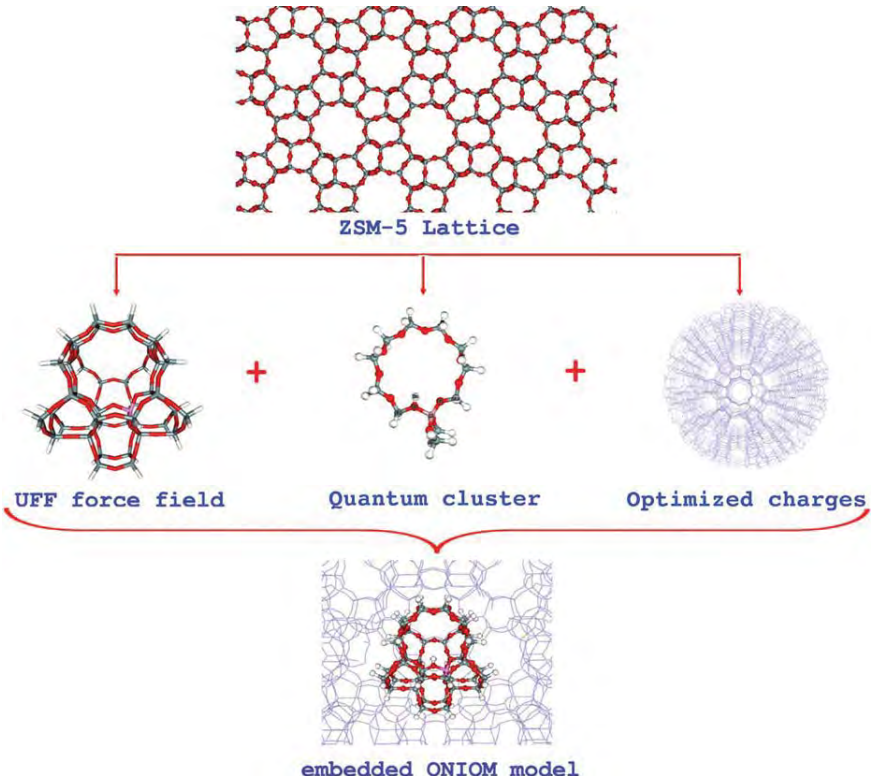

FIGURE 4. Embedded ONIOM Scheme. [Color figure can be viewed in the online issue, which is available at wileyonlinelibrary.com.]

optimized (typically there are a few thousand of them). We can define them by ΔQ, the vector of deviations from the values

$$Q'_{\text{outer}} = Q_{\text{outer}} + \Delta Q'' \tag{1}$$

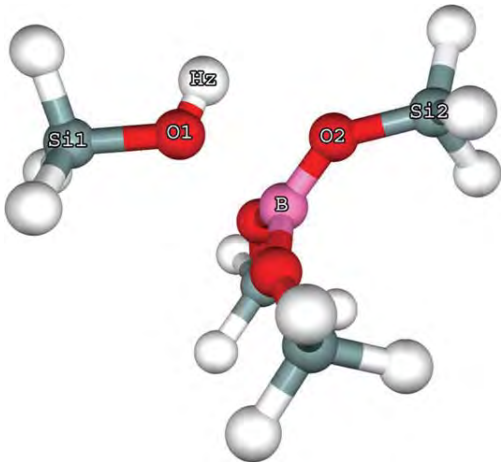

FIGURE 5. 5T-[B]-ZSM-5 cluster model. [Color figure can be viewed in the online issue, which is available at wileyonlinelibrary.com.]

where ΔQ is derived in the following way. The electrostatic potential from the infinite crystal is calculated at the grid points using the Ewald method. The electrostatic potential from the zeolite cluster and from the point charges in both zones are then subtracted from it as follows:

$$V_{\text{outside}} = V_{\text{ewald}} - V_{\text{cluster}} - V_{\text{inner/outer}} \tag{2}$$

We find the ΔQ that reproduces V_{outside} by solving the matrix of simultaneous linear equations:

$$A \cdot \Delta Q = V_{\text{outside}} \tag{3}$$

TABLE I

The distances (pm) of T—O1 in isolated H-ZSM-5 with B3LYP/6-31G (d, p) level of theory.

Level of theory	Al—O1	B—O1	Ga—O1
5T Cluster	185.60	207.16	193.22
12T Cluster	183.98	204.57	191.61
12T E-ONIOM	179.40	176.88	187.46

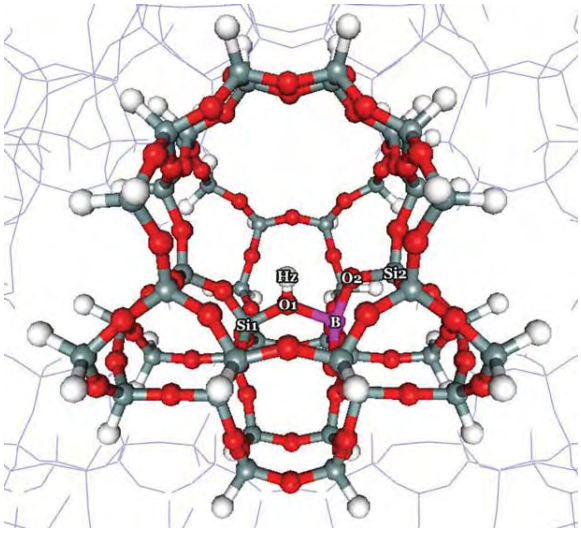

FIGURE 6. Embedded ONIOM 12T-[B]-ZSM-5 model. [Color figure can be viewed in the online issue, which is available at wileyonlinelibrary.com.]

$$A_{if} = 1/|R_i - R_j| \cdot R_i$$

where V_{outside} is a column matrix with m rows and m is the number of grid points. A is the distance matrix having m rows and n (the number of charges in the outer zone) columns. Its elements are defined as R_i being the position of grid point i, and R_j is the position of charge j. The Embedded ONIOM scheme is shown in Figure 4. We now have a complete set of charges consisting of the point charges in the inner zone and the optimized point charges in the outer zone and their respective positions. This allows us to add the crystal potential to the quantum region. The system of equations described in Eq. (3) also contains the four equations needed to guarantee the overall neutrality of charges and vanishing dipole moments along x, y, and z [31]. In all three models, the geometry optimizations were done at the B3LYP/6-31G (d, p) level. All calculations were performed using the GAUSSIAN 03 program [32].

TABLE III

PA and ν_{OH} calculated with B3LYP/6-31G (d, p) level of theory.

Substituted ZSM-5	PA (kcal/mol)	
	12T Cluster	E-ONIOM 12T
B-ZSM-5	320.12	363.69
Ga-ZSM-5	313.36	362.31
Al-ZSM-5	308.98	357.68
Acidity sequence	B-ZSM-5 < Ga-ZSM-5 < Al-ZSM-5	

Results and Discussion

THE EFFECTS OF THE ZEOLITE LATTICE FRAMEWORK

To take into account the effects of the electron correlation of a large basis set and of the BSSE correction in the determinations, the effects of the lattice framework were included by the use of the embedded ONIOM (E-ONIOM) method. It is outlined in Figure 1. It was found that the 5T cluster with the fully optimized model at B3LYP/6-31G (d, p) level of theory leads to structures that did not resemble experimental zeolite geometry, see Figure 5. The T—O1 distances are listed in Table I. However, the inclusion of the Madelung potential, which was determined by improving optimized point charges to reproduce the infinite zeolitic lattice crystal integrated into the ONIOM (E-ONIOM method), the optimized model with electron correlation, and the large basis set, B3LYP/6-31G (d, p), resulted in more accuracy (see Figure 6). Furthermore, OH distances and the acidic proton in zeolite obtained from embedded ONIOM models were able to predict the trend of acid strength as: B-ZSM-5 < Ga-ZSM-5 <

TABLE II

The distanced of O—H (pm) in isolated H-ZSM-5 with B3LYP/6-31G (d, p) level of theory.

Level of theory	Al-ZSM-5	B-ZSM-5	Ga-ZSM-5	Acidity
5T Cluster	96.80	96.45	96.83	B < Al < Ga
12T Cluster	96.98	96.66	97.01	B < Al < Ga
12T E-ONIOM	97.07	96.93	97.06	B < Ga < Al
Experimental sequence of acid strength		B-ZSM-5 < Ga-ZSM-5 < Al-ZSM-5		

TABLE IV

The distances (pm) of O—H_z in isolated H-ZSM-5 with B3LYP/6-31G (d, p) level of theory.

Level of theory	Al	B	Ga	Acidity trend
5T Cluster	96.80	96.45	96.83	B < Al < Ga
12T Cluster	96.98	96.66	97.01	B < Al < Ga
12T E-ONIOM	97.08	96.93	97.06	B < Ga < Al
ν_{OH} (cm^{-1}) calculated IR frequency	3604	3616	3608	B < Ga < Al

Al-ZSM-5, showing strong agreement with the experimental sequence (see Table II).

PROTON AFFINITY OF THE SUBSTITUTED ZSM-5

Proton affinity (PA) can serve as a measure of the acid strength of ZSM-5. While direct experiments related to PA are not feasible, the data can be easily obtained from quantum calculation in which PA is considered as the energy required to remove the acidic proton from the zeolite structure. This is calculated by equation (4):

$$PA = E_{ZO} - E_{ZOH} \quad (4)$$

In this equation, E_{ZO} and E_{ZOH} are the energies of the deprotonated and the neutral clusters, respectively. It is obvious that the larger the PA, the weaker the acidity of the bridged hydroxyl group. The predicted PA data listed in Table II are calculated from two models, the 12T cluster and the 12T E-ONIOM giving the same trends of acid strength. These results are consistent with the experimental trend: B-ZSM-5 < Ga-ZSM-5 < Al-ZSM-5. It is obvious that the larger the PA, the weaker the acidity of the bridged hydroxyl group. The PA data calculated from the three models 12T cluster, 12T ONIOM, and 12T E-ONIOM give the same trends of acid strength, which is consistent with the experimental trend: B-ZSM-5 < Ga-ZSM-5 < Al-ZSM-5 (see Table III).

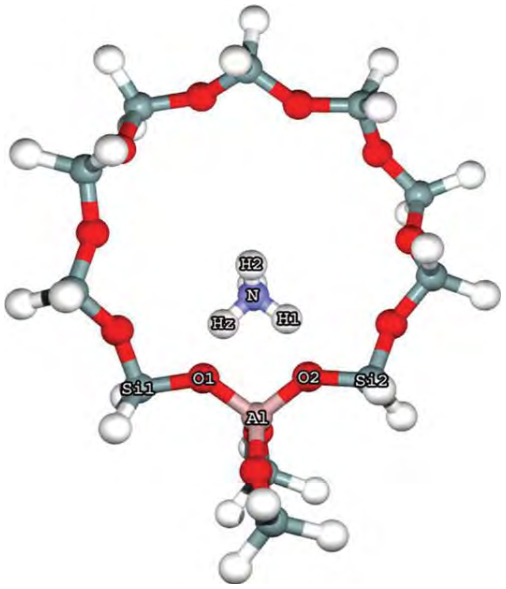

FIGURE 7. NH3/12T-[Al]-ZSM-5 complex. [Color figure can be viewed in the online issue, which is available at wileyonlinelibrary.com.]

OH STRETCHING FREQUENCY

It is generally accepted that the stretching frequency of the OH bond (ν_{OH}) can be taken as an indicator of Brønsted acidity [16]; and that the lower wave number of ν_{OH} is related to weaker O—H bond strength and hence corresponds to stronger acid strength. The calculations were performed directly after the geometry optimization by the B3LYP method with three different 12T models: cluster, ONIOM, and E-ONIOM. Positions of ν_{OH} are given in Table IV. The data calculated with 6–31G (d,p) require scaling by 0.950 [33]. It was shown that the

TABLE V

The charged form NBO population analysis using 12T E-ONOM model with B3LYP/6-31G (d,p) level of theory.

Substituted ZSM-5	NBO population analysis			
	q(M)	*q* (Hz)	*q*(O1)	Electronegativity
[B]-ZSM-5	1.3610	0.5722	−1.0415	2.01
[Ga]-ZSM-5	1.8265	0.5851	−1.1238	1.82
[Al]-ZSM-5	2.0013	0.5905	−1.1390	1.47
Acidity sequence	B-ZSM-5 < Ga-ZSM-5 < Al-ZSM-5			

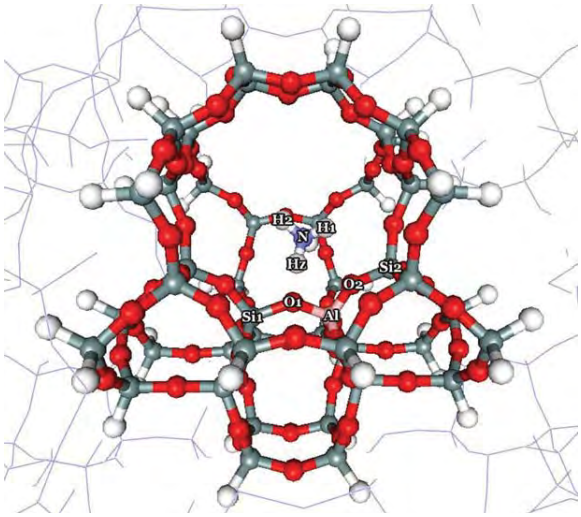

FIGURE 8. NH3/Embedded ONIOM-[Al]-ZSM-5 complex. [Color figure can be viewed in the online issue, which is available at wileyonlinelibrary.com.]

three different methods give different acidity sequences. The ν_{OH} calculated from the 12T E-ONIOM provide trends corresponding to the experimental result; and the results of this study also supported the ν_{OH} in the region 3600–3700 cm^{-1} suggested by Chu and Chang [9] as the fingerprint for Brønsted OH species. It was shown that the DFT method with the 12T E-ONIOM model was sufficient for this article.

THE NATURAL BOND ORBITAL POPULATION ANALYSIS OF ATOMIC CHARGE

The atomic charges from natural bond orbital (NBO) population analysis with M (M = B, Al, Ga), O1, and Hz (acidic proton) are presented in Table V. It has been shown that q(M), charges on heteroatom M, increase with the decrease of its electronegativity (1.47, 1.82, and 2.01 for Al, Ga, and B, respectively). The charge on the oxygen bridge atom (O1), q(O1), increase with the increases with the escalation of qM, leading to a boost in the charges on the acidic proton (qHz) corresponding with an increase of the acidity. It can be stated from the q(Hz) data that the acid strength of the substituted ZSM-5 increases in order: B-ZSM-5 < Ga-ZSM-5 < Al-ZSM-5, which is consistent with the PA.

TABLE VI

The calculated ν_{OH} with B3LYP/6-31G (d,p) level of theory.

		Tetrahedral atom		
ν_{OH} (cm^{-1})	Acidity trend	Al	Ga	B
12T E-ONIOM	B < Ga < Al	3604	3608	3616
12T Cluster	B < Al < Ga	3614	3612	3658
ν_{OH} [33] 8T cluster	B < Ga < Al	3816	3825	3830
ν_{OH} from IR [9]	B < Ga < Al	3610	3620	3725

ADSORPTION OF NH_3 ON ZSM-5

The optimized adsorption structures of NH_3 on ZSM-5 are shown in Figures 7 representing the cluster model and Figure 8 showing the E-ONIOM model. Table VI illustrates the energy of the adsorption of NH_3 on the acid site of the substituted ZSM-5 zeolites calculated by Eq. (5)

$$\Delta E_{ads} = E(\text{complex}) - E(\text{ZOH}) - E(NH_3) \quad (5)$$

The relative acid strength predicted by the adsorption energy of NH_3 is shown to be

TABLE VII

Comparisons of calculated adsorption energies of NH_3/zeolite including BSSE at 6-311++G (d, p) basis set with previous theoretical and experimental results.

	Level of theory	Cluster	Model	ΔE
Al	B3LYP/6-31G (d,p)	12T	E-ONIOM	33.98
Al [16]	B3LYP/3-21G	8T	Cluster	50.7
Al [33]	Experiment			33.5–35.6
Ga	B3LYP/6-31G (d,p)	12T	E-ONIOM	31.43
Ga [16]	B3LYP/3-21G	8T	Cluster	50.0
Ga [33]	Experiment			34.52–36.90
B	B3LYP/6-31G (d,p)	12T	E-ONIOM	24.86
B [16]	B3LYP/3-21G	8T	Cluster	41.0

consistent with that derived from the PA and ν_{OH} of this article, B-ZSM-5 < Ga-ZSM-5 < Al-ZSM-5. Moreover, the adsorption energies calculated with B3LYP/6-31G (d,p) for the 12T E-ONIOM model more strongly correspond with the experimental results compared to those of previous work [16, 33] (see Table VII).

Conclusions

It was shown that the acidity is the adsorption energy of NH_3 which showed that the acid strength of the substituted ZSM-5 increases in the sequence: B-ZSM-5 < Ga-ZSM-5 < Al-ZSM-5, in strong agreement with experimental results. The interaction of NH_3 with the BAS indicated that NH_3 becomes protonated in contact with the zeolite cluster and the configurations in which the protonated NH_3 interacts with two lattice oxygen atoms are favored energetically. In addition, the calculated adsorption energy of NH_3 on Al-ZSM-5 is comparable with the experimental data. This indicates that it is essential to take into account the effects of the Madelung potential due to atoms outside the quantum cluster by using the E-ONIOM method are essential to be taken into account. Furthermore, the results show a prospective trend to predict properties of metal-substituted zeolites, with a special emphasis on the Bronsted acid strength of zeolites.

References

1. Pirngruber, G. D.; Seshan, K.; Lercher, J. A. J Catal 2000, 190, 338.
2. Cerqueira, H. S.; Mihindou-Koumba, P. C.; Magnoux, P.; Guisnet, M. Ind Eng Chem Res 2001, 40, 1032.
3. Li, H.-Y.; Pu, M.; Liu, K.-H.; Zhang, B.-F.; Chen, B.-H. Chem Phys Lett 2005, 404, 384.
4. Ivanov, P.; Papp, H. Chem Ing Tech 2000, 72, 1213.
5. Kuznetsov, P. N. J Catal 2003, 218, 12.
6. Davis, R. J. J Catal 2003, 216, 369.
7. Coudurier, G.; Vedrine, J. C. Pure Appl Chem 1986, 58, 1389.
8. Alverado Swasigood, A. E.; Barr, M. K.; Hay, P. J.; Redondo, A. J Phys Chem 1991, 95, 10031.
9. Chu Cynthia, T. W.; Change, C. D. J Phys Chem 1985, 89, 1569.
10. Dong, M.; Wang, J.; Sun, Y. Micropor Mesopor Mater 2001, 43, 237.
11. Fricke, R.; Kosslick, H.; Lischke, G.; Richter, M. Chem Rev 2000, 100, 2303.
12. Langenaeker, W.; Coussement, N.; De Proft, F.; Geerlings, P. J Phys Chem 1994, 98, 3010.
13. White, J. C.; Hess, A. C. J Phys Chem 1993, 97, 8703.
14. Brand, H. V.; Curtiss, L. A.; Iton, L. E. J Phys Chem 1992, 96, 7725.
15. O'Malley, P. J.; Dwyer, J. J Phys Chem 1988, 92, 3005.
16. Yuan, S. P.; Wang, J. G.; Li, Y. W.; Peng, S. Y. J Mol Catal A: Chem 2002, 178, 267.
17. Shah, R.; Gale, J. D.; Payne, M. C. Chem Commun (Camb.) 1997, 131.
18. Jeanvoine, Y.; Angyan, J. G.; Kresse, G.; Hafner, J. J Phys Chem B 1998, 102, 5573.
19. Allouche, A. J Phys Chem B 1996, 100, 17915.
20. Ferrari, A. M.; Pacchioni, G. J Phys Chem B 1996, 100, 9032.
21. Allouche, A. J Phys Chem B 1996, 100, 1820.
22. Saunders, V. R.; Freyria-Fava, C.; Dovesi, R.; Salasco, L.; Roetti, C. Mol Phys 1992, 77, 629.
23. Ferro, Y.; Allouche, A.; Cora, F.; Pisani, C.; Girardet, C. Surf Sci 1995, 325, 139.
24. Stefanovich, E. V.; Truong, T. N. J Phys Chem B 1998, 102, 3018.
25. Limtrakul, J.; Jungsuttiwong, S.; Khongpracha, P. J Mol Struct 2000, 525, 153.
26. Limtrakul, J.; Khongpracha, P.; Jungsuttiwong, S.; Truong, T. N. J Mol Catal A 2000, 153, 155.
27. Treesukol, P.; Limtrakul, J.; Truong, T. N. J Phys Chem B 2001, 105, 2421.
28. Greatbanks, S. P.; Sherwood, P.; Hillier, I. H. J Phys Chem B 1994, 98, 8134.
29. Injan, N.; Pannorad, N.; Probst, M.; Limtrakul, J. Int J Quantum Chem 2005, 105, 898.
30. Derouane, E. G.; Fripiat, J. G. Zeolites 1985, 5, 165.
31. Derenzo, S. E.; Klintenberg, M. K.; Weber, M. J. J Chem Phys 2074, 2000, 112.
32. Frisch, M. J.; Trucks, G. W.; Schlegel, H. B.; Scuseria, G. E.; Robb, M. A.; Cheeseman, J. R.; Zakrzewski, V. G.; Montgomery, J. A.; Stratmann, R. E., Jr.; Burant, J. C.; Dapprich, S.; Millam, J. M.; Daniels, A. D.; Kudin, K. N.; Strain, M. C.; Farkas, O.; Tomasi, J.; Barone, V.; Cossi, M.; Cammi, R.; Mennucci, B.; Pomelli, C.; Adamo, C.; Clifford, S.; Ochterski, J.; Petersson, G. A.; Ayala, P. Y.; Cui, Q.; Morokuma, K.; Salvador, P.; Dannenberg, J. J.; Malick, D. K.; Rabuck, A. D.; Raghavachari, K.; Foresman, J. B.; Cioslowski, J.; Ortiz, J. V.; Baboul, A. G.; Stefanov, B. B.; Liu, G.; Liashenko, A.; Piskorz, P.; Komaromi, I.; Gomperts, R.; Martin, R. L.; Fox, D. J.; Keith, T.; Al-Laham, M. A.; Peng, C. Y.; Nanayakkara, A.; Challacombe, M.; Gill, P. M. W.; Johnson, B.; Chen, W.; Wong, M. W.; Andres, J. L.; Gonzalez, C.; Head-Gordon, M.; Replogle, E. S.; Pople, J. A. Gaussian 03, revision B.05; Gaussian, Inc.: Pittsburgh, PA, 2001.
33. Parrillo, D. J.; Lee, C.; Gorte, R. J.; White, D.; Farneth, W. E. J Phys Chem 1995, 99, 8745.

CHEMPHYSCHEM

DOI: 10.1002/cphc.201100047

Glycine Peptide Bond Formation Catalyzed by Faujasite**

Oranit Phuakkong,[a, b, c] Karan Bobuatong,[a, b, c] Piboon Pantu,[a, b, c] Bundet Boekfa,[b, c, d] Michael Probst,[e] and Jumras Limtrakul*[a, b, c]

The catalysis of peptide bond formation between two glycine molecules on H-FAU zeolite was computationally studied by the M08-HX density functional. Two reaction pathways, the concerted and the stepwise mechanism, starting from three differently adsorbed reactants, amino-bound, carboxyl-bound, and hydroxyl-bound, are studied. Adsorption energies, activation energies, and reaction energies, as well as the corresponding intrinsic rate constants were calculated. A comparison of the computed energetics of the various reaction paths for glycine indicates that the catalyzed reaction proceeds preferentially via the concerted reaction mechanism of the hydroxyl-bound configuration. This involves an eight-membered ring of the transition structure instead of the four-membered ring of the others. The step from the amino-bound configuration to glycylglycine is the rate-determining step of the concerted mechanism. It has an estimated activation energy of 51.2 kcal mol^{-1}. Although the catalytic reaction can also occur via the stepwise reaction mechanism, this path is not favored.

1. Introduction

Peptide bond formation is an essential step in the synthesis of proteins and peptides. Understanding this process allows the control of construction and organization of these polymers with useful applications in medical, biological, and food sciences.[1] Its reaction mechanism has attracted much attention over the last five decades. It is relevant to the synthesis of peptides from amino acids or their esters under prebiotic conditions[2] and numerous attempts from the experimental and computational side were performed to examine the basic steps of peptide bond formation.[3] Of even more practical importance is that many current works deal with designing peptides as parts of biocompatible units and take advantage of their self-assembly features. Peptides are also increasingly used as sensing devices.[1a–c,4]

For the acid/base-catalyzed aminolysis of alkyl esters, the mechanism of peptide bond formation has been studied experimentally in aqueous solution by Jencks et al.[3c–e] The basic step is the nucleophilic attack of the lone electron pair of the amino group onto the carbon atom of the carboxyl group followed by proton transfer from the amino group to one of the oxygen atoms of the carboxyl group. In the proposed concerted and/or stepwise reaction mechanisms, a possible formation of a relatively stable zwitterionic intermediate is considered. The relative stability of this adduct depends on the acid–base properties of the solvent, and its lifetime can be an important factor in the whole reaction mechanism.

Despite the intensive experimental works mentioned above and various studies using silica,[5] clays[5,6], and aluminas[5,7] as catalysts for the peptide formation, mechanistic discussions are rare and no detailed molecular picture is available for these processes. Nevertheless, some mechanisms have been suggested in the past to interpret the experimental evidence of the formation of small oligopeptides, albeit at the level of very simple schemes by Zamaraev et al.,[6a] for adsorption of glycine on zeolites and kaolinite and by Basiuk et al. for silica and alumina.[7a] Recently, zeolites have found potential applications in amino acid separation,[8] immobilized peptide synthesis,[9] and biomedical sensors.[10]

Theoretically, the mechanism of the uncatalyzed amide bond formation has been investigated by Oie et al. and Jensen et al.,[3g,h] who have shown that stepwise and concerted mechanisms may compete since both involve comparable activation energies. The latter authors also performed a study for the glycine + glycine reaction, and the main conclusion was that the model system glycine + glycine appears to be a good representative of a dipeptide system. Moreover, the mechanisms of amide bond formation in various catalytic systems have been

[a] O. Phuakkong, K. Bobuatong, Prof. Dr. P. Pantu, Prof. Dr. J. Limtrakul
Laboratory for Computational and Applied Chemistry, Department of Chemistry, Faculty of Science and Center of Nanotechnology
Kasetsart University Research and Development Institute
Kasetsart University, Bangkok 10900 (Thailand)
Fax: (+66) 2-562-5555 ext 2159
E-mail: Jumras.l@ku.ac.th

[b] O. Phuakkong, K. Bobuatong, Prof. Dr. P. Pantu, Dr. B. Boekfa, Prof. Dr. J. Limtrakul
Center for Advanced Studies in Nanotechnology and Its Applications in Chemical, Food and Agricultural Industries
Kasetsart University, Bangkok 10900 (Thailand)

[c] O. Phuakkong, K. Bobuatong, Prof. Dr. P. Pantu, Dr. B. Boekfa, Prof. Dr. J. Limtrakul
NANOTEC Center of Excellence, National Nanotechnology Center
Kasetsart University, Bangkok 10900 (Thailand)

[d] Dr. B. Boekfa
Chemistry Department, Faculty of Liberal Arts and Science
Kasetsart University Kamphaeng Saen Campus
Nakhon Pathom 73140 (Thailand)

[e] Prof. Dr. M. Probst
Institute of Ion Physics and Applied Physics
University of Innsbruck, 6020 Innsbruck (Austria)

[**] A Density Functional Theory Study

Supporting information for this article is available on the WWW under http://dx.doi.org/10.1002/cphc.201100047.

theoretically investigated. Rimalo et al. examined the role of Lewis and Brønsted catalysts on peptide formation using HF and AlF_3,[11] anorthite and sanidine[12] as the catalytic models, respectively. It has been found that the synergy of those catalysts dramatically lowers the activation barrier for the amide bond formation, a fact relevant in the prebiotic synthesis of peptides on the surface of oxide minerals that are rich in Lewis/Brønsted sites.

Brønsted acid sites are usually well characterized in the interior of zeolites. To our knowledge, their catalytic role in the peptide bond formation process has never been addressed together with a realistic representation of the zeolite. Therefore, we investigated the reaction mechanisms and kinetics of the zeolite-catalyzed peptide bond formation between two glycine molecules as the simplest model of such a reaction.

Quantum chemical calculations are reliable theoretical tools for studying chemical reactions which cannot be readily characterized by experimental techniques. Moreover, it is possible to compute valuable information about the nature of the transition states and the stable intermediate states as well as details of thermodynamics, kinetics of reaction, and spectroscopic properties such as the frequencies of vibration[13] of the system. Thus, direct insight into the reaction mechanism is possible, provided that the data are checked against available experimental results.

Zeolites usually possess hundreds of atoms per unit cell which makes the use of sophisticated methods, such as periodic ab initio calculations, computationally too expensive. The recent development of hybrid methods, such as the embedded cluster or combined quantum mechanics/molecular mechanics (QM/MM) methods,[13,14] has brought accurate results on large systems within reach.[14h,15] This was, for example, demonstrated in a study of the interaction of glycine with H-ZSM-5 zeolite.[15f] Complementary to this development, density functionals like the M06 set[16] can be applied to account for a more accurate treatment of the interactions in these systems, as has, for example, been done when studying the reactions of hydrocarbons inside zeolites.[14e,i,17] Herein we proceed along similar lines but apply a newer density functional and discuss its performance.

The aims of the present work are: 1) to investigate the peptide bond formation on zeolite and 2) to study the effect of the zeolite framework on the reaction. Two possible reaction mechanisms are investigated, a concerted and a stepwise one. The results of this study may be helpful for understanding the fundamentals of peptide formation of amino acid catalyzed by zeolite.

2. Results and Discussion

It was assumed that the reaction can either occur via a concerted reaction mechanism (Figure S1 in the Supporting Information) or by a stepwise reaction mechanism through the formation of the diolic intermediate (Figure S2 in the Supporting Information).

2.1. Concerted Reaction Mechanism

The peptide bond formation of two glycine molecules catalyzed by faujasite zeolite (Figure 1) via a concerted reaction mechanism is shown in Figure S1 in the Supporting Information. Depending on the site of initial adsorption, three possible energy profiles are presented for the concerted reaction in Figure 2a. The reaction is catalyzed by the Brønsted acidic proton acting as a proton donor to the oxygen atom of the amino group (amino-bound, Figure 3a), the carboxyl group (carboxyl-bound, Figure 4a), and the hydroxyl group (hydroxyl-bound, Figure 5a) of the glycine molecule, respectively. All of them are involved in the nucleophilic attack of the amino group on the

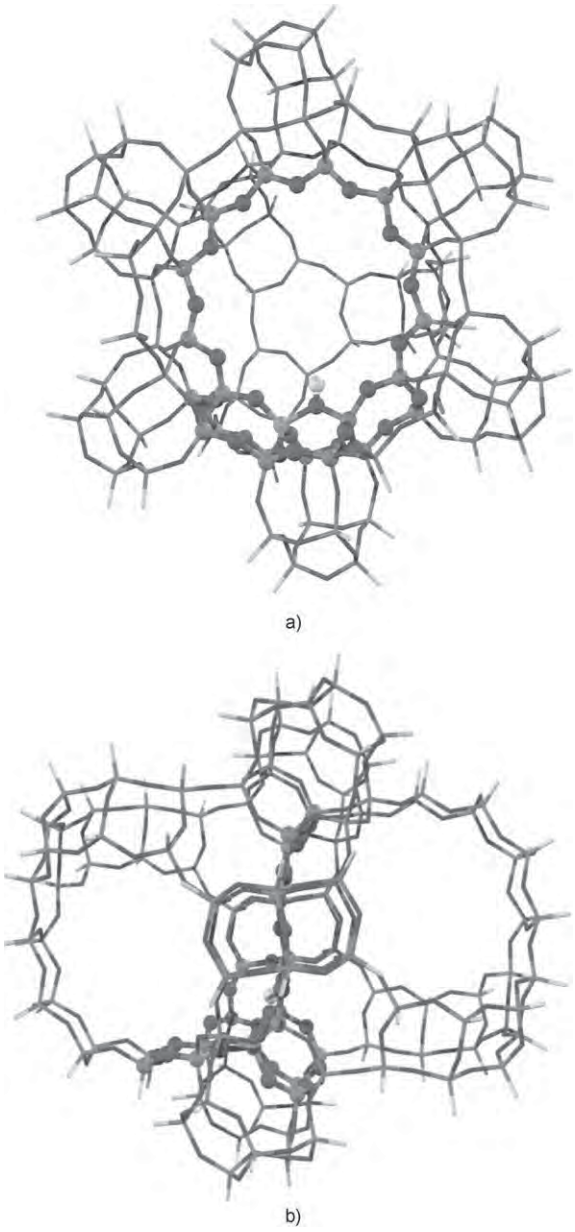

Figure 1. The 120T cluster models of H-FAU. Atoms belonging to the 21T quantum cluster are drawn as balls and sticks. a) Front view showing the 12-membered-ring window connecting the two supercages. b) Side view showing the two supercages connected to the 120T quantum cluster.

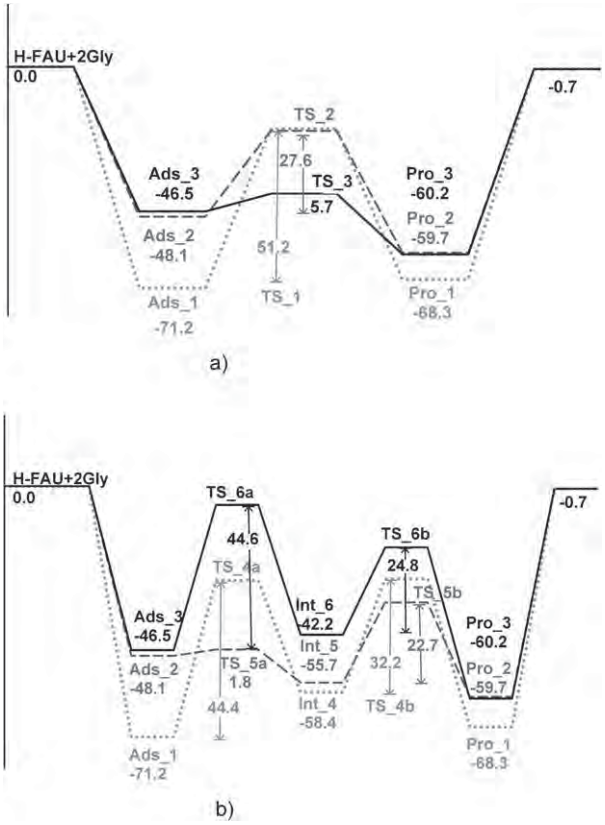

Figure 2. Energy profile (kcal mol^{-1}) of the peptide bond formation from different configurations of two glycine molecules interacting with H-FAU zeolite model 120T//21T calculated at the M08-HX/6-31G(d,p) level. Amino-bound configuration (•••••), carboxyl-bound configuration (– – –), and hydroxyl-bound configuration (——): a) concerted reaction mechanism; b) stepwise reaction mechanism.

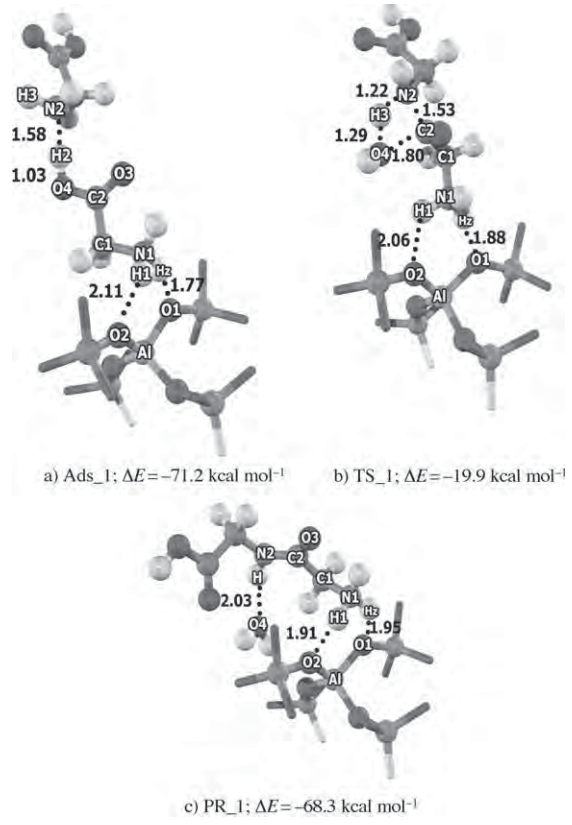

Figure 3. Optimized geometries of adsorption complexes, transition states, and products. a) Adsorption complex of the amino-bound configuration in the concerted reaction mechanism, Ads_1. b) Transition structure of the amino-bound configuration in the concerted reaction mechanism, TS_1. c) Adsorption complex of the products glycylglycine and water in the amino-bound configuration in the concerted reaction mechanism, Pro_1.

carboxyl carbon atom and the indirect transfer of a hydrogen atom from the nucleophilic amino group to a hydroxyl of another glycine molecule, which results in adsorbed glycylglycine and an adsorbed water molecule which is desorbed in the final step.

2.1.1. Interactions of Two Glycine Molecules in Different Configurations with H-FAU Zeolite

The calculated adsorption energies of two glycine molecules in different configurations on H-FAU zeolites are shown in the energy profile (Figure 2a) and in Table S1 in the Supporting Information, together with selected geometrical parameters.

The reaction proceeds as follows: First, two glycine molecules adsorb on the Brønsted acidic proton of the active zeolite site. This can occur via the amino group (amino-bound, Ads_1, Figure 3a), the carboxyl group (carboxyl-bound, Ads_2, Figure 4a) or the hydroxyl group (hydroxyl-bound, Ads_3, Figure 5a). In the first two configurations the adsorption (amino-bound and carboxyl-bound) of glycine is accompanied by a barrierless proton transfer from the active site to its C=O and $-NH_2$ groups. This causes the second hydroxyl group of glycine and the $-NH_3^+$ group to interact through two strong hydrogen bonds; the computed adsorption energies are −71.2 and −48.1 kcal mol^{-1}, respectively. In the hydroxyl-bound configuration glycine is adsorbed at the active site by hydrogen bonding between –OH of glycine and the Brønsted acidic proton. Its adsorption energy is −46.5 kcal mol^{-1}. It is difficult to directly compare calculated adsorption energies of glycine in zeolites with experimental results, and, to the best of our knowledge, there are no experimental data available on the glycine adsorption energy. The result for the amino-bound configuration can be compared with experimental data for ammonia which is protonated in zeolite with adsorption energies in the range of 24.9–25.6 kcal mol^{-1}.[18] Glycine is a more basic substance than NH_3. Moreover, the other glycine molecule is involved in the adsorption of the first one via hydrogen bonding between $-NH_3$ and the hydrogen atom of the carboxylic group of the first glycine, enhancing the adsorption energy of this configuration. Therefore, the adsorption energy of the amino-bound configuration over H-FAU should exceed that for ammonia, which agrees well with the known adsorption trend of this zeolite. The result shows that these adsorption energies are determined by both chemical (heat of protonation) and physical (confinement) factors. The latter, which arise from van der Waals interactions, cannot be ignored.

The first configuration is amino-bound (Ads_1, Figure 3a). Selected geometrical parameters of this configuration are pre-

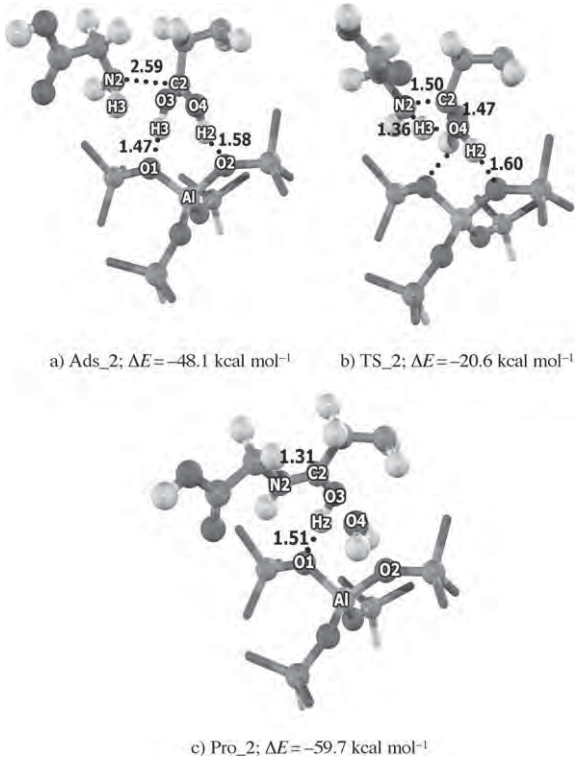

Figure 4. Optimized geometries of adsorption complexes, transition states, and products. a) Adsorption complex of the carboxyl-bound configuration in the concerted reaction mechanism, Ads_2. b) Transition structure of the carboxyl-bound configuration in the concerted reaction mechanism, TS_2. c) Adsorption complex of products glycylglycine and water of carboxyl-bound configuration in the concerted reaction mechanism, Pro_2.

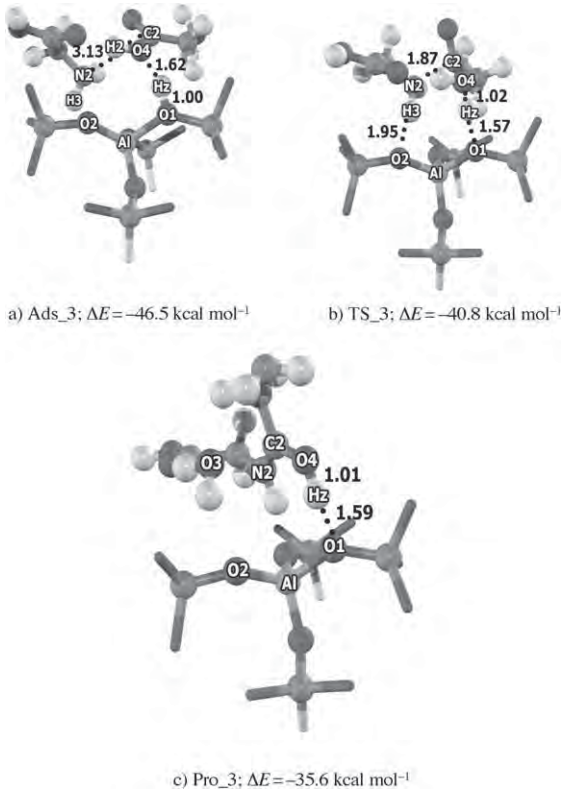

Figure 5. Optimized geometries of adsorption complexes, transition states, and products. a) Adsorption complex of the hydroxyl-bound configuration in the concerted reaction mechanism, Ads_3. b) Transition structure of the hydroxyl-bound configuration in the concerted reaction mechanism, TS_3. c) Adsorption complex of the products glycylglycine and water of the hydroxyl-bound configuration in the concerted reaction mechanism, Pro_3.

sented in Table S1 in the Supporting Information. The Brønsted acid of the zeolite O1–Hz bond is broken while the N1–Hz bond is formed. The O1···Hz distance in the amino configuration is about 1.77 Å. Both distances of N1–H1 and N1–Hz are virtually the same, indicating that there is a complete transfer of Brønsted acid. The second glycine is adsorbed by the hydrogen bond with a distance between H2···N2 of about 1.58 Å. The two hydrogen-bound adducts of glycine and zeolite (N1–Hz···O1 and N1–H1···O2) generate an "ion-pair-like structure" resulting in the highest adsorption energy of -71.2 kcal mol^{-1}.

For the carboxyl-bound configuration (Ads_2, Figure 4a), the adsorption of glycine involves a barrierless proton transfer from the active site to C=O. The O1–Hz bond distance of the Brønsted acidic proton is increased from 0.97 to 1.47 Å as compared to isolated H-FAU, indicating the weakening of the C=O bond. The C=O bond of glycine is elongated from 1.20 Å to 1.27 Å as compared to the isolated glycine molecule. The partial charge of the C atom changes from $+0.8$ in isolated glycine to $+0.9$ (Table 1). This shows that the catalyst facilitates the nucleophilic attack by the lone pair of the amine. Since the C2···N2 distance between the nitrogen atom of the $-NH_2$ group and this carbon atom (2.59 Å) is shorter than in the hydroxyl-bound configuration (3.13 Å) this co-adsorption complex is also stronger.

In the hydroxyl-bound configuration (Ads_3, Figure 5a) the hydrogen atom (H2) of the hydroxyl group of the first glycine points outward to interact with the oxygen atom (O5) of the carboxyl group of another glycine, with an O5···H2 distance of 1.58 Å and an O4–H2–O5 angle of 174.3°. The C2–O3 bond distance and the positive charge on the C atom at the reaction center are slightly increased with respect to the isolated glycine molecule. In summary, the carboxyl-bound configuration is more perturbed by the Brønsted acidic proton of H-FAU zeolite, explaining why the hydroxyl-bound configuration is the least stable one of the three configurations.

2.1.2. Peptide Bond Formation

The reaction pathways of the concerted mechanism for the three different configurations are shown in Figure S1 with selected geometries given in Table S1 of the Supporting Information. At the transition state of the amino-bound (TS_1, Figure 3b) and carboxyl-bound (TS_2, Figure 4b) configurations the concerted mechanism proceeds via four-center transition structures. This step is the nucleophilic attack of the lone electron pair of the amino group onto the carbon atom of the carboxyl group while simultaneously the proton transfer from the amino group to one of the oxygen atoms of the hydroxyl group takes place. The activation barriers in this step were cal-

Table 1. Activation barriers, ΔE_{ac} [kcal mol^{-1}], intrinsic rate constants for concerted and stepwise reaction mechanism, k, of peptide bond formation from two glycine molecules over H-FAU at 298 K [s^{-1}] and atomic charges, q(C), on the carbon atom of the carboxyl group of glycine at the reaction center (charges are in e).

	Concerted			Stepwise					
	Amino	Carboxyl	Hydroxyl	Amino		Carboxyl		Hydroxyl	
	TS_1	TS_2	TS_3	TS_4a	TS_4b	TS_5a	TS_5b	TS_6a	TS_6b
ΔE_{ac}	51.2	27.6	5.7	44.4	32.2	1.8	22.7	44.6	24.8
k	1.48×10^{-26}	6.37×10^{-9}	4.21×10^{3}	6.15×10^{-22}	1.95×10^{-9}	6.30×10^{10}	1.81×10^{-3}	2.35×10^{-20}	7.67×10^{-5}
q(C)	0.73	0.76	0.80	0.76	0.74	0.92	0.76	0.76	0.74

culated to be 51.2 and 27.6 kcal mol^{-1}, respectively, at which the adsorbed glycylglycine and a water molecule are formed.

In the transition state of the amino-bound configuration (TS_1, Figure 3b), C2 and N2 atoms form the peptide bond (C2···N2 distance: 1.53 Å) and the transfer of H3 from N2 to the oxygen atom of the hydroxyl group ends with an O4–H3 distance of 1.22 Å. The activation barrier of the amino-bound configuration, 51.2 kcal mol^{-1}, is similar to 47.7–52.7 kcal mol^{-1} for the uncatalyzed reaction of two glycine molecules obtained by MP2 calculations.[3h] This means that protonation of the amino group by the Brønsted acidic proton does not significantly enhance the electrophilicity of the C=O group. In summary, the high barrier is a consequence of the most stable adsorption configuration together with the strained four-center ring at the transition state.

The carboxyl-bound configuration is about 23.1 kcal mol^{-1} higher in adsorption energy. Since the transition state energy is similar, this brings the activation barrier down to 27.6 kcal mol^{-1} (Table 1). The transition structure is also a four-membered ring.

The hydroxyl-bound configuration is the least stable one and its transition state is also the lowest (TS_3, Figure 5b). The total activation barrier is therefore only 5.7 kcal mol^{-1}. The reason for such a low barrier is the presence of an eight-membered ring in the transition structure in which a double proton transfer occurs: one Brønsted acidic proton from the H-FAU zeolite toward the glycine OH group and the other one from NH_3 back to the H-FAU zeolite in order to regenerate the active site. The C–O2 distance is elongated from 1.37 Å to 2.05 Å and the peptide bond is generated by the C–N bond formation when the C···N distance decreases from 3.20 Å to 1.61 Å.

From the energetic data we calculated the intrinsic rate constants, k, to be 1.48×10^{-26}, 6.37×10^{-9}, and 4.21×10^{3} s^{-1} for the amino-bound, the carboxyl-bound, and the hydroxyl-bound configurations, respectively.

The peptide bond formation is endothermic with a reaction energy of 2.9 kcal mol^{-1} for the amino-bound configuration and exothermic with a reaction energy of 11.6 kcal mol^{-1} for the carboxyl-bound and 13.7 kcal mol^{-1} for the hydroxyl-bound configurations. The latter one is different from the first two because of the back donation of the proton from glycine to O4 instead of O3, which is the most stable position of the proton in H-FAU zeolite.[19] The endothermicity compares well with the value of 2.0–10.0 kcal mol^{-1} from a theoretical study of the uncatalyzed reaction reported by Jensen et al.[3h]

2.2. Stepwise Reaction Mechanism

Alternatively, the peptide bond formation of two glycine molecules can proceed via a stepwise mechanism [Eqs. (1)–(4)]:

$$2\,\text{Glycine} + \text{H-FAU} \rightarrow 2\,\text{Glycine–H-FAU} \quad (1)$$

$$2\,\text{Glycine–H-FAU} \rightarrow \text{Diol–H-FAU} \quad (2)$$

$$\text{Diol–H-FAU} \rightarrow \text{Glycylglycine–}H_2O\text{–H-FAU} \quad (3)$$

$$\text{Glycylglycine–}H_2O\text{–H-FAU} \rightarrow \text{Glycylglycine} + H_2O + \text{H-FAU} \quad (4)$$

First, step (1) is the adsorption of two glycine molecules on the active site of the H-FAU. Then, in step (2), the nucleophilic attack of the amino group on the carboxyl carbon atom coincides with the intramolecular hydrogen transfer in order to form a diolic intermediate. Step (3) involves the diolic intermediate and the intramolecular rearrangement to form glycylglycine and the water molecule adsorbed over H-FAU which is desorbed in the final step (4).

The energy profile of the reaction mechanisms from three starting orientations of the first glycine adsorption is shown in Figure 2b and selected geometric parameters are listed in Table S3 in the Supporting Information.

2.2.1. Interactions of Two Glycine Molecules in Different Configurations with H-FAU Zeolite

The same three configurations for the adsorbtion of two glycine molecules adsorbing on the active site are possible. Adsorption in the amino-bound (AD_1, Figure 3a), carboxyl-bound (AD_2, Figure 4a), and hydroxyl-bound (AD_3, Figure 5a) configuration is identical to the concerted mechanism discussed above. The adsorption energies are −71.2, −48.1, and −46.5 kcal mol^{-1} for the amino-bound, carboxyl-bound, and hydroxyl-bound glycine interaction, respectively.

2.2.2. Peptide Bond Formation

Starting from the amino-bound configurations, the peptide bond is generated simultaneously with hydrogen transfer in the four-membered transition structure (TS_4a, Figure 6a). The amino hydrogen atom from the second glycine is moved to the carboxyl oxygen atom on the first glycine as the C2–N2 bond is formed. At the first transition state, the C2···N2 dis-

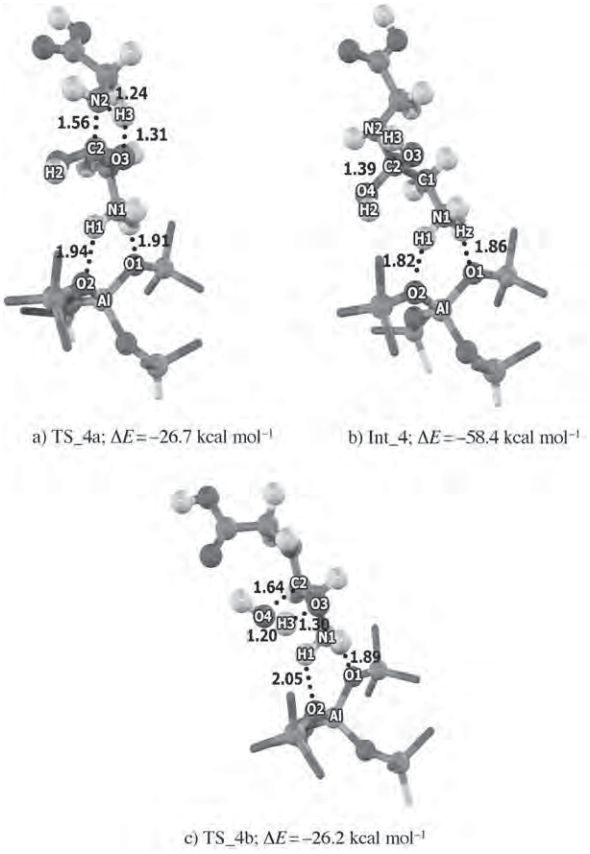

Figure 6. Optimized geometries of adsorption complexes, transition states, and products. a) First transition structure of the amino-bound configuration in the stepwise reaction mechanism, TS_4a. b) Intermediate of the amino-bound configuration in the stepwise reaction mechanism, Int_4. c) Second transition structure of the amino-bound configuration in the stepwise reaction mechanism, TS_4b.

For the carboxyl-bound configuration, the peptide formation involves only a nucleophilic attack of the amine nitrogen to the carboxyl carbon (TS_5a, Figure 7a). An activation energy of

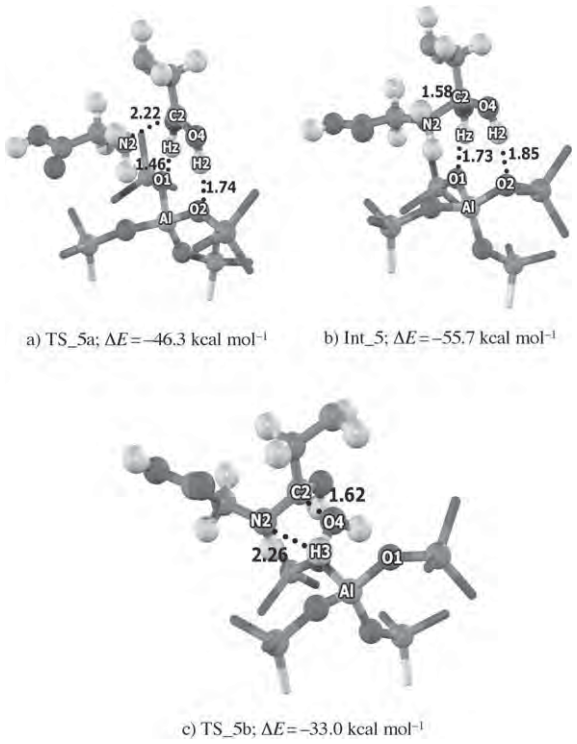

Figure 7. Optimized geometries of adsorption complexes, transition states, and products. a) First transition structure of the carboxyl-bound configuration in the stepwise reaction mechanism, TS_5a. b) Intermediate of the carboxyl-bound configuration in the stepwise reaction mechanism, Int_5. c) Second transition structure of the carboxyl-bound configuration in the stepwise reaction mechanism, TS_5b.

tance is 1.56 Å and N2–H3 is elongated to 1.24 Å. The activation barrier (44.4 kcal mol^{-1}) is smaller than for the hydrogen transfer in the concerted reaction mechanism (51.2 kcal mol^{-1}) from the amino group to the more basic oxygen atom of the carboxyl group and is preferred over the transfer to the less basic hydroxyl group. The diolic intermediate (Int_4, Figure 6b), with a tetrahedral sp^3 configuration on the carbon atom at the peptide bond, is produced and adsorbed over the deprotonated active site. Its energy is −58.4 kcal mol^{-1}.

At the second transition state (TS_4b, Figure 6c), water is eliminated from the planar four-membered ring transition structure and a distorted tetrahedral configuration at the carbon atom of the peptide bond of the diolic intermediate rearrangement is formed. Its activation energy is 32.2 kcal mol^{-1}. At the C2 atom previously linked to the N2 atom, H_2O is formed through hydrogen transfer from one hydroxyl group to the leaving one. The hydroxyl cleavage is accompanied by an extension of the C2–O4 distance from 1.39 Å to 1.64 Å and a contraction of the C–N bond from 1.43 Å to 1.39 Å. The water molecule is co-adsorbed between the framework and the newly formed glycylglycine (Pro_1). The relative energy of the product is −68.3 kcal mol^{-1}.

1.8 kcal mol^{-1} is required. The intermolecular C2···N2 distance is shortened to 2.22 Å while the reacting molecules move further from the active site by 1.46 Å. In the intermediate (Int_5, Figure 7b) the C2–N2 bond length is 1.58 Å and its energy is −55.7 kcal mol^{-1}. The intermediate consequently loses a water molecule through hydrogen abstraction from the amino group to the leaving group with an energy barrier of 22.7 kcal mol^{-1}. In the four-membered transition structure (TS_5b, Figure 7c) the N2–H3 bond length is extended to 2.26 Å and the O3–H4 distance is contracted to 0.96 Å. The departure of the hydroxyl group is promoted by a C2–O4 bond length of 1.62 Å. The final step is then again the co-adsorption of protonated glycylglycine (Pro_2) and water molecules over the zeolitic framework. The relative energy for this step is −59.7 kcal mol^{-1}.

Concerning the hydroxyl-bound configuration, no transfer of the zeolitic proton is involved in the first transition state (TS_6a, Figure 8a). The diolic intermediate (Int_6, Figure 8b) is generated via the four-membered transition state. The conversion, like for the amino-bound configuration discussed above, consists of the proton transfer and the formation of the intermolecular C2···N2 bond. The protonic H3 from the second glycine N2 moves towards O3 of the first glycine molecule as

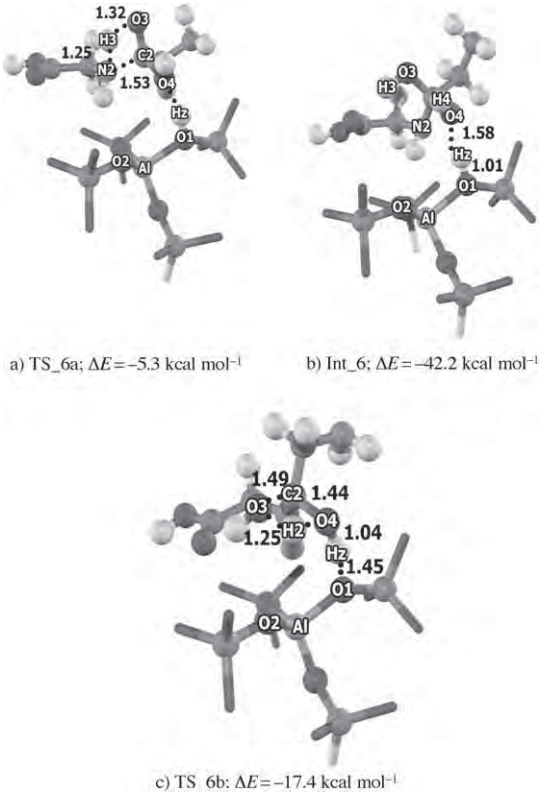

Figure 8. Optimized geometries of adsorption complexes, transition states, and products. a) First transition structure of the hydroxyl-bound configuration in the stepwise reaction mechanism, TS_6a. b) Intermediate of the hydroxyl-bound configuration in the stepwise reaction mechanism, Int_6. c) Second transition structure of the hydroxyl-bound configuration in the stepwise reaction mechanism, TS_6b.

shown in the distances of N2–H3 and O3–H3 of 1.25 Å and 1.32 Å, respectively. The C–O3 bond length is extended to 1.33 Å as O3 receives the proton H3. The intermolecular distance of C2–N2 is shortened from 3.13 Å to 1.53 Å. As the O1–Hz length is 1.01 Å and O4–Hz is 1.51 Å, the Brønsted proton is moving slightly closer to O2 of the first glycine and the reacting molecules are stabilized by adsorbing closer to the framework with a distance of 2.28 Å. At the adsorption complex of this configuration, the positive charge of the C atom at the reaction center (0.83) is in between the ones of the amino-bound and the carboxyl-bound configurations (0.82 and 0.890, respectively). The formed diolic intermediate has an adsorption energy of -42.15 kcal mol^{-1}. The four-membered transition structure (TS_6b, Figure 8c) is similar to the other configurations. The zeolitic proton is then transferred to the reacting molecule. The protonic H2 is abstracted from the leaving OH group and the transition structure adsorbs 2 Å closer to the framework. The process needs an activation energy of 24.8 kcal mol^{-1} yielding as products protonated glycylglycine (Pro_3, Figure 5d) and water located over the active region of the zeolite.

The barriers at the first transition state, 44.4, 1.8, and 44.6 kcal mol^{-1}, result in intrinsic rate constants, of 6.15×10^{-22}, 6.30×10^{10}, and 2.35×10^{-20} s^{-1} for the amino-bound, carboxyl-bound, and hydroxyl-bound configurations, respectively. The activation barriers of the second transition state for the three configurations (32.2, 22.7, and 24.8 kcal mol^{-1}, respectively) lead to intrinsic rate constants of 1.95×10^{-9}, 1.81×10^{-3}, and 7.67×10^{-5} s^{-1}, respectively.

For the stepwise reaction mechanism, the peptide bond formation is an exothermic reaction with a reaction energy of 0.7 kcal mol^{-1}. The energies required for desorption of the water molecule are 20.6, 14.2, and 15.0 kcal mol^{-1} for the amino-bound, carboxyl-bound, and the hydroxyl-bound configuration, respectively.

The complete energy profiles for the peptide formation mechanisms of glycine on H-FAU are shown in Figure 2. The three types of adsorptions, amino-bound, carboxyl-bound, and hydroxyl-bound have, for 2 glycine molecules, energies of -71.2, -48.4, and -46.5 kcal mol^{-1}, respectively. The reaction is exothermic. In the concerted mechanism, the activation energies are 51.2, 27.6, and 5.7 kcal mol^{-1} for amino-bound, carboxyl-bound, and hydroxyl-bound, respectively. In the stepwise mechanism the activation energies are 44.4 and 32.2 kcal mol^{-1} for amino-bound, 1.8 and 22.7 kcal mol^{-1} for carboxyl-bound and 44.6 and 24.8 kcal mol^{-1} for hydroxyl-bound configurations. The reaction via the amino-bound adsorbate in the concerted mechanism is the energetically preferred one.

3. Conclusions

The catalysis of peptide bond formation of two glycine molecules on H-FAU zeolite has been studied with density functional theory at the M08-HX level. There are three possible adsorption orientations for the first adsorbed glycine molecule which lead to different reaction pathways, these are, amino-bound, carboxyl-bound, and hydroxyl-bound configurations. For each of them, the concerted and the stepwise reaction mechanisms have been investigated.

In the concerted reaction, both the C–N bond formation and the release of water by N–H and C–O bond cleavages take place simultaneously. The catalytic activity of H-FAU zeolite influences the transition states for each reaction. The interaction to the Brønsted acidic proton increases the charge deficiency on the carbon atom of the carboxyl group and thus facilitates the nucleophilic attack by the lone electron pair of the amine.

The peptide bond is then generated by the dehydration of glycine taking place in a single step without a prior zwitterionic intermediate. The order of the activation barriers is amino-bound (51.2 kcal mol^{-1}) > carboxyl-bound (27.6 kcal mol^{-1}) > hydroxyl-bound (5.7 kcal mol^{-1}). The barrier height is significantly reduced by the presence of an eight-membered ring in the transition structure instead of the four-membered ring.

For the stepwise reaction mechanism, the reaction takes place through a stable diolic intermediate. Already in the first step, the C–N bond is formed through nucleophilic attack of the nitrogen on a carbon atom and simultaneous hydrogen transfer from ammonia to a carboxyl oxygen atom, except for the carboxyl-bound configuration, where a nucleophilic attack of the amine nitrogen on the carboxyl carbon was found.

In the second step, a water molecule is released by C–O and O–H bond cleavages. In contrast to the first mechanism, in which a hydrogen atom is transferred to hydroxyl oxygen from the ammonia, the stepwise reaction mechanism involves transfer of hydrogen to the carboxyl oxygen.

The concerted reaction mechanism should therefore dominate the overall reaction with an estimated activation barrier of 51.2 kcal mol^{-1}, starting from the amino-bound configuration. The overall reaction is predicted to be slightly endothermic.

Computational Methods

The cluster models of H-FAU are taken from the lattice structure of faujasite zeolite.[20] The active region consists of a 21T cluster, which is considered to be the smallest unit required to represent the acidic site of zeolite and the reactive molecules. In the 21T cluster, one of the silicon atoms in the faujasite zeolite is substituted by an aluminum atom, and a proton is added to one of the bridging oxygen atoms bonded directly to the aluminum atom, conventionally called the O1 position.[19,20] During the structure optimization, only the 5T part of the active site region [(≡SiO)$_2$(H)Al(OSi≡)$_2$] and the adsorbates are allowed to relax while the rest of the active region is fixed at the crystallographic coordinates. To represent the confinement effect of the zeolite pore structure, the extended structure of a 120T cluster (Figure 1) which includes two supercages is used in single point calculations. It is assumed that these models for the H-FAU zeolites are large enough to cover all the important framework effects that act on both the active site and on the adsorbates. Attempts have been made to demonstrate that the geometry constraints imposed in this work do not influence the results and the reliability of the M08-HX functional was compared with MP2 calculations. Some test calculations on glycine over the H-FAU zeolite have been performed relaxing 5T and 8T atoms (see Table S4 in the Supporting Information). All calculations were performed by means of the M08-HX density functional[21] and the 6-31G(d,p) basis set. For the transition structures, frequency calculations were performed in order to check whether the imaginary frequency mode corresponds to the reaction coordinate.

Atomic charges were computed from the natural population analysis (NPA). All calculations were performed using the Gaussian 03 code with the Minnesota density functionals module 3.1 by Zhao and Truhlar incorporated.[16a,22]

In order to analyze the kinetics of the reaction, classical transition state theory was used to derive the intrinsic rate constants k. They were calculated within the harmonic oscillator–rigid rotor approximation [Eq. (5)]:

$$k(T) = \frac{K_B T}{h} e^{-\Delta^{\neq} G^0/RT} \quad (5)$$

where k_B, T, h, $\Delta^{\neq}G^0$, and R are the Boltzmann constant, the temperature of the system (taken to be 298 K), Planck's constant, Gibbs free energy of activation, and the gas constant, respectively.

Acknowledgements

This work was supported in part by grants from the National Science and Technology Development Agency (2009 NSTDA Chair Professor funded by the Crown Property Bureau under the management of the National Science and Technology Development Agency and NANOTEC Center of Excellence funded by the National Nanotechnology Center), Kasetsart University Research and Development Institute (KURDI), the Thailand Research Fund (TRF), and the Commission on Higher Education, Ministry of Education (the "National Research University Project of Thailand (NRU)" and the "National Center of Excellence for Petroleum, Petrochemical and Advanced Materials (NCE-PPAM)"). Support from the Graduate School Kasetsart University and from the RFBR-FWF projects 09-03-91001-a and I200-N19 is also acknowledged. The authors are grateful to Donald G. Truhlar and Yan Zhao for their support with the M08-HX functional. We thank P. Khongpracha for helpful suggestions.

Keywords: density functional calculations · dipeptide · glycine · reaction mechanisms · zeolites

[1] a) J. Liu, Z. Cao, Y. Lu, *Chem. Rev.* **2009**, *109*, 1948–1998; b) Y. Ura, J. M. Beierle, L. J. Leman, L. E. Orgel, M. R. Ghadiri, *Science* **2009**, *325*, 73–77; c) K. J. Waldron, N. J. Robinson, *Nat. Rev. Microbiol.* **2009**, *7*, 25–35; d) I. Ben-Gera, G. Zimmermann, *Nature* **1964**, *202*, 1007–1008.

[2] a) L. E. Orgel, *Trends Biochem. Sci.* **1998**, *23*, 491–495; b) P. Davies, *Sci. Prog.* **2001**, *84*, 17–29; c) P. Davies, *Sci. Prog.* **2001**, *84*, 1–16.

[3] a) J. D. Bernal, *The Physical Basis of Life*, Routledge and Kegan Paul, London, **1951**; b) B. K. G. Theng, *The Chemistry of Clay-Organic Reactions*, Wiley, New York, **1974**; c) M. J. Gresser, W. P. Jencks, *J. Am. Chem. Soc.* **1977**, *99*, 6963–6970; d) C. C. Yang, W. P. Jencks, *J. Am. Chem. Soc.* **1988**, *110*, 2972–2973; e) M. M. Cox, W. P. Jencks, *J. Am. Chem. Soc.* **1981**, *103*, 572–580; f) A. C. Satterthwait, W. P. Jencks, *J. Am. Chem. Soc.* **1974**, *96*, 7018–7031; g) T. Oie, G. H. Loew, S. K. Burt, J. S. Binkley, R. D. MacElroy, *J. Am. Chem. Soc.* **1982**, *104*, 6169–6174; h) J. H. Jensen, K. K. Baldridge, M. S. Gordon, *J. Phys. Chem.* **1992**, *96*, 8340–8351.

[4] H. Yang, S.-Y. Fung, M. Pritzker, P. Chen, *Langmuir* **2009**, *25*, 7773–7777.

[5] J. Bujdak, B. M. Rode, *React. Kinet. Catal. Lett.* **1997**, *62*, 281–286.

[6] a) K. I. Zamaraev, V. N. Romannikov, R. I. Salganik, W. A. Wlassoff, V. V. Khramtsov, *Origins Life Evol. Biosphere* **1997**, *27*, 325–337; b) M. Meng, L. Stievano, J.-F. Lambert, *Langmuir* **2004**, *20*, 914–923; c) N. Lahav, D. White, S. Chang, *Science* **1978**, *201*, 67–69; d) M. Rao, D. G. Odom, J. Oro, *J. Mol. Evol.* **1980**, *15*, 317–331; e) A. J. A. Aquino, D. Tunega, M. H. Gerzabek, H. Lischka, *J. Phys. Chem. B* **2004**, *108*, 10120–10130.

[7] a) V. A. Basiuk, T. Y. Gromovoy, V. G. Golovaty, A. M. Glukhoi, *Origins Life Evol. Biosphere* **1991**, *20*, 483–498; b) J. Bujdák, B. M. Rode, *J. Mol. Evol.* **1997**, *45*, 457–466; c) J. Bujdak, B. M. Rode, *J. Mol. Catal. A* **1999**, *144*, 129–136; d) A. Rimola, L. Rodriguez-Santiago, P. Ugliengo, M. Sodupe, *J. Phys. Chem. B* **2007**, *111*, 5740–5747.

[8] a) J. E. Krohn, M. Tsapatsis, *Langmuir* **2005**, *21*, 8743–8750; b) J. E. Krohn, M. Tsapatsis, *Langmuir* **2006**, *22*, 9350–9356; c) F. Xu, Y. Wang, X. Wang, Y. Zhang, Y. Tang, P. Yang, *Adv. Mater.* **2003**, *15*, 1751–1753; d) S. Munsch, M. Hartmann, S. Ernst, *Chem. Commun.* **2001**, 1978–1979.

[9] G.-W. Xing, X.-W. Li, G.-L. Tian, Y.-H. Ye, *Tetrahedron* **2000**, *56*, 3517–3522.

[10] a) Y. Cui, Q. Wei, H. Park, C. M. Lieber, *Science* **2001**, *293*, 1289–1292; b) J. Kong, N. R. Franklin, C. Zhou, M. G. Chapline, S. Peng, K. Cho, H. Dailt, *Science* **2000**, *287*, 622–625.

[11] A. Rimola, S. Tosoni, M. Sodupe, P. Ugliengo, *Chem. Phys. Lett.* **2005**, *408*, 295–301.

[12] A. Rimola, M. Sodupe, P. Ugliengo, *J. Am. Chem. Soc.* **2007**, *129*, 8333–8344.

[13] R. Z. Khaliullin, A. T. Bell, V. B. Kazansky, *J. Phys. Chem. A* **2001**, *105*, 10454–10461.

[14] a) P. E. Sinclair, A. de Vries, P. Sherwood, C. R. A. Catlow, R. A. van Santen, *J. Chem. Soc. Faraday Trans.* **1998**, *94*, 3401–3408; b) M. Brändle, J. Sauer, *J. Am. Chem. Soc.* **1998**, *120*, 1556–1570; c) S. P. Greatbanks, I. H. Hillier, N. A. Burton, P. Sherwood, *J. Chem. Phys.* **1996**, *105*, 3770–3776; d) J. Limtrakul, T. Nanok, S. Jungsuttiwong, P. Khongpracha, T. N. Truong, *Chem. Phys. Lett.* **2001**, *349*, 161–166; e) T. Maihom, B. Boekfa, J. Sirijaraensre, T. Nanok, M. Probst, J. Limtrakul, *J. Phys. Chem. C* **2009**,

113, 6654 – 6662; f) T. Maihom, S. Namuangruk, T. Nanok, J. Limtrakul, *J. Phys. Chem. C* **2008**, *112*, 12914 – 12920; g) P. Treesukol, K. Srisuk, J. Limtrakul, T. N. Truong, *J. Phys. Chem. B* **2005**, *109*, 11940 – 11945; h) P. Pantu, S. Pabchanda, J. Limtrakul, *ChemPhysChem* **2004**, *5*, 1901 – 1906; i) B. Boekfa, S. Choomwattana, P. Khongpracha, J. Limtrakul, *Langmuir* **2009**, *25*, 12990 – 12999.

[15] a) S. Yuan, J. Wang, Y.-B. Duan, Y.-W. Li, H. Jiao, *J. Mol. Catal. A* **2006**, *256*, 130 – 137; b) A. Waclaw, K. Nowinska, W. Schwieger, *Appl. Catal. A* **2004**, *270*, 151 – 156; c) S. Kasuriya, S. Namuangruk, P. Treesukol, M. Tirtowidjojo, J. Limtrakul, *J. Catal.* **2003**, *219*, 320 – 328; d) K. Bobuatong, J. Limtrakul, *Appl. Catal. A* **2003**, *253*, 49 – 64; e) S. Namuangruk, P. Pantu, J. Limtrakul, *J. Catal.* **2004**, *225*, 523 – 530; f) B. Boekfa, P. Pantu, J. Limtrakul, *J. Mol. Struct.* **2008**, *889*, 81 – 88; g) C. Tuma, J. Sauer, *Phys. Chem. Chem. Phys.* **2006**, *8*, 3955 – 3965.

[16] a) Y. Zhao, D. G. Truhlar, *Theor. Chem. Acc.* **2008**, *120*, 215 – 241; b) Y. Zhao, D. G. Truhlar, *J. Phys. Chem. C* **2008**, *112*, 6860 – 6868.

[17] a) C. Kumsapaya, K. Bobuatong, P. Khongpracha, Y. Tantirungrotechai, J. Limtrakul, *J. Phys. Chem. C* **2009**, *113*, 16128 – 16137; b) B. Boekfa, P. Pantu, M. Probst, J. Limtrakul, *J. Phys. Chem. C* **2010**, *114*, 15061 – 15067; c) S. Wannakao, B. Boekfa, P. Khongpracha, M. Probst, J. Limtrakul, *ChemPhysChem* **2010**, *11*, 3432 – 3438.

[18] H. G. Karge, V. Dondur, J. Weitkamp, *J. Phys. Chem.* **1991**, *95*, 283 – 288.

[19] J.-R. Hill, C. M. Freeman, B. Delley, *J. Phys. Chem. A* **1999**, *103*, 3772 – 3777.

[20] D. H. Olson, E. Dempsey, *J. Catal.* **1969**, *13*, 221 – 231.

[21] a) Y. Zhao, D. G. Truhlar, *J. Chem. Theory Comput.* **2008**, *4*, 1849 – 1868; b) Y. Zhao, D. G. Truhlar, *J. Chem. Theory Comput.* **2011**, *7*, 669 – 676.

[22] *Gaussian 03* (*Revision B.05*), M. J. Frisch, G. W. Trucks, H. B. Schlegel, G. E. Scuseria, M. A. Robb, J. R. Cheeseman, J. A. Montgomery, Jr., T. Vreven, K. N. Kudin, J. C. Burant, J. M. Millam, S. S. Iyengar, J. Tomasi, V. Barone, B. Mennucci, M. Cossi, G. Scalmani, N. Rega, G. A. Petersson, H. Nakatsuji, M. Hada, M. Ehara, K. Toyota, R. Fukuda, J. Hasegawa, M. Ishida, T. Nakajima, Y. Honda, O. Kitao, H. Nakai, M. Klene, X. Li, J. E. Knox, H. P. Hratchian, J. B. Cross, C. Adamo, J. Jaramillo, R. Gomperts, R. E. Stratmann, O. Yazyev, A. J. Austin, R. Cammi, C. Pomelli, J. W. Ochterski, P. Y. Ayala, K. Morokuma, G. A. Voth, P. Salvador, J. J. Dannenberg, V. G. Zakrzewski, S. Dapprich, A. D. Daniels, M. C. Strain, O. Farkas, D. K. Malick, A. D. Rabuck, K. Raghavachari, J. B. Foresman, J. V. Ortiz, Q. Cui, A. G. Baboul, S. Clifford, J. Cioslowski, B. B. Stefanov, G. Liu, A. Liashenko, P. Piskorz, I. Komaromi, R. L. Martin, D. J. Fox, T. Keith, M. A. Al-Laham, C. Y. Peng, A. Nanayakkara, M. Challacombe, P. M. W. Gill, B. Johnson, W. Chen, M. W. Wong, C. Gonzalez, J. A. Pople, Gaussian, Inc., Pittsburgh, PA, **2003**.

Received: January 18, 2011
Published online on June 22, 2011

THE JOURNAL OF PHYSICAL CHEMISTRY A

ARTICLE

pubs.acs.org/JPCA

Density Functional Theory Study of the Carbonyl-ene Reaction of Encapsulated Formaldehyde in Cu(I), Ag(I), and Au(I) Exchanged FAU Zeolites

Sippakorn Wannakao,[†,‡,§] Pipat Khongpracha,[†,‡,§] and Jumras Limtrakul*[,†,‡,§]

[†]Laboratory for Computational and Applied Chemistry, Department of Chemistry, Faculty of Science and Center of Nanotechnology, Kasetsart University Research and Development Institute, Kasetsart University, Bangkok 10900, Thailand

[‡]Center for Advanced Studies in Nanotechnology and Its Applications in Chemical, Food and Agricultural Industries, Kasetsart University, Bangkok 10900, Thailand

[§]NANOTEC Center of Excellence, National Nanotechnology Center, Kasetsart University, Bangkok 10900, Thailand

Supporting Information

ABSTRACT: Carbonyl-ene reactions, which involve C−C bond formation, are essential in many chemical syntheses. The formaldehyde−propene reaction catalyzed by several of the group 11 metal cations, Cu^+, Ag^+, and Au^+ exchanged on the faujasite zeolite (metal-FAU) has been investigated by density functional theory at the M06-L/6-31G(d,p) level. The Au-FAU exhibits a higher activity than the others due to the high charge transfer between the Au and the reactant molecules, even though it is located at a negatively charged site of the zeolite. This site enables it to compensate for the charge of the Au^+ ion. The NBO analysis reveals that the 6s orbital of the Au atom plays an important role, inducing a charge on the probe molecules. Moreover, the effect of the zeolite framework makes the Au-FAU more active than the others by stabilizing the high charge induced transition structure. The activation energy of the reaction catalyzed by Au-FAU is 13.0 kcal/mol whereas that of Cu and Ag-FAU is found to be around 17 kcal/mol. The product desorption needs to be improved for Au-FAU; however, we suggest that catalysts with high charge transfer might provide a promising activity.

1. INTRODUCTION

Reactions involving carbon−carbon bond formation are essential for most chemical upgrading processes. Among the well-known C−C bond formations, the carbonyl-ene reaction is one of the top choices for synthesis.[1,2] The carbonyl-ene reaction is induced by Lewis acid[3] and generally requires a strongly electrophilic carbonyl compound. The reaction of formaldehyde and propene is an example of the carbonyl-ene reaction that yields as a product 3-buten-1-ol. This product can be used in chemical processes, e.g., the copolymerization of propylene for producing polypropylene. In addition, the formaldehyde−propene reaction is involved in the synthesis of tetrahydrofuran, one of the most popular organic solvents in the laboratory.

Because of its low boiling point (−19.5 °C), formaldehyde is difficult to handle. Moreover, it rapidly polymerizes to solid paraformaldehyde and trioxane. Then, its shelf life is quite short. To retain formaldehyde in its monomer state, Lewis acid treatment is used to depolymerize the polymer form. Unfortunately, the treatment causes problems of corrosion, handling, and toxic waste, making it environmentally unfriendly. For these reasons, formaldehyde has become limited in its application for organic synthesis. Finding storage materials that retain the monomeric formaldehyde should be a way for solving these problems.

Porous materials such as zeolites and metal organic frameworks (MOF),[4−11] a new type of designable material, widely used as gas storage and separation materials, are environmentally friendly candidates for formaldehyde storage. Successful utilization of a porous material for formaldehyde storage was achieved by Okachi et al.[12] in 2004. These authors found that Na/faujasite zeolite suppresses the decomposition and self-polymerization of formaldehyde while its reactivity toward nucleophiles remains the same. Recently, Tomita et al.[13] have theoretically demonstrated that formaldehyde does not tend to self-polymerize in alkaline-exchanged faujasite zeolite. Our previous ONIOM calculation of the formaldehyde-propene reaction on Na-exchanged faujasite zeolite has revealed that alkaline-exchanged zeolite can significantly reduce the reaction barrier in the reaction mechanism

Special Issue: Richard F. W. Bader Festschrift

Received: March 2, 2011
Revised: September 10, 2011
Published: September 26, 2011

compared to an uncatalyzed process.[14] Thus, it can be suggested not only that zeolite can be used for storage but that alkaline-exchanged zeolite can also enable catalyzation of this reaction. Zeolite can be used for not only these purposes but also metal organic frameworks.

In our recent study, the formaldehyde−propene reaction in MOF-11, in which the active site is Cu(II) in the paddle wheel unit ($Cu_2(CO_2)_4$), was theoretically investigated.[15] It was found that MOF-11 can reduce the activation energy of the reaction from 34.3 to 24.1 kcal/mol. A bare Cu^+, however, is much more reactive with an activation barrier of only 6.4 kcal/mol. Therefore, MOF-11 can be utilized in catalytic applications only with a moderated activity. Finding a structure that retains the high activity of the metal would be promising, not only for its academic interest but also for industrial applications.

Metals loaded on zeolites have been widely studied as their properties can be fine-tuned by varying the metals. Bell and coworkers have synthesized and characterized Cu(I)-exchange zeolite Y for catalyzing the dimethyl carbonate (DMC) reaction from oxidative carbonylation of methanol.[16−19] They found that Cu−Y provided a high reactivity for the reaction. Moreover, Ag(I) and Au nanoparticles exhibit good performances in reactions involving C−C bond formation.[20−22] The monomeric Au cation on zeolites has been successfully prepared,[23−29] and many theoretical studies have been conducted.[30−35] Ichikawa et al.[23,25] used CO adsorption and Fourier transform IR (FTIR) to study Au/NaY, Au/Na-mordenite, and Au/Na-ZSM-5 and concluded that Au(I) is the dominant active site for the decomposition of NO with CO and the water gas shift. Fierro-Gonzalez and Gates[26] have also synthesized and characterized monomeric Au(I) and Au(III) in zeolite NaY without zero valence Au clusters.

There is often little correlation between the catalytic activities of different cations on many reactions, even if the ions are chemically related. Thus, each cation has to be tested either theoretically or experimentally for any reaction of interest. Theoretical studies not only save a great deal of time and money compared to complicated experimental screening, but they also provide insight into why a particular cation has a higher activity, and thus a guide to synthesize the catalyst with the required characteristics. As a consequence, in this work, we investigate the formaldehyde-propene carbonyl-ene reaction on the Cu, Ag, and Au cation exchanged on FAU zeolite (M-FAU, M = Cu, Ag, and Au) by means of density functional theory with the M06-L functional.[36−38] Even though metal cations exchanged in zeolites have been widely studied, to the best of our knowledge, there is no theoretical study for the C−C bond formation processes with this series of metal-exchanged zeolites as a catalyst. This work thus investigates the possibility of using group 11 metal-exchanged zeolites as highly active catalysts for the carbonyl-ene reaction. We also make a comparison with other Lewis acid catatlysts (MOF-11 and Na-FAU).

2. MODELS AND METHOD

The faujasite zeolite is composed of sodalite building blocks that contain 192T (T is either a Si or an Al atom) atoms in the supercage unit cell.[39] The Cu(I) cation can be located in many different cation-exchange sites, as shown in Figure 1. Site I is located in the hexagonal prism, which is not accessible for the reaction to proceed. Site II is inside the FAU supercage on the hexagonal face and site III is also located in the supercage, but on the four-membered ring of the sodalite cage. An experimental

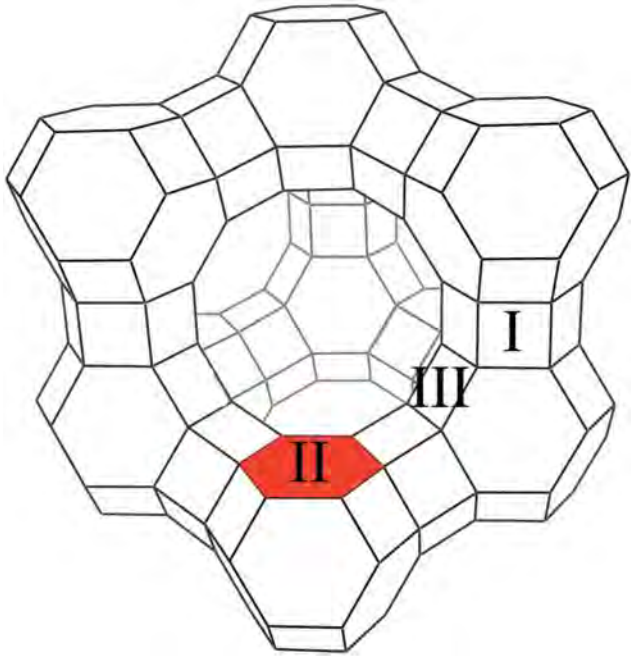

Figure 1. Cation exchanging sites of the faujasite zeolite (see text for explanations).

study by Drake et al.[40] shows that Cu(I) can replace all acidic protons of the H−Y zeolite, resulting in a ratio Cu/Al = 1.0. Moreover, these authors also concluded that site II is the site most occupied by Cu^+ ion. Site II was therefore chosen to represent the catalytically active site in this study. Furthermore, this site has also been studied for other metal cations in several previous reports.[19,30]

The selected 16T model (Figure 2) of site II consists of 6T from the hexagonal ring and the side extended four-membered rings to avoid interaction between terminating hydrogen atoms. To avoid the Al−OH group, which was not observed in experiments, Si atoms adjacent to the Al atom were included in the model. The metal ions were located in the middle of the hexagonal ring, as shown in Figure 2. Geometry optimizations were performed at the M06-L/6-31G(d,p) level of theory and Stuttgart ECP[41] were employed for the Cu, Ag, and Au atoms. The M06-L functional has been tested and found to be accurate and affordable from the Minnesota functional series for the energetic properties of systems containing transition metals and even in more sophisticated cases such as metal oxide systems.[37,42−47] Recent studies of chemical reactions regarding zeolite systems has demonstrated that this well calibrated series of functionals provides results in good agreement with experimental values.[48−51] Moreover, a theoretical study of the chemical reaction on transition metal oxide-exchanged zeolite shows that the M06-L functional provides acceptable results for both structure and adsorption energies when compared to the MP2[52] method. To avoid too many degrees of freedom during the optimization, only the metal atoms and the 4T region with the three oxygen atoms adjacent to the metal atoms ($-Si_3O_3Al-$) were allowed to relax while the rest were kept fixed at their crystallographic positions. Transition states were located by the Berny algorithm[53,54] and confirmed by normal-mode analyses that provide only one imaginary frequency corresponding to the designated reaction coordination. Total spin was kept to be singlet

Figure 2. Structures of the Cu-, Ag-, and Au-FAU catalysts obtained from M06-L/6-31G(d,p) optimizations.

Table 1. Partial Electronic Charges of the Metal Atom and the Probe Molecules

		NPA-charges/e		
step		Cu-FAU	Ag-FAU	Au-FAU
catalysts	metal	0.682	0.759	0.699
Ads	C	0.308	0.259	0.327
	O	−0.584	−0.547	−0.557
	HCHO	0.052	0.044	0.141
	metal	0.656	0.707	0.521
CoAds	C	0.217	0.266	0.284
	O	−0.617	−0.589	−0.593
	CoAds	−0.004	0.066	0.161
	metal	0.741	0.666	0.506
TS	C	−0.047	−0.040	−0.070
	O	−0.831	−0.786	−0.759
	TS	0.073	0.077	0.268
	metal	0.632	0.679	0.411

during the reaction pathway for all systems. Interaction between probe molecules and catalysts are reported as relative energies that relative to energies of isolated reactants which can be calculated by the equation, $E = E_{complex} - (E_{reactant1} + E_{reactant2} + ...)$. The charge distributions and population analyses of the complexes were also determined at the M06-L/6-31G(d,p) level of theory by the natural atomic orbital (NAO) and natural bond orbital analysis (NBO) methods.[55,56] The framework was then extended to 120T, covering a supercage structure of FAU, to perform the single point calculation with the same level of theory as the one used for evaluating the effect of the zeolite framework. Zero-point energies were also corrected for the quantum cluster of the 16T model of the zeolite system (Table S3, Supporting Information). All quantum chemical calculations were carried out with the Gaussian 03[57] code, modified to incorporate the Minnesota Density Functionals module 3.1 by Zhao and Truhlar.

3. RESULTS AND DISCUSSION

3.1. Metal-Exchanged Faujasite Zeolite. The optimized structures of the Cu-FAU, Ag-FAU, and Au-FAU models used in this study are illustrated in Figure 2. Partial charges and the electronic configuration of the systems are documented in Table 1 and Table S2 (Supporting Information), respectively. The calculated charges were found to be +0.682e, +0.759e, and +0.699e for the Cu, Ag, and Au atoms, respectively. This shows the compensation between the metal charges and the surrounding oxygen atoms in the 6-membered ring. The complexation energies between the metal cations and the zeolite were found to be −179.2, −147.9, and −154.2 kcal/mol for Cu-, Ag-, and Au-FAU, respectively. It is worth noting that the complexation energies with the amount of charge transfer between M^+ and the zeolite framework was revealed by the charge reduction of the exchanged cations ($Cu^+ > Au^+ > Ag^+$).

The structures and mechanisms of the encapsulated formaldehyde metal-FAU carbonyl-ene reaction are now investigated. The symbol M@S signifies that the molecule M is adsorbed on the active site S. The proposed reaction mechanism is similar to those of our previous calculations for Na-FAU catalyst as well as for MOF-11. The reaction is assumed to proceed on a concerted mechanism in which both reactants are involved in the rate limiting step. All optimized geometries are given in the Supporting Information, Table S1.

3.2. Encapsulated Formaldehyde in Metal-FAU. To keep formaldehyde in its monomer state and to keep it activated, the reaction begins with the encapsulation of formaldehyde on the metal-FAU catalysts like in the previous studies.[14,15] The oxygen atom of formaldehyde interacts with the Lewis acid metal site of the catalyst. The C−O distance is elongated from 1.20 to 1.23 Å, which is the same as in the alkaline exchange and the MOF-11 studies. The adsorption energies are found to be −16.9, −18.0, and −20.0 kcal/mol for Cu-, Ag-, and Au-FAU, respectively. From the NBO calculations we find highly ionic bonding characteristics between the Au and the O atom of the formaldehyde molecule, formed by the 6s orbital (8.45%) of the Au atom and the 2p orbital (91.55%) of the O atom (Figure 3). The interaction between the O and the Cu or Ag contains a contribution from the lone pair electron of the O atom to the metal (Figure 4). An electron back-donation from the metal to formaldehyde could not be observed at any significant level. The total occupancy of the Cu and Ag atoms were nearly unchanged whereas the Au atom received more electrons at the 6s orbital after the formaldehyde was encapsulated. This might be due to

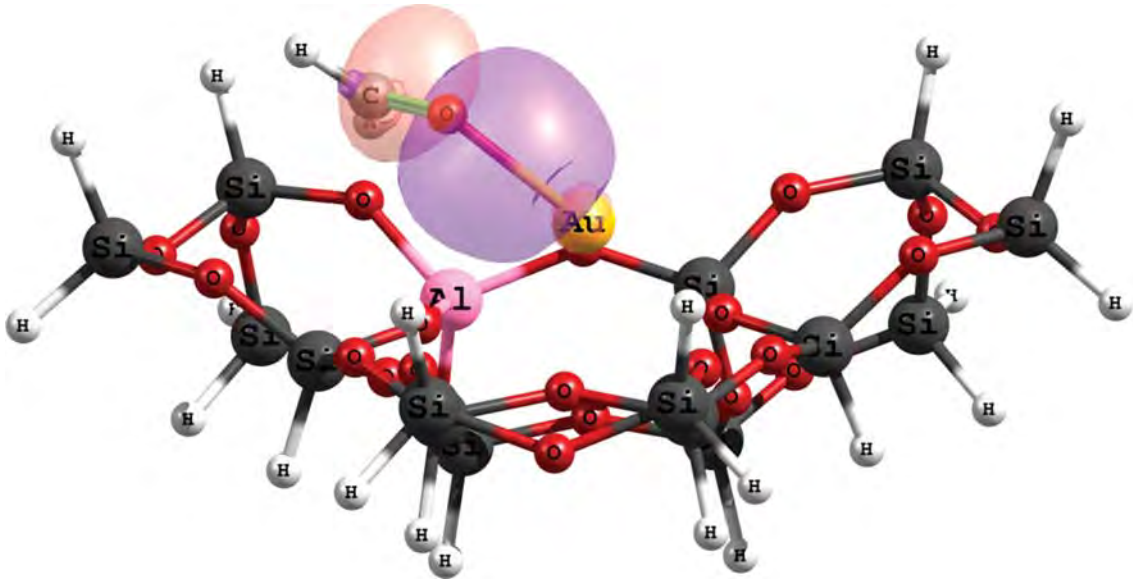

Figure 3. Illustration of the Au−O bonding character with contributions from (mostly) the 6s orbital of Au and the 2p orbital of the O atom. From the NBO calculations with the M06-L/6-31G(d,p) method.

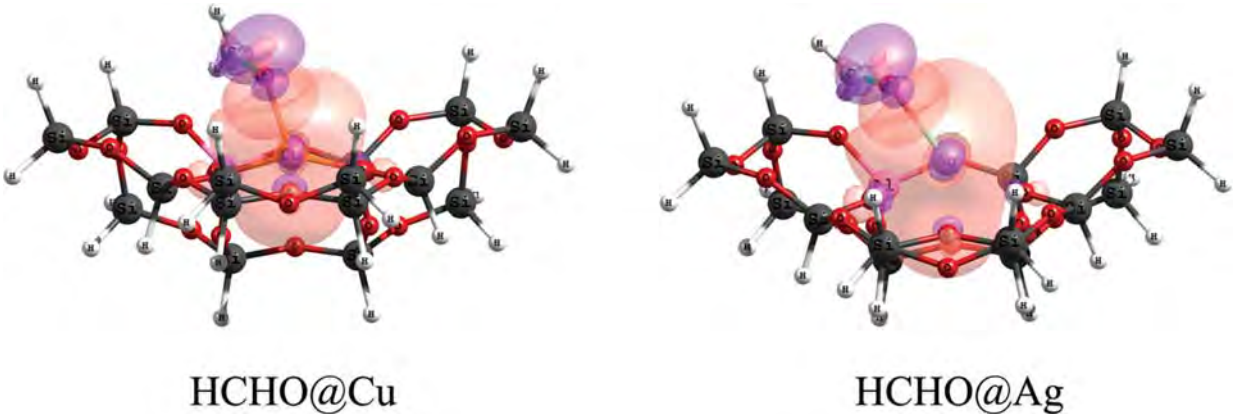

Figure 4. Illustration of the interaction between the 2p orbital of formaldehyde and the 4s orbital of Cu (left)/the 5s orbital of the Ag (right), analyzed from the NBO calculation with the M06-L/6-31G(d,p) method. The isosurface value is ±0.03 au.

the relativistic effect of a heavy metal atom like Au. Moreover, this may be the origin of the shorter length of the Au−O bond (2.26 Å) compared with the Ag−O bond (2.36 Å). The short Cu−O bond (2.07 Å) might originate from the smallest cation size of Cu when compared to that of others. The charge of the formaldehyde carbon atom was found to be +0.308e, +0.259e, and +0.327e in the Cu-, Ag-, and Au-FAU system, respectively. This indicates that Au-FAU causes the formaldehyde molecule to become an active electrophile, as a result the carbon of the HCHO@Au-FAU system favors the nucleophilic attack of another molecule.

An attempt has been made for predicting the carbonyl (CO) stretch vibrational frequencies of formaldehyde and its complexes with different Cu-, Ag-, and Au-FAU zeolites. Without scaling factors, our calculated CO vibrational frequencies of metal(I)/FAU complexes are predicted to be 1723, 1784, and 1747 cm^{-1} for Cu-FAU, Ag-FAU, and Au-FAU, respectively. For all the studied complexes, the carbonyl (CO) stretch vibration is red-shifted by 85−146 cm^{-1} with respect to the CO vibrational frequency (1869 cm^{-1}) in formaldehyde (cf. Table S4, Supporting Information). These values are higher than those calculated and experimental values for Cu and Ag embedded in other related types of zeolite, i.e., Cu and Ag-ZSM-5 reported by Datka et al.[58,59] However, our calculated C−O distances are longer for Cu- and Ag-FAU cases. This reflects one of the reasons the frequencies of our FAU zeolite are over shifted when compared to those values obtained from ZSM-5.

Metal cations without the zeolite structure (bare-metal cations) were investigated for comparison. The metal cations bind to the formaldehyde molecule with adsorption energies of −48.8, −32.2, and −38.8 kcal/mol for Cu^+, Ag^+, and Au^+, respectively. These energies correspond to the distance between the metal and the oxygen atom of the formaldehyde molecule, where Cu−O < Au−O < Ag−O (1.88, 2.20, and 2.23 Å). When the cations are adsorbed on the zeolite framework, the adsorption energies do not follow this trend due to the compensation

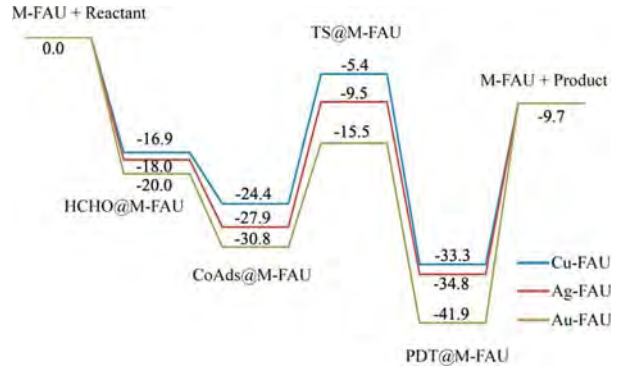

Figure 5. Zero-point corrected energy profiles of the reaction calculated by the 16T M06-L/6-31G(d,p) level of theory (all energies in kcal/mol).

charge transfer between the metals and the zeolite that we mentioned above. However, a large charge transfer character between formaldehyde and metal exchanged zeolite is still exhibited for the Au-FAU; it provides the highest adsorption energy. This indicated a good encapsulation capability of the formaldehyde even in a charge transferable solid support.

3.3. Carbonyl-ene Reaction between Encapsulated Formaldehyde in Metal-FAU and Propene. After the formaldehyde encapsulation, the reaction is followed by the coadsorption of propene to the encapsulated complex and then by a concerted transition state. The energetic reaction profile is summarized in Figure 5. In the coadsorption step, the propene bound to the encapsulated formaldehyde with the coadsorption energy increases by ~10 kcal/mol compared to the formaldehyde adsorption energies in all cases. The charge of the formaldehyde carbon atom is +0.217e, +0.266e, and +0.284e for the Cu-, Ag-, and Au-FAU, respectively. This again indicates that the formaldehyde carbon atom of the Au-FAU is ready to be attacked by the nucleophilic group. Propene and the encapsulated formaldehyde form a concerted transition structure in which new C−C1 and O−H bonds are formed simultaneously and the C3−H bond breaks (Table S1).

The C−O bond of formaldehyde is elongated from 1.23 Å to about 1.35 Å for the Cu and Ag systems whereas the one of the Au system is longer, 1.38 Å. This is compatible with the lowest activation energy for the reaction in Au-FAU, 15.3 kcal/mol, compared to 19.0 and 18.5 kcal/mol of that in Cu- and Ag-FAU, respectively. These results correlate well with the study of the same reaction with several Lewis acid catalysts by Yang et al.[60] They found that an electron withdrawing group at the formaldehyde C atom (providing a higher positive charge of the C atom) leads to a lower activation barrier for the reaction. In our case, the formaldehyde C atom is strongly induced to be highly positive by the metal cations. Moreover, these authors also showed that a more positive charge of the secondary C atom of propene, at the transition state, corresponds to a lower activation barrier. From our calculations, the charges of the propene secondary C atom at the transition state were +0.077e, +0.052e, and +0.157e for the Cu-, Ag-, and Au-FAU systems, respectively. The NBO analysis illustrates that the occupancy of the Au atom is almost unchanged when the propene is coadsorbed. Interestingly, the 6s orbital of the Au atom gains a significant occupation, from 0.45e to 0.59e, whereas the occupancies of Cu and Ag atoms remain almost unchanged when the reaction crosses the transition state.

Table 2. Relative Energies with Respect to the Reactants of the Systems and Desorption Energies (E_{des}) and Activation Energies (E_a) Calculated with 16T/M06-L/6-31G(d,p), 120T/M06-L/6-31G(d,p)//16T/M06-L/6-31G(d,p), and Bare-Metal Systems//16T/M06-L/6-31G(d,p) without Zero-Point Energy Corrections

	relative energies (kcal/mol)								
	Cu-FAU			Ag-FAU			Au-FAU		
	16T	120T	bare	16T	120T	bare	16T	120T	bare
Ads	−16.5	−20.0	−45.0	−19.0	−21.1	−30.0	−21.6	−24.5	−37.7
CoAds	−27.3	−32.7	−58.2	−30.6	−34.2	−41.7	−33.9	−38.1	−52.6
TS	−8.4	−15.4	−49.3	−12.5	−17.0	−29.5	−18.9	−25.1	−46.6
PDT	−39.7	−48.3	−72.1	−41.0	−46.2	−56.0	−48.8	−55.1	−65.2
E_{des}	24.7	33.3	57.1	26.0	31.2	41.0	33.8	40.1	50.2
E_a	18.9	17.4	8.8	18.0	17.2	12.2	15.0	13.0	6.1

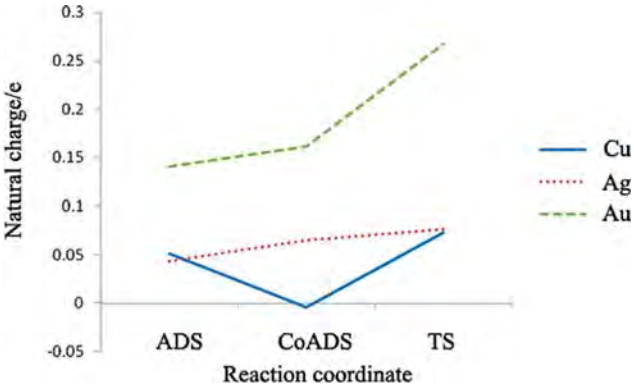

Figure 6. Evolution of the charge of the probe molecules (formaldehyde and propene) along the reaction coordinate.

Consequently, the relativistic effect, which can be inferred from the 6s orbital of the Au atom, might play an important role in the high activity of the Au system. The Au-FAU might have a problem with a high desorption energy (Table 2) when the full catalytic cycle is considered. However, we suggest that the catalyst that is active for this kind of reaction should have a character of high charge transfer to stabilize and activate the formaldehyde monomer.

We furthermore analyze the charges of the probe molecules bound to the metal-FAU systems (Table 1). The results show that the Au atom induces the highest charge of the probe molecules, in all cases and especially for the transition state, where the charge is +0.268e. With the Cu and Ag cations, the metals cannot induce charges of more than +0.100e in an elementary step. The charge evolution during the reaction pathway is shown in Figures 6 and 7.

3.4. Zeolite Framework Effect. In studies of zeolite systems, the framework effect, which contributes the confining van der Waals interactions, is found to be one of the important keys for understanding the adsorption phenomena and the catalytic activity. The extended 120T of the supercage structure of the faujasite zeolite was used for single point calculations to study the effects of the framework. The relative energies of the systems involved in the reaction are summarized in Table 2. We find that all systems are stabilized by the zeolite framework. Interestingly,

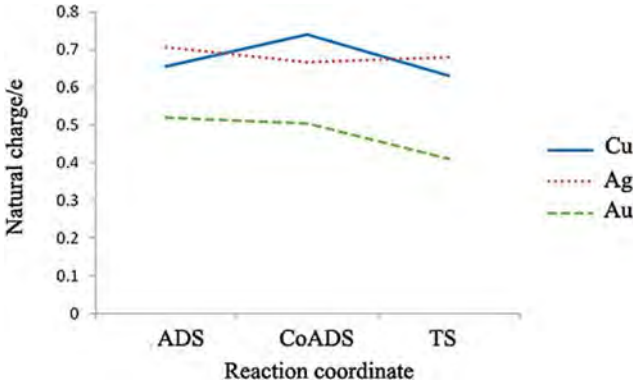

Figure 7. Evolution of the charge of the metal atoms along the reaction coordinate.

the Au-FAU framework structure reduces the activation barrier to only 13.0 kcal/mol and those of the Cu- and Ag-FAU systems remain around 17 kcal/mol (Table 2). This is consistent with a large induced charge flow from the Au atom and with the observation that the zeolite framework is more effective when the reaction proceeds via the ion pair intermediate.[48,61−65] From these results, one can state that the Au cation should work well for reactions promoted by Lewis acids in zeolite frameworks.

We also investigated systems without a zeolite framework. To avoid the effect of structural differences, single point calculations were performed on the optimized structures, but only with the metals and probe fragments (Table 2). The adsorption energies of the formaldehyde on the bare cations (−45.0, −30.0, and −37.7 kcal/mol for Cu, Ag, and Au) were found to be close to the optimized ones (−48.8, −32.2, and −38.8 kcal/mol). In comparison with our previous calculation on the bare-Cu^+ with the B3LYP functional,[15] we found that the single point calculations for the energetic profile of the Cu^+ ion were almost the same as the optimized one with B3LYP, especially the relative energy of the transition state (∼−49 vs −50 kcal/mol). This indicates that the structural difference does not affect the energetic properties as much as the effect of the charge compensation mentioned above. The activation energies of the extreme cases of metal cation systems were calculated to be 8.8, 12.2, and 6.1 kcal/mol for the Cu^+, Ag^+, and Au^+, respectively. Therefore, it can be concluded that the Au^+ ion shows a high activity for this reaction even after charge distribution between the cation and the zeolite occurred.

3.5. Comparison with the Na-FAU and MOF-11 Systems. From our previous study of the Na-exchanged FAU zeolite, we found that this alkaline exchanged zeolite can reduce the activation barrier from ∼34 kcal/mol for the uncatalyzed process to ∼25 kcal/mol. In comparison, the adsorption and coadsorption energies of the Na-FAU system were close to the results obtained for the transition metal exchanged systems. However, the transition metals provided higher activities by lowering the energy of the transition state, especially for the Au-FAU system. In contrast to the transition metals, the charge of Na was almost unchanged (∼+0.9e) during the whole reaction pathway whereas the charge transfers between the metals and probes are known to play an important role in the activity of transition metal exchanged zeolites.

The Cu site of the MOF-11 has also been used to catalyze this reaction. However, the activation energy was ∼24 kcal/mol whereas that of the bare Cu^+ ion was only 6.4 kcal/mol. This indicates that the MOF-11 structure cannot retain the high activity of the Cu^+ ion. In this work, the zeolite structure was found to be the more appropriate structure for loaded metal to catalyze this kind of reaction.

4. CONCLUSION

The carbonyl-ene reaction over Cu-, Ag-, and Au-exchanged FAU zeolites was investigated in quantum mechanical calculations with an efficient functional, M06-L. The Au^+ ion exhibits a high performance in the formaldehyde encapsulation process and shows a high catalytic activity. By analyzing the electronic configuration, we demonstrated that the 6s orbital of the Au atom plays an important role in this interestingly high activity: It accepts an electron and induces a large charge in the probe molecules. This inductive effect is enhanced by the framework of zeolite. Although the activity of the Cu- and Ag-FAU was not as high as that of the Au-FAU, the zeolite structures are suitable for use as a catalyst for this type of reaction. Moreover, these transition metals provide a higher activity than that of the alkaline-exchanged zeolites, which showed no significant charge transfer. In summary: the cation, which can maintain a charge transfer even in the presence of a charge compensating support is the most appropriate one for this reaction. From our results, we suggest that the Au-exchanged zeolites could be a potential catalyst for this type of reactions. However, the problem of high desorption energy should be improved for industrial applications.

■ ASSOCIATED CONTENT

Supporting Information. Optimized geometries, electronic structures, zero-point energies, and vibrational frequencies. This information is available free of charge via the Internet at http://pubs.acs.org.

■ AUTHOR INFORMATION

Corresponding Author

*E-mail: jumras.l@ku.ac.th. Tel: +66-2-562-5555, ext 2159.

■ ACKNOWLEDGMENT

This work was supported in part by grants from the National Science and Technology Development Agency (NSTDA Chair Professor and NANOTEC Center of Excellence), the Thailand Research Fund (to J.L.), the Kasetsart University Research and Development Institute (KURDI), the Commission on Higher Education, Ministry of Education ("the National Research University Project of Thailand (NRU)" and "Postgraduate Education and Research Programs in Petroleum and Petrochemicals and Advanced Materials"), and by a grant under the Royal Golden Jubilee Ph.D. program from the Thailand Research Fund (to S.W.). The Graduate School, Kasetsart University, is also acknowledged. The authors are grateful to Donald G. Truhlar and Yan Zhao for supplying them with the code for the M06-L functional.

■ REFERENCES

(1) Hoffmann, H. M. R. *Angew. Chem., Int. Ed. Engl.* **1969**, *8*, 556–577.

(2) Oppolzer, W.; Snieckus, V. *Angew. Chem., Int. Ed.* **1978**, *17*, 476–486.
(3) Yamanaka, M.; Mikami, K. *Helv. Chim. Acta* **2002**, *85*, 4264–4271.
(4) Düren, T.; Sarkisov, L.; Yaghi, O. M.; Snurr, R. Q. *Langmuir* **2004**, *20*, 2683–2689.
(5) Eddaoudi, M.; Kim, J.; Rosi, N.; Vodak, D.; Wachter, J.; O'Keeffe, M.; Yaghi, O. M. *Science* **2002**, *295*, 469–472.
(6) Frost, H.; Snurr, R. Q. *J. Phys. Chem. C* **2007**, *111*, 18794–18803.
(7) Furukawa, H.; Ko, N.; Go, Y. B.; Aratani, N.; Choi, S. B.; Choi, E.; Yazaydin, A. O.; Snurr, R. Q.; O'Keeffe, M.; Kim, J.; et al. *Science* **2010**, *329*, 424–428.
(8) Li, H.; Eddaoudi, M.; O'Keeffe, M.; Yaghi, O. M. *Nature* **1999**, *402*, 276–279.
(9) Rosi, N. L.; Eckert, J.; Eddaoudi, M.; Vodak, D. T.; Kim, J.; O'Keeffe, M.; Yaghi, O. M. *Science* **2003**, *300*, 1127–1129.
(10) Rowsell, J. L. C.; Yaghi, O. M. *Microporous Mesoporous Mater.* **2004**, *73*, 3–14.
(11) Yaghi, O. M.; O'Keeffe, M.; Ockwig, N. W.; Chae, H. K.; Eddaoudi, M.; Kim, J. *Nature* **2003**, *423*, 705–714.
(12) Okachi, T.; Onaka, M. *J. Am. Chem. Soc.* **2004**, *126*, 2306–2307.
(13) Tomita, M.; Masui, Y.; Onaka, M. *J. Phys. Chem. Lett.* **2010**, *1*, 652–656.
(14) Sangthong, W.; Probst, M.; Limtrakul, J. *J. Mol. Struct.* **2005**, *748*, 119–127.
(15) Choomwattana, S.; Maihom, T.; Khongpracha, P.; Probst, M.; Limtrakul, J. *J. Phys. Chem. C* **2008**, *112*, 10855–10861.
(16) Zhang, Y.; Bell, A. T. *J. Catal.* **2008**, *255*, 153–161.
(17) Zhang, Y.; Briggs, D. N.; de Smit, E.; Bell, A. T. *J. Catal.* **2007**, *251*, 443–452.
(18) Zhang, Y.; Drake, I. J.; Briggs, D. N.; Bell, A. T. *J. Catal.* **2006**, *244*, 219–229.
(19) Zheng, X.; Bell, A. T. *J. Phys. Chem. C* **2008**, *112*, 5043–5047.
(20) Baba, T.; Iwase, Y.; Inazu, K.; Masih, D.; Matsumoto, A. *Microporous Mesoporous Mater.* **2007**, *101*, 142–147.
(21) Sakurai, H.; Tsunoyama, H.; Tsukuda, T. *J. Organomet. Chem.* **2007**, *692*, 368–374.
(22) Tsunoyama, H.; Sakurai, H.; Ichikuni, N.; Negishi, Y.; Tsukuda, T. *Langmuir* **2004**, *20*, 11293–11296.
(23) Mohamed, M. M.; Salama, T. M.; Ichikawa, M. *J. Colloid Interface Sci.* **2000**, *224*, 366–371.
(24) Mohamed, M. M.; Salama, T. M.; Ohnishi, R.; Ichikawa, M. *Langmuir* **2001**, *17*, 5678–5684.
(25) Qiu, S.; Ohnishi, R.; Ichikawa, M. *J. Phys. Chem.* **1994**, *98*, 2719–2721.
(26) Fierro-Gonzalez, J. C.; Gates, B. C. *J. Phys. Chem. B* **2004**, *108*, 16999–17002.
(27) Gao, Z. X.; Sun, Q.; Chen, H. Y.; Wang, X.; Sachtler, W. M. H. *Catal. Lett.* **2001**, *72*, 1–5.
(28) Salama, T. M.; Shido, T.; Ohnishi, R.; Ichikawa, M. *J. Chem. Soc., Chem. Commun.* **1994**, 2749–2750.
(29) Qiu, S.; Ohnishi, R.; Ichikawa, M. *J. Chem. Soc., Chem. Commun.* **1992**, 1425–1427.
(30) Deka, A.; Deka, R. C.; Choudhury, A. *Chem. Phys. Lett.* **2010**, *490*, 184–188.
(31) Griffe, B.; Brito, J. L.; Sierraalta, A. *J. Mol. Catal. A: Chem.* **2010**, *315*, 28–34.
(32) Sierraalta, A.; Alejos, P.; Ehrmann, E.; Rodriguez, L. J.; Ferrer, Y. *J. Mol. Catal. A: Chem.* **2009**, *301*, 61–66.
(33) Sierraalta, A.; Hernandez-Andara, R.; Ehrmann, E. *J. Phys. Chem. B* **2006**, *110*, 17912–17917.
(34) Sierraalta, A.; Alejos, P.; Ehrmann, E. *Int. J. Quantum Chem.* **2008**, *108*, 1696–1704.
(35) Sierraalta, A.; Añez, R.; Diaz, L.; Gomperts, R. *J. Phys. Chem. A* **2010**, *114*, 6870–6878.
(36) Zhao, Y.; Truhlar, D. G. *J. Chem. Phys.* **2006**, *125*, 194101–194118.
(37) Zhao, Y.; Truhlar, D. G. *Acc. Chem. Res.* **2008**, *41*, 157–167.
(38) Zhao, Y.; Truhlar, D. G. *Theor. Chem. Acc.* **2008**, *120*, 215–241.
(39) Olson, D. H.; Dempsey, E. *J. Catal.* **1969**, *13*, 221–231.
(40) Drake, I. J.; Zhang, Y.; Gilles, M. K.; Teris Liu, C. N.; Nachimuthu, P.; Perera, R. C. C.; Wakita, H.; Bell, A. T. *J. Phys. Chem. B* **2006**, *110*, 11665–11676.
(41) Dolg, M.; Wedig, U.; Stoll, H.; Preuss, H. *J. Chem. Phys.* **1986**, *86*, 866–872.
(42) Valero, R.; Gomes, J. R. B.; Truhlar, D. G.; Illas, F. *J. Chem. Phys.* **2008**, *129*, 124710.
(43) Valero, R.; Gomes, J. R. B.; Truhlar, D. G.; Illas, F. *J. Chem. Phys.* **2010**, *132*, 124710.
(44) Valero, R.; Costa, R.; De P. R. Moreira, I.; Truhlar, D. G.; Illas, F. *J. Chem. Phys.* **2008**, *128*, 114103.
(45) Zhao, Y.; Truhlar, D. G. *J. Phys. Chem. C* **2008**, *112*, 6860–6868.
(46) Zhao, Y.; Truhlar, D. G. *J. Chem. Theory Comput.* **2009**, *5*, 324–333.
(47) Zheng, J.; Zhang, S.; Truhlar, D. G. *J. Phys. Chem. A* **2008**, *112*, 11509–11513.
(48) Boekfa, B.; Choomwattana, S.; Khongpracha, P.; Limtrakul, J. *Langmuir* **2009**, *25*, 12990–12999.
(49) Kumsapaya, C.; Bobuatong, K.; Khongpracha, P.; Tantirungrotechai, Y.; Limtrakul, J. *J. Phys. Chem. C* **2009**, *113*, 16128–16137.
(50) Maihom, T.; Boekfa, B.; Sirijaraensre, J.; Nanok, T.; Probst, M.; Limtrakul, J. *J. Phys. Chem. C* **2009**, *113*, 6654–6662.
(51) Maihom, T.; Pantu, P.; Tachakritikul, C.; Probst, M.; Limtrakul, J. *J. Phys. Chem. C* **2010**, *114*, 7850–7856.
(52) Wannakao, S.; Boekfa, B.; Khongpracha, P.; Probst, M.; Limtrakul, J. *ChemPhysChem* **2010**, *11*, 3432–3438.
(53) Gonzalez, C.; Schlegel, H. B. *J. Chem. Phys.* **1989**, *90*, 2154–2161.
(54) Schlegel, H. B. *J. Comput. Chem.* **1982**, *3*, 214–218.
(55) Reed, A. E.; Curtiss, L. A.; Weinhold, F. *Chem. Rev.* **1988**, *88*, 899–926.
(56) Reed, A. E.; Weinhold, F. *J. Chem. Phys.* **1983**, *78*, 4066–4073.
(57) Frisch, M. J.; Trucks, G. W.; Schlegel, H. B.; Scuseria, G. E.; Robb, M. A.; Cheeseman, J. R.; Montgomery, J. A., Jr; Vreven, T.; Kudin, K. N.; Burant, J. C.; Millam, J. M.; Iyengar, S. S.; Tomasi, J.; Barone, V.; Mennucci, B.; Cossi, M.; Scalmani, G.; Rega, N.; Petersson, G. A.; Nakatsuji, H.; Hada, M.; Ehara, M.; Toyota, K.; Fukuda, R.; Hasegawa, J.; Ishida, M.; Nakajima, T.; Honda, Y.; Kitao, O.; Nakai, H.; Klene, M.; Li, X.; Knox, J. E.; Hratchian, H. P.; Cross, J. B.; Adamo, C.; Jaramillo, J.; Gomperts, R.; Stratmann, R. E.; Yazyev, O.; Austin, A. J.; Cammi, R.; Pomelli, C.; Ochterski, J. W.; Ayala, P. Y.; Morokuma, K.; Voth, G. A.; Salvador, P.; Dannenberg, J. J.; Zakrzewski, V. G.; Dapprich, S.; Daniels, A. D.; Strain, M. C.; Farkas, O.; Malick, D. K.; Rabuck, A. D.; Raghavachari, K.; Foresman, J. B.; Ortiz, J. V.; Cui, Q.; Baboul, A. G.; Clifford, S.; Cioslowski, J.; Stefanov, B. B.; Liu, G.; Liashenko, A.; Piskorz, P.; Komaromi, I.; Martin, R. L.; Fox, D. J.; Keith, T.; Al-Laham, M. A.; Peng, C. Y.; Nanayakkara, A.; Challacombe, M.; Gill, P. M. W.; Johnson, B.; Chen, W.; Wong, M. W.; Gonzalez, C.; Pople, J. A. *Gaussian 03*, revision B.05; Gaussian, Inc.: Pittsburgh, PA, 2003.
(58) Datka, J.; Kozyra, P.; Kukulska-Zajac, E.; Kobyzewa, W. *Catal. Today* **2005**, *101*, 117–122.
(59) Broclawik, E.; Zalucka, J.; Kozyra, P.; Mitoraj, M.; Datka, J. *Catal. Today* **2011**, *169*, 45–51.
(60) Yang, Q.; Tong, X.; Zhang, W. *J. Mol. Struct. (THEOCHEM)* **2010**, *957*, 84–89.
(61) Injan, N.; Pannorad, N.; Probst, M.; Limtrakul, J. *Int. J. Quantum Chem.* **2005**, *105*, 898–905.
(62) Boekfa, B.; Pantu, P.; Limtrakul, J. *J. Mol. Struct.* **2008**, *889*, 81–88.
(63) Jansang, B.; Nanok, T.; Limtrakul, J. *J. Mol. Catal. A: Chem.* **2007**, *264*, 33–39.
(64) Maihom, T.; Namuangruk, S.; Nanok, T.; Limtrakul, J. *J. Phys. Chem. C* **2008**, *112*, 12914–12920.
(65) Sirijaraensre, J.; Limtrakul, J. *Phys. Chem. Chem. Phys.* **2009**, *11*, 578–585.

THE VERSATILE SYNTHESIS METHOD FOR HIERARCHICAL MICRO- AND MESOPOROUS ZEOLITE: AN EMBEDDED NANOCARBON CLUSTER APPROACH

Chularat Wattanakit[1,3,4], Chompunuch Warakulwit[1,3,4], Piboon Pantu[1,3,4], Boonruen Sunpetch[1,3,4], Metta Charoenpanich[2,3,4], Jumras Limtrakul[1,3,4*]

[1]Department of Chemistry, Faculty of Science and Center of Nanotechnology, Kasetsart University Research and Development Institute, Kasetsart University, Bangkok 10900, Thailand

[2]Department of Chemical Engineering, Faculty of Engineering, Kasetsart University, Bangkok 10900,Thailand

[3]NANOTEC Center of Excellence, National Nanotechnology Center, Kasetsart University, Bangkok 10900, Thailand

[4]Center for Advanced Studies in Nanotechnology and Its Applications in Chemical, Food and Agricultural Industries, Kasetsart University, Bangkok 10900, Thailand

Corresponding author's e-mail address: jumras.l@ku.ac.th

Abstract. *In this work, we are reporting for the first time the synthesis of hierarchical micro- and mesoporous zeolite by using silica-carbon (SiO_2/C) composites prepared by pyrolysis of carbonaceous gases in the presence of silica gel. The pyrolysis effectively yielded carbon deposited onto the raw silica material. The obtained SiO_2/C composites were utilized as a bifunctional material, mesoporous template and silica source, for the zeolite synthesis. Tetrapropylammonium hydroxide (TPAOH) was used as a microporous template. The combination of the obtained composites and the TPAOH for the hydrothermal synthesis resulted in the formation of hierarchical micro- and mesoporous ZSM-5. The results from the SEM, TEM, and N_2 adsorption/desorption isotherms, and ^{27}Al MAS NMR chracterizations of the synthesized samples obtained after the removal of the templates confirmed the successful formation of the micro- and mesoporous zeolites. The mesoporosity of the zeolites could be controlled by adjusting the carbon content in the SiO_2/C composites while the carbon content could be controlled by varying the deposition time and the concentration of the carbonaceous gases used. This controllable and efficient synthesis method is considered to be a promising method for creating hierarchical micro- and mesoporous zeolites.*

Keywords: *Micro/mesoporous zeolite, ZSM-5, pyrolysis of carbonaceous gases, solid templating*

INTRODUCTION

Zeolites have been widely used in the petrochemistry industry in a large number of applications such as cracking (Kung et al., 2000), isomerization (Houžvička et al., 1996; Trombetta et al., 1998) and hydrocarbon alkylation (Marcilly, 2000; Tanabe and Hölderich, 1999) due to their shape-selectivity, high thermal stability and suitable acidic properties (Beyerlein et al., 1988; Van Santen and Kramer, 1995). With reference to microporous zeolites (owing to their pore size being less than 2 nm, by IUPAC definition (Sing et al., 1985) or conventional zeolites, the active sites are located inside framework channels which play an important role for the shape-selective catalytic reaction. Based on such selectivity, the transformation of large reactant molecules or reactant molecules that yield large transition states and/or products could not succeed inside the micropores of conventional zeolites. Furthermore, the conventional zeolite catalysts also impose mass transfer limitations due to their micropore system. To overcome this problem, the combination of microporous and mesoporous characteristics within the structure of zeolites could be an alternative way to improve, not only, the viability to catalyze the reactions involving bulky reactants but also the viability to catalyze the reactions that involve the bulky transition states and/or products.

Hierarchical zeolites with networks of various pore sizes, i.e., micropore (< 2 nm), mesopore (2-50 nm) and macropore (> 50 nm), have attracted much attention as a result of their highly attractive properties, including superior mass/heat transfer characteristics (Ocampo et al., 2009; Zheng et al., 2009), enhanced resistance of the deactivation of the catalyst (Zhu et al., 2008), and lower restriction of the diffusion of molecules in the mesopores, which is mentioned above. Generally, the hierarchical dual micro- and mesoporous zeolites can be prepared by two approaches, non-templated (Groen et al., 2006; Pérez-Ramírez et al., 2009; Tao et al., 2006) and templated approaches (Egeblad et al., 2007; Jacobsen et al., 2000a; Kim et al., 2003; Perez-Ramirez et al., 2008; Tao et al., 2006; Xiao et al., 2006). For the former one, hierarchical zeolites are obtained by post synthesis treatments, e.g., extraction of metal atoms (demetalation) or silicon atoms (desilication) (Groen et al., 2006; Pérez-Ramírez et al., 2009; Tao et al., 2006). Nevertheless, these methods usually have some disadvantages, such as the required strong condition (due to the high stability of the zeolite structure) and difficulty in controlling the pore size (Egeblad et al., 2007). For the latter approach, the methods used can be mainly classified into three categories in terms of solid templating, supramolecular templating, and indirect templating (Egeblad et al., 2007). For the two previous cases, the porous structure of the zeolites is formed directly by solid or soft templates. For the case of indirect templating, the porous structure is formed indirectly by a controlled deposition of a zeolite onto a template material (Verhoef et al., 2001). Because the high purity

zeolite phase can be obtained by the direct templating method, various solid materials including carbon nanomaterials (Jacobsen et al., 2000a; Janssen et al., 2003; Perez-Ramirez et al., 2008; Schmidt et al., 2001), colloidal imprinted carbons (Kim et al., 2003), carbon aerogels (Tao et al., 2006), polymers (Wang et al., 2010; Xiao et al., 2006; Zhu et al., 2008), resins (Tosheva et al., 2000), solid biological templates (Davis et al., 1998) and various types of organized assemblies of surfactant templates (Mukti et al., 2009) have been used.

Compared with soft templates, it is generally known that hard templates have high confinement ability derived from their rigid structure (Tosheva et al., 2000). In addition, they usually contain many pore channels leading to the formation of zeolite with high porosity (Tosheva et al., 2000). Much attention has been focused on the synthesis of hierarchical zeolite by using carbon templates because either nanosized crystals or mesoporous zeolite single crystals with tunable porosity can be obtained simply by using porous carbon templates. The nanosized crystals can be produced in the confined space of porous carbons with little or no encapsulation of the carbon materials during synthesis (Tao et al., 2006) or in the voids of carbon blacks (Jacobsen et al., 2000a; Kustova et al., 2007) and carbon aerogels (Tao et al., 2005). While mesoporous zeolites can be produced by encapsulation of porous carbon materials during synthesis. After removal of the embedded carbon matrix, porous zeolites can be obtained (Jacobsen et al., 2000a). Nevertheless, it is possible to obtain a combination of nanosized and hierarchical mesoporous zeolite (Egeblad et al., 2007).

Recently, Kustova *et al.* (Kustova et al., 2007) prepared a hierarchical zeolite by using a silica-carbon composite from the decomposition of a sucrose solution which impregnated onto a silica raw material. Sequentially, the mesoporous zeolites were obtained after zeolite crystallization and combustion of the carbon residue. This method significantly extends the scope of the solid templating approach, a simple and inexpensive method. However, zeolites with low mesoporosity were obtained. This might be due to poorly dispersed sugar during the impregnation. Thus, the development of such a synthetic method remains a challenge. To the best our knowledge, the use of a silica-carbon (SiO_2/C) composite prepared by a pyrolysis of the carbonaceous gas has not previously been reported for the preparation of mesoporous zeolites. Herein, we approach this challenge and report for the first time the synthesis of hierarchical micro- and mesoporous ZSM-5 zeolites by using the SiO_2/C composites that were prepared by pyrolysis of carbonaceous gases in the presence of silica gel under an inert ambient. We believed that such pyrolysis could effectively improve the carbon deposition onto the silica yielding a good formation of hierarchical micro- and mesoporous zeolites.

EXPERIMENTAL SECTION

1. MATERIALS

For the synthesis of zeolites, the chemicals used were silica gel with a particle size of 0.063-0.200 mm and pore volume of 1.0 cm^3/g (Merck, silica gel 100), NaOH (Carlo Erba), tetrapropylammonium hydroxide (TPAOH, 20 wt%, Fluka), $NaAlO_2$ (Riedel-de Haën), acetylene (C_2H_2, 99.9%, Praxair), propane (C_3H_8, 99.5%, BOC Scientific) and nitrogen gas (N_2, 99.999%, Praxair). All chemicals were used as received without further purification.

2. PREPARATION OF BIFUNCTIONAL CARBONIZED SILICA (SiO_2/C COMPOSITES)

The carbon/silica composites were prepared by pyrolyses of carbonaceous gas (acetylene or propane, C_xH_y) over silica gel. Typically, for each synthesis, 5 g of silica gel was introduced into the middle zone of a fixed-bed tubular reactor. Nitrogen gas (N_2) was then introduced into the reactor with a flow rate of 180 or 190 ml/min depending on the desired concentration of the reactant gas. Nitrogen gas easily displaced air and therefore it formed an inert atmosphere in the chamber. The reactor temperature was gradually increased to 1123 K under the nitrogen flow. After that, the reactant gas (C_xH_y) was introduced into the reactor. The gas mixture concentration was 5 or 10 v/v% of C_xH_y in N_2 with a total flow rate of 200 ml/min. After 1 or 2 h, the C_xH_y flow was stopped. The work tube was cooled down to room temperature under the nitrogen flow. The obtained carbon/silica composites were used as bifunctional materials for the zeolite syntheses. The silica gel part of the composites was used as a silica source of the zeolites. The carbon residue formed in the composite was used as a template for the mesopores of the zeolites.

3. HYDROTHERMAL SYNTHESIS OF HIERARCHICAL MICRO- AND MESOPOROUS ZSM-5

$NaAlO_2$ was used as an alumina source. TPAOH was used as a structure-directing agent for the ZSM-5 micropores. The molar composition of the synthetic gel was 1 Al_2O_3 : 181 SiO_2 : 36 TPA_2O : 15 Na_2O : 1029 H_2O. Typically, for a synthesis, the aluminate solution was prepared by mixing 0.016 g of $NaAlO_2$ and 0.11 g of NaOH in 1.7 mL of deionized (DI) water. Then, the aluminate solution was then added into 6.77 g of 20 wt% of TPAOH in water under stirring. The mixture was stirred continuously until a clear solution was obtained. The prepared SiO_2/C composite (1 g of SiO_2) was sequentially added into the solution. The obtained mixture was then transferred into a Teflon-lined stainless-steel autoclave and then crystallized at 453K for 3 days. The resulting material was collected by filtration (using Whatman, No. 42 filter paper) and then washed with DI water until the pH of the filtrate was about 8. The obtained product was then dried at 383 K for 10 h. Finally, the organic template and the carbon particles were removed by calcination in air at 823 K for 20 h.

4. CHARACTERIZATIONS

Several different carbon contents in the SiO_2/C composite materials achieved by varying the concentration of the gas mixture and the pyrolysis time were investigated by a thermal gravimetric analysis (TGA). The textural properties of the composites were determined by using a N_2 adsorption/desorption isotherms analysis performed at 77 K on a Micromeritics ASAP 2010 instrument. For this characterization, the samples were degassed at 623 K in a vacuum for 20 hours before measurements were taken. The specific surface areas (S_{BET}) of the samples were calculated by the Brunauer-Emmett-Teller (BET) method. The total pore volume (V_{tot}) was estimated by measuring the amount of adsorbed nitrogen at 0.97 P/P_0. The *t*-plot method was used to calculate the micropore volume (V_{micro}). The volume of mesopore and macropore ($V_{meso+macro}$) was calculated from the difference between the V_{tot} and V_{micro} (Lippens and de Boer, 1965). The size distribution of the mesopores was obtained by applying a Barret-Jovner-Halenda (BJH) model (Barrett et al., 1951).

The MFI structure of the synthesized zeolites was confirmed by an X-Ray Diffraction (XRD) measurement performed on a Rigaku TTRAX III, 18kW diffractometer using Cu Kα radiation. The measurement was operated at an accelerating voltage of 30 kV and a current of 40 mA. The diffraction patterns were collected at 2θ angles ranging from 5° to 50° with a scan speed of 1.2 deg/min and a step size of 0.02 deg. The morphology of the samples was investigated by scanning electron microscopy (SEM, JEOL- JSM 6301F). The pores of the samples were observed by transmission electron microscopy (TEM, JEOL JEM-2010). The nature of the Al species in the zeolite framework was characterized by a ^{27}Al magic-angle spinning (MAS) NMR spectroscopy (^{27}Al MAS NMR) was recorded at 78.20 MHz, using a Bruker Biospin (DPX-300, 300 MHz) spectrometer with a 2 μs pulse, 4 s delay time and 800 scans.

RESULTS AND DISCUSSION

1. SiO_2/C COMPOSITES

The carbon content in the composites, “carbon (wt%)”, synthesized by using various experimental conditions measured by TGA analysis, is shown in Table 1. The amount of carbon deposited was found to correspond well with the deposition time and the concentration of hydrocarbon gas (acetylene and propane) used. Increasing the deposition time and the concentration of hydrocarbon gas resulted in increasing the carbon content. Therefore, it can be suggested that the amount of deposited carbon can be varied by simply varying the deposition time and concentration of carbonaceous gases. Furthermore, it was found that acetylene yielded a higher amount of carbon deposit than propane in the same experimental conditions. In the case of propane, in order to obtain the same carbon content as in the case of acetylene, a longer deposition time is required. For

example, in order to obtain about 10 wt% of carbon content, at the 5 v/v% of C_xH_y, the deposition time required for acetylene and propane were 60 and 120 min, respectively. Although propane has a higher molar ratio of carbon atoms than acetylene, its thermal stability during the pyrolysis process is higher than that of acetylene (ΔG_f^o of propane and acetylene are 45.72 and 40.62 kcal/mol at 1000 K, respectively (Alberty and Burmenko, 1986; Chao et al., 1973)), this results in less reactive and less carbon deposit when propane is utilized. The nature of carbon deposit on silica gel was investigated by XRD characterization (data is not shown). The crystalline peak was not found in the XRD pattern, indicating that such carbon deposit is amorphous carbon.

The textural properties, including the specific surface area calculated by the BET method (S_{BET}), the total pore volume (V_{tot}), the mesopore volume (V_{meso}), and the mesopore diameter (D_{BJH}) of the raw silica gel and the prepared SiO_2/C composites obtained by using the N_2 adsorption/desorption method are shown in Table 1. By using the *t*-plot method, the micropore volume (V_{micro}) was calculated to be nearly zero in all cases. The mean pore size obtained from the maximum BJH pore size distribution (D_{BJH}) of the starting silica gel was found to be ca. 11 nm. Its N_2 adsorption/desorption isotherms were of type IV (see Figure S1). Since parts of porosity could be obtained as the free space occurred as a result of carbon combustion during the calcination step. Thus, in order to clarify that the use of SiO_2/C composite significantly yielded mesoporosity rather than microporosity, the ratios of mesopore volume to micropore volume, $V_{meso+macro}/V_{micro}$, were calculated for all zeolite samples and reported in Table 2. The significant increase of $V_{meso+macro}/V_{micro}$ ratios resulted from increasing the carbon content in the SiO_2/C composites, thus verifying that using SiO_2/C composite significantly yielded the mesopore formation rather than the micropore formation.

Due to the decrease of V_{meso} and the appearance of the black color of the composites, it can be suggested that carbon was not only deposited inside the mesopores of the silica gel but also onto the outer surface of the silica gel. From the textural properties characterized by N_2 adsorption/desorption analysis, in the cases of acetylene, it was found that increasing the deposition time and the concentration of the reactant gas decreased the V_{meso} of the silica gel. This result was in contrast to that of the propane cases where increasing the concentration of the reactant gas did not result significantly in the decreasing of the V_{meso} of the silica gel (see 5% C_3H_8-120 min-SiO_2/C and 10% C_3H_8-120 min-SiO_2/C samples). The results indicated that carbon mainly deposited on the outer surface of silica gel in the case of propane (compared to that of acetylene). The values of D_{BJH} were found to corresponding quite well with the V_{meso} values.

2. HIERARCHICAL MICRO- AND MESOPOROUS ZSM-5 PREPARED FROM SiO_2/C COMPOSITES

2.1. POWDER X-RAY DIFFRACTION (XRD)

The XRD pattern of the raw silica gel, a reference zeolite sample (commercial ZSM-5, ALSI-PENTA Zeolithe GmbH (APZ)), and the synthesized samples are shown in Figure 1. The pattern of the silica gel indicates the amorphous structure. The XRD patterns of the synthesized samples are comparable to that of the reference ZSM-5 confirming the characteristic of the MFI structure. In addition, it was observed that the diffraction peaks of the samples were sharp and contained a very low background signal. This indicated that the samples were synthesized with high crystallinity and purity.

2.2. SCANNING ELECTRON MICROSCOPY (SEM) AND TRANSMISSION ELECTRON MICROSCOPY (TEM)

The SEM and TEM images showing the morphology and the porosity of the selected zeolite samples (0% carbon-ZSM-5, 5% C_2H_2-60 min-ZSM-5, 5% C_2H_2-120 min-ZSM-5, and 10% C_2H_2-120 min-ZSM-5 samples) compared to those of the commercial ZSM-5 are shown in Figure 2 (see Figure S2 for 5% C_3H_8-120 min-ZSM-5, 10% C_3H_8-120 min-ZSM-5 samples). The commercial ZSM-5 had large crystal sizes of over than 4 μm (see Figure 2a). The SEM image of the sample 1 shows the formation of small well-faceted cubic zeolite crystals with the size widely distributed in the range of 150-400 nm (see Figure 2b). Because, under the synthesis conditions, the concentration of the structure-directing agent or TPAOH was high, it can thus be suggested that a large amount of nuclei could be formed leading to the formation of small crystals. The sample prepared by using of the SiO_2/C composite with low carbon content of about 10 wt% comprised nearly cubic crystals with the size of about 200-500 nm (see Figure 2c). In the case of the synthesized micro- and mesoporous ZSM-5 obtained by using the SiO_2/C composites with high carbon content, e.g., 5% C_2H_2-120 min-SiO_2/C and 10% C_2H_2-120 min-SiO_2/C which contain 18 and 29 %w/w, respectively, the ZSM-5 nanocrystal aggregates were formed with the size widely distributed in the range of about 500-900 nm (see Figures 2d and 2e). The size of each nanocrystal was less than 50 nm. As we found during the TEM measurement that this aggregate structure could be preserved during a sonication, thus, these aggregates were considered as fully bound-nanocrystal aggregates. It should be noted that the presence of high carbon content lead to a relatively high nucleation rate compared to the growth rate, as a result, the formation of small zeolite crystals was preferable compared to that of large crystals (Jacobsen et al., 2000b).

The bright area in the TEM image of the zeolites is indicative of the porosity (Janssen et al., 2001; Zhu et al., 2008). The TEM images of the samples synthesized by using of the SiO_2/C composites show more bright spots compared to those of the sample synthesized without using SiO_2/C composite and the commercial ZSM-5 implying the presence of the mesopores. In addition, it was observed that the amount of the bright spots in the

TEM images of the samples corresponded well with the amount of carbon content. This result implies that increasing the carbon content in the SiO_2/C composites resulted in increasing the mesopores in the samples.

2.3. SURFACE AREA AND POROSITY CHARACTERISTICS

The N_2 adsorption/desorption isotherms and the distribution of the pore sizes with respect to the mesopore calculated by the BJH method (derived from adsorption branch isotherms) of the synthesized samples and the commercial ZSM-5 are shown in Figures 3a and 3b, respectively. From the N_2 adsorption/desorption isotherms of samples, the adsorption at low relative pressure corresponding to the micropore filling (Schneider, 1995) was observed for all samples. A significant adsorption/desorption at high relative pressure ($P/P_0>0.9$) of 0% carbon-ZSM-5 sample indicates the presence of interparticle voids (Figure 3a). Because the crystal size of this sample was small, the amount of interparticle voids or macropore volume was high. The isotherms of 5% C_2H_2-60 min-ZSM-5, 5% C_2H_2-120 min-ZSM-5, 10% C_2H_2-120 min-ZSM-5, 5% C_3H_8-120 min-ZSM-5, and 10% C_3H_8-120 min-ZSM-5 samples significantly differ from those of 0% carbon-ZSM-5 sample and commercial ZSM-5. The presence of the hysteresis loop at $0.4<P/P_0<0.9$ in the isotherms of 5% C_2H_2-60 min-ZSM-5, 5% C_2H_2-120 min-ZSM-5, 10% C_2H_2-120 min-ZSM-5, 5% C_3H_8-120 min-ZSM-5, and 10% C_3H_8-120 min-ZSM-5 samples caused by a capillary condensation in the mesopore void space (Gregg and Sing, 1982), clearly demonstrates the formation of the mesopores in the samples whereas the N_2 isotherms of the commercial ZSM-5 exhibited the type I isotherms belonging to pure microporous material. The interpreted distributions in the pore sizes with respect to the mesopores of the samples show a significant increase of the mesopores in the 5% C_2H_2-60 min-ZSM-5, 5% C_2H_2-120 min-ZSM-5, 10% C_2H_2-120 min-ZSM-5, 5% C_3H_8-120 min-ZSM-5, and 10% C_3H_8-120 min-ZSM-5 samples compared to the 0% carbon-ZSM-5 sample and the commercial ZSM-5. The size of the mesopores of 5% C_2H_2-60 min-ZSM-5, 5% C_2H_2-120 min-ZSM-5, 10% C_2H_2-120 min-ZSM-5, 5% C_3H_8-120 min-ZSM-5, and 10% C_3H_8-120 min-ZSM-5 samples was distributed depending on the carbon content. Increasing the carbon content in the samples increases the amount of the mesopores and spreads the size distribution of the mesopores.

Table 2 shows the surface area and porosity of the prepared samples. By introducing the carbon content into the silica, the surface areas of the micropores of sample 1 and the commercial ZSM-5 were slightly higher than that of the other samples (ca. 15%) while their external surface areas were significantly lower than that of 5% C_2H_2-60 min-ZSM-5, 5% C_2H_2-120 min-ZSM-5, 10% C_2H_2-120 min-ZSM-5, 5% C_3H_8-120 min-ZSM-5, and 10% C_3H_8-120 min-ZSM-5 samples, especially for the commercial ZSM-5. The calculated pore volumes of the samples are related to the measured surface area. Increasing the carbon content in the SiO_2/C composites

resulted in a significant increase of the total pore volume which was reflected by the increase of the mesopore volume. As mentioned above, the micropores were formed by the presence of the TPAOH template, thus, the micropore volume of the samples that were prepared by using SiO_2/C composites only slightly decreased from that of sample 1. The results confirm the success of introducing the mesopores into the ZSM-5 zeolite yielding hierarchical micro- and mesoporous ZSM-5 by the presence of the carbon deposit in the silica source prepared by pyrolysis of hydrocarbon gas such as acetylene and propane.

2.4. ^{27}Al MAS NMR

A typical ^{27}Al MAS solid state NMR spectrum of the zeolite samples prepared in this work showing the environment around the aluminum atoms in the framework of the synthesized ZSM-5 is depicted in Figure 4. The spectrum contains a strong peak at the chemical shift of about 55 ppm corresponding to the tetrahedrally coordinated aluminum in the framework. A peak at the chemical shift at 0 ppm, which corresponds to the extra framework octahedrally coordinated aluminum, was not observed in synthesized samples. This result indicates that all aluminum atoms of the synthesized zeolites were incorporated into the zeolite framework during the synthesis.

Conclusively, by using silica-carbon (SiO_2/C) composites prepared by pyrolysis of carbonaceous gases in the presence of silica gel, it is possible to tailor hierarchical micro- and mesoporous zeolite with significant mesoporosity and acceptable mesopore size distribution compared to that obtained by using other carbon materials, e.g. carbon black (Jacobsen et al., 2000a), carbon nanotube (Schmidt et al., 2001), carbon nanofiber (Janssen et al., 2003) in which high amount of carbon precursors is generally required and that obtained by using sucrose mesopore-directing agent (Kustova et al., 2007) in which sugar solution is difficult to be dispersed into the pores of silica gel during the impregnation, thus, leading the formation of low mesoporosity zeolite. Hence, these developed synthesis method could potentially extend the scope of the solid carbon templating approach and mesopore-directing agent approach. In addition, this method could be scaled up due to the ease of C/SiO_2 composite preparation.

CONCLUSION

In summary, the hierarchical micro- and mesoporous ZSM-5 zeolites were successfully synthesized by using the SiO_2/C composites that were prepared by pyrolysis of hydrocarbon gas in the presence of silica gel. The SiO_2/C composite acted as a bifunctional material, a mesoporous template and a silica source, for the zeolite synthesis. The results from the SEM, TEM, N_2 adsorption/desorption isotherms, and ^{27}Al MAS NMR chracterizations revealed the successful synthesis of hierarchical micro- and mesoporous ZSM-5 by using the

composites. It was found that the mesoporosity of the zeolites could be controlled by adjusting the carbon content of the SiO_2/C composites. Increasing the carbon content in the composites resulted in significantly increasing the total pore volume, which was reflected in the increase of the mesopore volume whereas the micropore volume of the samples was not significantly altered. Because this controllable and efficient synthetic method is expected to be generalized for other types of zeolites, it is considered to be a promising method for creating hierarchical micro- and mesoporous zeolites that could overcome mass transport limitation of the catalytic process, especially in the reaction including the bulky molecule.

ACKNOWLEDGEMENTS

This work was supported in part by grants from The National Science and Technology Development Agency (2009 NSTDA Chair Professor funded by The Crown Property Bureau under the management of The National Science and Technology Development Agency and NANOTEC Center of Excellence funded by The National Nanotechnology Center), Kasetsart University Research and Development Institute (KURDI), The Thailand Research Fund (TRF), and The Commission on Higher Education, Ministry of Education (The "National Research University Project of Thailand (NRU)" and The "National Center of Excellence for Petroleum, Petrochemical and Advanced Materials (NCE-PPAM)"). C.W. also thanks The Thailand Research Fund (TRF) for a Royal Golden Jubilee Ph.D. Fellowship (3.C.KU/50/A.2).

REFERENCES

Alberty, R. A. and E. Burmenko, "Standard Chemical Thermodynamic Properties of Alkyne Isomer Groups," J. Phys. Chem. Ref. Data **15**(4), 1339-1349 (1986).

Barrett, E. P., L. G. Joyner and P. P. Halenda, "The Determination of Pore Volume and Area Distributions in Porous Substances. I. Computations from Nitrogen Isotherms," J. Am. Chem. Soc. **73**(1), 373-380 (1951).

Beyerlein, R. A., G. B. McVicker, L. N. Yacullo and J. J. Ziemiak, "Influence of Framework and Nonframework Aluminum on the Acidity of High-Silica, Proton-Exchanged FAU-Framework Zeolites," J. Phys. Chem. **92**(7), 1967-1970 (1988).

Chao, J., R. C. Wilhoit and B. J. Zwolinski, "Ideal Gas Thermodynamic Properties of Ethane and Propane," J. Phys. Chem. Ref. Data **2**(2), 427-438 (1973).

Davis, S. A., H. M. Patel, E. L. Mayes, N. H. Mendelson, G. Franco and S. Mann, "Brittle Bacteria: A Biomimetic Approach to the Formation of Fibrous Composite Materials," Chem. Mater. **10**(9), 2516-2524 (1998).

Egeblad, K., C. H. Christensen, M. Kustova and C. H. Christensen, "Templating Mesoporous Zeolites," Chem. Mater. **20**(3), 946-960 (2007).

Gregg, S. J. and K. S. W. Sing, "Adsorption Surface Area, and Porosity." Academic Press Ltd, London (1982).

Groen, J. C., J. A. Moulijn and J. Perez-Ramirez, "Desilication: On the Controlled Generation of Mesoporosity in MFI Zeolites," J. Mater. Chem. **16**(22), 2121-2131 (2006).

Houžvička, J., O. Diefenbach and V. Ponec, "The role of Bimolecular Mechanism in the Skeletal Isomerisation of *n*-butene to Isobutene," J. Catal. **164**(2), 288-300 (1996).

Jacobsen, C. J. H., C. Madsen, J. Houzvicka, I. Schmidt and A. Carlsson, "Mesoporous Zeolite Single Crystals," J. Am. Chem. Soc. **122**(29), 7116-7117 (2000a).

Jacobsen, C. J. H., C. Madsen, T. V. W. Janssens, H. J. Jakobsen and J. Skibsted, "Zeolites by Confined Space Synthesis - Characterization of the Acid Sites in Nanosized ZSM-5 by Ammonia Desorption and ^{27}Al/^{29}Si-MAS NMR spectroscopy," Microporous Mesoporous Mater. **39**(1-2), 393-401 (2000b).

Janssen, A. H., A. J. Koster and K. P. de Jong, "Three-Dimensional Transmission Electron Microscopic Observations of Mesopores in Dealuminated Zeolite Y," Angew. Chem. Int. Ed. **40**(6), 1102-1104 (2001).

Janssen, A. H., I. Schmidt, C. J. H. Jacobsen, A. J. Koster and K. P. de Jong, "Exploratory study of mesopore templating with carbon during zeolite synthesis," Microporous Mesoporous Mater. **65**(1), 59-75 (2003).

Kim, S.-S., J. Shah and T. J. Pinnavaia, "Colloid-Imprinted Carbons as Templates for the Nanocasting Synthesis of Mesoporous ZSM-5 Zeolite," Chem. Mater. **15**(8), 1664-1668 (2003).

Kung, H. H., B. A. Williams, S. M. Babitz, J. T. Miller, W. O. Haag and R. Q. Snurr, "Enhanced Hydrocarbon Cracking Activity of Y Zeolites," Top. Catal. **10**(1), 59-64 (2000).

Kustova, M., K. Egeblad, K. Zhu and C. H. Christensen, "Versatile Route to Zeolite Single Crystals with Controlled Mesoporosity: In situ Sugar Decomposition for Templating of Hierarchical Zeolites," Chem. Mater. **19**(12), 2915-2917 (2007).

Lippens, B. C. and J. H. de Boer, "Studies on Pore Systems in Catalysts. V. The t Method," J. Catal. **4**(3), 319-323 (1965).

Marcilly, C., "Where and How Shape Selectivity of Molecular Sieves Operates in Refining and Petrochemistry Catalytic Processes," Top. Catal. **13**(4), 357-366 (2000).

Mukti, R. R., H. Hirahara, A. Sugawara, A. Shimojima and T. Okubo, "Direct Hydrothermal Synthesis of Hierarchically Porous Siliceous Zeolite by Using Alkoxysilylated Nonionic Surfactant," Langmuir **26**(4), 2731-2735 (2009).

Ocampo, F., H. S. Yun, M. M. Pereira, J. P. Tessonnier and B. Louis, "Design of MFI Zeolite-Based Composites with Hierarchical Pore Structure: A New Generation of Structured Catalysts," Cryst. Growth Des. **9**(8), 3721-3729 (2009).

Pérez-Ramírez, J., S. Abelló, A. Bonilla and J. C. Groen, "Tailored Mesoporosity Development in Zeolite Crystals by Partial Detemplation and Desilication," Adv. Funct. Mater. **19**(1), 164-172 (2009).

Perez-Ramirez, J., C. H. Christensen, K. Egeblad, C. H. Christensen and J. C. Groen, "Hierarchical Zeolites: Enhanced Utilisation of Microporous Crystals in Catalysis by Advances in Materials Design," Chem. Soc. Rev. **37**(11), 2530-2542 (2008).

Schmidt, I., A. Boisen, E. Gustavsson, K. Stahl, S. Pehrson, S. Dahl, A. Carlsson and C. J. H. Jacobsen, "Carbon Nanotube Templated Growth of Mesoporous Zeolite Single Crystals," Chem. Mater. **13**(12), 4416-4418 (2001).

Schneider, P., "Adsorption Isotherms of Microporous-Mesoporous Solids Revisited," Appl. Catal. A: Gen. **129**(2), 157-165 (1995).

Sing, K. S. W., D. H. Everett, R. A. W. Haul, L. Moscou, R. A. Pierotti, J. Rouquerol and T. Siemieniewska, "Reporting Physisorption Data for Gas/Solid Systems with Special Reference to the Determination of Surface Area and Porosity (Recommendations 1984)," Pure Appl. Chem. **57**, 603-619 (1985).

Tanabe, K. and W. F. Hölderich, "Industrial Application of Solid Acid-Base Catalysts," Appl. Catal. A: Gen. **181**(2), 399-434 (1999).

Tao, Y., H. Kanoh, L. Abrams and K. Kaneko, "Mesopore-Modified Zeolites: Preparation, Characterization, and Applications," Chem. Rev. **106**(3), 896-910 (2006).

Tao, Y., H. Kanoh and K. Kaneko, "Synthesis of Mesoporous Zeolite A by Resorcinol–Formaldehyde Aerogel Templating," Langmuir **21**(2), 504-507 (2005).

Tosheva, L., V. Valtchev and J. Sterte, "Silicalite-1 Containing Microspheres Prepared Using Shape-Directing Macro-Templates," Microporous Mesoporous Mater. **35-36**, 621-629 (2000).

Trombetta, M., G. Busca, S. Rossini, V. Piccoli, U. Cornaro, A. Guercio, R. Catani and R. J. Willey, "FT-IR Studies on Light Olefin Skeletal Isomerization Catalysis: III. Surface Acidity and Activity of Amorphous and Crystalline Catalysts Belonging to the SiO_2-Al_2O_3 System," J. Catal. **179**(2), 581-596 (1998).

Van Santen, R. A. and G. J. Kramer, "Reactivity Theory of Zeolitic Brønsted Acidic Sites," Chem. Rev. **95**(3), 637-660 (1995).

Verhoef, M. J., P. J. Kooyman, J. C. van der Waal, M. S. Rigutto, J. A. Peters and H. van Bekkum, "Partial Transformation of MCM-41 Material into Zeolites: Formation of Nanosized MFI Type Crystallites," Chem. Mater. **13**(2), 683-687 (2001).

Wang, L., Z. Zhang, C. Yin, Z. Shan and F.-S. Xiao, "Hierarchical Mesoporous Zeolites with Controllable Mesoporosity Templated from Cationic Polymers," Microporous Mesoporous Mater. **131**(1-3), 58-67 (2010).

Xiao, F.-S., L. Wang, C. Yin, K. Lin, Y. Di, J. Li, R. Xu, D. S. Su, R. Schlögl, T. Yokoi and T. Tatsumi, "Catalytic Properties of Hierarchical Mesoporous Zeolites Templated with a Mixture of Small Organic Ammonium Salts and Mesoscale Cationic Polymers13," Angew. Chem. Int. Ed. **45**(19), 3090-3093 (2006).

Zheng, J., X. Zhang, Y. Zhang, J. Ma and R. Li, "Structural Effects of Hierarchical Pores in Zeolite Composite," Microporous Mesoporous Mater. **122**(1-3), 264-269 (2009).

Zhu, H., Z. Liu, D. Kong, Y. Wang and Z. Xie, "Synthesis and Catalytic Performances of Mesoporous Zeolites Templated by Polyvinyl Butyral Gel as the Mesopore Directing Agent," J. Phys. Chem. C **112**(44), 17257-17264 (2008).

FIGURE CAPTIONS

Figure 1. XRD patterns of (a) raw silica gel, (b) the reference zeolite sample (ZSM-5, ALSI-PENTA Zeolithe GmbH (APZ)), (c) 0% carbon-ZSM-5, (d) 5% C_2H_2-60 min-ZSM-5, (e) 5% C_2H_2-120 min-ZSM-5, (f) 10% C_2H_2-120 min-ZSM-5, (g) 5% C_3H_8-120 min-ZSM-5, and (h) 10% C_3H_8-120 min-ZSM-5

Figure 2. SEM and TEM images of (a) a commercial ZSM-5 (ALSI-PENTA Zeolithe GmbH (APZ)), (b) 0% carbon-ZSM-5, (c) 5% C_2H_2-60 min-ZSM-5, (d) 5% C_2H_2-120 min-ZSM-5, (e) 10%C_2H_2-120 min-ZSM-5

Figure 3. (a) N_2 adsorption/desorption isotherms of the synthesized zeolite samples and the commercial ZSM-5

(b) Size distribution of their mesopores calculated from the adsorption branch of the isotherm

Figure 4. Typical ^{27}Al MAS NMR spectrum of the synthesized ZSM-5 sample. This spectrum is taken from 10% C_2H_2-120 min-ZSM-5 sample.

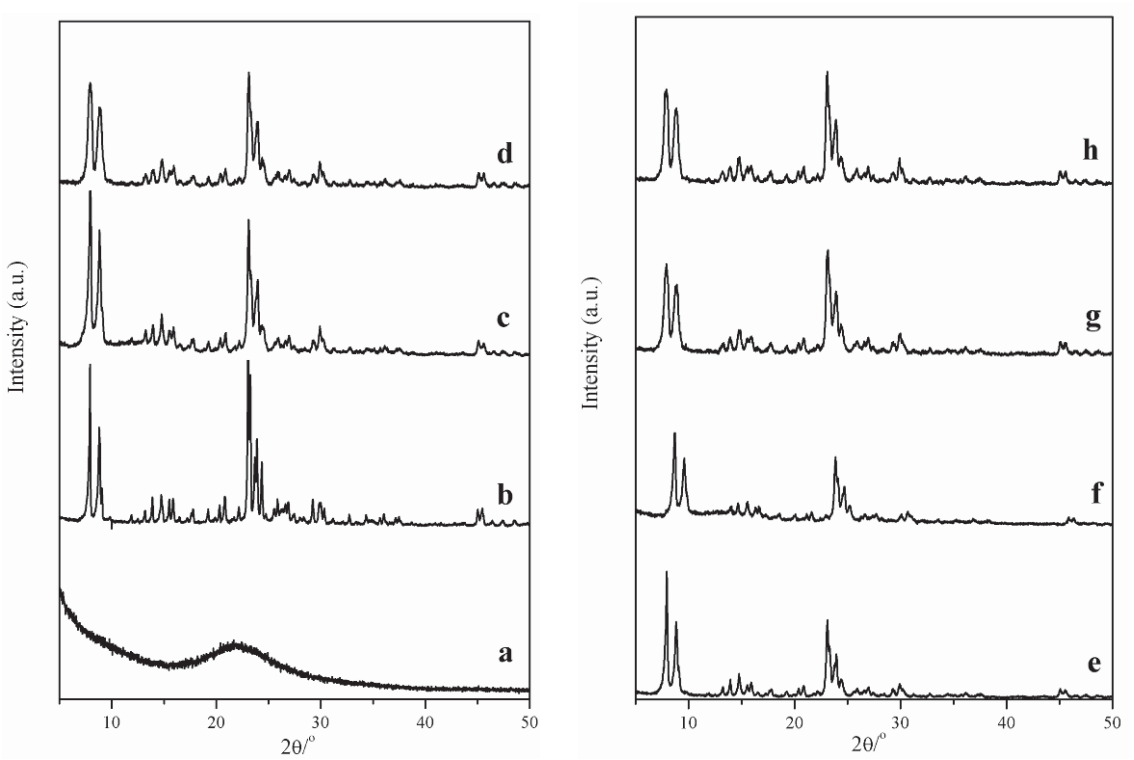
Intensity (a.u.)
d
c
b
a
10
20
30
40
50
2θ/°
Intensity (a.u.)
h
g
f
e
10
20
30
40
50
2θ/°

Figure 1.

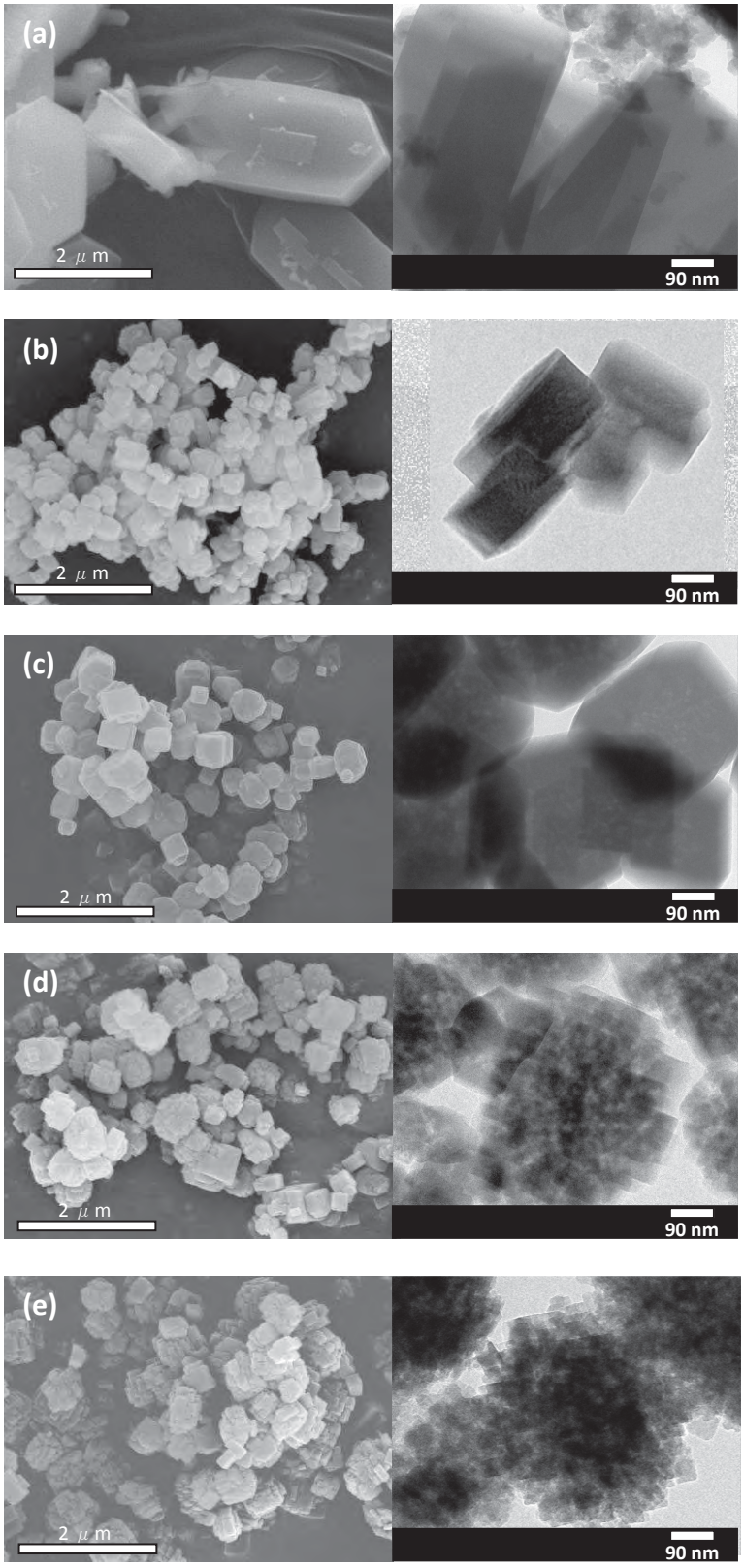

Figure 2.

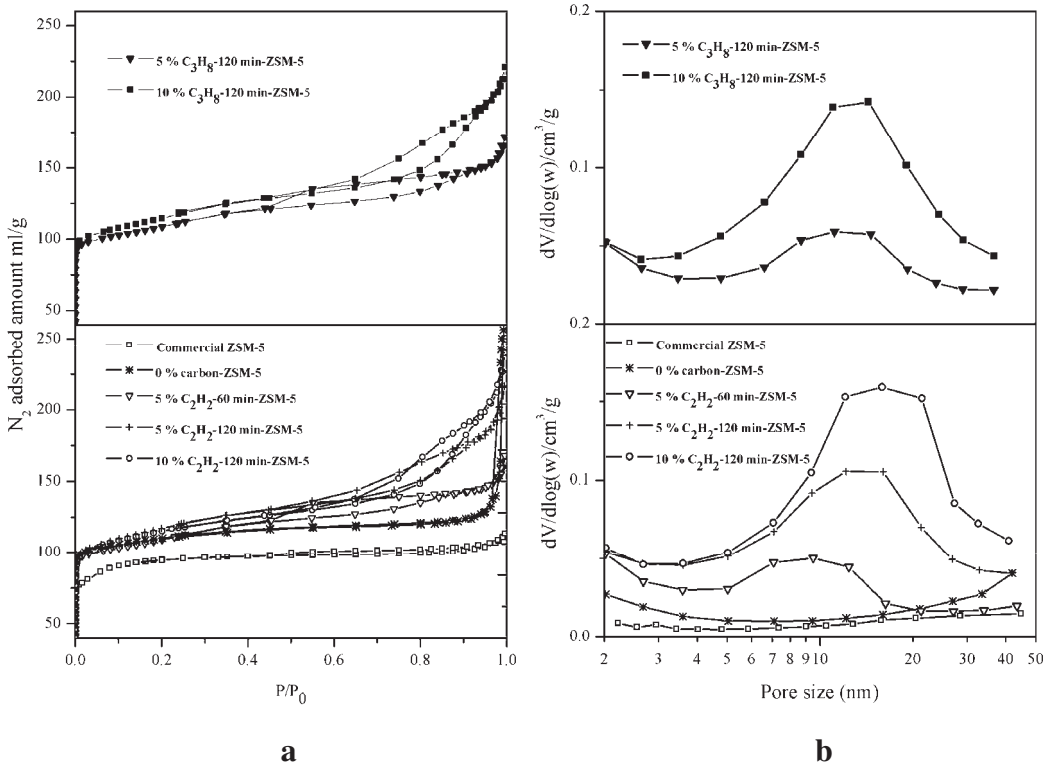

Figure 3.

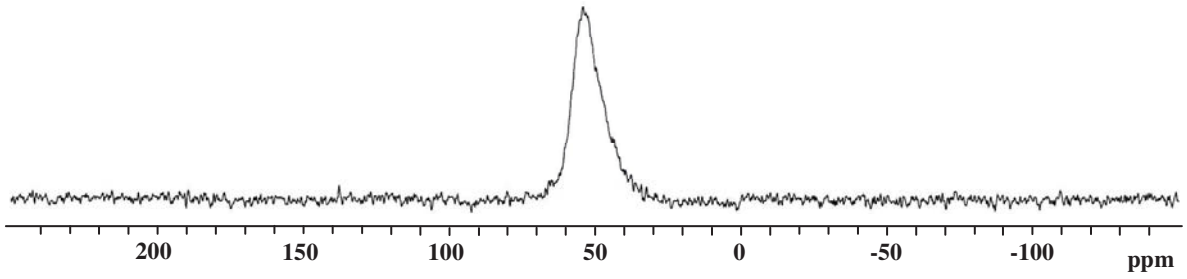

Figure 4.

Table 1. Carbon content and textural properties of the raw silica gel and the SiO_2/C composites prepared by using various experimental conditions.

Sample	Carbon precursor	Deposition time (min)	Carbon (wt%)	S_{BET}[a] (m^2/g)	V_{meso}[b] (cm^3/g)	D_{BJH}[c] (nm)
SiO_2	-	-	-	366	1.00	11
5% C_2H_2-60 min-SiO_2/C	5 v/v% C_2H_2	60	10	323	0.78	9
5% C_2H_2-120 min-SiO_2/C	5 v/v% C_2H_2	120	18	361	0.67	8
10% C_2H_2-120 min-SiO_2/C	10 v/v% C_2H_2	120	29	312	0.51	7
5% C_3H_8-120 min-SiO_2/C	5 v/v% C_3H_8	120	11	276	0.83	11
10% C_3H_8-120 min-SiO_2/C	10 v/v% C_3H_8	120	22	294	0.85	11

[a]S_{BET}: Specific surface area calculated by the BET method in the P/P_0 range of 0.05-0.35

[b]V_{meso}: Mesopore volume calculated by V_{tot}-V_{micro}. The total pore volume, V_{tot}, was calculated at P/P_0 of 0.99.

[c]D_{BJH}: Mesopore diameter calculated from adsorption branch of nitrogen isotherms using BJH method.

Table 2. Surface area and porosity of the synthesized ZSM-5 samples and the commercial ZSM-5.

Sample	S_{BET}[a] (m^2/g)	S_{micro}[b] (m^2/g)	S_{ex}[c] (m^2/g)	V_{tot}[d] (cm^3/g)	V_{micro}[e] (cm^3/g)	$V_{meso+macro}$[f] (cm^3/g)	$V_{meso+macro}/V_{micro}$ (cm^3/g)
0% carbon-ZSM-5	428	335	93	0.22	0.13	0.09[g]	0.69
5% C_2H_2-60 min-ZSM-5	418	281	137	0.23	0.11	0.12	1.09
5% C_2H_2-120 min-ZSM-5	437	269	168	0.30	0.11	0.19	1.73
10% C_2H_2-120 min-ZSM-5	431	281	150	0.33	0.11	0.22	2.00
5% C_3H_8-120 min-ZSM-5	415	278	137	0.24	0.11	0.13	1.18
10% C_3H_8-120 min-ZSM-5	440	280	160	0.30	0.11	0.19	1.73
Commercial ZSM-5	343	321	22	0.16	0.14	0.02	0.14

[a]S_{BET}: From the BET method (P/P_0=0.001-0.03). [b]S_{micro}: from the *t*-plot method. [c]S_{ex}: calculated by S_{BET}-S_{micro}.
[d]V_{tot}: at P/P_0 of 0.97. [e]V_{micro}: calculated by the *t*-plot method. [f]$V_{meso+macro}$: calculated by V_{tot} - V_{micro}..
[g]the macropore volume resulted from the interparticle void space.

บทความทางวิชาการที่เกี่ยวข้องกับ
วัสดุที่มีรูพรุนชนิดอื่นๆ
จำนวน 16 ผลงาน

Journal of Molecular Graphics and Modelling 28 (2009) 62–69

Contents lists available at ScienceDirect

Journal of Molecular Graphics and Modelling

journal homepage: www.elsevier.com/locate/JMGM

Gas sensing properties of platinum derivatives of single-walled carbon nanotubes: A DFT analysis

P. Pannopard [a,b], P. Khongpracha [a,b], M. Probst [c], J. Limtrakul [a,b,*]

[a] Laboratory for Computational & Applied Chemistry, Chemistry Department, Faculty of Science, Kasetsart University, Bangkok 10900, Thailand
[b] Center of Nanotechnology, Kasetsart University Research and Development Institute, Kasetsart University, Bangkok 10900, Thailand
[c] Institute of Ion Physics and Applied Physics, Innsbruck University, Technikerstraße 25, 6020 Innsbruck, Austria

ARTICLE INFO

Article history:
Received 31 October 2008
Received in revised form 23 March 2009
Accepted 11 April 2009
Available online 20 April 2009

Keywords:
Sensor
NO_2
NH_3
Pt–CNT assemblies
Defected CNTs
DFT

ABSTRACT

The limitations of intrinsic carbon nanotube (CNT) based devices to examine toxic gases motivate us to investigate novel sensors which can possibly overcome sensitivity problems. Pt–CNT assemblies (with Pt deposited externally as well as internally Pt-doped ones) interacting with NO_2 and NH_3 are studied and compared with unmodified CNTs. DFT calculations show that Pt can enhance adsorption and charge transfer processes to a very large degree. Incoming gas molecules cause changes in the electronic structure and charge distribution of the Pt-substituted CNTs that are both larger and more far-reaching than in their unmodified counterparts. Their relatively high stability is unaffected by the complexation with NO_2 and NH_3. CNTs with defective surface were also investigated. The sensing performance of Pt-doped CNT is found to be superior to defected CNTs.

1. Introduction

Chemical sensors based on nanowires of semiconducting single-walled carbon nanotubes (SWCNTs) that perform well have been utilized for detecting pollutant and toxic gases like NO_2 and NH_3. Such nano-scale assemblies can achieve high sensitivity and fast response times, even at ambient temperature [1]. The fundamental sensing mechanism for these devices is the modulation of the conductivity of the SWCNT as a result of the charge transfer between it and analyzed gas. Former computational studies indicate that both NO_2 and NH_3 are physisorbed on unmodified-CNT surfaces, causing only a small charge transfer and mildly triggered conductance responses [2–5].

Therefore, there were many attempts to elucidate why experimentally strong signals are observed. Eventually, there are still several assumptions involved. Concerning NO_2 and NH_3, an indirect mechanism is regularly proposed. For instance, in the case of NO_2, NO_3 formation by the reaction of NO_2 with pre-adsorbed oxygen species or, for NH_3, activation by water vapor [1,3], is assumed to be the first step. Such complicated phenomena generally exclude the rational design of improved sensors. We did not consider them when we investigated modified CNTs with respect to their NO_2 and NH_3 sensing capabilities as discussed below.

Amongst the many possible strategies to tailor the selectivity and sensitivity of CNTs, the generation of new active sites on their surface is classically the premier strategy to overcome the drawback of the intrinsically inert CNT structure. The introduction of structural defects on the walls of CNTs, especially ones associated with vacancies, can be expected to enhance the sensitivity for small molecules like NO_2 and NH_3 [6–8]. Furthermore, embedding of foreign atoms or doping makes it possible to detect a wide range of gases by altering the dopants. B-, N- and Al-doped SWCNTs have proven to be highly sensitive to NH_3, NO_2, CO, H_2O and HCOH [9–12]. Interestingly, the so-called decoration of a SWCNTs network with various transition metals allows the fabrication of single-chip devices [13]. This can enlarge the diversity of identified molecular species by combining CNTs decorated with different metals, each for one particular gas. Recent reports impart that the deposited metal–CNTs exhibit enhanced sensitivity, compared to bare CNTs [14]. For example, Pt- and Au-functionalized MWCNTs are more sensitive by an order of magnitude for NH_3 and NO_2 detection. Not only the catalytic role but also the engineering of transducer platforms are vital for sensor development. Typically, the efficiency of sensory support strongly depends on the amount of active locus on the surface which can boost the reactivity and sensitivity. In particular, for the metal–CNTs hybrid scaffold, the generation of small size metal clusters

* Corresponding author at: Laboratory for Computational & Applied Chemistry, Chemistry Department, Faculty of Science and Center of Nanotechnology, Kasetsart University Research and Development Institute, Kasetsart University, Bangkok 10900, Thailand. Tel.: +66 256 25555x2169; fax: +66 256 25555x2176.
E-mail address: jumras.l@ku.ac.th (J. Limtrakul).

1093-3263/$ – see front matter © 2009 Elsevier Inc. All rights reserved.
doi:10.1016/j.jmgm.2009.04.005

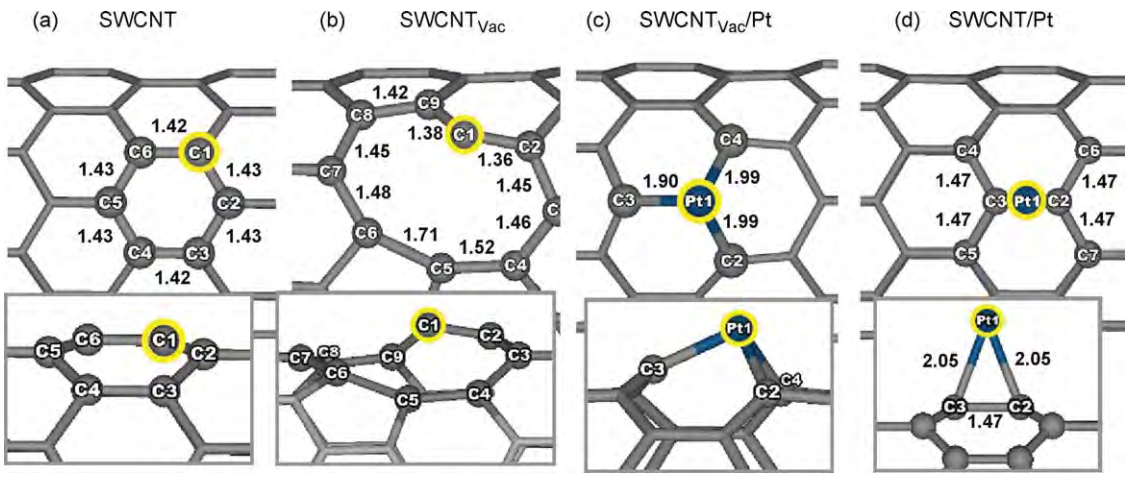

Fig. 1. (a) pristine SWCNT, (b) vacancy SWCNT, (c) Pt-doped SWCNT and (d) Pt-deposited SWCNT. Side views are shown under corresponding pictures. The yellow marks indicate the active site studied for the SWCNTs (a–d). Atom–atom distances (Å) around the active centers are also depicted.

with high content and uniform distribution is indeed realized. The surface adsorption of metal clusters on CNT-sidewalls is a well-known technique in sensing technology [13–16], nevertheless the large size of the metal clusters on the CNT produced by this technique often leads to an unfavorably small specific surface. Recent experiments and calculations indicate that defective CNTs are also capable of improving the Pt loading content and size distribution [17], and also that Pt atoms prefer to adsorb on a vacancy site, resembling conventional doping. Impurity doping works by changing the local chemical reactivity. Pt itself is well-known for its adsorption capabilities of small molecules [18–21]. We compare corresponding properties of pristine SWCNTs, of SWCNT with vacancies ($SWCNT_{Vac}$) and with Pt-deposited on perfect SWCNT (SWCNT/Pt). Ammonia (NH_3) and nitrogen dioxide (NO_2) have been chosen because of their importance as pollutants and industrial toxicants and also because they are good models for electron donors and electron acceptors, respectively.

2. Methodology

Fully optimized geometries and the properties of the systems were derived by means of density functional calculations in the spin-unrestricted generalized gradient approximation by using the DMol^3 code [22,23] with double-numerical polarized (DNP) basis sets. Concerning the density functional we faced certain restrictions with respect to CPU time and the implementation of periodic boundary conditions. This prohibits, for example, using new density functionals like MPWB1K [24–26]. Our calculations were performed with the PW91 [27] density functional which, while not including dispersion energy contributions, can efficiently be applied to large periodic systems. It has been used on a large number of comparable systems in good agreement with experimental information. The interactions between core and valence electrons are represented by DFT semicore pseudopotentials [28]. The real-space orbital cutoff was set to 4.0 Å, the force threshold for optimizations was 0.01 eV and the Brilloiouin zone *k*-point sampling was performed in a $1 \times 1 \times 2$ Monkhorst–Pack mesh [29]. These values of the parameters correspond to a medium-quality calculation which delivers the highest accuracy still computationally feasible for such large systems. Periodic-boundary conditions were applied with a tetragonal unit cell of $20 \times 20 \times 12.78$ Å^3. This is large enough to virtually avoid interactions with images in neighboring cells. An (8,0)SWCNT with 96 carbon atoms was chosen as a model of an unmodified SWCNT. This is a semiconducting SWCNT, a feature that is necessary for the sensor circuit. For this model, we calculated a HOMO–LUMO energy gap of 0.63 eV which agrees well with previous DFT studies [30,31]. From this SWCNT, the models for the Pt-deposited, and Pt-doped, and SWCNTs with vacancy defects were derived. They are shown and explained in Fig. 1.

We investigated different sites of the gas molecules above the hexagonal carbon ring structure of the CNT. NO_2 was oriented parallel or perpendicular to the SWCNT surface. For the latter one, we considered three orientations with N pointing to the SWCNT, with a single O atom or both O atoms pointing to the SWCNT. Likewise, NH_3 was placed above a carbon atom, between two carbons and above the center of a hexagonal ring. For each case, N, one H atom or all three H atoms were oriented towards the CNT surface. The N–H bonds were parallel to the hexagonal carbon framework or rotated away by 60°. Detailed graphs of the initial and optimized structures are available as supplementary information (S1 and S2, respectively).

The binding energies between the gas molecules and the SWCNT were calculated according to:

$$E_b = E_T(\text{support} : \text{gas}) - E_T(\text{support}) - E_T(\text{gas})$$

where E_T (support:gas) is the total energy of a gas molecule adsorbed on the active site of support and E_T (support) and E_T (gas) are the total energies of the support and the gas molecule, respectively. All E_T values refer to quantum chemical energies at optimized geometries. The electronic structure of the energetically most favorable complexes was analyzed in order to estimate the sensing susceptibility with respect to the following properties: partial and net charge transfers were obtained from a Mulliken population analysis. The partial and total density of states (PDOSs and DOSs) were calculated and the frontier molecular orbitals were analyzed. Electron density difference maps of optimized structures were calculated with a plane-wave basis set and ultrasoft pseudopotentials [32] as implemented in the CASTEP program [33].

3. Results and discussion

3.1. Energetics and optimized geometries

We start by considering the optimized geometries of pristine, defective, Pt-doped and Pt-deposited SWCNTs (Fig. 1) which serve as the sensing platforms. Fig. 1a shows the common SWCNT with a typical C–C bond length of about 1.42 Å and a nanotube diameter of 6.38 Å closely matching that of previous studies [30]. In Fig. 1b,

Table 1
Binding energies E_b between Pt and SWCNT and $SWCNT_{Vac}$ and binding energies of NO_2 and NH_3 to the four types of SWCNTs. The structures are shown in Figs. 2 and 3, respectively. The energies are given in kcal/mol.

Sensing support		E_b (SWCNT/Pt)
$SWCNT_{Vac}$/Pt		163.62
SWCNT/Pt		53.39
Sensing support	**E_b (support:NO_2)**	**E_b (support:NH_3)**
SWCNT	1.96	1.33
$SWCNT_{Vac}$	55.90	2.76
$SWCNT_{Vac}$/Pt	50.91	30.52
SWCNT/Pt	34.92	40.96

the single vacancy defected SWCNT is shown. It results from the 12-membered ring created by removing one carbon atom from the graphene sheet and the subsequent reconstruction to a 5-membered ring and a 9-membered ring. It holds one unsaturated carbon (C1), slightly sticking out from the tube surface. The rearrangement deforms the structure to obtain an elliptical cross section with major and minor diameters of 6.56 Å and 6.17 Å, respectively. Doping of the large Pt atom to the vacancy (Fig. 1c) causes a deformation of the nearby hexagonal rings in the doping region. The Pt–C distance is 1.9 Å and Pt protrudes outside of the SWCNT surface. Even though in this structure the SWCNT is apparently distorted (elliptic diameters: 6.49 Å and 6.28 Å), the Pt atom is bound with 163.62 kcal/mol (Table 1). This value is similar to the one reported in [17]. This stabilization can be ascribed to the saturation of the dangling C bonds and the formation of stable hexagonal rings. Consequently, the binding energy in Pt-deposited SWCNT is smaller (53.39 kcal/mol). Fig. 1d shows the energetically most favorable conformation with Pt residing above the C2–C3 bond [34–35] with a Pt–C distance of 2.05 Å. The geometry of the tube is changed due to strong Pt–CNT interaction causing nonidentical diameters with 6.48 Å and 6.29 Å of the longest and the shortest ones, respectively. In a long-lived sensor, the attachment of Pt to the SWCNT must be stable enough to withstand temperature and environmental effects. Although this is difficult to quantify, also the Pt-deposited SWCNT should still be a stable enough device.

3.1.1. NO_2

The most stable optimized geometries, their geometrical parameters and the binding energies of NO_2 adsorption on each support are given in Fig. 2 and Table 1. Nevertheless, there are some experimental and computational studies revealing that the nitro derivative on fullerenes can be found [36,37]. Though, due to the chemically inert CNT system, the functionalization of NO_2 on the CNT sidewall should be more difficult than that of a fullerene surface. One can see that the NO_2 molecule is merely physisorbed on the pristine SWCNT with the lowest absorption energy (1.96 kcal/mol) and a distance of 3.11 Å between N and C. The monomer geometries of the SWCNT and the NO_2 molecules are undisturbed.

In $SWCNT_{Vac}$, the unsaturated carbon atom (C1) binds to the nitrogen atom of NO_2 (r_{C-N} = 1.46 Å) with an interaction energy of 55.90 kcal/mol. The binding can be attributed to the under-coordinated carbon atoms near the vacancy. C1 is the most negatively charged carbon and attracts the partially positively charged N atom of NO_2. Excess electrons are located in the antibonding orbitals of the NO_2 molecule causing a change of the N–O distance from 1.21 Å to 1.24 Å, The stability of the $SWCNT_{Vac}$/Pt:NO_2 complex (50.91 kcal/mol) is similar to that of $SWCNT_{Vac}$. Pt bonds to both oxygens of NO_2 causing an elongation of the N–O bond to 1.28 Å. The interaction between NO_2 and the Pt atom in SWCNT/Pt:NO_2 is similar to the one described above. In our SWCNT/Pt:NO_2 model, the SWCNT–Pt distances increased from 2.05 Å to 2.11 Å after NO_2 binding, indicating that the strong binding of NO_2 (34.92 kcal/mol) comes at the expense of a destabilization of the Pt–SWCNT stability.

3.1.2. NH_3

The most stable optimized geometries of NH_3 adsorbed on each support are shown in Fig. 3, together with the relevant distances. Their binding energies are tabulated in Table 1. In agreement with previous studies [5,9] in the preferred orientation, the hydrogen atoms of NH_3 point towards the SWCNT (Fig. 3a). NH_3 is noncovalently bound with only 1.33 kcal/mol and a C–H distance of about 3.3 Å. In contrast to NO_2, the interaction in $SWCNT_{Vac}$:NH_3 is only slightly stronger (2.76 kcal/mol) because in both cases a hydrogen bonded interaction is the only possibility. Here, the more negatively charged C1 acts as the electron donor and a C···H–N hydrogen bond can be formed (Fig. 3b). These weak interactions mean that materials consisting of both SWCNT and $SWCNT_{Vac}$ are inappropriate sensing platforms for NH_3 detection. In $SWCNT_{Vac}$/Pt:NH_3 and SWCNT/Pt:NH_3, NH_3 is strongly bound. In $SWCNT_{Vac}$/Pt:NH_3 and SWCNT/Pt:NH_3, ammonia is bound by 30.52 and 40.96 kcal/mol. The Pt–N distances are 2.29 and 2.14 Å, respectively. The strong binding of NH_3 to Pt via its nitrogen atom has a larger influence on the active region than the one caused by its

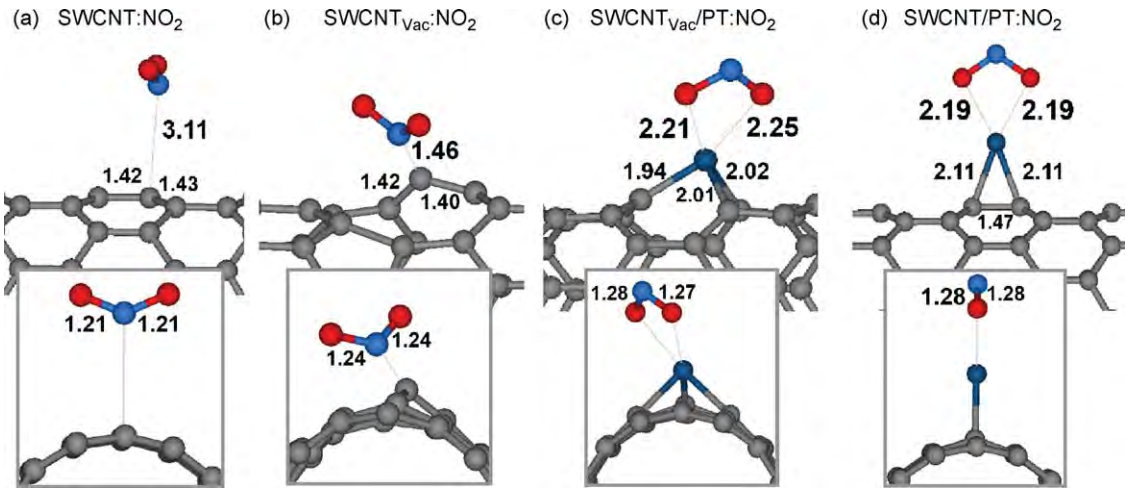

Fig. 2. Front and side views of the most favorable binding geometries of NO_2 on each support type, (a) pristine SWCNT, (b) vacancy SWCNT, (c) Pt-doped SWCNT and (d) Pt-deposited SWCNT, accompanied with their binding distances. Pt–C and some C–C distances (Å) are also given.

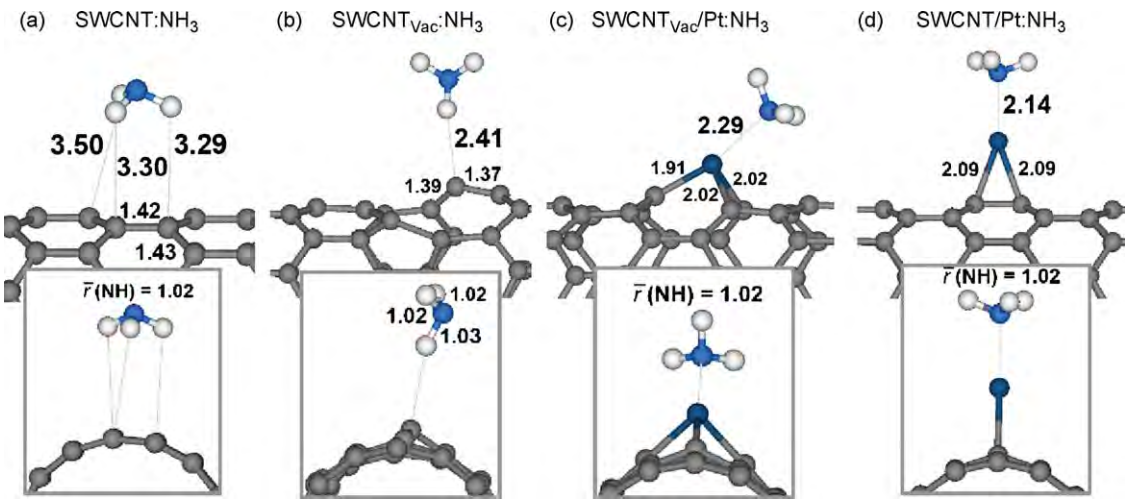

Fig. 3. Front and side views of the most favorable binding geometries of NH3 on each support type, (a) pristine SWCNT, (b) vacancy SWCNT, (c) Pt-doped SWCNT and (d) Pt-deposited SWCNT, accompanied with their binding distances. Pt–C and some C–C distances (Å) are also given..

weak H-bonded interaction with $SWCNT_{Vac}$, as can be seen from the redistribution of electron density (Fig. 4). As expected, the SWCNT–Pt distances increase somewhat from 2.05 Å to 2.09 Å after the NH_3 complexation. The N–H distances of all adsorbed NH_3 molecules are unaffected by the complexation and stay at 1.02 Å. The affinity of SWCNT/Pt to NH_3 approaches already the binding energy of the attached Pt to the SWCNT, which is a disadvantage since it might in practice lead to its destruction.

3.2. Electronic properties of the platform and sensitivity to NO_2 and NH_3

We investigated the effects of gas adsorption on the electronic properties of the SWCNTs by computing the charge transfers (q_{Gas}) between the gas molecule and support and the HOMO–LUMO energy gap modulations (ΔE_g). The results are summarized in Table 2. The quantities in this table are defined as:

$$\Delta E_g = E_g\,(\text{support} : \text{gas}) - E_g\,(\text{bare support})$$
$$\Delta q_{SWCNT} = q_{SWCNT}\,(\text{support} : \text{gas}) - q_{SWCNT}\,(\text{bare support})$$
$$\Delta q_{Pt} = q_{Pt}\,(\text{support} : \text{gas}) - q_{Pt}\,(\text{bare support})$$

In addition, electron densities difference maps HOMO and LUMO orbitals and electronic densities of states (DOSs) have been derived. They are depicted in Figs. 4–8.

3.2.1. NO_2

Since NO_2 is an electron-withdrawing molecule with an unusually large electron affinity between 2 eV and 3 eV [38], electrons are transferred from supports to it (Table 2). For $SWCNT_{Vac}$:NO_2, $SWCNT_{Vac}$/Pt:NO_2 and SWCNT/Pt:NO_2 these shifts amount to −0.27, −0.38 and −0.35*e*, respectively. The values for SWCNT/Pt:NO_2 and $SWCNT_{Vac}$/Pt:NO_2 are similar, but a more detailed analysis shows some differences. The positive value of Δq_{SWCNT} in $SWCNT_{Vac}$/Pt:NO_2 (0.32*e*) is larger than the one in SWCNT/Pt:NO_2 (0.22*e*). Three-dimensional plots of the differential electron density can give detailed information of the rearrangement of the complex formation. Fig. 4 shows isosurfaces of certain density changes. It can be seen that NO_2 adsorption (Fig. 4a–d) on $SWCNT_{Vac}$/Pt causes a depletion of electron density (Fig. 4c) throughout, which is expected to change the electric properties of the nanotube dramatically. In contrast, electron relocation in SWCNT/Pt:NO_2 occurs only locally at the Pt–NO_2 moiety. The change of the energy gap (ΔE_g) during the adsorption process is also related to the sensitivity of a sensor for a particular analyte. In Table 2, a negative sign of ΔE_g refers to a reduction of the energy gap in the complex compared to the bare support. We find that the energy gaps of all systems decrease after NO_2 adsorption by −0.32, −0.14, −0.25 and −0.41 eV for SWCNT:NO_2, $SWCNT_{Vac}$:NO_2, $SWCNT_{Vac}$/Pt:NO_2 and SWCNT/Pt:NO_2, respectively. This agrees

Table 2
Partial molecular and atomic charges $q(e)$ and values of the HOMO–LUMO gap E_g (eV) of all studied complexes. Partial charge transfers and energy gap changes are indicated by the prefix delta (Δ). Refer to text for the definitions of the quantities.

System	E_g	q_{SWCNT}	q_{Pt}
SWCNT	0.63	0.00	
$SWCNT_{Vac}$	0.26	0.00	
$SWCNT_{Vac}$/Pt	0.39	0.12	−0.12
SWCNT/Pt	0.58	0.05	−0.05

System	E_g	q_{SWCNT}	q_{Pt}	q_{Gas}	[a]ΔE_g	[b]Δq_{SWCNT}	[c]Δq_{Pt}
SWCNT:NO_2	0.31	0.05		−0.05	−0.32	0.05	
$SWCNT_{Vac}$:NO_2	0.12	0.27		−0.27	−0.14	0.27	
$SWCNT_{Vac}$/Pt:NO_2	0.14	0.44	−0.06	−0.38	−0.25	0.32	0.06
SWCNT/Pt:NO_2	0.17	0.27	0.08	−0.35	−0.41	0.22	0.13
SWCNT:NH_3	0.63	−0.01		0.01	0.00	−0.01	
$SWCNT_{Vac}$:NH_3	0.28	0.01		−0.01	0.02	0.01	
$SWCNT_{Vac}$/Pt:NH_3	0.29	−0.09	−0.18	0.27	−0.10	−0.21	−0.06
SWCNT/Pt:NH_3	0.62	−0.06	−0.22	0.28	0.04	−0.11	−0.17

[a] $\Delta E_g = E_g$ (support:gas) − E_g (bare support).
[b] $\Delta q_{SWCNT} = q_{SWCNT}$ (support:gas) − q_{SWCNT} (bare support).
[c] $\Delta q_{Pt} = q_{Pt}$ (support:gas) − q_{Pt} (bare support).

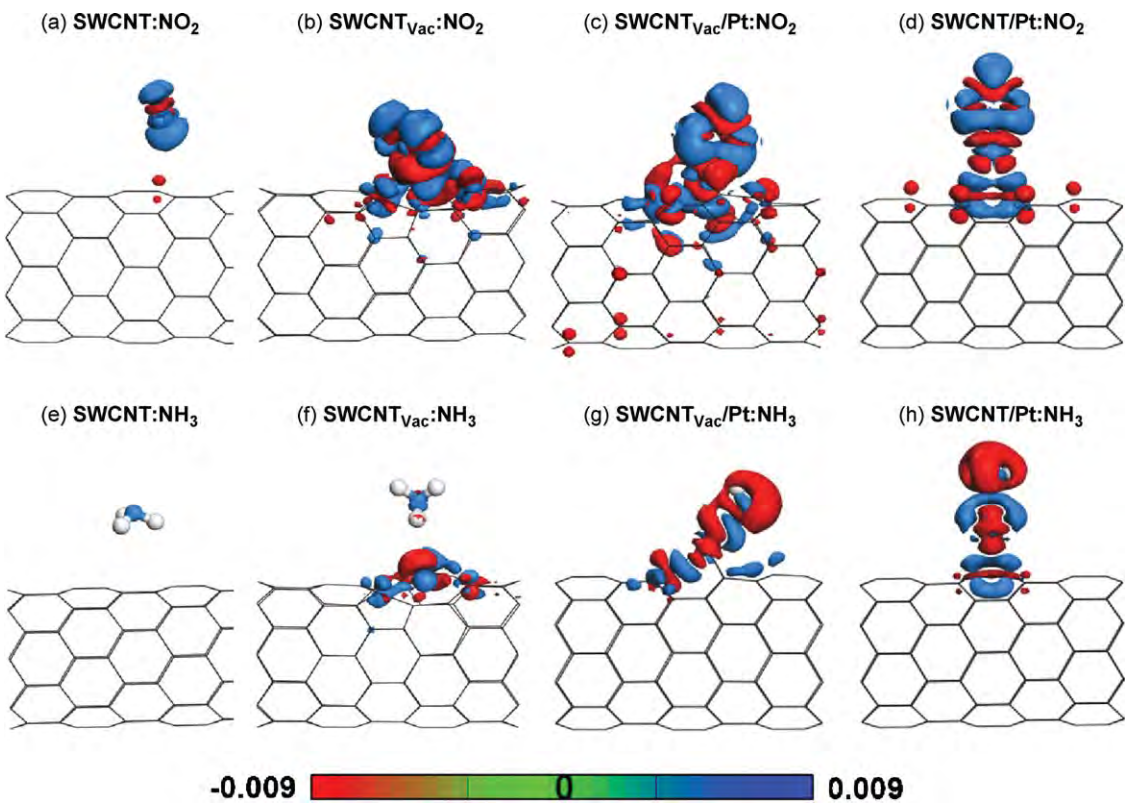

Fig. 4. Plots of the differential electron densities of all studied support-gas complexes, support-NO_2 complexes (a–d) and support-NH_3 complexes (e–h). The 3D-surfaces are plotted at isovalues of $\pm 0.009e/Å^3$. A red color denotes loss of density whereas blue denotes gain of electron density.

well with experimental reports that the conductivity of CNTs, defected-CNTs and Pt-doped–CNTs increase when exposed to NO_2 [1,4,14]. Electron density transfer to NO_2 generates holes in the support. The enhanced conductivities are directly related to the abundance of hole carriers, so these pristine and modified SWCNTs behave as p-type semiconductors as well and are also susceptible to become metallic after stimulated by NO_2, especially in the $SWCNT_{Vac}$:NO_2, $SWCNT_{Vac}$/Pt:NO_2 and SWCNT/Pt:NO_2 systems.

One can further see that the ΔE_g values are proportional to the amount of charge transfer, except for ΔE_g of SWCNT where NO_2 is very weakly bound. To clarify this further, we analyze the DOSs and PDOSs (Fig. 5). Comparing the DOS diagrams of SWCNT:NO_2 and SWCNT (Fig. 5e and a, respectively), one sees the appearance of an acceptor state in the middle of the HOMO–LUMO gap of the SWCNT, when NO_2 is bound [39]. When this state receives electrons from the valence band of the SWCNT the resistance of the system should decrease. Since this state is contributed from the NO_2 radical, as is indicated by the PDOSs and LUMO scheme of SWCNT:NO_2 (Figs. 5i and 6e, respectively), it is plausible that the measured energy gaps vary with the number of NO_2 molecules. SWCNT/Pt exhibits the highest change ΔE_g of its energy gap when NO_2 is bound to it (Table 2). However, that does not much affect the electronic structure of the SWCNT, as can be seen by the charge and electron density differences in Table 2 ($\Delta q_{SWCNT} = 0.22e$) and Fig. 4d, respectively. Moreover, the HOMO and LUMO orbitals (Fig. 6d and h, respectively), to which ΔE_g is related, have prominent contributions only in the area close to Pt and NO_2 and mostly involve the d-orbitals of Pt. Also the partial density of states distribution (Fig. 5n) shows the density near the Fermi level in SWCNT/Pt:NO_2 originating from these d-orbitals. The HOMO and LUMO of $SWCNT_{Vac}$/Pt:NO_2 (Fig. 6c and g, respectively) contain AO contributions from Pt and from the p-orbitals of the NO_2 oxygen atoms as well as from the nanotube mixed into the molecular orbitals of the whole system whereas in SWCN/Pt:NO_2, solely the first two and not the nanotube contribute to the frontier orbitals. Accordingly, despite the larger value of ΔE_g, in SWCNT/Pt:NO_2, its localized response to NO_2 binding makes it less suitable as a sensor.

3.2.2. NH_3

In this section we discuss the sensitivity of the three supports to NH_3 detecting. The lone pair electrons at the N atom of NH_3 can readily be donated to the molecule interacting with it. Consequently, the charge of adsorbed NH_3 is positive by 0.01, 0.27 and $0.28e$ in SWCNT:NH_3, $SWCNT_{Vac}$/Pt:NH_3 and SWCNT/Pt:NH_3, respectively, except for $SWCNT_{Vac}$:NH_3 ($-0.01e$) where C···H–N resembles a hydrogen bond and H–N behaves as the electron acceptor. The complexes with weak adsorption via the H atom, i.e. SWCNT:NH_3 and $SWCNT_{Vac}$:NH_3, also exhibit insignificant charge transfers of only 0.01 and $-0.01e$, respectively. Together with the unnoticeable electron density difference, the energy gap is also unchanged. This is associated with the bare SWCNT character of the PDOSs near the Fermi level (Fig. 7i and j) and is also visible in the HOMO–LUMO pictures of both complexes (Fig. 8a, b, e and f). This infers that SWCNT and $SWCNT_{Vac}$ have very low sensibility to NH_3 gas.

Extraordinary large charge transfers are found in $SWCNT_{Vac}$/Pt:NH_3 and SWCNT/Pt:NH_3 with values of 0.27 and $0.28e$, respectively. Amounts and directions of NH_3 charge transfer of both complexes are quite similar and also their electron density difference maps are similar as shown in Fig. 4g and h, respectively. The better efficiency is derived from the existence of the Pt active site and N-contacted mode which enhance the outflow of nitrogen lone pair electron density. Generally, giving up electrons from NH_3 to a p-type semiconductor support reduces the hole carrier density and thus decreases the conductivity of the system, correlated with the widening of its HOMO–LUMO gap [1]. Even though the flows of

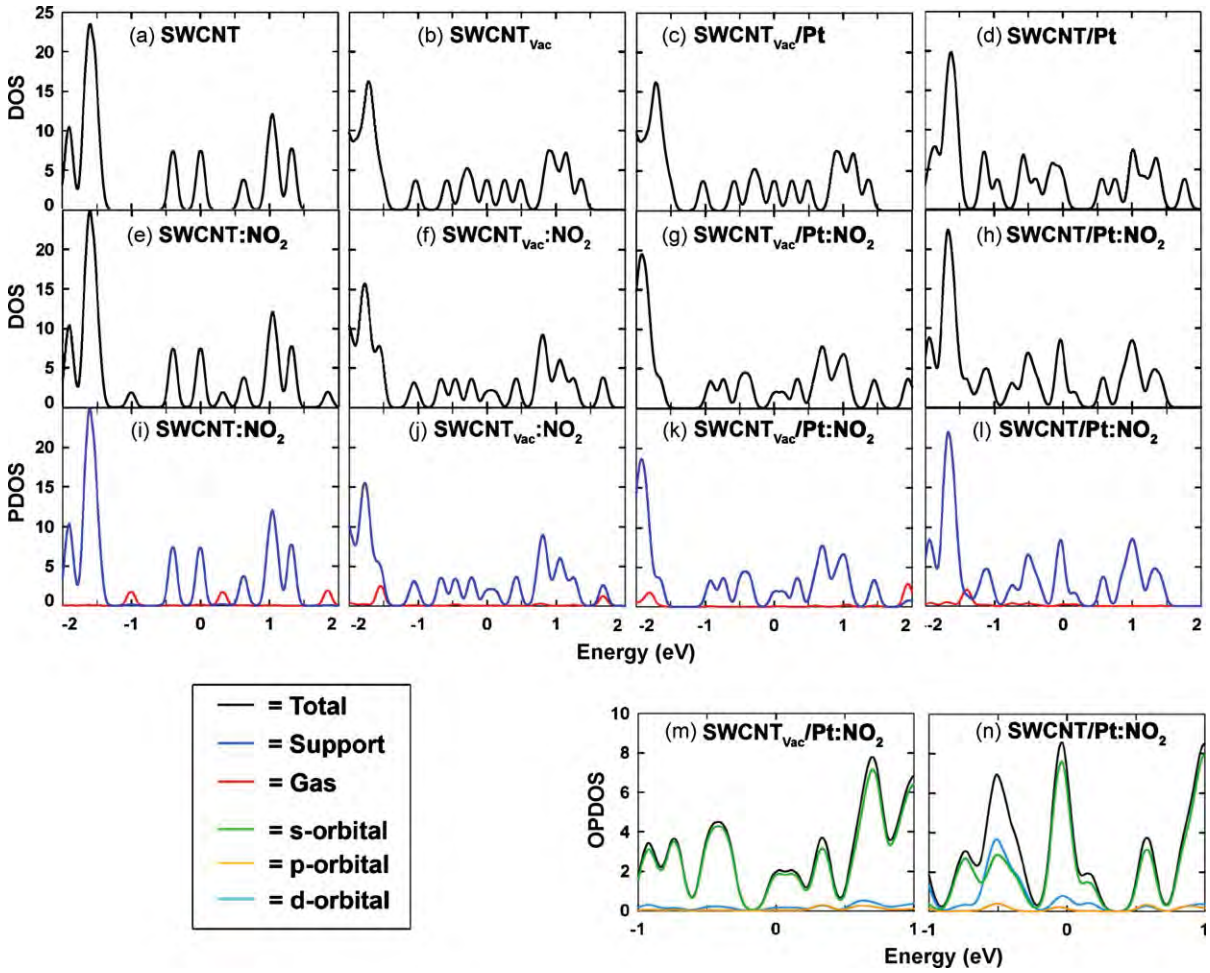

Fig. 5. Density of states (DOSs) for the studied supports (a–d) and their NO_2 complexes (e–h). Partial density of states (PDOSs) of all support-gas complexes (i–l) and orbital partial density of states (OPDOSs) of $SWCNT_{Vac}/Pt:NO_2$ and $SWCNT/Pt:NO_2$ (m and n) are also plotted for comparison. The Fermi levels (defined as the HOMO energies) are calibrated to locate at 0 eV.

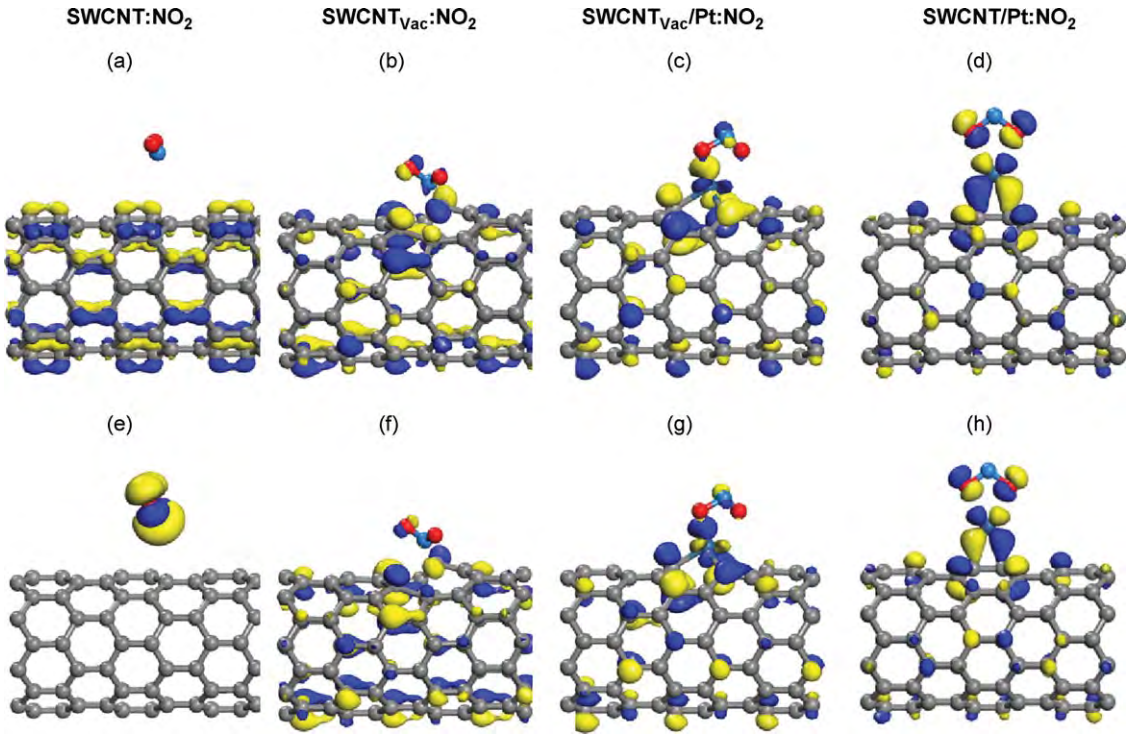

Fig. 6. Frontier molecular orbitals of the complexes with NO_2: HOMOs (a–d) and LUMOs (e–h).

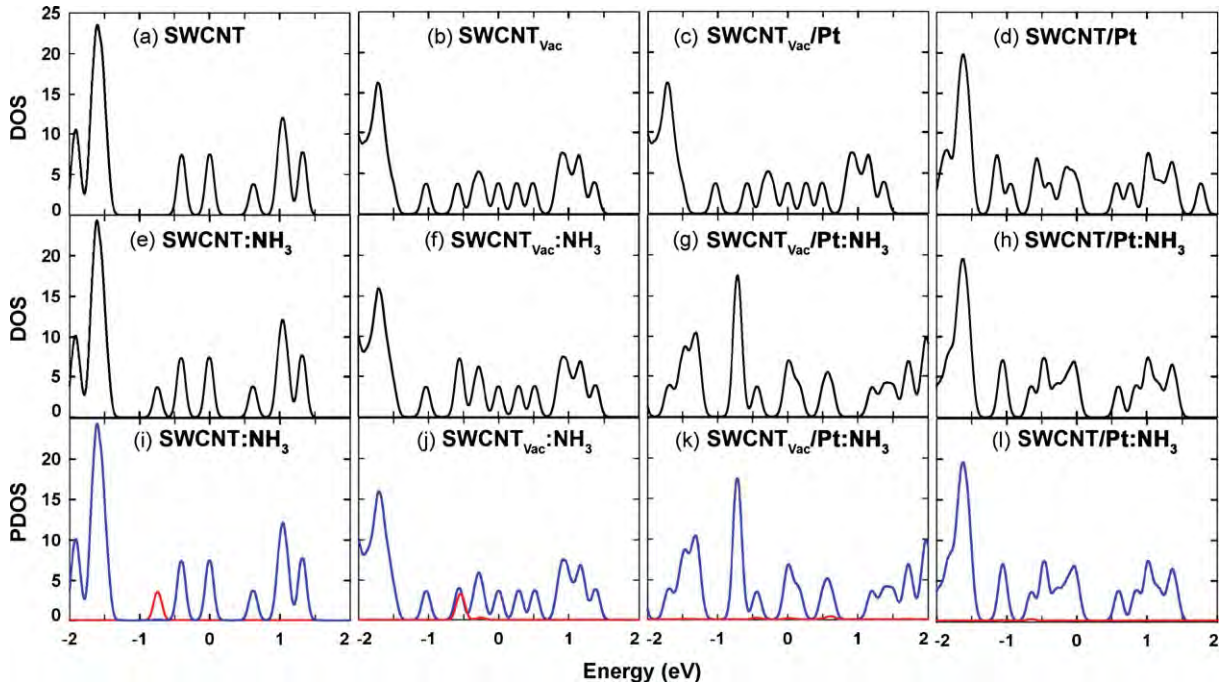

Fig. 7. Density of states (DOS) for all studied supports (a–d) and their NH_3 complexes (e–h). Partial density of states (PDOS) of all support-gas complexes (i–l) are also plotted for comparison (blue lines: support; red lines: contributions from NH_3). The Fermi levels (defined as HOMO energies) are calibrated to locate at 0 eV.

NH_3 electrons into SWCNT$_{Vac}$/Pt:NH_3 and SWCNT/Pt:NH_3 have the same direction, which indicates that they become less conductive, the signs of their ΔE_g values which represent how the conductivity changes are opposite. The energy gap of SWCNT/Pt:NH_3 is slightly widened (0.04 eV) whereas that of the SWCNT$_{Vac}$/Pt:NH_3 is significantly narrowed (−0.10 eV). These phenomena should principally interrelate to the electron redistribution in the support, especially of the SWCNT since the PDOSs near the Fermi level (Fig. 7k and l) and HOMO–LUMO features of both complexes (Fig. 8c, d, g and h) are merely contributed from it. Both Δq_{SWCNT} values of SWCNT$_{Vac}$/Pt:NH_3 and SWCNT/Pt:NH_3 are negative (−0.21e and −0.11e, respectively) due to the accumulation of electrons in the SWCNTs. Remarkably, the SWCNT$_{Vac}$/Pt:NH_3 tube can receive twice the electron density than SWCNT/Pt:NH_3 does. This can change its electrical characteristic from p-type to n-type, which explains the observed increase in the conductivity after NH_3 adsorption. The reason for the poorer electron transfer to SWCNT in SWCNT/Pt:NH_3 is the weaker interaction between SWCNT and

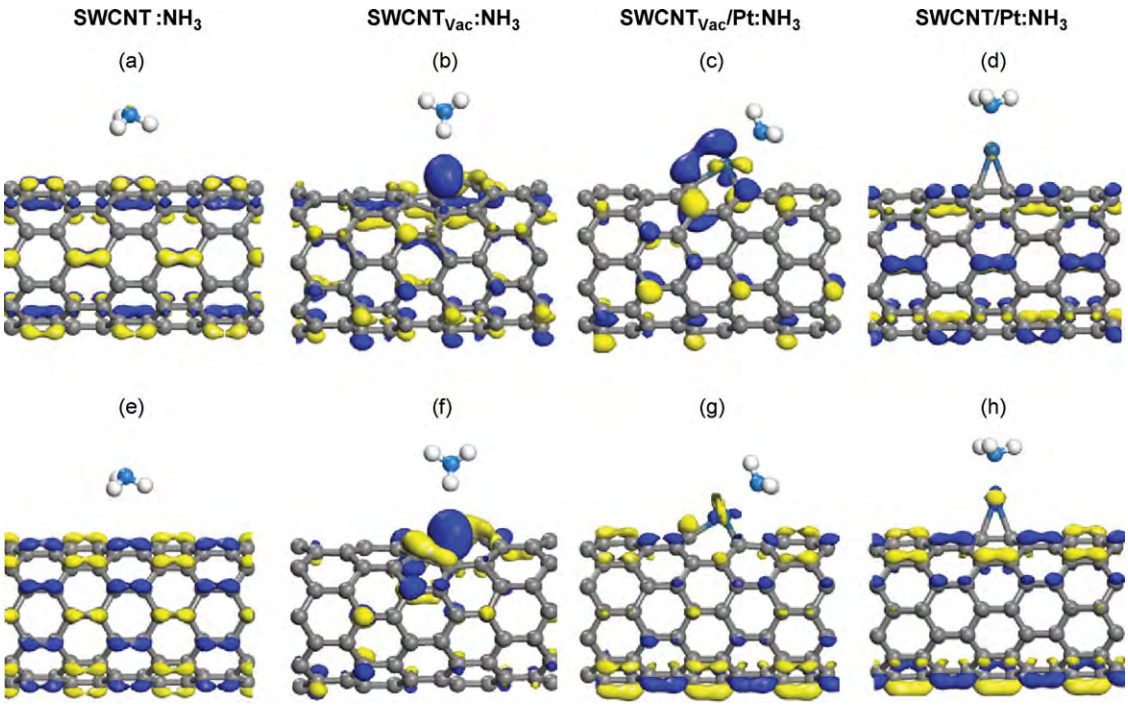

Fig. 8. Frontier molecular orbitals of all studied support-NH_3 complexes, HOMOs (a–d) and LUMOs (e–h).